BLAST PERFORMANCE OF REINFORCED CONCRETE BEAMS CONSTRUCTED WITH HIGH-STRENGTH CONCRETE AND HIGH-STRENGTH REINFORCEMENT

By

Yang Li

Thesis submitted to the
Faculty of Graduate Studies and Research
in partial fulfillment of the requirements for the degree of
Master of Applied Sciences
in Civil Engineering

uOttawa

Department of Civil Engineering
Faculty of Engineering
University of Ottawa

ABSTRACT

This thesis focuses on the dynamic and static behaviour of reinforced concrete beams built using high-strength concrete and high-strength steel reinforcement. As part of this study, a total of 8 high-strength concrete beams, built with and without steel fibres, and reinforced with high strength ASTM A1035 bars are tested under simulated blast loading using the University of Ottawa shock-tube, with an additional 3 companion beams tested under quasi-static loading. The variables considered in this study include: concrete type, fibre content, steel reinforcement ratio and steel reinforcement type. The behaviour of the beams with high-strength steel bars is compared to a companion set of beams reinforced with conventional steel reinforcement. The criteria used to evaluate the blast performance of the beams includes: overall blast capacity, maximum and residual displacements, secondary fragmentation and crack control. The dynamic results show that high strength concrete beams reinforced with high-strength steel are able to resist higher blast loads and reduce displacements when compared to companion beams with conventional steel reinforcement. The results also demonstrate that the addition of steel fibres is effective in controlling crack formation, minimizing secondary blast fragments, reducing displacements and further increasing overall blast capacity. However, the use of high-strength steel and high-strength concrete also shows potential for brittle failures under extreme blast pressures. The static results show that specimens with high-strength steel bars do not increase beam stiffness, but significantly increase peak load carrying capacity when compared to beams with the same ratio of conventional steel reinforcement. The analytical research program aims at predicting the response of the test beams using dynamic inelastic single-degree-of-freedom (SDOF) analysis and includes a sensitivity analysis examining the effect of various modelling parameters on the response predictions. Overall the analytical results demonstrate that SDOF analysis can be used to predict the blast response of beams built with high-strength concrete and steel reinforcement with acceptable accuracy.

ACKNOWLEDGEMENTS

I would like to take this opportunity to express my gratitude to all whom supported me through this project.

In particular, I would like to thank my thesis supervisor, Dr. Hassan Aoude, for offering his support and knowledge while guiding me through my research. I would also like to thank Dr. Gamal Elnabelsya and Dr. Muslim Majeed for their help in the lab and my colleagues for their help with the process of preparing, casting and testing my various specimens, I would like to thank my fellow colleagues Omar Algassem, Ahmed Sulaiman, Sarah De Carufel, Tommy Hains and Steve Castonguay.

Finally, thanks also go to my family whom always encouraged me to do my best and never give up.

NOTATIONS

Symbol	Definition
A	Area impacted by the blast pressure
d_b	Steel reinforcement bar diameter
d_f	Fibre diameter
E_c	Modulus of elasticity, concrete
E_s	Modulus of elasticity, steel
f_{ctf}	Fibre reinforced concrete tensile stress
f_{cu}	Unconfined concrete stress
f_{cuf}	Unconfined fibre reinforced concrete stress
f_c'	Compressive concrete strength
f_{cu}'	Unconfined compressive concrete strength
f_{cuf}'	Unconfined compressive fibre reinforced concrete strength
f_{dc}'	Design compressive concrete strength
f_{du}	Design steel ultimate stress
f_{dy}	Design steel yield stress
$f_{fct,eq}$	Equivalent flexural strength
f_s	Steel stress
f_{sh}	Steel strain hardening stress
f_u	Steel ultimate stress
f_y	Steel yield stress
F_m	Mean load
I_r	Reflected impulse
K_{LM}	Load mass transformation factor
L_d	Driver length
l_f	Fibre length
m	Total mass of the system
P_r	Reflected pressure
P_d	Driver pressure
R	Resistance of the member
RI_v	Reinforcing index
t_P	Positive phase duration
u	Deflection at mid-height
$\ddot{u}$	Acceleration at mid-height
v_f	Fibre volume ratio
ε_{20cu}	Unconfined concrete strain at 20% of peak stress
ε_{50cu}	Unconfined concrete strain at 50% of peak stress
ε_{cu}	Unconfined concrete strain

ε_{cuf}	Unconfined fibre reinforced concrete strain
ε_0	Unconfined concrete strain at peak stress
ε_{0f}	Unconfined fibre reinforced concrete strain at peak stress
ε_s	Steel strain
ε_{sh}	Steel strain hardening strain
ε_u	Steel ultimate strain
ε_y	Steel yield strain
$\dot{\varepsilon}$	Strain rate
$\dot{\varepsilon}_s$	Static strain rate
δ_{anls}	Analytical displacement
δ_{exp}	Experimental displacement
δ_{max}	Maximum displacement
δ_{res}	Residual displacement
θ_{max}	Maximum support rotation
τ_{bond}	Matrix bond strength

ACRONYMS

Acronym	Definition
ACI	American Concrete Institute
ASTM	American Society of Testing and Materials
ATC	Applied Technology Council
BLS	Blast loading simulator
CEB	Comité euro-international du béton (Euro-international Concrete Committee)
CSA	Canadian Standards Association
DIF	Dynamic increase factor
FRP	Fibre reinforced polymer
HL	Hairline (crack width)
HS	High strength (steel reinforcement)
HSC	High strength concrete
HSFRC	High strength fibre reinforced concrete
HSS	Hollow steel section
LTD	Load transfer device
LVDT	Linear variable displacement transducer
MMFX	Microcomposite multistructural formable steel
NBCC	National Building Code of Canada
NEHRP	National Earthquake Hazards Reduction Program
NS	Normal strength (steel reinforcement)
NSC	Normal strength concrete
NSR	Normal strength reinforcement
RPC	Reactive powder concrete
SCC	Self-consolidating concrete
SDOF	Single degree of freedom
SFRC	Steel fibre reinforced concrete
SHPB	Split Hopkinson Pressure Bar
TNT	Trinitrotoluene
UFC	Unified Facilities Criteria

Table of content

Lists of Figures

Lists of Tables

CHAPTER 1. INTRODUCTION

1.1. GENERAL CONTEXT

The mitigation of blast loads on reinforced concrete structures has become a major concern for the safety of people and resilience of buildings and infrastructure. Historical events including accidental explosions such as the Tolouse ammonium nitrate plant explosion (France, 2001), the Texas City disaster (USA, 1947), the Halifax harbour explosion (Canada, 1917) and the Lac-Mégantic rail disaster (Canada, 2013), and terrorist incidents, such as the Oklahoma City bombing (USA, 1995) and Khobar Towers Bombing (Saudi Arabia, 1996) demonstrate the necessity to investigate effective methods to increase the blast resilience of concrete structures.

High-strength concrete (HSC) and high-strength reinforcement offer engineers an effective way to increase member resistance, while also allowing for reductions in structural dimensions and reinforcement congestion. The use of high-strength concrete and steel may also be effective in increasing the blast capacity of reinforced concrete elements. However, the reduced ductility of these materials may make structural components more susceptible to brittle failures under blast loads. The use of steel fibres is one potential solution to this problem. The provision of steel fibres can be used to reduce the brittleness of high-strength concrete, while also increasing its toughness and fragmentation resistance. Fibres can also be effective in increasing the shear capacity and flexural ductility of elements reinforced with high-strength bars. There are limited studies in the literature related to the blast performance of large-scale reinforced concrete members built with high-strength concrete and steel materials. There is a need for research data to examine the potential benefits of implementing these materials in structural components subjected to extreme blast loading.

1.2. RESEARCH OBJECTIVES

The primary objective of this thesis is to conduct an experimental study in order to investigate the static and blast performance of reinforced concrete beams built with high-strength concrete and high-strength reinforcement. The study investigates the influence of various parameters such as concrete strength, steel fibres, reinforcement ratio and type. The research program also examines the suitability of using dynamic inelastic single-degree-of-freedom (SDOF) analysis to predict the blast response of reinforced concrete beams built with high-strength concrete and steel materials.

1.3. SCOPE OF WORK

A total of eleven reinforced concrete beams are tested in this study, including eight beams which are tested under blast loading, and three companion beams which are tested under quasi-static four-point bending. The design parameters investigated in the study include:

- The effect of concrete strength, with two types of concrete: normal-strength self-consolidating concrete (SCC) and high-strength concrete (HSC);

- The effect of longitudinal reinforcement ratio, with beams constructed with 2-#4, 2-#5, and 2-#6 ASTM A1035 Grade 100 high-strength (HS) steel;
- The effects of steel fibres, with companion high-strength concrete beams constructed with and without steel fibres (0 vs. 1% fibre content);
- The effect of the steel reinforcement type, with the performance of the beams with HS steel compared to a companion set of beams with normal-strength (NS) steel.

In the dynamic series, the specimens were tested under gradually increasing blast pressures using the University of Ottawa Shock-Tube. The effects of the variable parameters are investigated by comparing the performance of companion beams subjected to the same blast histories. Performance criteria for dynamic testing include the magnitude of failure blasts, failure mode, the maximum and residual displacements, crack control and secondary fragmentation mitigation. For the static testing, load resistance, ductility and failure mode are considered as performance criteria. Dynamic inelastic single-degree-of-freedom (SDOF) analysis, with the development of resistance curves using strain-rate dependent material models, is conducted to predict the dynamic response of the test specimens. The analytical study also includes a sensitivity analysis examining the effect of material model and DIF combinations on the analytical predictions.

1.4. THESIS BREAKDOWN

This document contains seven chapters divided as listed below:

Chapter 1 - Introduction:

- Introduces the significance of this research, describes the various objectives and defines the scope of work.

Chapter 2 - Literature review:

- Provides background information related to the thesis topic and summarizes previous research on the static and blast performance of reinforced concrete flexural members built with high-strength concrete, steel fibres, and high-strength steel reinforcement.

Chapter 3 - Experimental program:

- Describes the static and dynamic experimental programs, including the definition of specimens, material parameters, test setups and testing protocols.

Chapter 4 – Results and discussion of the static tests:

- Summarizes the data obtained from the static experimental program, and discusses the effects of the reinforcement ratio and strength of the reinforcement on flexural response.

Chapter 5 – Experimental results of the dynamic tests:

- Summarizes the data obtained from the dynamic experimental program and describes the individual behaviour of the specimens for each blast test.

Chapter 6 – Discussion of the dynamic test results:

- Summarizes various observations related to the effects of the concrete strength, steel fibres, the reinforcement ratio and the steel reinforcement type by comparing the response and damage criteria of companion specimens.

Chapter 7 – Dynamic and static analysis:

- Defines material and dynamic increase factor (DIF) models considered in the analysis, and the prediction of the blast response (maximum displacements) of each specimen using a single-degree-of-freedom (SDOF) approach.
- Presents the analytical predictions of the static beam resistance curves and compares the experimental and analytical results.
- Compares the effect of various material and DIF model combinations on the accuracy of the analytical displacement predictions.

Chapter 8 – Conclusion:

- Presents final remarks and highlights the conclusions from this research and proposes recommendation for further research.

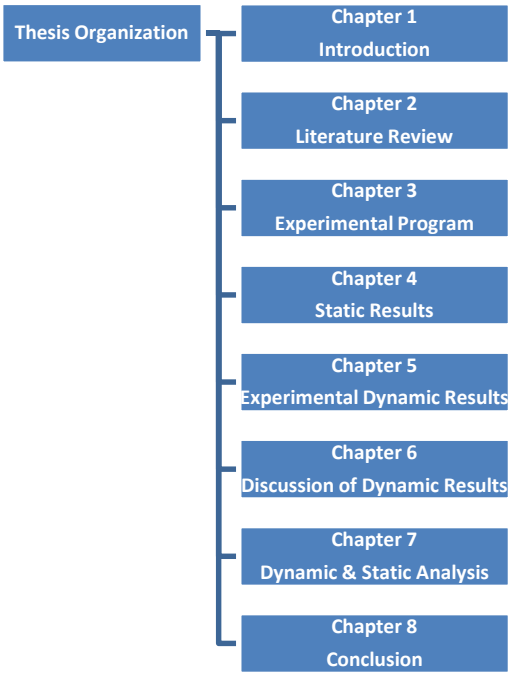

Figure 1-1 Thesis organization

CHAPTER 2. LITERATURE REVIEW

2.1. CHAPTER OVERVIEW

This chapter provides a literature review related to the thesis research topic. The chapter begins with an introduction to the materials used in this study. The effect of dynamic loading on material properties is also reviewed. Next a review of previous research focussing on the flexural behaviour of reinforced concrete beams built with high-strength reinforcement or HSFRC is presented. The chapter ends with an overview of previous experimental research on reinforced concrete flexural elements tested under blast loads, with a focus on beams as well as research which has investigated the performance of members built with high-strength concrete, steel fibres or high-strength steel reinforcement.

2.2. MATERIALS REVIEW

This section provides a brief introduction to the materials used in the research study which include: high-strength concrete (HSC), high-strength fibre reinforced concrete (HSFRC) and high-strength ASTM A1035 steel reinforcement. The section ends with an introduction to high strain-rate effects on material properties with a review of dynamic increase factor models.

2.2.1. HIGH-STRENGTH REINFORCEMENT

2.2.1.1. Types of high-strength steel reinforcement and design guidelines

In the last few decades, steel reinforcement with yield strength of 60 ksi (400 MPa) has been widely utilized in reinforced concrete structures. In the early 1960s the American Society for Testing and Materials (ASTM) published specifications related to Grade 60 and 75 bars, and shortly thereafter the 1963 edition of the ACI 318 code permitted the use of steel reinforcement with yield strength of 60 ksi (ATC, 2014). Based on extensive research, design requirements for the use of this reinforcement type are now well established in North American design standards.

High-strength reinforcement can be defined as steel with a yield strength of 72 ksi (500 MPa) or greater (NEHRP, 2014). This type of reinforcement is now commonly available worldwide. High-strength reinforcing bars developed in Japan include: USD 685 & USD 980 intended for use as flexural reinforcement with yield strengths of 100 ksi (690 MPa) & 142 ksi (980 MPa), and USD 785 & USD1275 intended for use as transverse reinforcement with yield strengths of 114 ksi & 185 ksi (1275 MPa), respectively. In North America, Grade 80 reinforcement is referenced in the ASTM A615 and A706 specifications. The steel used in the current study (MMFX) is referenced in ASTM A1035 "Standard specification for deformed and plain, low-carbon chromium, steel bars for concrete reinforcement", and includes Grade 100 and 120 steel bars. The structural use of high-

strength bars has potential benefits which include reduced reinforcement congestion, improved constructability and more efficient design sections.

Current North American design codes such as the ACI 318 code and CSA A23.3 standard impose limits related to the design strength of reinforcing bars in structural components. For example, the CSA A23.3-14 standard limits the design yield strength of bars in flexural members to 500 MPa (70 ksi). Similarly, both the ACI-318 and CSA A23.3 impose strict requirements related to use of high-strength reinforcement in seismic design applications.

ACI ITG-6R "*Design Guide for the Use of ASTM A1035/A1035M Grade 100 Steel Bars for Structural Concrete*" (ACI, 2011a) provides design recommendations for the structural use of ASTM A1035 reinforcement in elements such as beams, columns, slabs, walls and foundations. The recommendations in this report propose guidelines to address limitations related to use of high-strength bars in the ACI 318 code.

ICC Evaluation Service Report ESR 2107 (ICC-ES, 2014) provides additional guidance and acceptance criteria for the design of concrete structures utilizing ASTM A1035 Grade 100 bars and complies with the 2012 International Building Code. Table 2-1 shows recommended specified yield strengths for the design of various types of structural members reinforced with Grade 100 MMFX bars.

Table 2-1 Specified yield strengths for design of members using ASTM A1035/A1035M GRADE 100 reinforcement (Adapted from ICC Evaluation Report ESR 2107, 2014)

TYPE OF MEMBER	LONGITUDINAL REINFORCEMENT		TRANSVERSE REINFORCEMENT		
	Tension, psi (MPa)	Compression, psi (MPa)	Shear, psi (MPa)	Torsion, psi (MPa)	Confinement, psi (MPa)
Beams and one-way slabs	100,000 (690)	80,000 (550)	80,000 (550)	60,000 (410)	N/A
Columns	100,000 (690)	80,000 (550)	80,000 (550)	60,000 (410)	100,000 (690)[2]
Tension ties	80,000 (550)	N/A	N/A	N/A	N/A
Compression struts	N/A	80,000 (550)	N/A	N/A	N/A
Two-way slabs	100,000 (690)	80,000 (550)	60,000 (410)	60,000 (410)	N/A
Walls	100,000 (690)	80,000 (550)	80,000 (550)	N/A	100,000 (690)[3]
Footings and pile caps	100,000 (690)	80,000 (550)	80,000 (550)	60,000 (410)	N/A
Mat foundations	100,000 (690)	80,000 (550)	80,000 (550)	N/A	N/A

2.2.1.2. Overview of ASTM A1035 (MMFX) steel

MMFX bars are low-carbon, chromium alloy reinforcing bars which meet the requirements of ASTM 1035/1035M. The typical chemical compositions of this steel type are shown in Table 2-2. ASTM A1035 Grade 100 and Grade 120 steel have lower carbon content and significantly higher chromium content than conventional Grade 80 and Grade 60 steel. These bars, which have high-strength and high corrosion resistance, are produced using a controlled rolling and manufacturing

process, where steel is rolled within specified temperature ranges and cooled at specific rates (MMFX, 2014)).

Table 2-3 shows the tensile, yield and elongation properties of this steel type as specified in ASTM A1035. The chemical composition and manufacturing process of ASTM A1035 Grade 100 and Grade 120 steel result in high yield strengths of 100 ksi (690 MPa) and 120 ksi (830 MPa), respectively, and ultimate tensile strength of 150 ksi (1030 MPa). An additional advantage is superior corrosion resistance when compared to conventional steel.

Table 2-2 Steel reinforcement chemical properties (Adapted from ASTM A1035/A1035M-16)

Element	MMFX
Carbon	0.15%
Chromium	8-10.9%
Manganese	1.50%
Silicon	0.50%
Phophorus	0.035%
Sulfur	0.045%
Nitrogene	0.5%

Table 2-3 Tensile Properties of ASTM A1035 Reinforcement (ASTM, 2011)

	Grade 100	Grade 120
Yield strength (0.2% Offset Method), minimum	690 MPa (100 ksi)	830 MPa (120 ksi)
Tensile strength, minimum	1030 MPa (150 ksi)	1030 MPa (150 ksi)
Stress corresponding to an extension of 0.0035, minimum	550 MPa (80 ksi)	620 MPa (90 ksi)
Elongation, bar size		
3 through 11	7%	7%
14, 18	6%	N.A.

One of the design challenges associated with high-strength reinforcement is that these bars show different stress-strain behaviour when compared to conventional (Grade 60) reinforcement. Figure 2-1 shows typical stress-strain curves for Grade 100 high-strength reinforcement together with those of ASTM A706 Grade 60 and 80 bars (ATC, 2014). Unlike the Grade 60 and Grade 80 bars, which have well-defined yield points, the rounded stress-strain response of the ASTM A1035 Grade 100 steel does not include a yield plateau.

Figure 2-2 presents three methods which can be used to determine the yield strengths of steels with different stress-strain curves. The "yield point method" is suitable for steels which have well-defined yield plateaus such as those of the ASTM A706 Grade 60 and Grade 80 steel bars. The offset method can be used for steel which does not exhibit a well-defined yield point and where the material shows a specified limiting deviation from stress-strain proportionality. In this method a line *mn* which has the same slope as the initial linear line *OA* is drawn at an offset strain of 0.2% (0.002). The point *r*, where line *mn* intersects the actual stress-strain curve is taken as the yield point of the material. The 0.2% offset method is commonly used to determine the yield strength of ASTM A1035 reinforcement. The extension under load (EUL) method is also used for steel without a well-defined sharply-yielding curve. In this method the yield strength is determined at a specified extension such as 0.35% or 0.5%.

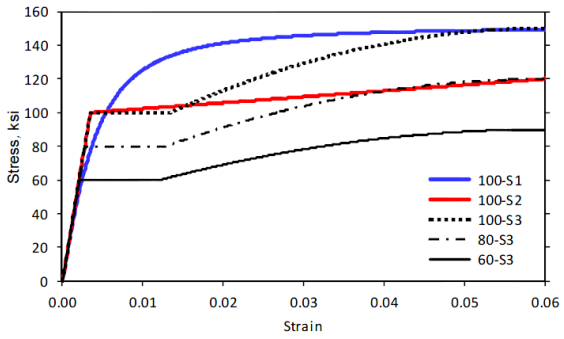

Figure 2-1 Types of stress-strain curves for high-strength reinforcement with distinct shapes (Adapted from NIST GCR 14-917-30, 2014)

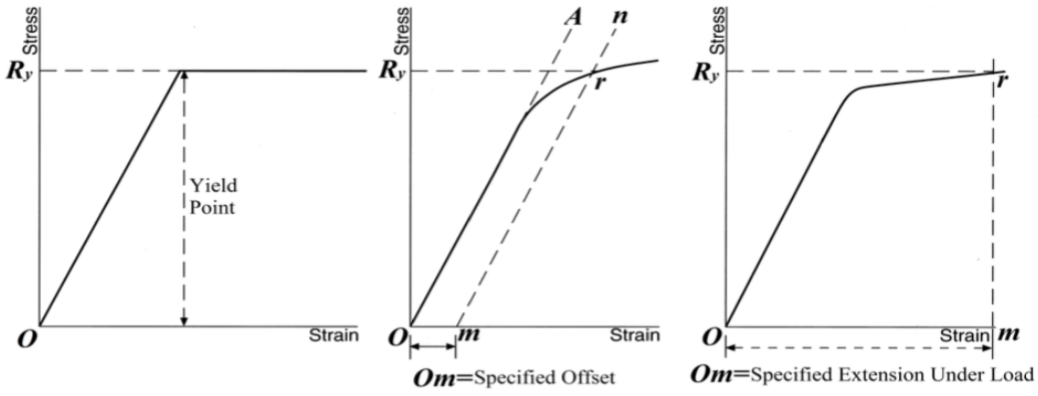

Figure 2-2 Stress-strain diagrams showing methods of yield stress determination (Adapted from RGA 04-13, 2013)

The NIST GCR 14-917-30 report (NEHRP, 2014) indicates that the maximum elongation (rupture strain) of high-strength ASTM 1035 bars relates to bar size, with 7% being typical for No. 3 through No. 11 bars, and 6% for No. 14 and No. 18 bars. It is noted that the maximum elongation of these bars is less than that of ASTM A706 Grade 60 and Grade 80 reinforcement, which typically show maximum elongations in the range of 12-15%.

2.2.1.3. Models to predict the stress-strain response of ASTM A1035 (MMFX) steel

As noted previously, the ACI ITG-6R-10 guide (ACI, 2011a) provides a framework for the design of concrete members reinforced with high-strength ASTM 1035 bars. The guide also provides an approach for modelling the stress-strain response of this reinforcement using equation (2–1). The ACI ITG-6R-10 suggested that the yield and ultimate strengths are 690 MPa and 1040 MPa, respectively. Figure 2-3 compares the stress-strain curve obtained using this model to actual stress-strain curves from #5 MMFX steel reinforcing bars.

$$f_s = \begin{cases} 200{,}000\varepsilon_s & \varepsilon_s \le 0.0024 \\ 1170 - \dfrac{2.96}{\varepsilon_s + 0.0019} & 0.0024 < \varepsilon_s \le 0.02 \\ 1040 & 0.02 < \varepsilon_s \le 0.06 \end{cases} \quad \textbf{(2–1)}$$

As an alternative, equation (2–2) shows an idealized bi-linear stress-strain curve proposed by Mast (2006) which can also be used to model the stress-strain response of this reinforcement.

$$f_s = \begin{cases} 200{,}000\varepsilon_s & \varepsilon_s \le 0.00241 \\ 1172 - \dfrac{2.379}{\varepsilon_s + 0.00104} & 0.00241 < \varepsilon_s \le 0.06 \end{cases} \quad \textbf{(2–2)}$$

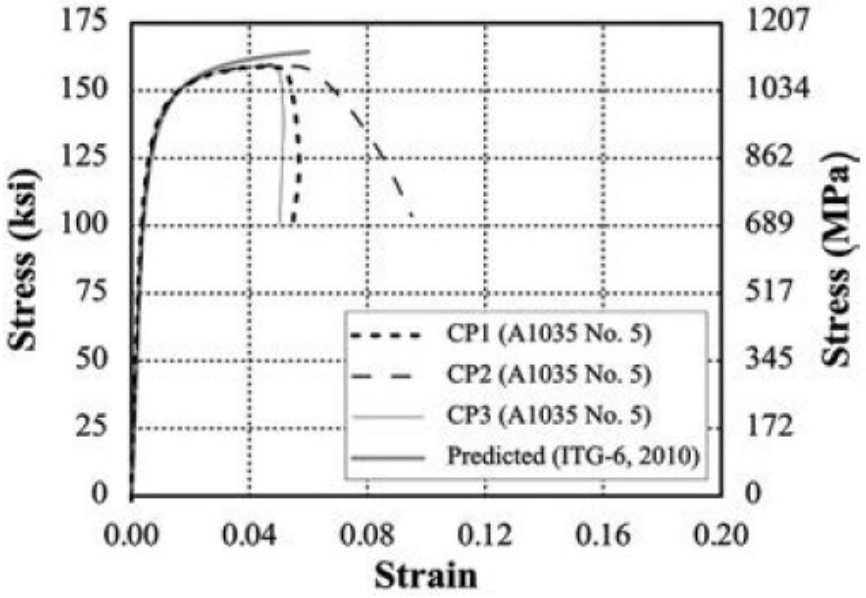

Figure 2-3 Stress-strain curves of actual test and ACI ITG-6R model (Adapted from Cheng & Giduquio, 2014)

The Ramberg-Osgood function, seen in Equation (2–3), is another method which can be used to express the stress-strain relationship of high-strength steel reinforcement not having a distinct yield plateau. The method to determine the parameters A, B, and C is outlined by Collins and Mitchell (1997) and follows these five steps:

- Represent the actual stress-strain relationship as two straight lines connected by a curve.
- Determine E_p from the slope of the first line.
- Determine A from the slope of the second line, where the slope is AE_p.
- Determine B from the intersection of the second line and the f_p axis. The value of f_p at the intersection is $E_p(1-A)/B$.
- Determine C by trial and error to give an appropriate transition curve. A high value of C gives an abrupt transition.

$$f_s = 200{,}000\varepsilon_s \times \left(A + \frac{1-A}{[1+(B\varepsilon)^C]^{\frac{1}{C}}} \right) \leq f_u \qquad \textbf{(2–3)}$$

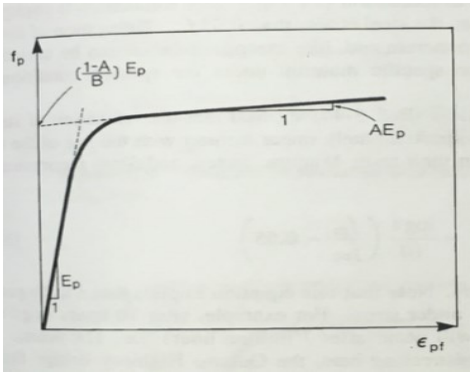

Figure 2-4 Method to determine the parameters A, B and C (Adapted from Collins and Mitchell, 1997)

2.2.2. HIGH-STRENGTH CONCRETE (HSC)

High-strength concrete (HSC) is defined as concrete with a 28-day strength ranging from 70 MPa to 125 MPa (Wight & Macgregor, 2009). High compressive strength is achieved by using supplementary cementitious materials such as silica fume and slag which improve the dispersion of cement in the mix, resulting in a low void-ratio. Most high-strength concretes also have a low water-to-cementitious-materials ratio ranging from 0.25 to 0.35 (Wight & Macgregor, 2009). Chemical admixtures such as superplasticizers are typically used to ensure workability to allow for low w/cm ratios. The aggregates in high-strength concrete typically consist of strong fine-grained gravel with a rough surface to allow for the high paste-aggregate bond required to develop high concrete strength.

Figure 2-5 (b) compares typical compressive stress-strain relationships for concretes having strengths varying between 30 and 120 MPa. As can be seen in the figure, HSC shows higher compressive strength, peak strain and stiffness when compared to NSC. HSC also tends to have a more linear ascending branch, with a steeper descending branch. The failure mode is typically associated with fracture of the aggregates on smooth planes parallel to the loading direction. HSC typically shows an unstable and brittle post-peak branch due to the release of large amounts of energy at failure (Mier et al. 1997).

Figure 2-5 (a) and equations in Table 2-4 (a) show the modified Hognestad model which is often accepted for plain concrete with strength of less than 45 MPa. Expressions for the compressive behaviour of high-strength concrete were reviewed by Popovics (1973). Thorenfeldt et al. (1987) adapted some of these expressions as shown in Table 2-4 (b) in order to model the stress-strain response of high-strength concrete. The resulting model is suitable for concretes having strengths from 15 to 125 MPa. The curves shown in Figure 2-5 (b) were plotted using these expressions.

Table 2-4 Equations used in the Modified Hognestad and Popovics stress-strain models

a) Modified Hognestad model for NSC	b) Popovics model for HSC
$f_c = \begin{cases} f_c'[\frac{2\varepsilon_c}{\varepsilon_0} - (\frac{\varepsilon_c}{\varepsilon_0})^2] & \text{for } \varepsilon_c/\varepsilon_0 \le 1 \\ f_c' - \frac{0.15 f_c'}{0.0038 - \varepsilon_0}(\varepsilon_c - \varepsilon_0) & \text{for } \varepsilon_c/\varepsilon_0 > 1 \end{cases}$	$\frac{f_c}{f_c'} = \frac{n(\varepsilon_c/\varepsilon_0)}{n-1+(\varepsilon_c/\varepsilon_0)^{nk}}$ $k = \begin{cases} 1 & \text{for } \varepsilon_c/\varepsilon_0 \le 1 \\ 0.67 + \frac{f_c'}{62} \ge 1.0 & \text{for } \varepsilon_c/\varepsilon_0 > 1 \end{cases}$ $n = 0.8 + \frac{f_c'}{17}$ $\varepsilon_0 = \frac{f_c'}{E_c}(\frac{n}{n-1})$

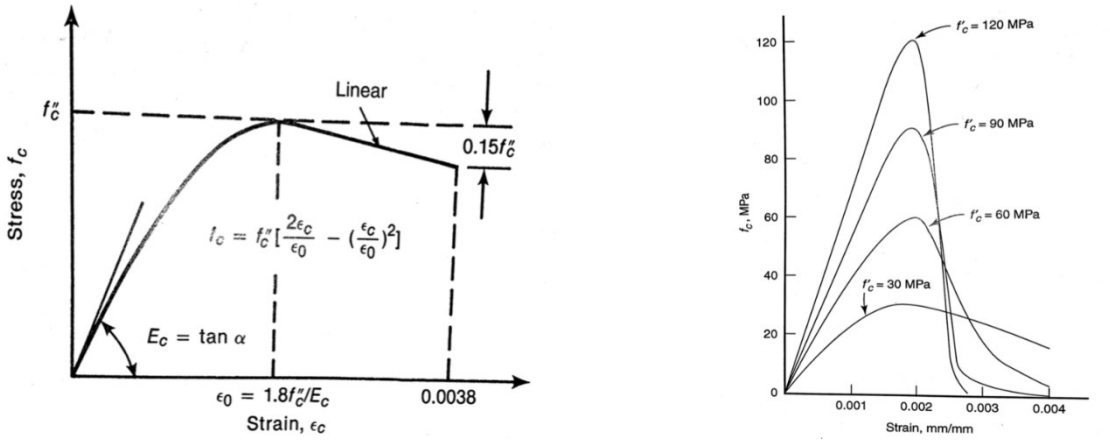

a) Modified Hognestad model b) Curves obtained using Popovics model

Figure 2-5 Typical stress-strain curve for normal and high-strength concrete

2.2.3. HIGH-STRENGTH FIBRE-REINFORCED CONCRETE (HSFRC)

As noted in the previous section, high-strength concrete shows brittle response with brittle failure under compressive loading. As with all conventional concretes, HSC also has limited tensile capacity. The addition of fibres to HSC transforms these characteristics, and provides the material with improved ductility under compressive loads and an ability to carry tensile stresses after cracking.

High-strength fibre-reinforced concrete (HSFRC) is defined as a composite material, which is composed of high-strength concrete and randomly oriented short discrete steel fibres. The use of steel fibres provides post-cracking resistance to concrete, which enhances tensile resistance. At the low-to-moderate contents used in structural applications ($0.5\% \leq v_f \leq 1.5\%$), the addition of steel fibres slightly increases the compressive strength and elastic of modulus of concrete. However, the confining effect of the steel fibres allows for an improvement in post-peak behaviour and increases ultimate strain and toughness.

Mansur et al. (1999) studied the compressive behaviour of HSFRC cylinders having compressive strengths ranging between 70 and 120 MPa, with steel fibre contents which varied from 0.5% to 1.5% by volume of concrete. Figure 2-6(a) shows typical stress-strain curves for HSC and HSFRC with different fibre contents as obtained from these tests. It can be noticed that the addition of fibres significantly improves the toughness and post-peak response under compressive loading, with the enhancement being proportional to the increase in fibre content. As part of this study the researchers also proposed a model to predict the stress-strain response of HSFRC in compression. Over the years a number of other researchers have also proposed models to predict the compressive behaviour of normal and high-strength fibre reinforced concrete (for a review of these models refer to Bencardino et al., 2008; Figure 2-6(b) also shows some examples). Table 2-5 summarizes the expressions used in the Mansur et al. model (1999), and a second model proposed by Ou et al. (1999). The Mansur et al. expressions are applicable for HSFRC with compressive strengths varying between 70-120 MPa.

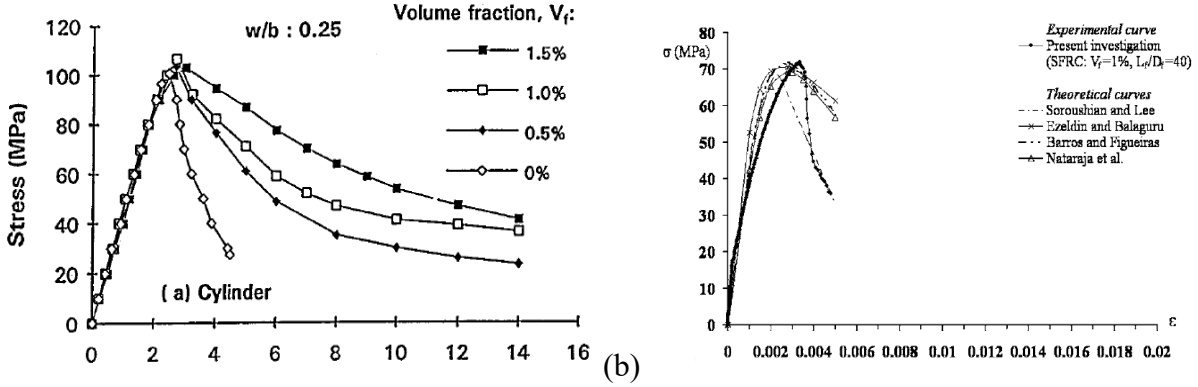

Figure 2-6 (a) Stress-strain response of HSFRC with different fibre contents (Mansur et al. 1999); (b) Examples of models for SFRC with 1.0% fibres (Bencardino et al., 2008)

Table 2-5 Two popular stress-strain expressions for HSFRC

Ou et al. model (1999)	***Mansur et al. model (1999)***	***Remark***
$f_{cf}(\varepsilon_c) = f'_{cf}\left[\frac{n\left(\frac{\varepsilon_c}{\varepsilon_{0f}}\right)}{n-1+\left(\frac{\varepsilon_c}{\varepsilon_{0f}}\right)^n}\right]$ $f_{cf} = f'_{cu} + 2.35(\frac{v_f L_f}{d_f})$ $\varepsilon_0 = \varepsilon'_c + 0.0007(\frac{v_f L_f}{d_f})$ $n = 0.71(\frac{v_f L_f}{d_f})^2 - 2.00\left(\frac{v_f L_f}{d_f}\right) + 3.05$	Ascending branch: $f_{cf}(\varepsilon_c) = f'_{cf}\left[\frac{n\left(\frac{\varepsilon_c}{\varepsilon_{0f}}\right)}{n-1+\left(\frac{\varepsilon_c}{\varepsilon_{0f}}\right)^n}\right]$ $n = \frac{1}{1-\frac{f'_{cf}}{\varepsilon_{cu}E_c}}$ Descending branch: $f_{cf}(\varepsilon_c) = f'_{cf}\left[\frac{k_{f1}n(\varepsilon_c/\varepsilon_{0f})}{k_{f1}n-1+(\varepsilon_c/\varepsilon_{0f})^{k_{f2}n}}\right]$ $k_{f1} = (\frac{50}{f'_{cf}})^{3.0}[1+2.5(\frac{v_f L_f}{d_f})^{2.5}]$ $k_{f2} = (\frac{50}{f'_{cf}})^{1.3}[1-0.11(\frac{v_f L_f}{d_f})^{-1.1}]$	$RI = \frac{v_f L_f}{d_f}$ v_f= fibre content L_f= length of fibre d_f= diameter of fibre f'_{cf}= Peak compressive strength of fibre reinforced and plain concrete ε_{0f}= Peak strain for fibre reinforced E_c= initial elastic modulus

2.2.4. EFFECTS OF HIGH STRAIN RATES ON MATERIAL PROPERTIES

Dynamic loading results in the application of loads at varying high strain-rates. As shown in Figure 2-7, this strain rate varies depends on the type of loading, with the largest strain rates recorded under impact and blast loads. Research shows that application of blast and impact leads to an increase in member strength and stiffness when compared to quasi-static loading. The increases in member strength and stiffness are affected by the strain rate, and result from the apparent increase in concrete and steel material strength properties under dynamic loading.

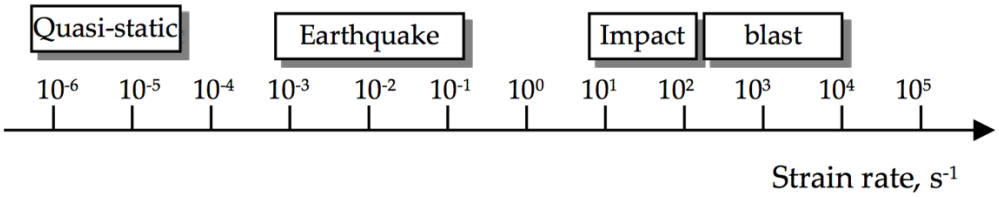

Figure 2-7 Strain rate for various types of loading (Adapted from Ngo et al., 2007)

The effect of strain-rate on increasing the strength of materials is typically taken into account using a dynamic increase factor (DIF), defined as the ratio of dynamic to static strength. Figure 2-8 shows typical strength enhancements for concrete and steel reinforcement under dynamic loading. For concrete, the compressive strength is increased in proportion to the increase in strain rate, with

the dynamic stress-strain curve obtained by scaling the entire quasi-static stress-strain curve using the DIF of concrete in compression. For steel reinforcement, both the yield and ultimate strengths are increased under dynamic loading, although the increase in yield strength has been found to be more important. Research shows that the modulus of elasticity of steel remains unchanged under dynamic loading.

For design, blast design guidelines such as the UFC 03-340-02 2008 and the Canadian CSA S850 blast standard provide conservative DIF values which can be used in the blast-resistant design of reinforced concrete members (UFC 03-340-02, 2008; CSA S850, 2012) The values depend on the type of blast load (close-in vs. far range) and type of stress being resisted in the structural member. Table 2-6 shows the dynamic increase factors suggested by the CSA S850.

Over the years, researchers have also proposed strain-rate dependent models for predicting the DIF of concrete and steel materials, some of these models are discussed in the sub-sections that follow.

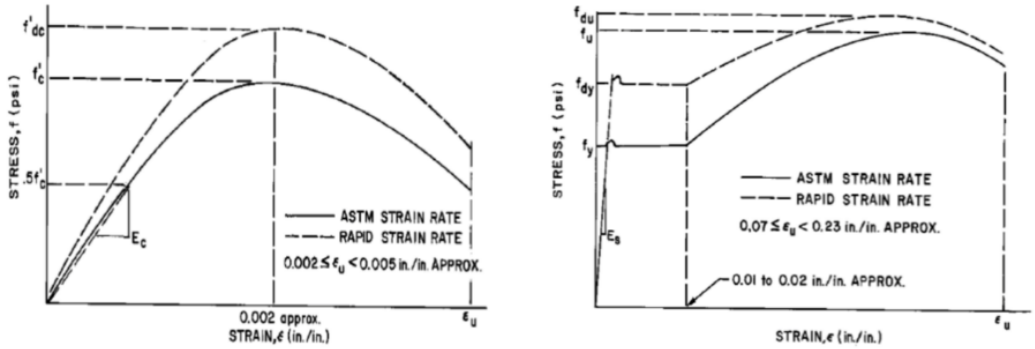

Figure 2-8 Typical stress-strain response under quasi-static and dynamic loading (Adapted from UFC 03-340-02 2008)

Table 2-6 Dynamic increase factors for reinforcing steel, concrete, and masonry (Adapted from CSA S850, 2012)

Stress type	DIF			
	Reinforcing steel		Concrete	Masonry
	Fdy/Fy	Fdu/Fu	f'dc/f'c	f'dm/f'm
Flexure	1.17	1.05	1.19	1.19
Compression	1.10	1.00	1.12	1.12
Diagonal tension	1.00	1.00	1.00	1.00
Direct shear	1.10	1.00	1.10	1.00
Bond	1.17	1.05	1.00	1.00

2.2.4.1.Concrete in Compression – CEB model (1990)

The Comité euro-international du béton (CEB) Model Code 90 (1990) proposes a bilinear curve (on semi-log scale) for the DIF of concrete in compression as a function on strain rate. Based on experimental results, the slope of the bilinear curve shows a sharp transition at a strain-rate of 30 s^{-1}. In this model the quasi-static strain rate is taken as 30 x 10^{-6}, which means there is no predicted increase in compressive strength before reaching this value. It is noted that despite high-scatter in research data, this model predicts reduced DIF for high-strength concrete when compared to normal-strength concrete (see Figure 2-9). The DIF expressions used in this model are defined in Chapter 7.

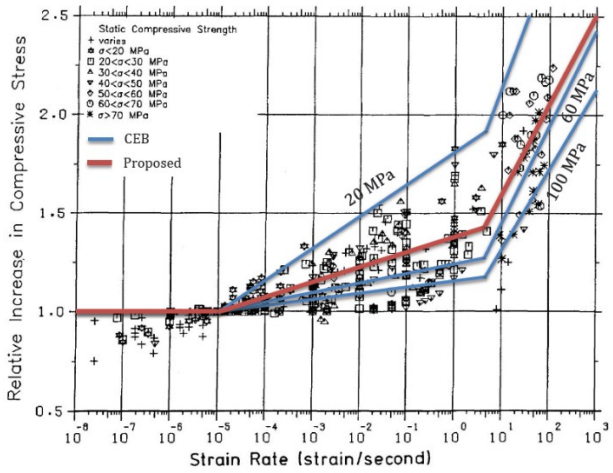

Figure 2-9 Effect of strain rate on concrete compressive strength (Adapted from Biscoff and Perry, 1991)

2.2.4.2.Concrete in Tension – Malvar & Ross (1998)

The purpose of a study by L. Malvar & C. Ross (1998) was to revise the dynamic increase factor of the CEB model for concrete in tension based on a review of existing research data. The authors plotted all the research data conducted by Ross et al. (1998) and other researchers on a log-scale diagram as shown in Figure 2-10. It was found that concrete in tension shows similar strain-rate sensitivity with a similar trend to that of concrete in compression when plotting the results on a log-scale. However, it was observed that the slope of this bilinear curve is closer to 1 s^{-1}, which is different than CEB suggested value of 30 s^{-1}. Based on this finding a revised bi-linear model for concrete in tension was proposed by the authors. It is noted that the quasi-static strain-rate was chosen as 10^{-6} s^{-1}. The expressions used in this model are summarized in Chapter 7 of this thesis.

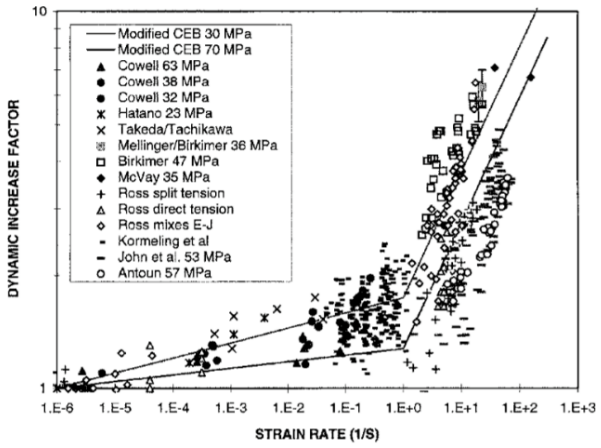

Figure 2-10 Proposed modified CEB curves for concrete in tension (Adapted from Malvar & Ross, 1998)

2.2.4.3.HSC & HSFRC in Compression – Zhang & Mindess (2011)

The purpose of this paper by Zhang and Mindness in 2011 was to conduct the DIF formulation of high-strength concrete with fibres based on dynamic experimental results. A split Hopkinson pressure bar and drop weight impact machine were used to apply the impact loading. The specimens in this study had varying compressive strengths of 50 MPa, 90 MPa and 110 MPa. The drop height ranged from 250 mm to 1000 mm, which resulted in various strain rates. These strain rates were then combined with Riisgaard's (2007) experimental results and compared to the results of the CEB model. It was found that the CEB model did not accurately predict the results. A modified CEB model, called the RCM model, was therefore proposed. The RCM model changed the turning point of the bilinear curve based on the concrete compressive strength instead of on the 30 s^{-1} of the CEB model. Most predicted data ranged from a 3-15% difference from the experiment results. It was also noted that concrete with higher strength improved lower-strength concrete under impact load.

2.2.4.4.Steel in tension - Malvar (1998)

The purpose of a study was to determine dynamic increase factor expressions of steel at yield and ultimate stress. The author reviewed existing data on the quasi-static and dynamic strengths of steel reinforcement and plotted them in diagrams. Figure 2-11 provides a graph showing DIF versus strain rate for ASTM A615 Grade 40, 60, and 75 steel reinforcement bars for both yield and ultimate strength.

From the diagrams, it can be observed that the DIF versus strain rate curves follow linear relationships when strain-rate is plotted on logarithmic scale. It can also be noted that the DIF at a given strain-rate is greater at yield strength than ultimate strength. Finally, it can also be noted that the DIF decreases with the increase in steel grade level. Based on this study, the author proposed

DIF formulations for yield and ultimate stress, respectively. The formulations are valid for steels having yield stress ranging from 290 to 710 MPa (see Chapter 7).

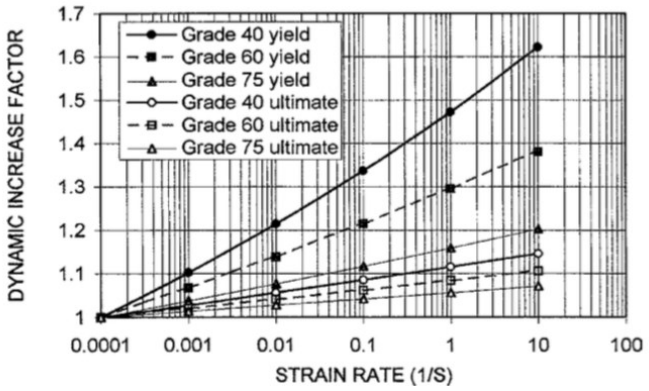

Figure 2-11 DIF for ASTM A615 Grade 40, 60, and 75 steel reinforcement bars (Adapted from Malvar, 1998)

2.2.4.5. Saatcioglu et al. (2011)

This study by Saatcioglu et al. (2011) investigated high-strain rate effects on concrete and steel reinforcement. As part of the experimental study the dynamic behaviour of reinforced concrete columns and slabs under blast loading was investigated. Eighteen columns which differed by section size, concrete strength, and reinforcement detailing were tested at the University of Ottawa Shock Tube Facility. The experiment results were then compared with analysis results obtained using single-degree-of-freedom analysis. The average ratio of predicted maximum displacement and experimental maximum displacement was 1.05, which indicated an accurate prediction. The authors also reviewed existing reinforced concrete material models and DIF equations. In addition, the authors also proposed simplified bi-linear models to predict the DIF of concrete in compression and steel reinforcement. It is noted that unlike the CEB model the DIF of concrete is assumed to be unaffected by concrete strength. The DIF models are different for steel at yield and ultimate strength and are applicable to grade 400 steel bars (see chapter 7).

2.3. PREVIOUS RESEARCH ON QUASI-STATIC PERFORMANCE OF BEAMS WITH ASTM A1035 HIGH-STRENGTH STEEL

This section reviews previous research which has focused on the quasi-static behaviour of reinforced concrete beams built with high-strength (ASTM A1035) steel reinforcement. Studies which have examined the shear, flexural and cyclic behaviour of beams built with high-strength reinforcement are reviewed. In addition, a limited number of studies which have focused on the behaviour of beams built with high-strength bars and steel fibres are also discussed. Table 2-7 summarizes the experimental parameters and beam properties in the various studies. It is noted that there is limited research which has focused on the behaviour of beams built with ASTM A1035 steel and high-strength concrete.

Table 2-7 Summary of the database results of reinforced ASTM A1035 beams in this parametric study

Focus of study	Authors	Range of main parameters											
		No. of specimens	b (mm)	h (mm)	Clear span (mm)	a/d ratio	f_c' (MPa)	ρ (long.)	ρ (trans.)	Load type	Fibre properties		
											v_f	L_f	df
Shear behaviour	Hassan et al. - 2008	6	460	915	4900	1.9, 2.7	32-51	0.44-0.72%	0	3-point	-	-	-
	Sumpter et al. - 2009	9	305	406	4877	2.62, 3.08	26.9-32.6	3.12%	0.46%-0.92%	4-point	-	-	-
	Munikrishna et al. - 2011	13	406-610	559-711	4000, 5800	3.1	32.4-40	0.9%-2.2%	0-0.31%	4-point	-	-	-
	Desalegne & Lubell - 2010	6	300	305, 600	2675, 4830	3.5	49-59	0.45%, 0.225%	0	3-point	-	-	-
	Desalegne & Lubell - 2015	8	300	1000	5460	2.92, 3.08	48-52	0.55-1.6%	0.10%, 0.20%	3-point	-	-	-
Flexural behaviour	Talboys & Lubell - 2014	6	310	310, 1000	1488-5712	3	29.9-41.2	0.4-2.61%	0	3-point	1%	30	0.55
	NCHRP – 2014	6	305	406	6096	6.25	89, 114	0.9%-2%		4-point	-	-	-
	Garay & Lubell - 2016	8	300	607	4760	1.19, 2.38	39-48	0.52-2.29%	0.10%	4-point	-	-	-
Cyclic behaviour	Cheng et al. - 2014	3	250	600	1800	-	38	0.65%	0.44%	Cyclic	-	-	-

2.3.1. SHEAR STUDIES – BEAMS BUILT WITH MMFX BARS

2.3.1.1.Hassan et al. (2008)

The aim of a research project by Hassan et al. (2008) was to investigate the shear behaviour of large concrete beams reinforced with ASTM A1035 Grade 100 high-strength steel bars. In total, six large-size concrete beams with a constant dimension of 460 x 915 x 4900 mm and no transverse reinforcement were included in this research. The test parameters included the shear span ratio (a/d =1.9 or 2.7), reinforcement ratio (0.44 - 0.72%) and type of reinforcement (60 ksi or 100 ksi). The beams were tested under 3-point bending. Figure 2-12 shows the experiment load-deflection curves for all specimens. Predictions were made using the ACI 318-05 simplified strut-and-tie model. Observations and conclusions from this research project can be summarized as follows:

- Reinforcing the beams with high-strength steel was found to affect failure mode. The specimens with conventional steel showed diagonal shear failures. The failure of beams with high-strength reinforcement was controlled by the compressive strength of diagonal struts (compression shear failure), allowing the failure to take place in the concrete struts at higher loads.

- As a result of the change in failure mode, the use of high-strength steel was able to increase shear capacity. Furthermore, specimens with high-strength steel had reduced shear crack widths compared to companions with conventional steel (Grade 60) at equivalent loads.
- Specimens with a lower a/d ratio resulted in higher shear capacity, although this parameter did not affect failure mode.
- Predictions made using the ACI 318-05 model overestimated the shear resistance of the beams. The authors suggested that the errors result from the model not accounting for size effect and the properties of the longitudinal steel reinforcement.

Table 2-8 Details and prediction of the specimens (Adapted from Hassan et al., 2008)

Specimen	Group A		Group B		Group C	
	G-1.9-51	M-1.9-51	G-1.9-38	M-1.9-38	G-2.7-32	G-2.7-32
Shear span-depth ratio (a/d)	1.9	1.9	1.9	1.9	2.7	2.7
Concrete compressive strength, MPa (psi)	51 (7400)	51 (7400)	38 (5500)	38 (5500)	32 (4650)	32 (4650)
Type of longitudinal reinforcement	G*	M†	G*	M†	G*	M†
Bottom reinforcement ratio, %	0.72	0.44	0.72	0.44	0.72	0.44
Top reinforcement ratio, %	0.36	0.22	0.36	0.22	0.36	0.22
Diagonal cracking load, kN (kips)	670 (150)	670 (150)	670 (150)	670 (150)	445 (100)	445 (100)
Failure load, kN (kips)	871 (195)	1560 (350)	753 (170)	1364 (306)	552 (124)	638 (143)
Predicted failure load using ACI 318-05, kN (kips)	1103 (248)	1917 (431)	1103 (248)	1418 (319)	690 (155)	690 (155)
$P_{Test}/P_{\text{ACI 318-05}}$	0.8	0.81	0.68	0.96	0.80	0.92

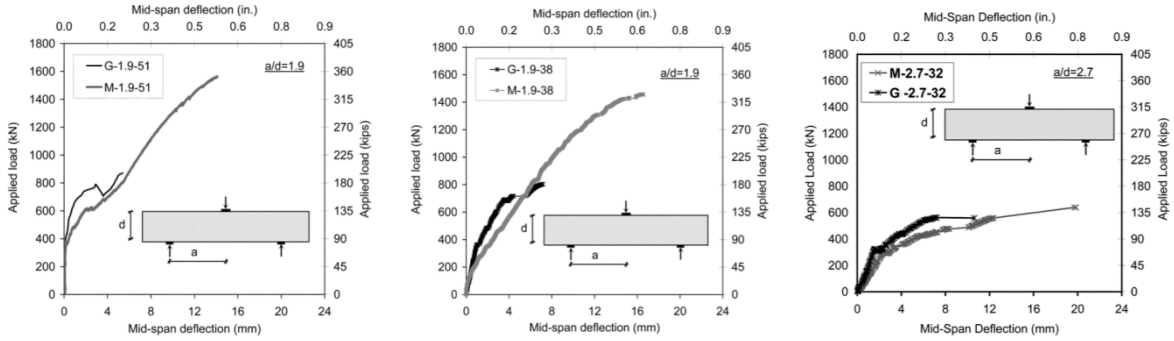

a) Group A b) Group B c) Group

Figure 2-12 Experiment load-displacement curves (Adapted from Hassan et al., 2008)

2.3.1.2.Sumpter et al. (2009)

The purpose of this study by Sumpter et al. (2009) was to investigate the shear behaviour of concrete beams reinforced with high-strength steel. Beams in this study were reinforced with either conventional ASTM A615 Grade 60 bars (C) or high-strength ASTM A1035 steel bars (M). The beams had a 12 in. x 16 in. (305 mm x 406 mm) cross-section and were reinforced with No. 9 bars for longitudinal reinforcement (top and bottom) and No. 3 bars for the stirrups. The compressive strength of concrete was around 30 MPa. The main variables in the study were the type of longitudinal reinforcement, type of transverse steel, and spacing of the stirrups. The test program

included nine beams which were divided into three sets based on stirrup spacing. Each set contained three specimens: a beam reinforced with conventional longitudinal bars and conventional stirrups (C-C), a beam with conventional longitudinal bars and MMFX stirrups (C-M), and a beam reinforced with MMFX bars and MMFX stirrups (M-M). Conclusions from this study are summarized below:

- All beams failed in shear, with shear-compression failures regardless of steel type and stirrup spacing. For all steel combination cases, specimens with higher shear reinforcement ratios had higher shear capacities.
- The use of MMFX stirrups was able to slightly increase shear capacity and reduce crack widths. For example, for set 1 (6 inches spacing), the specimen reinforced with MMFX stirrups (C-M) showed a 5% increase in shear strength when compared to a companion specimen with conventional steel stirrups (C-C) (383 kN versus 364 kN).
- The use of MMFX steel for longitudinal reinforcement was able to further increase shear capacity. For example, the M-M beam in set 1 (MMFX stirrups & MMFX longitudinal bars) showed 11% and 17 % increases in shear strength when compared to companion beams with C-M and C-C bar combinations.
- The use of MMFX bars also led to reduced shear crack widths under service loads, with the best performance for beams with M-M bars.
- The shear resistance of the beams was predicted using the shear equations in the ACI 318-05 code, CSA A23.3-04 and AASHTO LRFD Bridge code, with the best predictions obtained using the Canadian CSA A23.3 standard.
- The capacities were also predicted using program *Response 2000* which is based on modified compression field theory (MCFT). The average measured-to-predicted shear load ratio was 1.01, which was more accurate than the code-based equations.

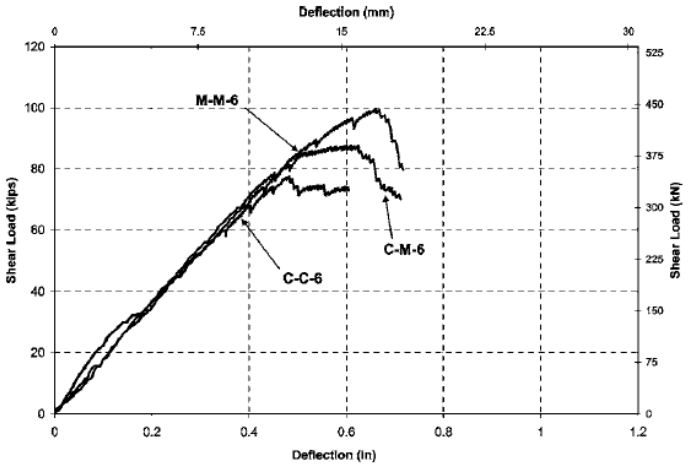

Figure 2-13 Load – deflection curve for 6 inch set (Adapted from Sumpter et al., 2009)

2.3.1.3.Munikrishna & Hosny (2011)

The goal of this research study by Munikrishna and Hosny (2011) was to investigate the flexural and shear behaviour of concrete beams reinforced with ASTM A1035 Grade 100 high-strength steel. Thirteen beams were tested under a single point load with a constant shear span-effective depth ratio of 3.1 as shown in Figure 2-14. Two sets of dimensions were used: 406 x 559 x 4000 mm and 610 x 711 x 5800 mm. Other variable parameters were the longitudinal reinforcement ratio (0.9 - 2.2%) and type (grade 60 vs. grade 100), transverse reinforcement ratio (0 - 0.31%), and transverse reinforcement strength (conventional: C, high-strength grade 80 and 100: M80 and M100). The beams were divided into three groups; group1 and 2 had different loading spans and included control beams with conventional longitudinal and transverse steel as well as beams with MMFX longitudinal steel and varying stirrup properties. The concrete compressive strength was 28 MPa. The following conclusions were made:

- Reinforcing the beams with high-strength stirrups and a higher longitudinal reinforcement ratio resulted in an increase in shear capacity. The use of high-strength steel for longitudinal steel was also shown to increase flexural strength.
- The use of high-strength stirrups and a lower shear reinforcement ratio resulted in an increase in the shear crack width when compared to specimens with conventional stirrups.
- The pre-cracking stiffness of beams with the same reinforcement ratio was identical.
- The shear capacities of the beams were predicted using several codes. The CSA and AASHTO models gave more accurate predictions when compared to the ACI 318 model, which can be explained by the fact that the ACI 318 is based on a 45-degree truss model, while the CSA and AASHTO codes are based on the modified compression field theory (MCFT).

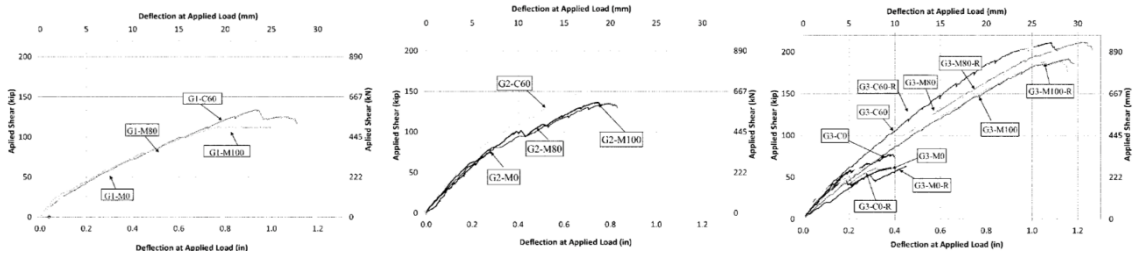

a) Group 1 b) Group 2 c) Group 3

Figure 2-14 Experiment load-deflection curves (Adapted from Munikrishna & Hosny, 2011)

2.3.1.4.Desalegne & Lubell (2010)

This study by Desalegne and Lubell (2010) investigated the shear behaviour of beams reinforced with high-strength steel. The study included six beams with a constant a/d ratio of 3.5 which were tested under three-point loading. The parameters investigated included: the longitudinal steel

reinforcement ratio, which ranged from 0.45% to 0.225%; and the member depth which was either 305 mm or 600 mm. Finally, an equation for predicting the shear resistance of beams with high-strength was proposed and compared to five other methods (ACI 318-08, CSA A.23.3-04, Hoult et al., Response 2000, and VecTor2). Figure 2-15 shows sample test results from this study. Table 2-9 shows the shear predictions made using the different models. The following conclusions and observations were made:

- As shown in Figure 2-15, the four specimens with a higher reinforcement ratio failed in shear while the two specimens with a lower reinforcement ratio failed in a flexural-shear mode. The ultimate capacity and stiffness were increased with the increase of the reinforcement ratio.
- Table 2-9 shows the predictions based on the six different models considered in the study. The CSA A23.3-04 and Hoult et al. shear models gave the most accurate predictions. The ACI 318 and EC2 were found to overestimate the shear capacities, which could result in unsafe designs; these models fail to consider the effects of member depth (size effect) and reinforcement strains (strain effect) on shear resistance.

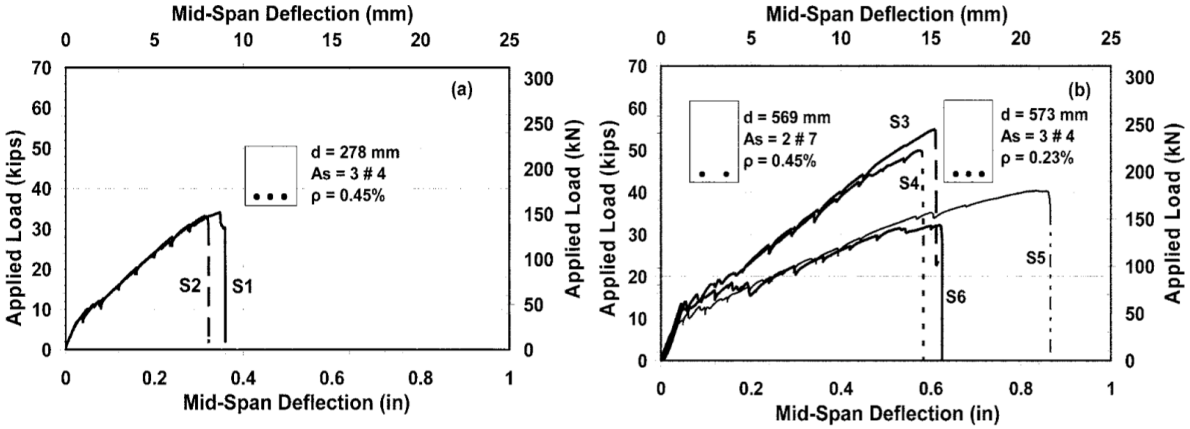

a) Specimens with h = 305 mm b) Specimens with h = 600 mm

Figure 2-15 Experiment load – deflection curves for all specimens (Adapted from Desalegne & Lubell, 2010)

Table 2-9 Prediction results by different models (Adapted from Desalegne & Lubell, 2010)

Specimen	Test load to predicted load ratios							P_{TEST}, kN (kips)
	P_{TEST}/P_{ACI}	P_{TEST}/P_{EC2}	P_{TEST}/P_{CSA}	P_{TEST}/P_{HOULT}	P_{TEST}/P_{R2K}	P_{TEST}/P_{VT2}	P_{TEST}/P_{PROP}	
S1	0.74	0.94	1.20	1.11	1.20	1.20	1.27	153 (34)
S2	0.68	0.88	1.14	1.05	1.23	1.16	1.18	149 (33)
S3	0.61	0.89	1.14	1.08	1.28	1.17	1.46	245 (55)
S4	0.52	0.77	1.00	0.94	1.00	0.97	1.23	223 (50)
S5	0.44	0.81	1.23	1.10	1.08	1.31	—	182 (41)
S6	0.33	0.62	0.97	0.86	0.83	1.10	—	144 (32)
M-2.7-32	0.86	1.27	1.01	0.98	0.96	0.97	1.32	638 (143)
P_{TEST}/P_{Model} (average)	0.60	0.88	1.10	1.02	1.08	1.12	1.29	—
Coefficient of variation	0.31	0.22	0.09	0.09	0.15	0.11	0.08	—

2.3.1.5.Desalegne & Lubell (2015)

This study examined the flexural and shear behaviours of eight beams with dimensions of 300 x 1000 x 5460 mm and reinforced with high-strength bars. The beams were tested under three-point loading with a constant shear-span to depth ratio (a/d) of 3.5. The parameters that were varied included the longitudinal reinforcement ratio (0.55-1.6%), transverse reinforcement ratio (0.1%, 0.2%), and reinforcement type. Specimens contained ASTM A1035 high-strength (MMFX) longitudinal reinforcement and stirrups consisted of either MMFX or Grade 60 hoops. All beams had compressive strength of 50 MPa. Sample experimental load-deflection curves can be seen in Figure 2-16. The following observations and conclusions were made from this study:

- The use of MMFX steel for stirrups resulted in a higher shear capacity when compared to the specimens containing conventional steel stirrups. For example, specimen MM2 with MMFX steel stirrups showed a 9.4% increase in ultimate strength compared to the specimen MR2 with conventional stirrups. Similarly, beams with MMFX stirrups showed reduced shear crack widths at ultimate conditions.
- Reinforcing the beams with a higher longitudinal reinforcement ratio resulted in higher stiffness and load resistance. Using stirrups at smaller spacing increased shear capacity.
- The failure mode of the beams changed with an increase in the reinforcement ratio. For example, specimens MM1 and MM2 (ρ=0.55% and 0.69%) showed a shear-flexure failure, while specimen MM3 (ρ=1.6%) resulted in a shear-compression failure.
- The shear resistance of the beams was predicted using the ACI ITG-6R shear design recommendations and a modified version of the CSA general method as proposed by Hoult et al. (2008) which recalibrates the V_c equation for cases of higher longitudinal strains. The predictions made using the ACI ITG-6R model were not conservative, while the modified CSA shear model showed good agreement with the experimental results.

Table 2-10 Specimen details, test results and analytical predictions (Adapted from Desalegne & Lubell, 2015)

	MM series				MR series			
ID	MM1	MM2	MM3	MM4	MR1	MR2	MR3	MR4
d, mm	935	935	885	885	935	935	885	885
f_c', MPa	50	52	48	48	49	50	48	50
Age, days	49	48	45	52	56	51	43	56
A_s, mm^2	1548	1935	4257	4257	1548	1935	4257	4257
ρ_L, %	0.55	0.69	1.60	1.60	0.55	0.69	1.60	1.60
Two leg stirrups	No. 3 @ 440	No. 3 @ 440	No. 3 @ 440	No. 3 @ 220	10M @ 440	10M @ 440	10M @ 440	10M @ 220
f_{yt}, MPa	830*	830*	830*	830*	430	430	430	430
P_{max}, kN	933	957	1409	1822	915	875	1109	1510
$M_{test}/M_{n\text{-}s}$	1.41	1.16	0.84	1.09	1.39	1.07	0.66	0.90
$M_{test}/M_{n\text{-}g}$	0.98	0.83	0.77	0.99	0.96	0.77	0.60	0.81
$\frac{V_{test}}{bd\sqrt{f_c'}}$	0.24	0.25	0.38	0.48	0.23	0.22	0.29	0.40
$\frac{V_{Test}}{V_{ITG\text{-}6R}}$	0.95	0.96	1.53	1.48	0.91	0.86	1.17	1.16
$\frac{V_{Test}}{V_{MCSA}}$	1.32	1.19	1.35	1.39	1.28	1.07	1.04	1.11

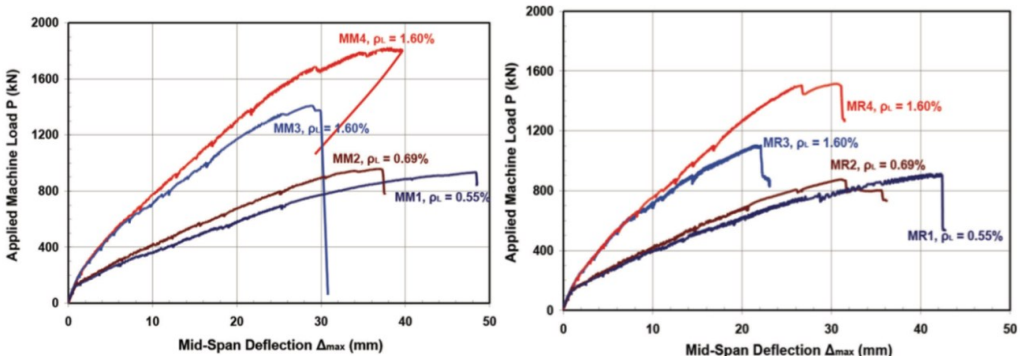

a) Specimens with MMFX stirrups b) Specimens with Grade 60 stirrups

Figure 2-16 Experiment load-deflection curves (Adapted from Desalegne & Lubell, 2015)

2.3.2. FLEXURAL STUDIES – BEAMS WITH MMFX BARS

2.3.2.1.NCHRP Report 679 – Transportation Research Board (2014)

This National Cooperative Research Program (NCHRP) report published by the Transportation Research Board (TRB, 2011) outlined a static test program which containing six beams reinforced with MMFX high-strength steel. All the specimens had the same cross-section, 12 in. x 16 in. (305 mm x 406 mm), with a total span of 22 feet (6706 mm). The beams were subdivided into two groups based on concrete strength (69 MPa and 103 MPa) with the three beams within each group designed based on three strain targets for the longitudinal bars: a tension-controlled strain limit of 0.008, a transition strain of 0.006, and a strain of 0.011. The specimens were tested under four-point bending with a/d ratio of 3.3. In addition to the experimental study, software Response 2000 (Bentz 2000) was used for analysis. Three types of stress-strain relationships were considered in the analysis: a bilinear design curve with an initial elastic modulus of 200,000 MPa and a yield strength of 690 MPa; a stress-strain curve defined using the Ramberg-Osgood function shown in Equation (2–3); and the Mast (2006) equation shown in Equation (2–2). In order to define the stress-strain relationship in Response 2000 using the Ramberg-Osgood function, the reinforcement was modeled as prestressing tendons without prestrain. Sample load-deflection curves are shown in Figure 2-17. The ratios of the analysis and experimental results and specimen properties are included in Table 2-11.

The following conclusions can be made from this study:

- Beams reinforced with a higher reinforcement ratio resulted in higher stiffness and ultimate strength. However, it also resulted in a reduction in ductility, with a reduction in mid-span deflection before failure.
- At failure, the average failure strain of concrete was 0.0033. The authors noted that the selection of a failure strain of 0.003 is reasonable when analyzing beams reinforced with high-strength A1035steel.

- The predictions of maximum load which used the Ramberg-Osgood function were close to the measured values. However, the results predicted using the f_y=100 ksi assumption were conservative.

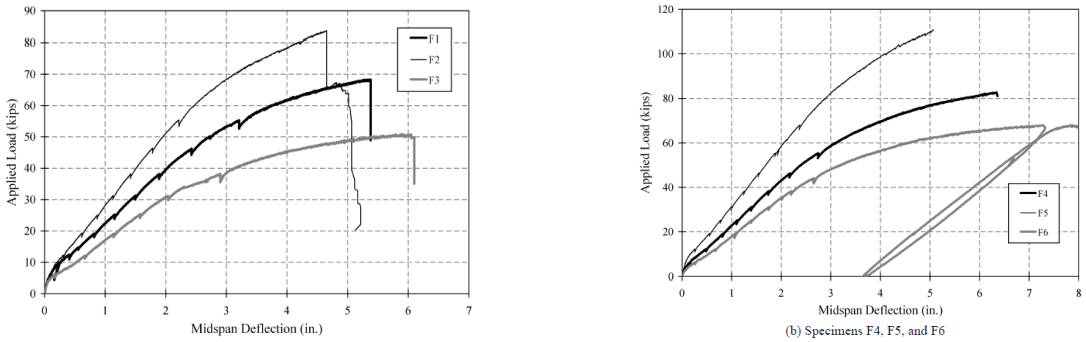

Figure 2-17 Load-deflection curves of the specimens (Adapted from NCPRP, 2014)

Table 2-11 Specimens properties and ratio of measured to computed capacity

Specimen	Concrete compressive strength (MPa)	Reinforcement ratio	Max. deflection	Stress-strain relationship		
				EPP* with f_y = 100 ksi	Mast. (2006)	Ramberg-Osgood
F1	69	1.2%	L/44	1.47	1.12	1.07
F2	69	1.7%	L/48	1.31	1.11	1.08
F3	69	0.7%	L/39	1.54	1.08	1.01
F4	103	1.6%	L/38	1.37	1.08	1.02
F5	103	2.2%	L/47	1.35	1.19	1.14
F6	103	1.2%	L/29	1.44	1.06	0.991

2.3.2.2.Garay-Moran & Lubell (2016)

This recent study by Garay-Moran and Lubell (2016) investigated the static behaviour of deep beams reinforced with high-strength steel bars. Eight beams built with ASTM A1035 Grade 100 steel and 45 MPa concrete were included in this study. The main parameters of the 300 mm by 607 mm rectangular beams were the shear-span to depth ratio a/d (1.19, 1.78, and 2.38), the longitudinal reinforcement ratio ρ (0.52-2.29%), and the presence of web reinforcement. The serviceability conditions, such as crack width and deflection limits, were also considered. Predictions were made by modifying the ACI 318 strut-and-tie model for ASTM A1036 high-strength steel using a sectional design model of the ACI ITG-6R-10. A number of conclusions from this research can be summarized as follows:

- As shown in Figure 2-18, the load capacity was increased with the increase of the reinforcement ratio, while ductility was decreased.
- The load capacity was also shown to increase with a decrease of the a/d ratio.
- Reinforcing the beams with web steel reinforcement was able to improve the strength and ductility of the beams.
- The failure mode was affected by the reinforcement ratio; with an increase in the reinforcement ratio, the failure mode changed from flexure to concrete crushing.
- The ACI ITG-6R-10 sectional model provided conservative predictions of beam strength (since it does not account for the increase in shear strength due to direct strut action), while the ACI 318 approach provided non-conservative predictions.

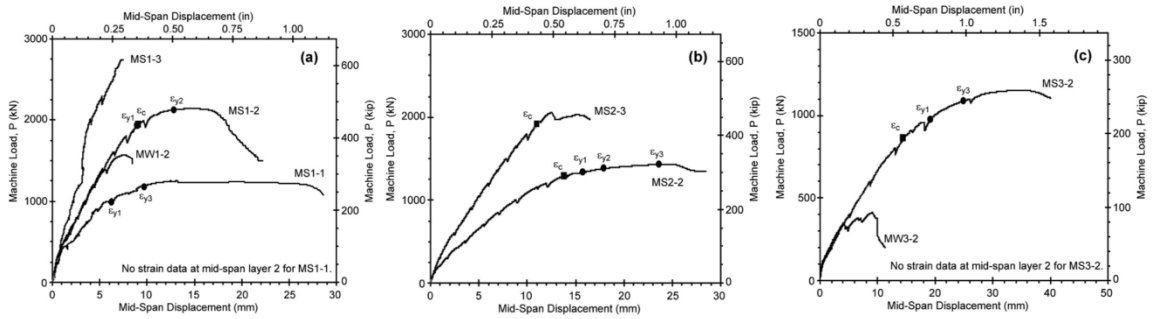

a) a/d = 1.19 b) a/d = 1.79 c) a/d = 2.38

Figure 2-18 Load – deflection curves for varied a/d specimens (Adapted from Garay-Moran & Lubell, 2016)

2.3.2.3.Mast et al. (2008)

In this analytical study, Mast et al. (2008) presented a simplified method to analyze the flexural capacity of concrete beams reinforced with high-strength steel bars. Three high-strength steel stress-strain curves were considered in the analysis. The first considered the actual stress-strain behaviour of high-strength steel as obtained from test data. The second model was a bilinear curve with yield strength of 550 MPa (80 ksi), based on the current ACI limitation. The third model was proposed by the authors and is composed of a bilinear curve with initial elastic modulus of 200,000 MPa and yield strength of 690 MPa (100 ksi) as defined previously in Equation (2–2). Finally, a bi-linear curve with conventional strength of 400 MPa (60 ksi) was also considered for comparison (Figure 2-19 (a) shows the different curves). The nominal moment capacity of a single reinforced concrete section was analyzed using the different steel material models, and the nominal capacity of the beam using the various models and cracked sectional analysis was plotted as a function of reinforcement ratio as shown in Figure 2-19 (b). Data from beam tests conducted by the Florida DOT and University of North Florida (NOF) were also included in the plot. The conclusions from this study are as follows:

- The balanced reinforcement ratios ρ_b were calculated as 3.95%, 2.60%, and 1.85% for the sections using the Grade 60 (400 MPa), 80 ksi (550 MPa), and 100 ksi (690 MPa) material models, respectively;
- At reinforcement ratios greater than 3.95%, the moment capacities using all models was the same, as the failure of the sections was governed by crushing of the concrete prior to yielding of the steel reinforcement;
- At reinforcement ratios less than 3.95% the higher strength steel models tended to predict larger moment capacities. At reinforcement ratios less than 1.75%, which represents most practical beam designs, the 100 ksi model under-predicted the capacities as compared to actual behaviour, while this model slightly over-predicted nominal capacity (by 2.5%) at ratios of 1.75-2.7%;
- To examine the benefit of using high-strength reinforcement, the strength of an example beam with 1% reinforcement was predicted using the different models. When the actual stress-strain model was used the beam capacity was 95% higher than the case with grade 60 (400 MPa) steel. This improvement dropped to only 31% when the ACI limitation of 80 ksi (550 MPa) was used. The simplified 100 ksi model predicted an increase of 60% in moment capacity. The actual reserve capacities using the ACI limitation and 100 ksi models were 33% and 18%, respectively, indicating that the 100 ksi model allows for efficient use of high-strength reinforcement, while providing acceptable reserve capacity.

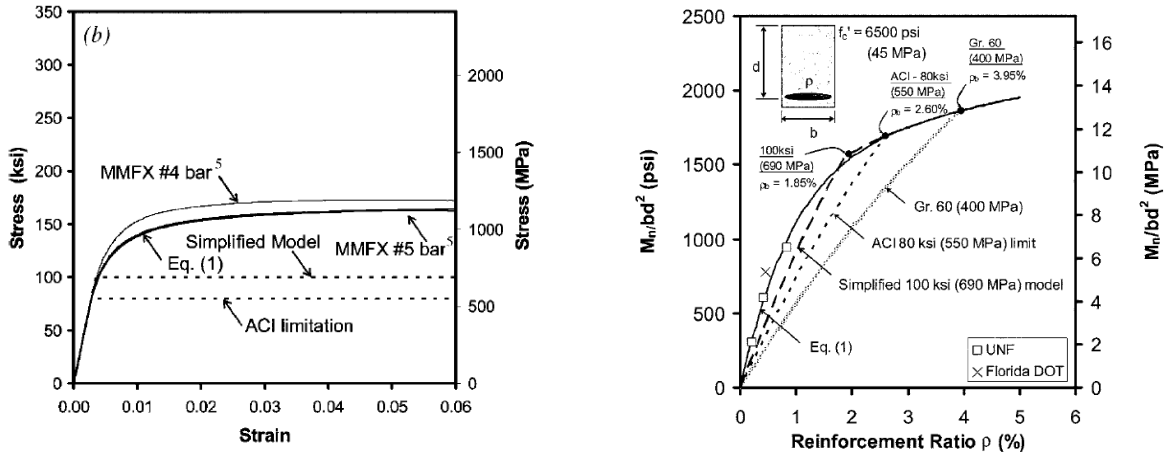

a) Existing and proposed limitations and material models

b) Nominal moment capacity as a function of reinforcing ratio

Figure 2-19 Stress-strain relationship of reinforcement and nominal moment capacity (Adapted from Mast et al., 2008)

The authors also proposed a simplified method for flexural design of concrete beams with high-strength reinforcement using a modified version of the ACI 318 simplified procedure. The design

uses an elastic-plastic material model with yield strength of 690 MPa (100 ksi) and modified strain limits for the resistance factor ϕ as shown in Equation (2–4). The design procedure was shown to result in beams with comparable flexural strength characteristics when compared to members using conventional Grade 60 reinforcing bars and current ACI 318 requirements.

$$\phi = \begin{cases} 0.65 & \varepsilon_t \le 0.004 \\ 0.45 + 50\varepsilon_t & 0.004 < \varepsilon_t < 0.009 \\ 0.9 & \varepsilon_t \ge 0.009 \end{cases} \quad \textbf{(2–4)}$$

2.3.3. CYCLIC LOADING – BEAMS CONTAINING HIGH-STRENGTH REINFORCEMENT

2.3.3.1.Cheng & Giduquio (2014)

The purpose of a recent study by Cheng & Giduquio (2014) was to investigate the behaviour of reinforced concrete beams containing high-strength steel bars under cyclic loading. Two types of high-strength steel reinforcement were considered in this study (SD685 and ASTM A1035 Grade 100). Both reinforcements have specified yield strength of 100 ksi (690MPa), with the difference being that SD685 steel has a yield plateau, while the ASTM A1035 steel lacks a well-defined yield point. Furthermore, the SD685 steel is relatively more ductile than the ASTM A1035 with rupture strains of 0.115 and 0.006 for these two bar types.

Three specimens were included in this research. Beams SP1, SP2, and SP3 were reinforced with conventional (Grade 60), SD685, and ASTM A1035 steel, respectively. The cross-section of the beams was 250 mm x 600 mm, with a 2100 mm long shear span The control specimen SP1 was reinforced with two No. 7 and one No. 5 steel bars at both top and bottom. Beams SP2 and SP3 were reinforced with three No. 5 bars at both the top and bottom to match the longitudinal reinforcement strength in beam SP1. The target compressive strength of concrete in this study was 37 MPa. Cyclic loading was applied using a displacement-controlled hydraulic actuator. The test results can be seen in Figure 2-20. The following conclusions can be drawn from this study:

- The peak moments and crack patterns of specimens SP1 and SP2 were similar. This can be explained by the fact that the SD685 bars did not reach ultimate stress due to rupture of the bars under cyclic loading, Beam SP3 showed a 35% increase in moment capacity when compared to the SP1 and SP2 specimens.
- All the specimens failed in flexure, however the SP3 specimen showed more brittle behaviour when compared to the SP1 and SP2 specimens, with larger crack widths and smaller failure drift. It is also noted that SP1 specimen exhibited the largest energy dissipation capacity, followed by beams SP2 and SP3.

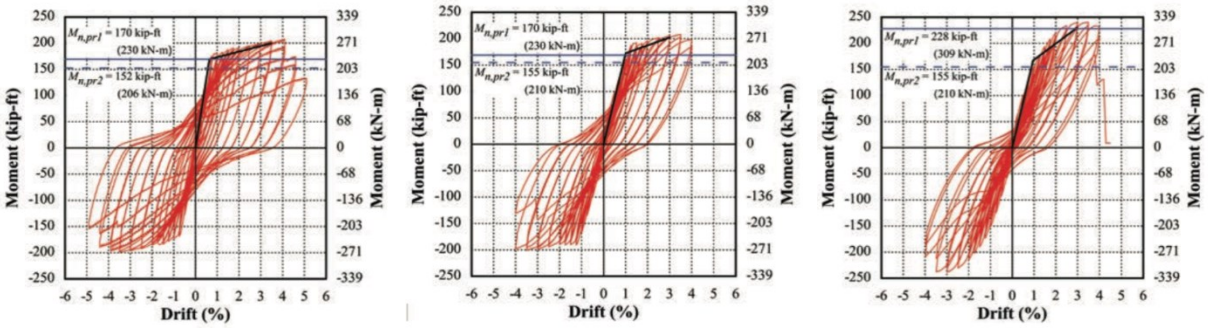

a) SP1 b) SP2 c) SP3

Figure 2-20 Results of the experiment (Adapted from Cheng & Giduquio, 2014)

2.4. RESEARCH ON STEEL FIBRE-REINFORCED CONCRETE BEAMS

2.4.1. SUMMARY OF PREVIOUS RESEACH ON HSFRC BEAMS

Table 2-12 shows a summary of the studies which have focussed on studying the shear and flexural behaviour of HSFRC beams. In this section, only a brief overview of the effect of steel fibres on shear and flexural behaviour of high-strength concrete beams is presented.

It is well known that the addition of steel fibre increases its tension capacity. In high-strength concrete beams subjected to shear the resulting increase in diagonal capacity results in an increase in shear capacity. Figure 2-21 (a) shows an example from Noghabai (2000), where beams $HSC_{S60/0.7/0.5}$ and $HSC_{S60/0.7/0.75}$ (with 0.5% and 0.75% fibres) show increased shear resistance when compared to the reference HSC beam (HSC_{REF}). The addition of sufficient amount of fibres has also been shown to allow for replacement of steel shear reinforcement. As seen in Figure 2-21 (b), the control specimen S0F0 (beams without fibres and stirrups) fails in shear, while the specimens without stirrups but containing steel fibres fail in flexure (Tahenni et al., 2016). Moreover, research shows that the shear strength of HSFRC beams decreases with an increase of the shear span-depth ratio a/d, which can be seen Figure 2-21 (c). For specimens with 1.5% fibres, the ultimate strength reduces from 750 kN to 370 kN, when increasing the shear span-depth ratio a/d from 1.0 to 2.0 (Ashour et al., 1992). Finally, the aspect ratio (ratio of fibre length and diameter) also affects the performance of HSFRC specimens. Comparing specimens with 1% fibres in Figure 2-21 (b), beam S0F1.0-80 (aspect ratio of 80) shows slightly larger resistance when compared to beam S0F1.0-65 (aspect ratio of 65).

The effect of steel fibres on flexural resistance is more moderate, where fibres have a more significant effect on ductility when compared to ultimate moment capacity. This effect can be seen in Figure 2-21 (b) from Tahenni's study. When compared to the plain concrete specimen with stirrups (S1F0), the fibre-reinforced specimens without stirrups and 1% or greater fibre content show a slight increase in ultimate strength and initial stiffness, with an enhancement in ductility (see beams S0F1.0-65, S0F2.0-65 and S0F3.0-65, with 1%, 2% and 3% fibres).

The next sub-section focuses on studies which have focussed on beams reinforced with high-strength steel bars and steel fibres.

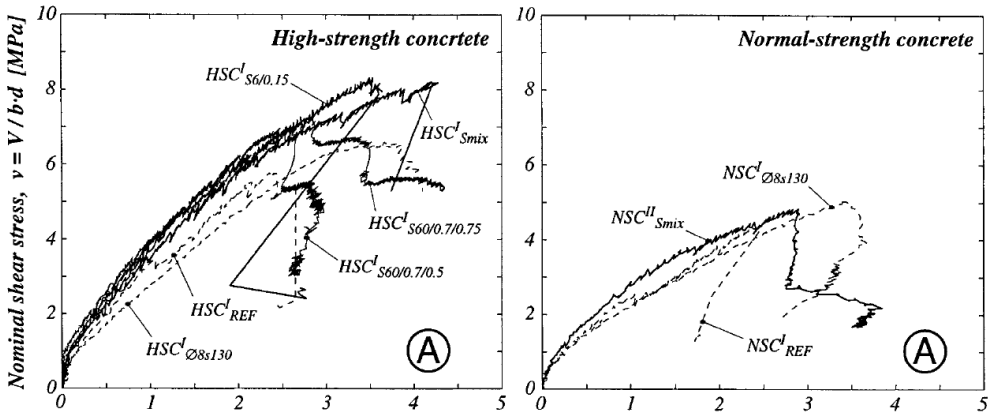

a) Effect of high-strength concrete and fibre content (Adapted from Noghabai, 2000)

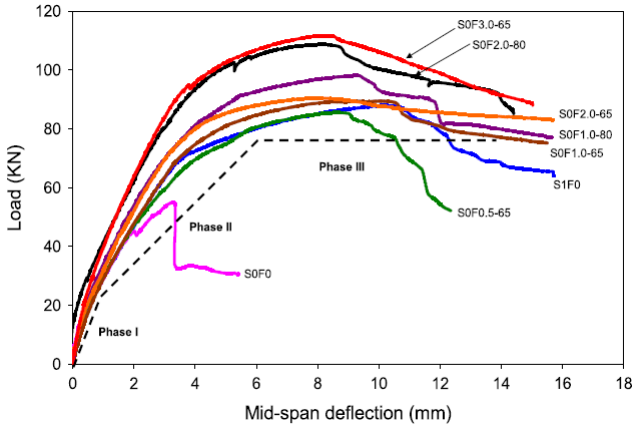

b) Effect of aspect ratio and fibres on shear and flexural resistance (Adapted from Tahenni et al., 2016)

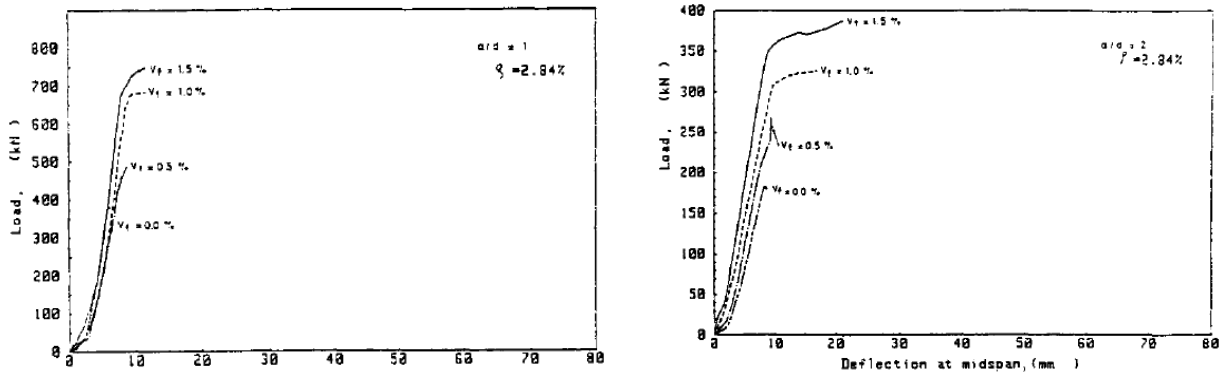

c) Effect of fibre content and shear span-depth ratio (Adapted from Ashour et al., 1992)

Figure 2-21 Effects of various parameters on shear and flexural behaviour of HSFRC beams

Table 2-12 Summary of previous studies which have focussed on HSFRC beams

Authors	Geometry				Material Properties		Fibres			
	Beams No.	b (mm)	h (mm)	a/d	f_c' (MPa)	ρ(%)	Fibre type	V_f (%)	L_f (mm)	d_f(mm)
Tahenni et al. (2016)	24	100	150	2.2	30-65	1.16	H	0-3.0	35, 65	0.54,0.75
Lbarra & Bishaw (2016)	8	254	254	1.0-3.0	93-118	1.2	H	0.5, 1	33	0.55
Guen et al. (2013)	11	150	250-350	-	60	0.77-2.7	H	0.5-2.0	32	0.9
Kang et al. (2012)	12	125,200	250,355	2.75,5.5	32-69	1.0-3.0	H	0-0.75	50, 60	0.75
Kwak et al. (2003)	12	125	250	2.0-4.0	31-65	1.5	H	0-0.75	50	0.8
Noghabai (2000)	32	200-300	250-701	2.9-3.3	39-93	2.8-3.3	S-H, H	0.5-1.0	/	/
Casanova et al. (1999)	5	125	250	2.89	90	2.2-3.5	H	1.2	30	0.5
Gustafsson et al. (1999)	20	200-300	250-700	2.9-3.3	98-129	0.5-1.0	S, H	0.5-1.0	6,30,60	0.15,0.6,0.7
Imam et al. (1994)	16	200	350	1.0-6.0	110	0.37-4.58	H	0-1.5	60	0.8
Ashour et al. (1992)	18	125	250	1-6	90	0.37-4.58	H	0.5-1.5	60	0.8
Narayanan & Darwish (1987)	33	85	150	2.0-3.5	36-75	2-5.72	C	0.25-3.0	30,40	0.3

H = Hooked end steel fibres S = Straight steel fibres C = Crimped steel fibres

2.4.2. PREVIOUS RESEARCH ON SFRC BEAMS CONSTRUCTED WITH HIGH-STRENGTH STEEL

2.4.2.1.Talboys & Lubell (2014)

The purpose of research conducted by Talboys and Lubell (2014) was to investigate the shear behaviour of large-scale beams reinforced with high-strength ASTM A1035 steel bars and steel fibres. In total, six beams were included in this research. The concrete had target strength of 35 MPa and was reinforced with a 1% volume of steel fibres, which had a length of 30 mm, tensile strength of 1100 MPa, and an aspect ratio of 55. All of the specimens were reinforced longitudinally with MMFX steel bars. The S300-B1 and S300-A2 specimens had the same dimensions with a width of 300 mm, a height of 300 mm and length of 1500 mm. The other four specimens had a 1000 mm by 300 mm rectangular cross-section, with a span length of 5500 mm. The reinforcement ratio ranged from 0.4% to 2.61%. All specimens had the same ratio of span to effective depth ratio (a/d). The load was applied using a displacement-controlled loading protocol at mid-span. The conclusions from this research can be summarized as follows:

- All the specimens failed due to diagonal shear failure. A higher reinforcement ratio resulted in higher flexure stiffness and higher load capacity.

- Shear stress at failure decreased with an increase of the member depth and increase in the strain in the longitudinal reinforcement.
- The authors also concluded that a size effect (and strain effect) does occur in SFRC members, and this size effect in shear is not affected by reinforcement type.
- Two concrete shear design models (ACI 318-11 and Desalegne & Lubell) were used to predict the shear strength of the beams. In both cases the models resulted in conservative prediction of the beam shear capacities since the models do not account for fibres. The ACI model showed an average test-to-analytical shear ratio which was closer to unity but showed large CoV since it does not account for the size or strain effect in shear. The Desalegne and Lubell model resulted in a lower CoV, and when combined with a multiplier to account for the steel fibres, the model was able to conservatively predict the shear capacities of SFRC beams with ASTM A1035 bars.

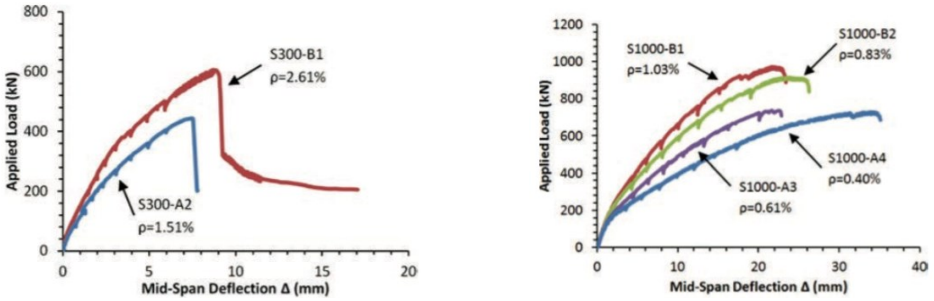

a) h=300 mm specimens b) h=1000 mm specimens

Figure 2-22 Load – deflection curves for specimens (Adapted from Talboys & Lubell, 2014)

2.4.2.2. Lbarra and Bishaw (2016)

The purpose of research by Lbarra and Bishaw (2016) was to investigate the behaviour of high-strength fibre reinforced concrete beam-columns containing high-strength steel under monotonic or cyclic loading. Eight beams were included in this research, with a concrete strength of 83 MPa. Details can be seen in Table 2-13. The experiment variables considered were yield strength of longitudinal reinforcement (Grade 60 and Grade 100), fibre content (0, 0.5%, and 1%), load type (monotonic and cyclic loading) and amount of transverse steel. Figure 2-23 shows the experimental results in terms of the force-drift ratio relationships. Observations and conclusions are summarized as follows:

- Under monotonic loading, the use of high-strength steel in HSC 60% in yielding and ultimate strengths but reduced ductility (from 10.6 to 3.6). Combined use of fibres and high-strength steel led to further increase in stiffness and strength at yield and ultimate, but did not lead to an increase ductility. The specimens without fibres experienced spalling during the test, while the specimens with fibres did not show this behaviour.

- Under cyclic loading, spalling of the HSC elements was observed, resulting in a reduction of the strength capacity. The use of HSFRC improved the performance of the beams and increased ultimate strength by approximately 10%. HSFRC specimens also had better crack control. However, specimens with fibres did not show an increase in the drift ratio and were more brittle than specimens without fibres (HSCfy60 & HSCfy100).
- The drift ratio at peak was larger for beams tested under monotonic vs. cyclic loading.
- Specimens with larger transverse reinforcement and larger steel fibre contents had slight increases in their drift ratios before failure.

Table 2-13 Details of all the specimens (Adapted from Lbarra and Bishaw, 2016)

No.	Type	$f'_{c,28}$*, ksi (MPa) at 28 days	$f'_{c,test}$, ksi (MPa) at test day	Nominal f_y, ksi (MPa)	Fibers, % by volume	A_{sh}/sb_c specimen	A_{sh}/sb_c† (ACI 318)	Loading protocol
S1	HSCfy60	15.0 (103.4)	15.8 (108.9)	60 (413.7)	—	0.0148	0.025	Monotonic
S2	HSCfy60	17.4 (120.0)	19.0 (131.0)	60 (413.7)	—	0.0148	0.031	Cyclic
S3	HSCfy100	14.0 (96.5)	14.4 (99.3)	100 (689.5)	—	0.0148	0.012	Monotonic
S4	HSCfy100	13.5 (93.1)	14.2 (97.9)	100 (689.5)	—	0.0148	0.012	Cyclic
S5	HSFRC	14.6 (100.7)	15.5 (106.9)	100 (689.5)	1.0	0.0148	0.013	Monotonic
S6	HSFRC	14.3 (98.6)	15.3 (105.5)	100 (689.5)	1.0	0.0148	0.013	Cyclic
S7	HSFRC	15.3 (105.5)	17.1 (117.9)	100 (689.5)	1.0	0.0087	0.014	Cyclic
S8	HSFRC	13.6 (93.8)	15.3 (105.5)	100 (689.5)	0.5	0.0087	0.013	Cyclic

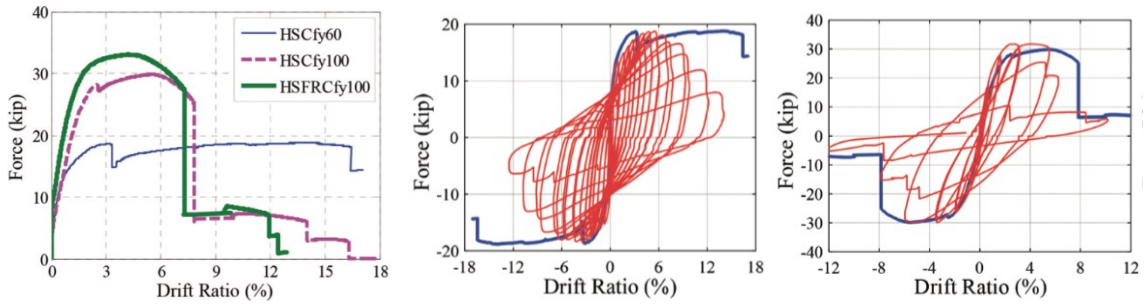

a) S1, S3, S5 b) S2 c) S4

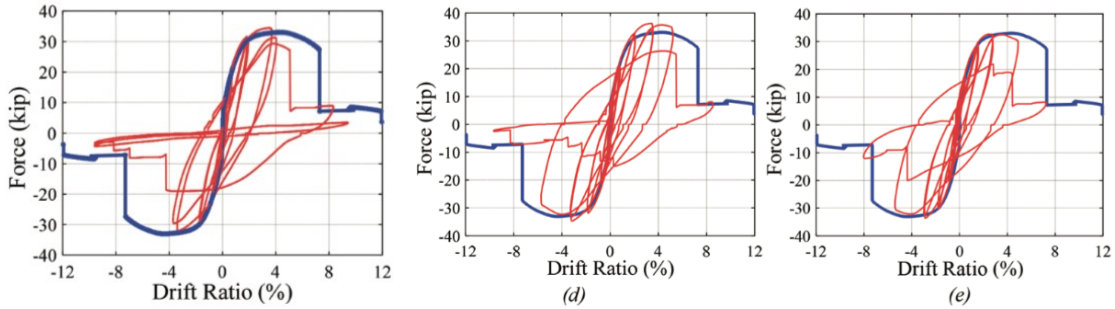

d) S6 e) S7 f) S8

Figure 2-23 Force – drift ratio for all specimens (Adapted from Lbarra and Bishaw, 2016)

2.5. RESEARCH ON THE BLAST PERFORMANCE OF BEAMS

2.5.1. RESEARCH ON BLAST PERFORMANCE OF REINFORCED CONCRETE BEAMS

2.5.1.1. A. Feldman & C. P. Siess - Part 1, Part 2 & Part 3 (1956-1962)

The purpose of a three-part study by A. Feldman & C.P. Siess (1956 – 1962) was to examine the dynamic behaviour of reinforced concrete beams subjected to impulsive loading. In addition to conducting one of the first experimental studies on the topic, the authors conducted dynamic analysis of the beams using an *ILLIAC* computing system and a SDOF analysis approach. In this series of reports, a total of 8 beams were tested. Each of the specimens had an identical cross-section, measuring 6 inches by 12 inches (150 mm x 300 mm), with a span length of either 9 ft / 108 inches (2743 mm) or 152 inches (3860 mm). The tested compressive strength of concrete was 45 MPa and the tensile yield strength of steel reinforcement was 327.5 MPa. Tension and compression reinforcement consisted of No. 7 bars, and No. 6 bars respectively, while shear reinforcement consisted of No. 3 stirrups (the tension, compression and shear reinforcement ratio was varied). In total 43 beams were tested, with 10 beams tested under single point loading at midspan, and 33 beams tested under two-point loading (with loads placed 18 inches each side of midspan). In the second set of tests, 8 beams were tested statically, with 25 beams tested dynamically. Impulsive load was applied using a pneumatic system and the sudden release of pressurized gas. In addition to the beam tests, a total of thirty-four steel specimens consisting of No. 6, No. 7 and No. 9 two-foot long bars were tested under variable strain rates. Variable parameters investigated included the span-to-depth ratio (a/d = 3.6 or 5.8), tension reinforcement ratio, presence of compression reinforcement, web reinforcement details, and the loading rate.

A few of the conclusions from the experimental program can be summarized as follows:

- The yield strength of steel reinforcement increased by approximately 40-50% under rapid rates of loading (10^0 in/in/sec) when compared to static loading (10^{-5} in/in/sec). However, high strain rates were not found to increase the failure strain.
- The various test variables were found to affect beam response under both static and dynamic loading and resulted in various modes of flexural and shear failure.
- In general, companion beams exhibited similar behaviour under static and dynamic loading, and the type of loading was not found to change failure mode or configuration (damage) at collapse. Some exceptions were noted where failure mode changed from flexure to shear under dynamic loading (the authors noted that these cases corresponded to beams having nearly balanced shear and flexural capacities).
- In some cases, the dynamic test beams could be subjected to additional blows or static loading after crushing had already occurred in the compression zone. This was for example the case of beams with compression reinforcement.
- The use of compression reinforcement was able to increase the collapse deflection of the beams (deformation before collapse), resulting in additional ductility. The effectiveness of

this steel was noted to be dependent on the spacing and configuration of the steel ties which prevent it from buckling.

- The test results did not show a clear trend with regards to the effect of tie detailing (welded ties, ties hooked in tension vs. compression region) on collapse deflection. However, the type of detailing did affect the opening of the ties under dynamic loading.
- Although not clearly observed in the experiments, the authors noted shear failure is more likely in beams with increased reinforcement ratio, decreased moment/shear or span/depth ratio, and decreased percentages or absence of web reinforcement.
- In general companion sets showed an increase in collapse deflection for beams tested under dynamic loading. This increase was attributed to a possible upward shift in the neutral axis under dynamic loading

In addition to the experiments, the authors conducted analytical work which aimed at predicting the dynamic response of beams under impulsive loading. The authors also examined various procedures to develop beam resistance functions which can be used in dynamic analysis. The reader can refer to Parts I-III of the Feldman and Siess (1956-1962) reports for further details.

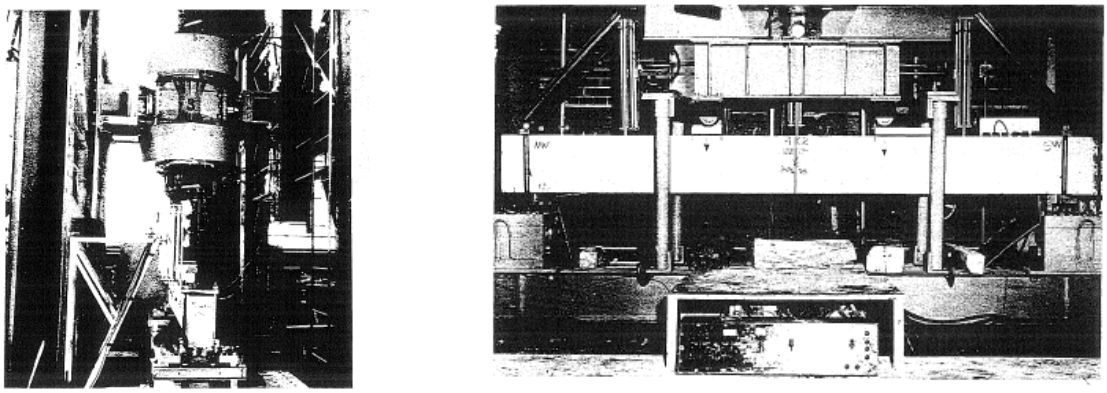

a) Rapid Load machine b) Test setup

Figure 2-24 Load machine and test setup (Adapted from A. Feldman & C. P. Siess, 1962)

2.5.1.2.Kujikake et al. (2009)

The purpose of the research study by Kujikake et al. (2009) was to investigate the behaviour of reinforced concrete beams under impact loading through experiments and analysis. Twelve beams divided into three series with the same cross-section measuring 150 mm by 250 mm, and a span length of 1700 mm, were included in this research. The target concrete compressive strength was 42 MPa and the yield strength of the steel was 400 MPa. The impact load was applied using a drop hammer device. A 400 kg hammer was released from different heights, which were 0.15 m, 0.3 m, 0.6 m and 1.2 m for beams reinforced in the D1616 series and 0.3 m, 0.6 m, 1.2 m and 2.4 m for beams reinforced in the D1322 and D2222 series. D1322 means two D13 rebars were used at the

top and two D22 reinforcement bars were used at the bottom. The cross-sections of the D13, D16 and D22 bars were 63.4, 198.5 and 387 mm^2, respectively.

Dynamic analysis was conducted using a two-degree-of-freedom system approach and an equation proposed by the authors. Moment-curvature relationships were determined using section analysis. DIF equations proposed by Fujikake et al. (2001), Ross et al. (1989) and JSCE (1993) were used for concrete in compression, concrete in tension and steel for tension. The resistance curves were obtained by integrating the curvature distribution over half the beam length. Sample results from this study can be seen in Figure 2-25. Some conclusions from the research are summarized below:

- The reinforcement ratio was found to affect failure mode. In the case of longitudinal reinforcement ratio, beams with lower amounts of reinforcement failed in flexure, while beams with larger amounts of reinforcement suffered flexural failure and local failure near the impact point. For the compressive reinforcement ratio, local failure was reduced with an increase of the reinforcement ratio.
- Maximum impact load, impulse, duration of impact load, maximum mid-span deflection, and duration to reach the maximum deflection, were increased with an increase in the height at which the hammer was dropped.
- The results predicted by both dynamic analysis methods showed a good agreement with the experimental deflections.

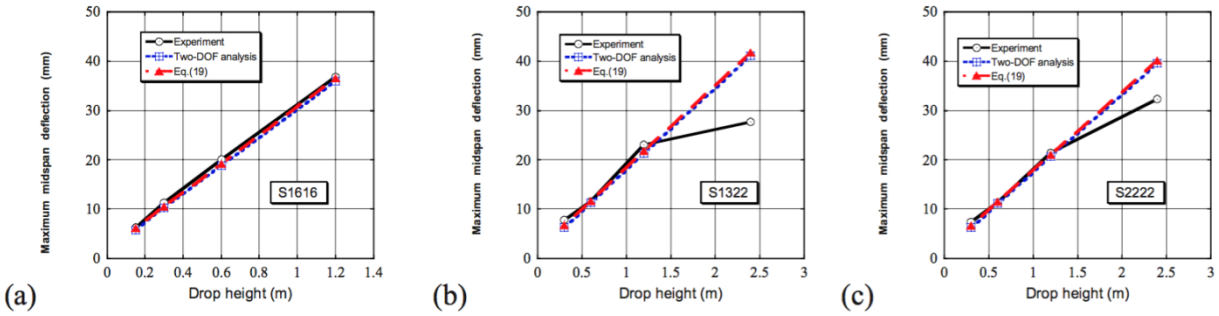

Figure 2-25 Relationship between maximum mid-span deflection and drop height: a) S1616; b) S1322; and c) S2222 (Adapted from Kujikake et al., 2009)

2.5.1.3. Adhikary et al. (2014)

The purpose of this research by Adhikary et al. (2014) was to investigate the behaviour of reinforced concrete beams under variable impact loads. In total, 24 beams were tested with an identical cross-section measuring 150 mm by 250 mm and a concrete compressive strength of 40 MPa. The longitudinal reinforcement ratio on the tensile side was 0.84%. The main variable parameters in this research were the shear reinforcement ratio ($\rho_{shear} = 0, 0.11\%, and\ 0.15\%$), loading rate ($4 \times 10^{-4}, 4 \times 10^{-2}, 4 \times 10^{-1}, and\ 2 \times 10^{0}\ m/s$), shear span–depth ratio (a/d = 3.3 or 4.4), and the reinforcement ratio on the compressive side ($\rho = 0\ or\ 0.84\%$). Some of the research conclusions can be summarized as follows:

- The beams with a higher shear reinforcement ratio resulted in higher shear capacity when compared to beams with lower shear ratio at the same strain rate.
- The ultimate resistance, energy absorption, and cracked stiffness increased with the increase in the loading rate.
- Shear span-depth ratios were found to affect failure mode, since specimens with a lower shear span-depth ratio of 3.3 failed in shear, while those with a higher ratio of 4.4 failed in flexure. Specimens with a higher shear span-depth ratio resulted in a higher maximum displacement at mid-span compared to the specimen with a lower shear span-depth ratio (80 mm vs. 40 mm).
- The authors also investigated the effect of compressive reinforcement ratio, however no clear trend was found due to limited and scattered data points.

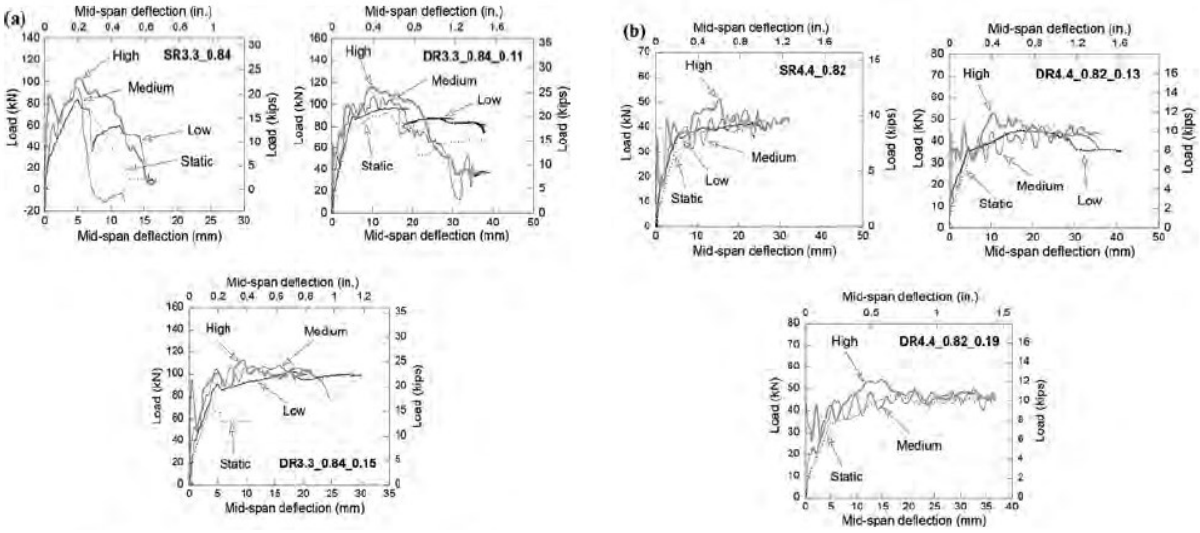

a) a/d=3.3 b) a/d=4.4

Figure 2-26 Load versus mid-span deflection of series specimens under varying loading rates (Adapted from Adhikary et al., 2014)

2.5.2. RESEARCH ON BLAST PERFORMANCE OF FLEXURAL MEMBERS BUILT WITH STEEL FIBRES OR HIGH-STRENGTH REINFORCEMENT

2.5.2.1.Magnusson et al. (2009)

This study by Magnusson et al. (2009) aimed to investigate the behaviour of high-strength concrete beams with fibres under blast loading, and included experimental work and an analytical study. In total, 49 beams were tested, with 38 beams tested under dynamic air-blast loading and 11 beams tested under static loads. The dimensions of the beams were 160 mm x 300 mm x 1720 mm. The

compressive strength of concrete varied from 40 MPa to 200 MPa, and all the beams were reinforced with conventional longitudinal steel bars with nominal yield strength of 550 MPa. The reinforcement ratio and steel fibre content were also varied. The details of the specimens can be seen in Table 2-14. Several beams were also cast in two layers with two different concrete strengths. A four-point load setup was used for the static test, and the dynamic load was simulated with a shock-tube.

Table 2-14 Specimen details (Adapted from Magnusson et al., 2009)

Beam type	Compressive strength, f_{cc}: MPa	Tensile reinforcement	Mechanical reinforcement ratio, ω_s	Reinforcement yield stress, f_{sy}: MPa	Remarks
B40	43	5ϕ16 mm	0·34	604	—
B100(16)	109	5ϕ16 mm	0·14	604	—
B100(12)	81	4ϕ12 mm	0·081	555	—
B140	92	6ϕ12 mm	0·10	544	—
B140F	90	6ϕ12 mm	0·10	544	Steel fibres (1·0 vol-%)
B140F/40	113/46	6ϕ12 mm	0·083	544	Two concrete layers, steel fibres (1·0 vol-%) in the HSC
B150	133	6ϕ12 mm	0·075	555	—
B200	173	5ϕ16 mm	0·082	555	—
B200F	205	5ϕ16 mm	0·072 static test 0·078 dynamic test	604 555	Steel fibres (2·4 vol-%) Steel fibres (2·4 vol-%)
B200/40	173/54	5ϕ16 mm	0·082	555	Two concrete layers
B200F/40	167/48	5ϕ16 mm	0·098	597	Two concrete layers, steel fibres (2·4 vol-%) in the HSC

Figure 2-27 shows the static and dynamic test results. Observations and conclusions from this research can be summarized as follows:

- Increasing the reinforcement ratio and concrete strength resulted in a higher load capacity, but also decreased the ductility of the beams.
- The failure mode changed with an increase of the reinforcement ratio. The B100 (16) specimen with 5 Φ 16 mm reinforcing bars failed in shear with a larger deflection than the B100 (12) specimen reinforced with 4 Φ12mm steel bars.
- Reinforcing the beams with steel fibres was found to slightly increase peak load, significantly increase ductility, prevent a sudden drop in the load-resistance at failure, and reduce crack widths. The same observations were made for both the static and dynamic tests. Reinforcing the beams with steel fibres was also found to reduce the maximum and residual displacement under dynamic loads.
- Using two concrete layers of different strengths in the beams resulted in a reduction of stiffness and peak load.
- In comparing the failure modes of static tests and dynamic tests, the same type of beams failed in different modes. Companion beams which failed in flexure in the static tests were sometimes found to fail in shear in the dynamic tests.
- Using steel fibres was found to be effective in preventing shear failures under dynamic loading

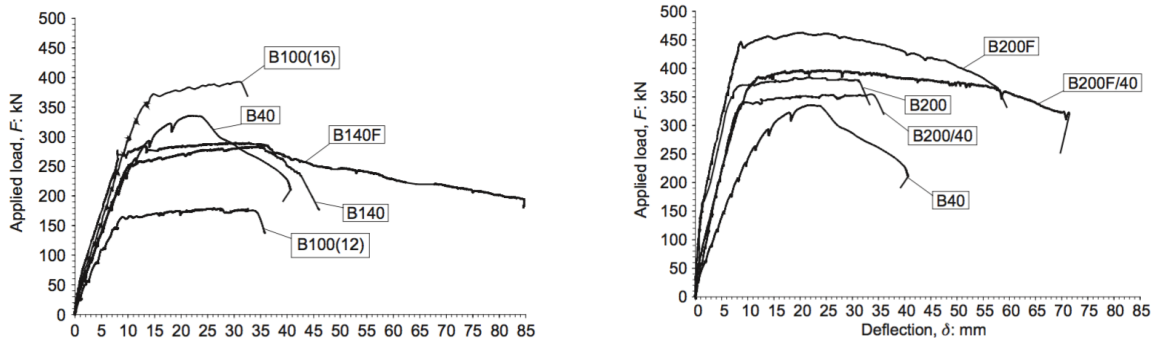

a) Static test results

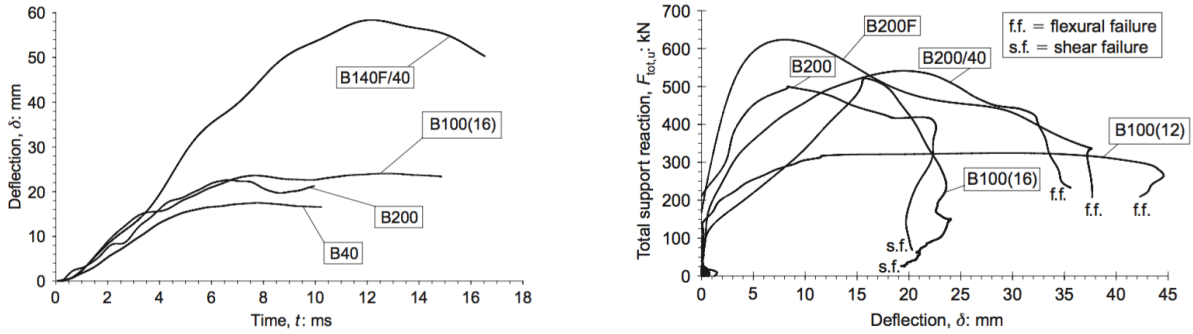

b) Dynamic test results

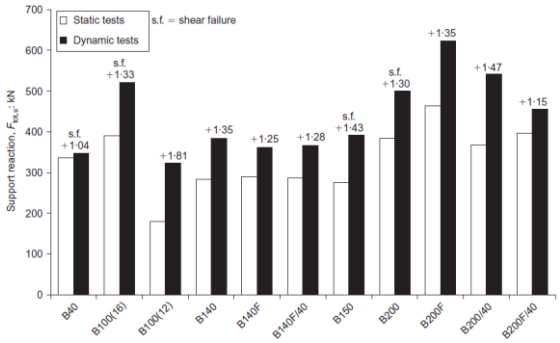

c) Ratios of Dynamic and static results

Figure 2-27 Static and dynamic load-deflection curve (Adapted from Magnusson et al., 2009)

2.5.2.2.Magnusson et al. (2010)

This second paper by Magnusson et al. (2010) presents the theoretical analysis of the beams presented in the previous study by the same authors. The software Ansys Autodyn (Autodyn, 2003) was used to analyze the beams and predict failure mode and maximum deflections.

Concrete in compression was modelled using the RHT material model proposed by Riedel (2000). A bi-linear crack softening model proposed by Gylltoft (1983) and a linear crack softening model were used for concrete in tension. The original J&C constitutive model proposed by Johnson and

Cook (1983) and the modified J&C constitutive model proposed by Westerling (2005) were used for longitudinal reinforcement. The bond stress–slip relationship was modelled using the CEB (1993) and a modified model proposed by Magnusson (2000). The dynamic increase factor (DIF) for concrete in compression and steel followed the CEB-FIP (1993) and Malvar and Crawford (1998) models.

A summary of simulation cases is presented in Table 2-15. The mesh sizes for the beams with 12 mm and 16 mm reinforcement were 4 mm x 4 mm and 3.1 mm x 3.1 mm respectively.

Table 2-15 Summary of simulation cases (Adapted from J. Magnusson et al., 2010)

Simulated beam	Tested beam (Magnusson *et al.*, 2009)	Compressive strength, f_{cc}: MPa	Tensile strength, f_{ct}: MPa	Reinforcement yield strength, f_{sy}: MPa	Tensile reinforcement	Remarks
S40a	B40	50	6·0	549	5ϕ16 mm	Linear crack softening Original J&C model
S40b	B40	50	4·1	549	5ϕ16 mm	Linear crack softening Original J&C model
S40c	B40	50	4·1	549	5ϕ16 mm	
S40d	B40	50	4·1	549	5ϕ16 mm	Reinforcement interface
S100	B100(16)	109	5·0	549	5ϕ16 mm	Reinforcement interface
S140F/40a	B140F/40	113/46	6·5/3·5	523	6ϕ12 mm	
S140F/40b	B140F/40	113/46	6·5/3·5	523	6ϕ12 mm	Reinforcement interface
S200	B200	175	9·0	549	5ϕ16 mm	Reinforcement interface

The simulated displacement–time history curves are shown in Figure 2-28. A summary of the results and conclusions are as follows:

- The RHT model combined with a bi-linear model for the crack softening of concrete in tension were found to be suitable for dynamic analysis for both NSC and HSC elements.
- Beam S40c, analyzed using the modified version of J&C material model resulted in more accurate results when compared to Beam S40b, which was analyzed using the original J&C model. This difference was attributed to the different ways in which strain-rate effects are considered in the models (the original model uses a constant yield stress up to a strain of 1.0 s-1, while the modified models vary yield stress with strain rate).
- Comparing predictions S40a and S40d, a better prediction of maximum displacements was obtained when using a bilinear vs. linear strain softening model for concrete in tension. However, the bilinear model results in a slightly stiffer stiffness.
- The use of a modified bond model in the beam simulations gave good approximations of the real bond behaviour in the beams.

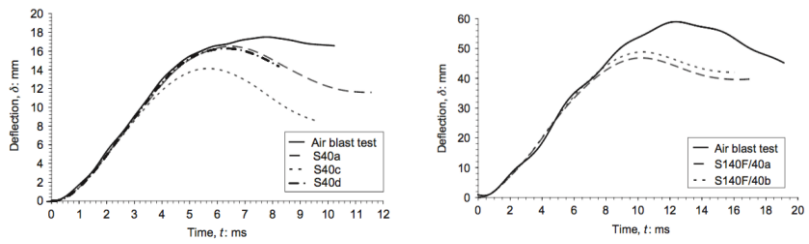

Figure 2-28 Sample simulated displacement-time history curves (Adapted from J. Magnusson et al., 2010)

2.5.2.3.Burrell et al. (2015)

This purpose of this study by Burrell et al. (2015) was to investigate the behaviour of steel fibre-reinforced concrete (SFRC) columns under blast loading. All the specimens had the same dimensions of 152 mm x 152mm x 2468mm. The main variable parameters were concrete type (concrete vs. SFRC), transverse reinforcement spacing (38 mm and 75 mm; non-seismic and seismic), fibre content (0 - 1.5%), fibre type. Each column was subjected to varying degrees of blast load simulated by a shock-tube until failure. The driver pressures of Blasts 1, 2 and 3 were 10psi, 35psi, 80psi, respectively, with a 9ft driver length. *RCBlast* software, based on a single-degree-of-freedom approach, was used for theoretical analysis.

Figure 2-29 shows sample comparisons of maximum and residual displacements at Blast 3. The following conclusions can be drawn from this study:

- SFRC resulted in a better control of maximum and residual displacement and an increase in damage tolerance, such as the reduction of secondary fragmentation, when compared to conventional concrete.
- Increasing the fibre content from 0.5% to 1.5% was effective in better controlling displacements at equivalent loads. Furthermore, use of 1% or more fibres was able to match the response of a conventional concrete column with seismic detailing.
- The use of seismic detailing (reduced transverse reinforcement spacing) was able to reduce displacements and prevent rebar buckling, thus allowing the columns to sustain a larger blast load before failure.

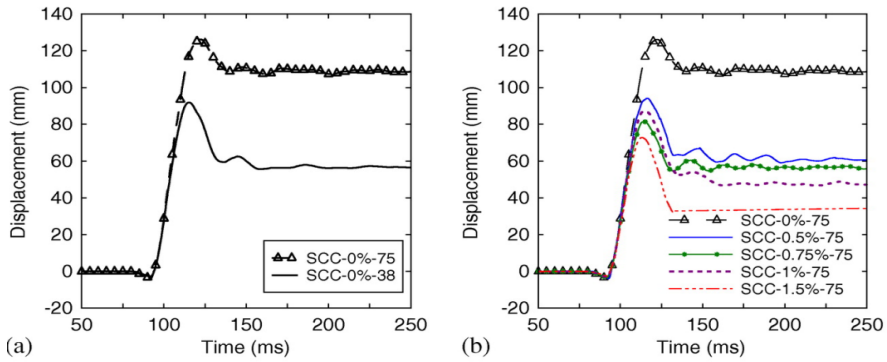

Figure 2-29 Comparison of displacements at Blast 3: a) effect of seismic detailing, b) effect of fibres (Adapted from Burrell et al., 2015)

2.5.2.4. Thiagarajan et al. (2014)

This study by Thiagarajan et al. (2014) investigated the performance of doubly reinforced concrete slabs under blast loads. Four slabs were included in this research, and all the specimens had the same dimensions of 1652 mm x 857 mm x 102 mm. The four specimens included slabs with: HSC and high-strength reinforcement (HSC-VR), HSC and normal-strength steel reinforcement (HSC-NR), normal-strength concrete with high-strength reinforcement (NSC-VR), and normal-strength

concrete with normal-strength reinforcement (NSC-NR). The specimens were reinforced with 9.5 mm diameter bars in the top and bottom layers with a spacing of 102 mm and 305 mm along the length and width of the slabs, respectively. Software LS-DYNA was used for the FEM analysis of the slabs. Various material models and mesh sizes were considered in the analysis. The experiment results and numerical results are shown in Figure 2-30. Some of the observations from the results are as follows:

- High-strength concrete and high-strength reinforcement showed improvement in maximum displacement control. The best results were obtained when both high-strength concrete and steel were used, with benefits also associated with the use of either high-strength steel bars or high-strength steel bars. The displacements of NSC-VR, NSC-NR, HSC-VR, HSC-NR were: 129 mm, 221 mm, 122 mm, and 140 mm, respectively.

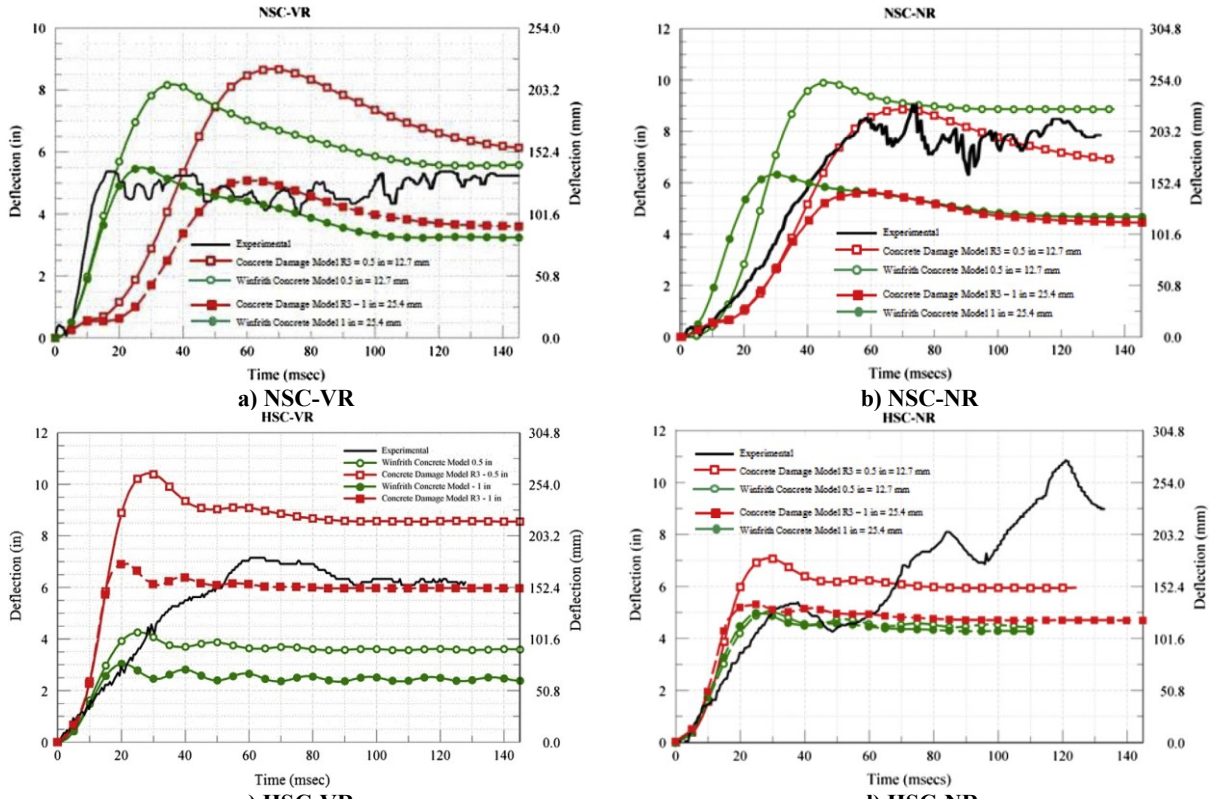

Figure 2-30 Experiment and numerical results
(Adapted from Thiagarajan & Kadambi et al., 2014)

2.5.2.5.Stolz et al. (2014)

The purpose of a study by Stolz et al. (2014) was to investigate the static and dynamic behaviour of ductile DUCON concrete slabs reinforced with normal-strength or high-strength reinforcement having tensile strengths of 350-400 MPa and 750-850 MPa. The compressive strength of concrete was 100-130 MPa. There were three types of configurations, with three specimens included in

each configuration; the specimens varied in terms of plate thickness, mesh size and micro malt reinforcement ratio. For the static test, all the specimens had a 60 cm clear span and 10 cm width and were tested under four-point bending. For the dynamic test, the specimens had a width of 1.14 m, a clear span of 2.31 m with loading applied using a shock-tube. The applied loading levels were 35 kPa, 40 kPa, 67 kPa, 104 kPa, 147 kPa, 200 kPa and 250 kPa. In addition, single-degree-of-freedom analysis with derivation of resistance functions were used to derivate the elastic and fracture limits of the slabs in the form of pressure-impulse diagrams for each loading level. The limit and fracture limit were plotted together with experimental pressure and impulse. The damage level was determined from the experiments. Some of the observations and conclusions are as follows:

- Slabs with a larger depth resulted in a higher capacity and similar ductility, defined by the ratio of ultimate and elastic displacements.
- Use of high-strength steel resulted in reduced mid-span displacements and were more effective in controlling cracking.
- The slabs with less reinforcement had more ductility compared to the specimens with a higher amount of reinforcement. It was also found that specimens with higher reinforcement ratios had higher dynamic bending strengths
- All the specimens were observed to have similar damage levels and distribution at failure.
- The crack pattern under dynamic load was close to the static test result.

2.6. SUMMARY

This chapter presented a literature review related to the materials used in this research study and the effects of high-strain rate loading on material properties. It also reviewed previous studies on beams reinforced with high-strength steel and/or fibres under static and dynamic loading. Some conclusions can be summarized below:

- High-strength concrete (HSC) and high-strength (HS) steel reinforcement show distinct properties when compared to normal-strength concrete and steel. In particular, the high strength of these materials is associated with reduced ductility. In the case of HSC, the addition of steel fibres can be used to reduce brittleness in compression, while also enhancing tensile resistance. Models for predicting the stress-strain behaviour of HSC, HSFRC and high-strength reinforcement were introduced in this chapter. In the case of HS steel the ACI ITG-6R model, Mast et al. can be predicted the stress-strain relationship of MMFX steel.
- Application of dynamic loading results in an increase in the strength of concrete and steel, which can be accounted for using dynamic increase factors (DIF). DIF models for concrete in compression/tension, HSFRC and steel reinforcement were reviewed. The CEB model for concrete in compression predicts a reduction in strain-rate sensitivity for HSC when compared to NSC, while other models neglect this effect due to high scatter in experimental

data. The DIF of steel is more significant at yield than ultimate. There is no research on the DIF of ASTM A1035 steel, however the Malvar (1998) study shows that the DIF reduces as the steel strength grade is increased.

- Current research on beams reinforced with ASTM A1035 steel has focused primarily on shear behaviour, where studies show that the use of this high-strength steel as longitudinal or transverse reinforcement increase shear resistance. For flexure, the use of high-strength steel results in an increase in ultimate capacity. However, the response of such beams can be brittle, with no distinct yield plateau owing to the stress-strain behaviour of this steel type. Research on the cyclic response of beams reinforced with ASTM A1035 steel bars shows that use of high-strength steel can increase peak moment capacity, although ductility can reduce. It is also noted that limited research has been conducted on HSC beams reinforced with high-strength bars.
- In general, using yield strengths of 690 and 550 MPa for analysis results in conservative predictions of the ultimate moment capacity of beams reinforced with ASTM A1035 bars.
- Provision of steel fibres enhances the response of high-strength concrete beams by increasing shear capacity. In flexure fibres result in an increase in HSC beam ductility. Limited research has been conducted to examine the flexural response of HSFRC beams reinforced with high-strength steel bars.
- Research on reinforced concrete beams tested under impact and blast loading indicates that member strength increases under dynamic loads. Research also shows that increasing the reinforcement ratio can change the failure mode of reinforced concrete beams from flexure to shear under dynamic loading.
- A limited number of studies have investigated the blast response of HSFRC structural members. Research on SFRC columns shows that fibres reduce maximum and residual displacements and improves damage tolerance under blast loading. Research on beams shows that fibres are effective in preventing shear failure under dynamic loading.
- Limited studies have examined the blast behaviour of reinforced concrete members containing high-strength (HS) steel. Research on NSC and HSC slabs indicates HS reinforcement can reduce maximum displacements under blast loading. There are no studies in the literature on the blast behaviour of HSFRC members reinforced with high-strength steel bars.

CHAPTER 3. EXPERIMENTAL PROGRAM

3.1. CHAPTER OVERVIEW

This experimental project examines the blast and static performance of reinforced concrete beams constructed with high-strength concrete and high-strength steel reinforcing bars. As part of the study, eight beams were tested under simulated blast loading using the University of Ottawa Shock-tube, and three companion beams were tested under quasi-static four point bending. The parameters investigated include the effect of concrete strength, the effect of steel fibres, and the effect of the ratio and strength of the longitudinal steel-reinforcement.

This chapter outlines the details of the experimental program and provides information regarding the beam designs, material properties, experimental setups and test procedures.

3.2. SPECIMEN SPECIFICATIONS

A total of eleven beams were included in this research study. Eight of the beams were tested under simulated blast loads. Among the dynamic beams, two beams were constructed with normal-strength, self-consolidating concrete (SCC), three beams were built with high-strength concrete (HSC), and three beams were built with high-strength fibre reinforced concrete (HSFRC). The remaining three beams consisted of a companion set of high-strength concrete (HSC) beams which were tested under quasi-static loads. In all cases the beams were built with high-strength steel reinforcing bars.

As shown in Figure 3-1, all specimens had a length of 2440 mm, a depth of 250 mm and a width of 125 mm. The specimens were tested under four-point bending over a simply-supported span of 2232 mm, with shear spans of 741 mm. The longitudinal reinforcement consisted of two ASTM A1035 Grade 100 (MMFX) bars which varied in size to examine effect of reinforcement ratio (ρ): 2 - No. 4, 2 - No. 5 or 2 - No. 6 American size bars (ρ = 0.9%, 1.5% and 2.2%). In order to provide proper development length, the No.4 and No.5 bars were detailed with 90° hooks. Due to difficulty in bending larger diameter high-strength reinforcement, the No.6 bars were kept straight and extended over the entire length of the beams. All beams contained transverse reinforcement which consisted of stirrups made from 6.3 mm smooth steel wire. This shear reinforcement was spaced at 100 mm in the shear spans. In order to facilitate construction and placement of the stirrups 2 - 6.3 mm bars were also provided as compression reinforcement (these bars did not extend beyond the shear spans). In all cases the bottom clear cover to the stirrups was kept at 35 mm. The HSFRC specimens were built with high-strength concrete reinforced with a volumetric ratio of 1% of hooked-end steel fibres (78 kg/m^3).

The specimens can be divided into three categories based on concrete type, which include the: SCC series, HSC series and HSFRC series. Table 3-1 shows a summary of the design details for

the various beams in this research study, including concrete type, fibre content, steel reinforcement details and loading type (D = Dynamic, S = Static). Nomenclature for the specimens follows the following logic:

CONCRETE TYPE –F(FIBRE CONTENT)- SIZE OF REINFORCING BARS- STIRRUP

For example, SCC-F0-#4-S is the label for a beam constructed with plain normal-strength self-consolidating concrete (SCC) and reinforced with No.4 MMFX steel bars and stirrups. Similarly, HSC-F1-#4-S is the label for a beam constructed with high-strength concrete containing 1% steel fibres (i.e. HSFRC), and containing No.4 MMFX bars and stirrups.

Table 3-1 Specimen matrix

Series	Specimen ID	Concrete Type	Fibre content V_f(%)	Longitudinal Reinforcing Bars	Transverse Reinforcement	Load Type
SCC Series	SCC-F0-#4-S	SCC	0	2 - No.4	6.3 mm stirrups @ s = 100 mm	D
	SCC-F0-#5-S			2 - No.5		
HSC Series	HSC-F0-#4-S	HSC		2 - No.4		D&S
	HSC-F0-#5-S			2 - No.5		
	HSC-F0-#6-S			2 - No.6		
HSFRC Series	HSC-F1-#4-S		1%	2 - No.4		D
	HSC-F1-#5-S			2 - No.5		
	HSC-F1-#6-S			2 - No.6		

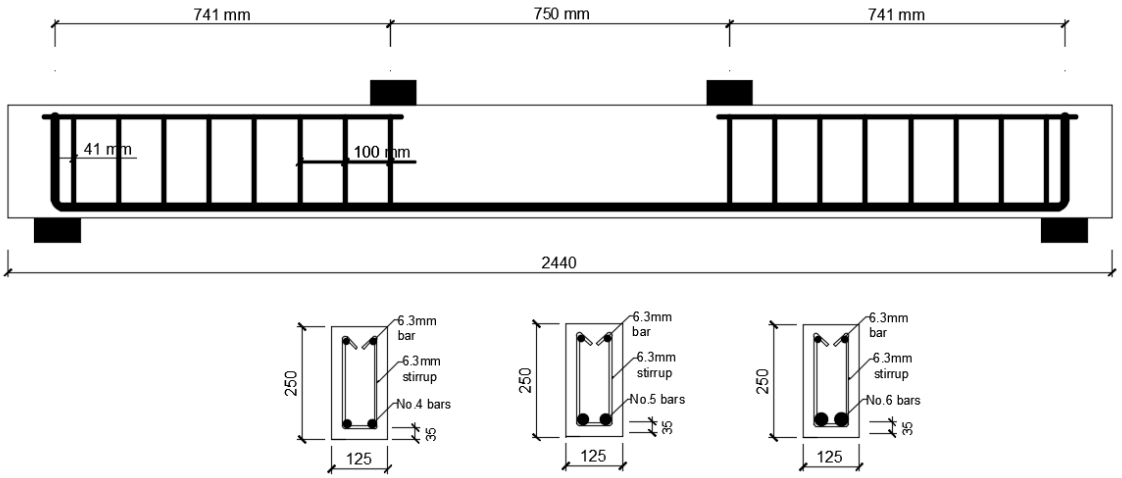

Figure 3-1 Specimen dimensions and reinforcement details

3.2.1. THE SELF-CONSOLIDATING CONCRETE (SCC) SERIES

The self-consolidating concrete (SCC) series included two dynamic specimens: SCC-F0-#4-S and SCC-F0-#5-S. No static beams were included in this series. Both specimens were constructed with plain normal-strength SCC and were reinforced with stirrups in the shear spans. The only difference between them was that they were reinforced with different sized high-strength longitudinal steel bars. The SCC-F0-#4-S beam was reinforced with 2 - No.4 MMFX steel bars, while the SCC-F0-#5-S beam was reinforced with 2 - No.5 MMFX steel bars.

3.2.2. THE HIGH-STRENGTH CONCRETE (HSC) SERIES

The high-strength concrete (HSC) series consisted of three dynamic specimens and three companion static specimens: HSC-F0-#4-S, HSC-F0-#5-S, HSC-F0-#6-S. These specimens were constructed with plain high-strength concrete (HSC) and were reinforced with 2 - No.4, 2 - No.5, and 2 - No.6 MMFX steel bars respectively. Stirrups were included in the shear spans for all specimens.

3.2.3. THE HIGH-STRENGTH FIBRE REINFORCED CONCRETE (HSFRC) SERIES

This series included three beams which were tested under dynamic loading. The HSC-F1-#4-S, HSC-F1-#5-S and HSC-F1-#6-S specimens were built using high-strength fibre reinforced concrete (HSFRC) and reinforced with stirrups and 2 - No.4, 2 - No.5, and 2 - No.6 MMFX steel bars, respectively. No static beams were included in this series. The only difference between the companion specimens in the HSFRC and the HSC series was the concrete type, with the HSFRC beams built with HSC containing 1% steel fibres by volume of concrete (78 kg/m^3).

3.3. MATERIALS

This section provides details regarding the materials used in this study. The sub-sections that follow summarize the properties of the different concrete mixtures, steel fibres, and steel reinforcement used in the construction of the beam specimens.

3.3.1. CONCRETE PARAMETERS

Three types of concrete mixtures were used in this study. All concrete was mixed using a large pan-mixer at the University of Ottawa Structures Laboratory. The normal-strength concrete specimens were cast using a self-consolidating concrete (SCC) mix. Table 3-2 shows the properties of the pre-packaged MS-S10 SCC mix (manufactured by *King Packaged Materials Company*). The mix has a specified strength of 40 MPa, maximum aggregate size of 10 mm, a fine-to-aggregate ratio of 0.55 and contains admixtures in the form of dry powder. This mix has similar hardened properties to those of conventional concrete, but does not require consolidation during casting due its self-levelling properties.

Table 3-3 shows the properties of the HSC and HSFRC mixtures used in this study. The same base mix with a target strength of 100 MPa was used for both concretes with the only difference being an increased amount of super-plasticizer and provision of 1% steel fibres (78 kg/m^3) in the HSFRC mixture. The base mix consisted of Type 1 (GU) Portland cement, silica fume, slag, two sizes of coarse aggregate (19 mm and 9.5 mm), sand, water and admixtures which included a set-retarder and super-plasticizer. As noted previously, to ensure adequate workability when adding fibres, more super-plasticizer was used for the HSFRC mix.

Table 3-2 KING SCC mix properties

Component	Content
HSF Cement	500 kg/m^3 of concrete
Coarse Aggregate	765 kg/m^3 of concrete
Fine Aggregate	915 kg/m^3 of concrete
Mass Density	2300 kg/m^3

Table 3-3 HSC and HSFRC mix properties

Component	Content	Content (For two beams)
Portland Cement (GU)	440.3 kg/m^3	67.14 kg
Slag	193.6 kg/m^3	29.52 kg
Coarse Aggregate 1 (19 mm)	661 kg/m^3	100.8 kg
Coarse Aggregate 2 (9.5 mm)	661 kg/m^3	100.8 kg
Silica Fume	56.7 kg/m^3	8.64 kg
Sand	872.1 kg/m^3	133 kg
Water	185.6 kg/m^3	28.3 kg
Retarder	3.3 L/m^3	0.5 L
Super Plasticizer	13.1 L/m^3	2 L or 2.2 L
Steel fibres (V_f = 0 or 1%)	0 or 78 kg/m^3 of concrete	0 or 11.43 kg

Cement	Coarse Aggregate 1 (19 mm)	Coarse Aggregate 2 (9.5 mm)	Sand
Silica fume	Slag	Super-plasticizer	Retarder

Figure 3-2 Materials used in the base HSC mix

3.3.2. STEEL REINFORCEMENT PARAMETERS

Two types of steel reinforcement were used for this research, including high-strength ASTM A1035 Grade 100 (also called MMFX) bars with varied sizes (used as longitudinal reinforcement), and 6.3 mm steel wire (used for the shear reinforcement and top bars).

Table 3-4 summarizes the properties of the steel used in the current study, including identification, type of reinforcement, bar diameter, bar area, as well as strain and strength at yield (ε_y and f_y) and ultimate state (ε_u and f_u). All samples were tested in direct tension using the 600 kN GALDABINI universal testing machine shown in Figure 3-3. Figure 3-4 shows stress-strain curves for three samples for each bar type, and Figure 3-5 compares typical stress-strain relationships for the 6.3 mm wire and the No. 4, 5 and 6 MMFX reinforcement. The 6.3 mm steel reinforcement shows a yield plateau allowing for identification of the yield point. On the other hand, the high-strength MMFX steel reinforcement shows a roundhouse curve with no clear yield point; the 0.2% offset method was used to determine the yield strain and stress for this reinforcement type.

The smooth steel wire was used for the top reinforcement and stirrups. This reinforcement had a diameter (d_b) of 6.35 mm, cross-sectional area (A_b) of 32 mm^2, an average yield stress of 577 MPa at a strain of 0.0028, with an average ultimate stress of 645 MPa at a strain of 0.0701 mm/mm. The average strain at rupture was 0.16 mm/mm.

The American size No.4, No.5, and No.6 MMFX steel bars, with diameters of 12.7, 15.9, and 19.1 mm, and cross-sectional areas of 129, 200 and 284 mm^2, were used for the bottom longitudinal steel reinforcement in the beams. These reinforcing bars were found to have average yield strengths of 904 MPa, 929 MPa, and 855 MPa at strains of 0.0067 mm/mm, 0.0070 mm/mm and 0.0066 mm/mm, respectively. They had ultimate strengths of 1077 MPa, 1217 MPa, and 1153 MPa at strains of 0.0560 mm/mm, 0.0485 mm/mm and 0.0528 mm/mm, respectively. As seen in Figure 3-5, the No.4 MMFX bar were more ductile when compared to the No.5 and No.6 MMFX bars.

This research program is a companion to a study conducted by Algassem (2016) which examined the blast performance of HSC and HSFRC beams built with conventional (grade 400 MPa) steel reinforcement. Figure 3-4 compares the stress-strain response of the high-strength No. 4, 5 and 6 bars with the stress-strain response of the regular grade No. 4, 15M, and 20M bars used in Algassem's study; it is noted that MMFX bars show higher strength, but more brittle behaviour when compared to the conventional steel reinforcing bars.

Table 3-4 Steel reinforcement mechanical properties

ID	Steel Reinforcement	Bar Diameter d_b(mm)	Bar Area A_b (mm^2)	Yield Strain ε_y	Yield Strength f_y (MPa)	Ultimate Strain ε_u	Ultimate Strength f_u MPa)
6.3NS	Non-deformed	6.35	32	0.0028	577	0.0701	645
No.4	MMFX2	12.7	129	0.0067	904	0.0560	1077
No.5	MMFX2	15.9	200	0.0070	929	0.0485	1217
No.6	MMFX2	19.1	284	0.0066	855	0.0528	1153

Figure 3-3 GALDABINI Universal Floor Standing Testing Machine; testing steel rebar

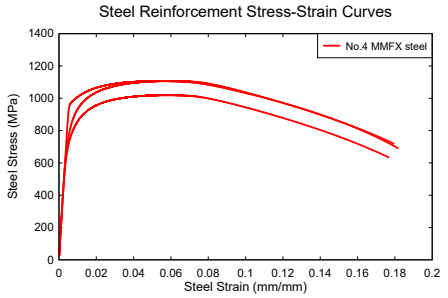

a) No. 4 MMFX bar

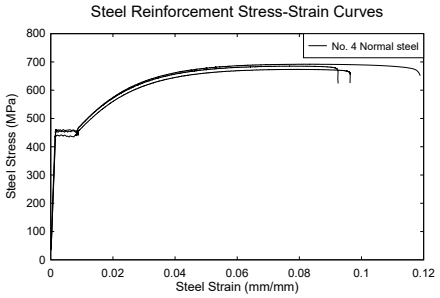

b) No. 4 Normal-Strength bar

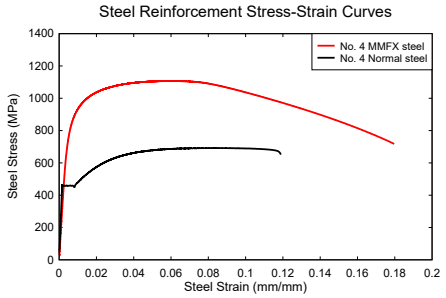

c) No.4 MMFX vs. No.4 Normal-Strength

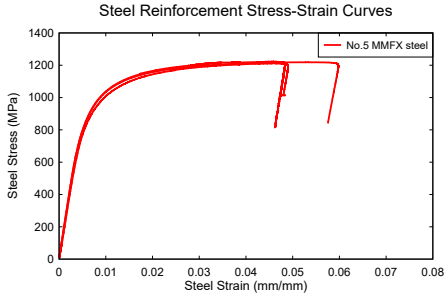

d) No. 5 MMFX bar

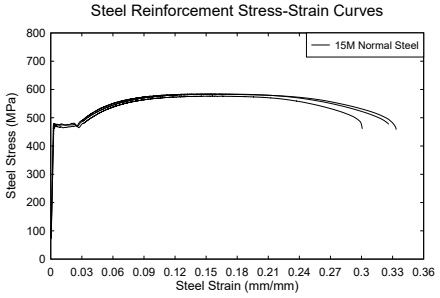

e) 15M Normal-Strength bar

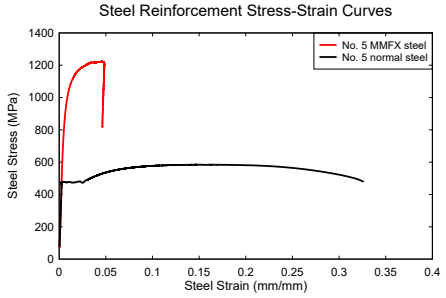

f) No.5 MMFX vs. 15M Normal-Strength

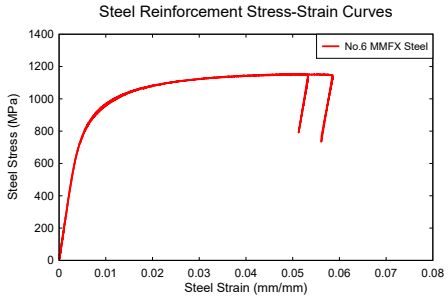

g) No.6 MMFX bar

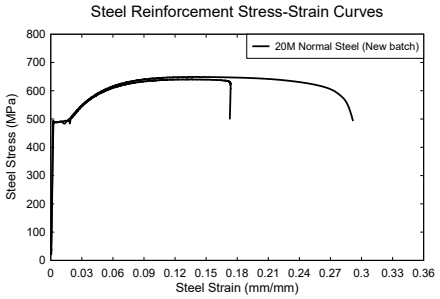

h) 20M Normal Strength bar

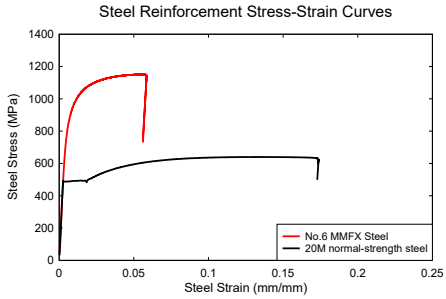

i) No.6 MMFX vs. 20M Normal-Strength

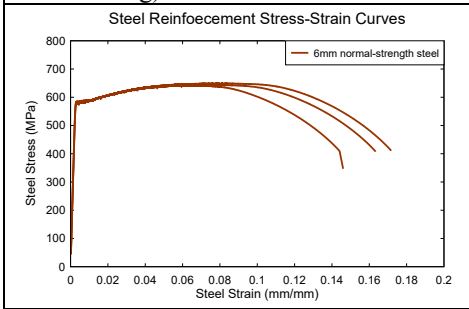

j) 6.3mm steel wire

Figure 3-4 Steel reinforcement stress-strain relationships for different bar types and sizes

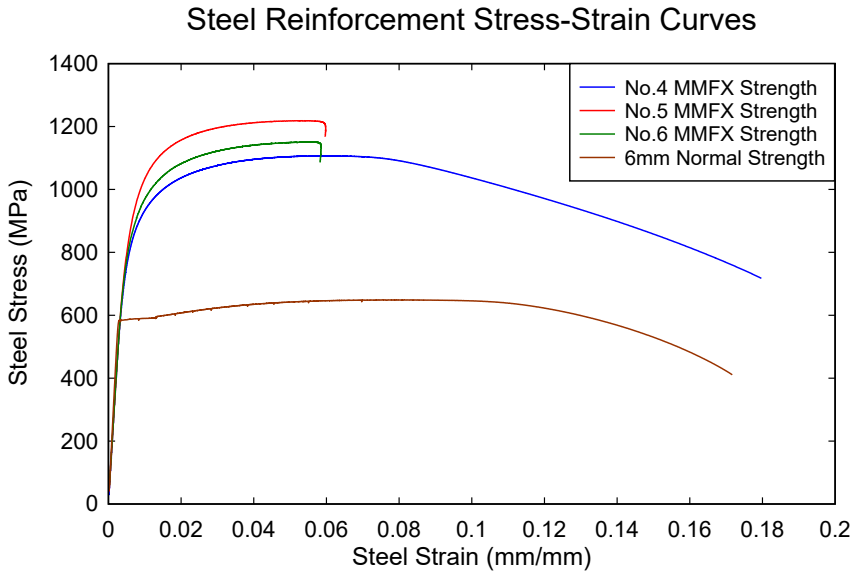

Figure 3-5 Typical steel reinforcement stress-strain relationships

3.3.3. STEEL FIBRE PARAMETERS

In this research, one type of hooked-end steel fibre was used for all HSFRC specimens. Photographs of the ZP fibres manufactured by BEKAERT under the Dramix ZP305 (3D) brand are shown in Figure 3-6. These fibres had length (L_f) of 30 mm, diameter (d_f) of 0.55 mm, aspect ratio (L_f/d_f) of 55 and tensile strength of 1350 MPa.

Table 3-5 Steel fibre properties

Fibre ID	Fibre Name	Length L_f (mm)	Diameter d_f (mm)	Aspect Ratio (mm/mm)	Tensile Strength (MPa)
ZP	ZP 305	30	0.55	55	1350

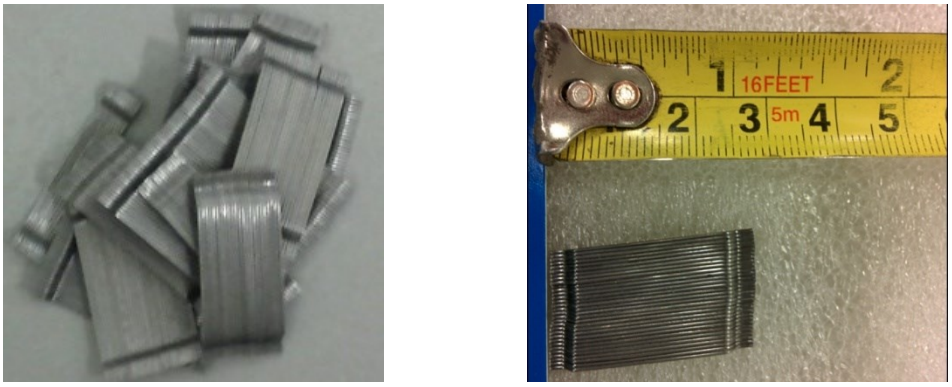

a) ZP 305 fibre

Figure 3-6 Steel fibre photographs

3.4. CONSTRUCTION OF TEST SPECIMENS

The beams used in this research were all constructed at the University of Ottawa Structures Laboratory. Construction followed these steps: preparing the formwork, bending the steel reinforcing bars and stirrups, applying the strain gauges, forming the steel cages, casting of the concrete and curing of the specimens.

3.4.1. PREPARATION

Twelve 250 x 2440 mm sheets of 19 mm thick plywood and several 38 x 64 mm wood studs were used to construct the formwork used to cast the beam specimens. The form allowed for the casting of 5 specimens at one time. Wood studs were placed at regular spacing along the form side-walls to provide lateral support to the formwork during casting. Prior to placing the steel cages, plastic chairs were used to keep a clear cover of approximately 50 mm to the tensile side of the main steel longitudinal reinforcement (clear cover of approximately 35 mm to stirrups). Using a brush, motor oil was spread into each row of the form to allow for easier removal of the specimens and to avoid damaging the formwork so that it could be reused. Figure 3-7 (a) shows a photograph of the formwork after construction. The No.4 and No.5 MMFX longitudinal bars were bent to have 90° hooks with hook extensions of 170 mm. The No.6 MMFX bars were found to be too strong to bend using the bending machine in the structures laboratory; therefore, they were kept straight but extended beyond the supports over the entire 2440mm length of the beams. Strain gauges were installed in the mid-span of the steel reinforcing bars of all dynamic and static beams to monitor the strains in the longitudinal reinforcement. Cages were made using the MMFX longitudinal bars, with the 6.3 mm reinforcement used for the top bars and stirrups. The stirrups were placed at a spacing of 100 mm in the shear span (41 mm at the beam ends). Figure 3-7 (b) includes a photograph of the cages after construction. This photograph shows, from left to right, cages reinforced with No.6 MMFX bars, No.5 MMFX bars, and No.4 MMFX bars.

a) Formwork

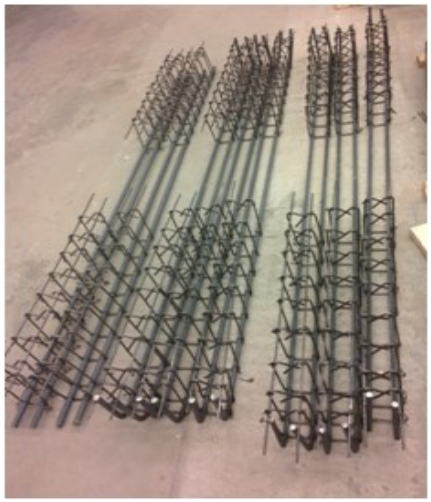

b) Cages

Figure 3-7 Preparation of formwork and cages after construction

3.4.2. MIXING AND CURING

Concrete was mixed at the University of Ottawa Structures Laboratory using a large pan mixer, as shown in Figure 3-8. The pre-packaged SCC series materials could be poured directly into the pan mixer and only required addition of water during mixing. On the other hand, the HSC and HSFRC mixtures required the weighing of specific materials before they could be poured and mixed in the pan mixer. Enough material to cast two beams was used for each batch. To ensure homogeneous mixing, materials were put into the pan mixer in this order: half of the coarse aggregate, half of the fine aggregate (sand), half of the cement, slag, silica fume and the remaining half parts of the materials. Then, the dry material was mixed for about five minutes before adding water that was pre-mixed with retarder and super plasticizer. Mixing continued for 5 minutes after addition of the water for the plain SCC and HSC mixtures. In the case of the HSFRC mixtures, the fibres were added gradually over 1 minute after the HSC mix became uniform, and mixing continued for 2 minutes after completing the fibre addition to ensure uniform fibre distribution. After the mixing process was completed, the concrete was poured into a wheelbarrow, and shovels were used to transfer the concrete to the forms. A vibrator was used to consolidate the concrete in the beam forms (for HSC and HSFRC beams only). Concrete cylinders and flexural beam prisms were also cast to determine the properties of each concrete batch. After levelling the beams, the specimens, cylinders and prisms were covered with wet burlap and plastic sheets to cure for seven days. At the end of this seven-day period, the beams were removed from the forms and air-cured in the structures laboratory until the testing day.

Figure 3-8 Concrete pan mixer used to cast all beams

3.4.3. FRESH STATE PROPERTIES

Slump flow tests for the SCC series were conducted according to the ASTM C1611 “Standard Test Method for Slump Flow of Self-Consolidating Concrete”. After mixing, the slump cone mould was filled with SCC without compaction, and the top of the concrete was levelled. Next, the mould was raised and there was a wait period until the fresh concrete stopped flowing. The maximum diameters in the two perpendicular directions (d1 and d2) were recorded, and the average of the two diameters was recorded as the slump flow.

Slump tests for the HSC and HSFRC series were completed in accordance with the ASTM C143 "Standard Test Method for Slump of Hydraulic-cement Concrete." Using a scoop, the concrete was placed in the slump cone mould in three layers, and each layer was consolidated 25 times using a metal rod having circular cross-section. After levelling the top of the concrete, the mould was lifted and the slump was measured as the vertical distance between the upper part of the mould and the top of the concrete.

Figure 3-9 shows sample photographs of the concrete after the slump tests, and Table 3-6 provides a summary of the slump test values for the batch used for each beam specimen. As shown in Figure 3-9, the SCC mix showed high flowability and this mix did not require vibration during casting of the beams. Due to the addition of super plasticizer the HSC showed high slump. As expected the addition of fibres reduced this slump value, which translated into a reduction of workability for the HSFRC when compared to the HSC during casting. Nonetheless the fibre-reinforced concrete remained uniform, and workability was acceptable during casting.

Table 3-6 Concrete fresh state properties

Specimen ID	Concrete Mix	Bar Type	Load type	Fibre Ratio	Slump (mm)
SCC-F0-#4-S	SCC	#4	D	0.00%	630/640
SCC-F0-#5-S	SCC	#5	D	0.00%	630/640
HSC-F0-#4-S	HSC	#4	D	0.00%	240
HSC-F0-#5-S	HSC	#5	D	0.00%	240
HSC-F0-#6-S	HSC	#6	D	0.00%	240
HSC-F1-#4-S	HSC	#4	D	1.00%	180
HSC-F1-#5-S	HSC	#5	D	1.00%	180
HSC-F1-#6-S	HSC	#6	D	1.00%	180
HSC-F0-#4-S	HSC	#4	S	0.00%	230
HSC-F0-#5-S	HSC	#5	S	0.00%	230
HSC-F0-#6-S	HSC	#6	S	0.00%	230

a) SCC – 0% b) HSC-0% c) HSFRC-1%

Figure 3-9 Typical photographs of concrete after slump tests

3.4.4. HARDENED STATE PROPERTIES

For each mix, several cylinders and flexural concrete prisms were prepared during casting. Three cylinders with a diameter of 100 mm and a height of 200 mm were tested at the University of Ottawa Structures Laboratory to determine the compressive strength of each batch at 28 days. The cylinders were tested under pure axial compression using a 1000 KN PILOT compression machine. Table 3-7 shows the compressive strength of the three cylinders for each beam specimen, as well as their averages. Cylinders from each batch were also tested to determine the complete compressive stress-strain response of the SCC, HSC and HSFRC, with axial strains captured using an extensometer with 140 mm gage length which was attached to the cylinder specimens. Typical stress-strain curves are shown in Figure 3-11. Typical photographs of cylinders after testing are shown in Figure 3-12. As expected the HSC showed very brittle response with explosive failure after reaching peak stress. In contrast the provision of fibres allowed the high-strength fibre-reinforced concrete to carry stresses beyond peak and prevented brittle crushing of the concrete with gradual failure.

Figure 3-10 Cylinder testing setup

Table 3-7 Concrete compressive strength summary

Specimen ID	Concrete Mix	Bar Type	Load type	Fibre Ratio	Cylinder Test Compressive Strength (MPa)			
					#1	#2	#3	Avg.
SCC-F0-#4-S	SCC	#4	D	0.00%	60.46	55.53	69.5	61.83
SCC-F0-#5-S	SCC	#5	D	0.00%	60.46	55.53	69.5	61.83
HSC-F0-#4-S	HSC	#4	D	0.00%	101.33	95.11	92.75	96.40
HSC-F0-#5-S	HSC	#5	D	0.00%	101.33	95.11	92.75	96.40
HSC-F0-#6-S	HSC	#6	D	0.00%	87.82	104.48	/	96.15
HSC-F1-#4-S	HSC	#4	D	1.00%	110.42	103.89	97.7	104.00
HSC-F1-#5-S	HSC	#5	D	1.00%	110.42	103.89	97.7	104.00
HSC-F1-#6-S	HSC	#6	D	1.00%	99.19	106.08	93.3	99.52
HSC-F0-#4-S	HSC	#4	S	0.00%	99.48	90.57	/	95.0
HSC-F0-#5-S	HSC	#5	S	0.00%	99.48	90.57	/	95.0
HSC-F0-#6-S	HSC	#6	S	0.00%	99.48	90.57	/	95.0

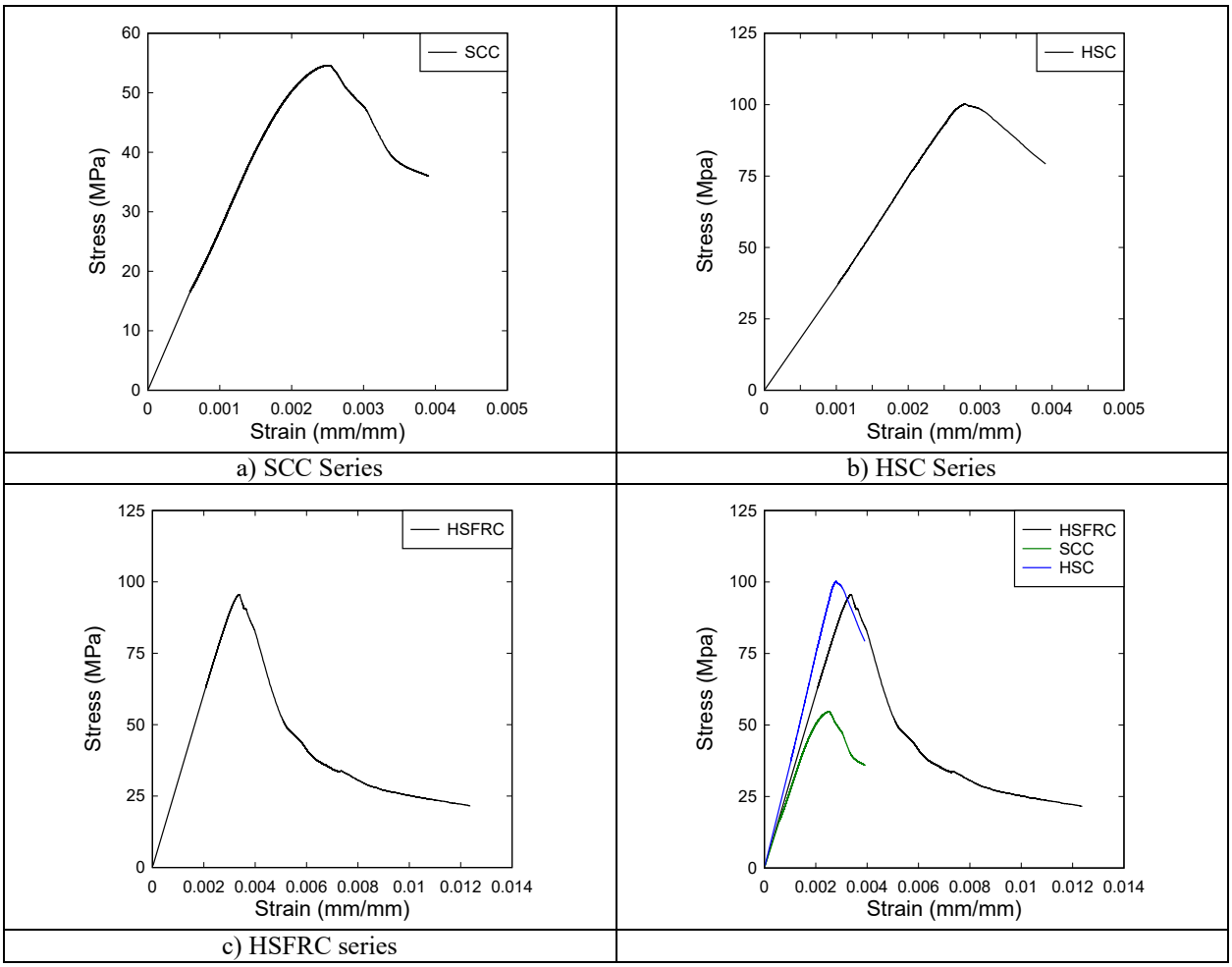

a) SCC Series | b) HSC Series

c) HSFRC series

Figure 3-11 Typical concrete stress-strain relationships for cylinder samples

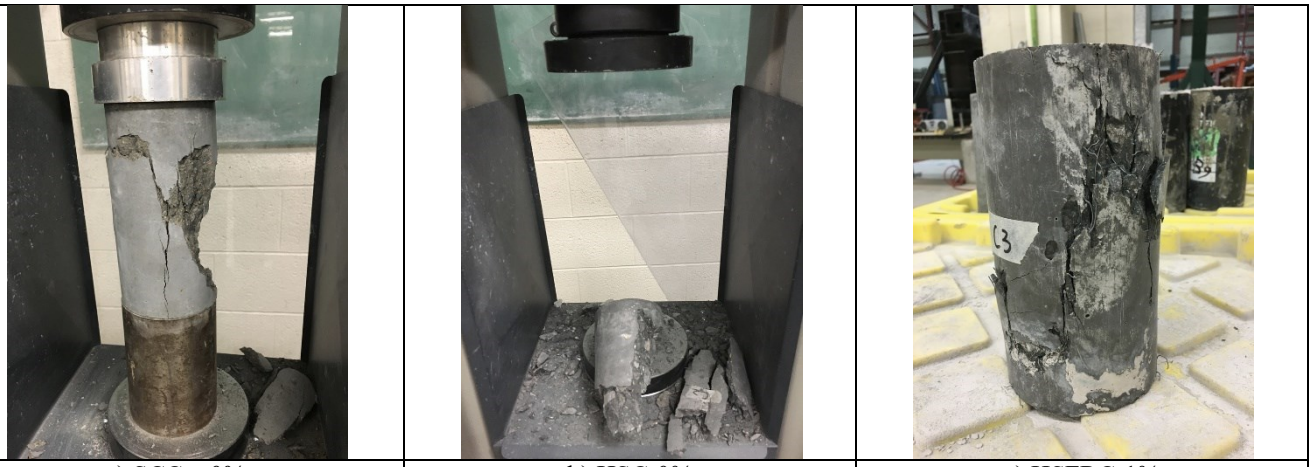

a) SCC – 0% | b) HSC-0% | c) HSFRC-1%

Figure 3-12 Sample concrete cylinder testing failures

Flexural prisms for each batch were also tested under third-point loading to evaluate the flexural strength and toughness of concrete, according to the ASTM C1609 standard test method. The dimensions of the flexural beams were 100 mm by 100 mm by 400 mm, with testing conducted over a span of 300 mm. As specified in ASTM C1609, the initial loading rate is varied from 0.025 mm/min to 0.075 mm/min, and beyond a net deflection of L/900, the rate of increase can be take between 0.05 to 0.2 mm/min. A constant loading rate under deflection control of 0.075 mm/min was used during testing. The deflections were measured at midspan using a "yoke" and LVDT as specified in the ASTM C1609 method, as seen in Figure 3-13. Results from the ASTM 1609 toughness tests are listed in Table 3-8, and typical load-deformation curves can be seen in Figure 3-14. As expected the plain SCC and HSC showed linear elastic response with brittle failure after first cracking. In contrast, the addition of fibres allowed the HSFRC to carry stresses beyond cracking, with enhanced flexural toughness when compared to the plain HSC.

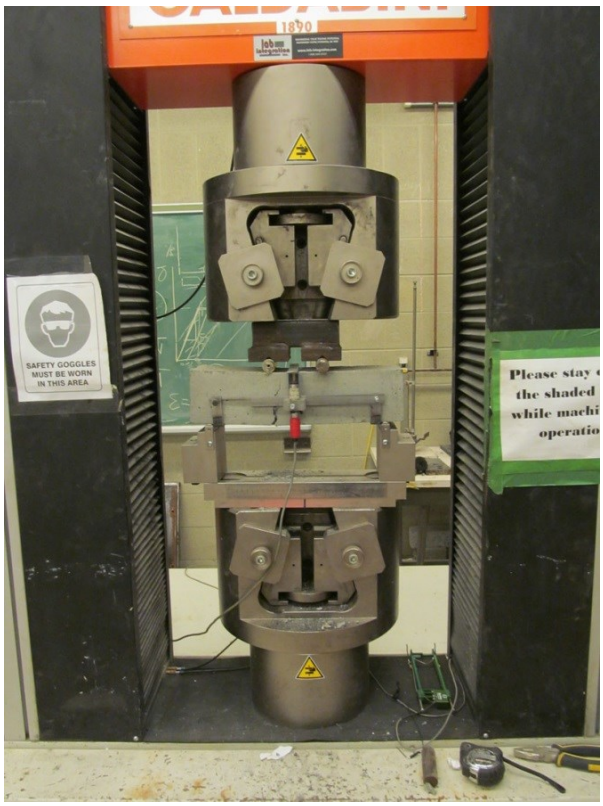

Figure 3-13 Flexural beam testing setup

Table 3-8 Results from the ASTM C1609 toughness tests

Concrete Mix	ASTM C1609										
	P_1	δ_1	P_p	δ_p	f_1	f_p	P_{600}	f_{600}	P_{150}	f_{150}	T_{150}
SCC Series	23.4	0.10	23.4	0.10	7.02	7.02	-	-	-	-	1.6
HSC Series	31.8	0.09	31.8	0.09	9.54	9.54	-	-	-	-	1.86
HSFRC Series	32.5	0.06	32.5	0.06	9.75	9.75	13.8	4.14	4.8	1.44	22.96

L = Span Length (300 mm), (L/600 = 0.5, L/150 =2)
P_1= First-Peak Load (kN)
δ_1= Net Deflection at First-Peak Load (mm)
P_p= Peak Load (kN)
δ_p= Net Deflection at Peak Load (mm)
f_1= First-Peak Strength (MPa)
f_p= Peak Strength (MPa)
P_{600}= Residual Load at net deflection of L/600 (kN)
f_{600}= Residual Strength at net deflection of L/600 (MPa)
P_{150}= Residual Load at net deflection of L/150 (kN)
F_{150}= Residual Strength at net deflection of L/150 (MPa)
T_{150}= Area under load vs. net deflection curve (0 to L/150), (kN*mm)
FT = Flexural Toughness Factor = $(T_{150}*L)/(L/150 *b*d^2)$

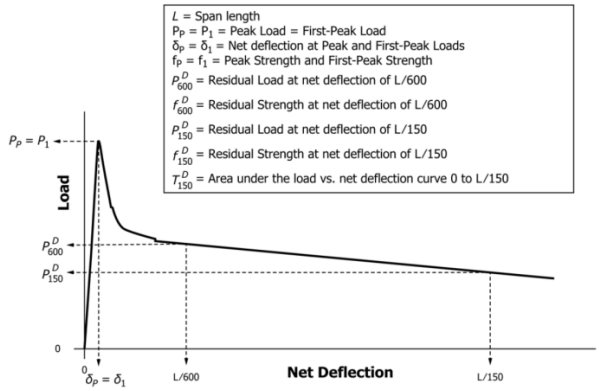

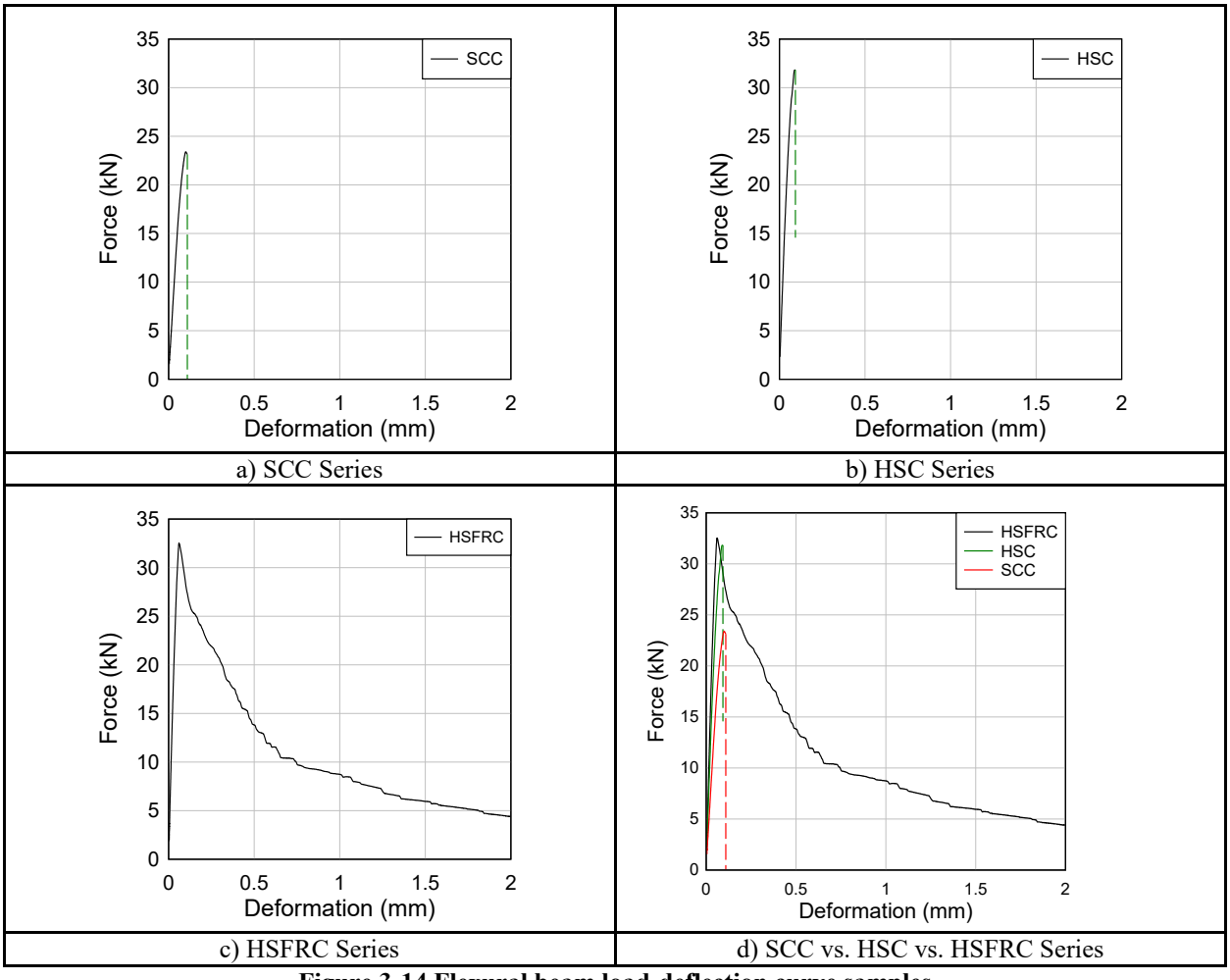

a) SCC Series

b) HSC Series

c) HSFRC Series

d) SCC vs. HSC vs. HSFRC Series

Figure 3-14 Flexural beam load-deflection curve samples

3.5. EXPERIMENTAL SETUP

This sub-section describes the various equipments used in the experiments, including the shock-tube, load transfer device, instrumentation, data acquisition equipment, and high-speed cameras which were used for the dynamic tests. In addition, the sub-section discusses the setup and instrumentation used in the static tests.

3.5.1. SHOCK-TUBE

The University of Ottawa shock-tube is capable of simulating shock waves generated by hemispherical free air surface bursts of high explosives (Lloyd et al., 2010). As shown in Figure 3-15 to Figure 3-17, the shock-tube contains four sections: the variable-length driver, the spool section, the expansion chamber, and the rigid end test frame.

The driver length varies in size from 305 mm (1 ft) to 5158 mm (17 ft) and is used to control the positive phase duration of the shock wave. In the current study the driver length was kept constant at 2745 mm (9 ft). The spool section is composed of a double diaphragm firing system. Aluminum sheets with specified gauge thickness are added for each blast, with one set placed between the driver and the spool section, and the other set installed between the spool and the expansion chamber. The thickness of the foils depended on the target driver pressure. The expansion section increases the shock-tube section from a 597 mm diameter circular section to a 2032 mm square section over a length of 6096 mm. The rigid end test frame and load-transfer device (LTD) are used to attach the beam specimens to the shock-tube.

Prior to firing, air pressure was pumped into the driver and spool sections separately. The proper thickness of aluminum sheets was selected to avoid the rupture of foils before the desired pressure was reached. After reaching this pressure, the next step was to release the pressure from the spool section. The differential pressure between the driver and the spool section results in the rupture of the foils releasing the pressure into the expansion chamber, which then transfers pressure to the LTD and beam specimens as discussed in the next section.

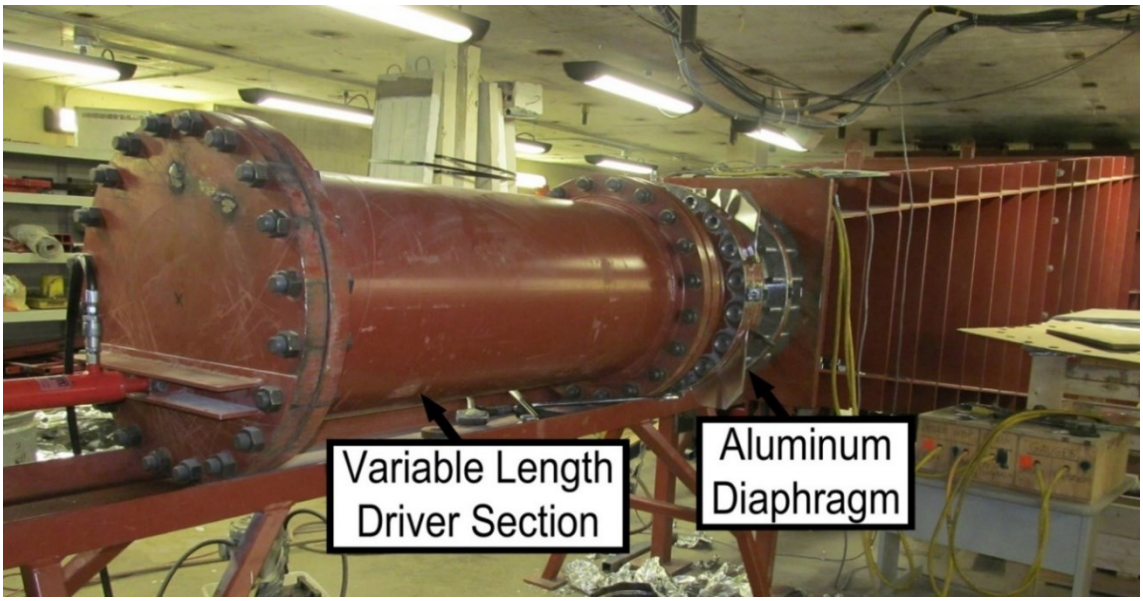

Figure 3-15 Shock-tube's driver section

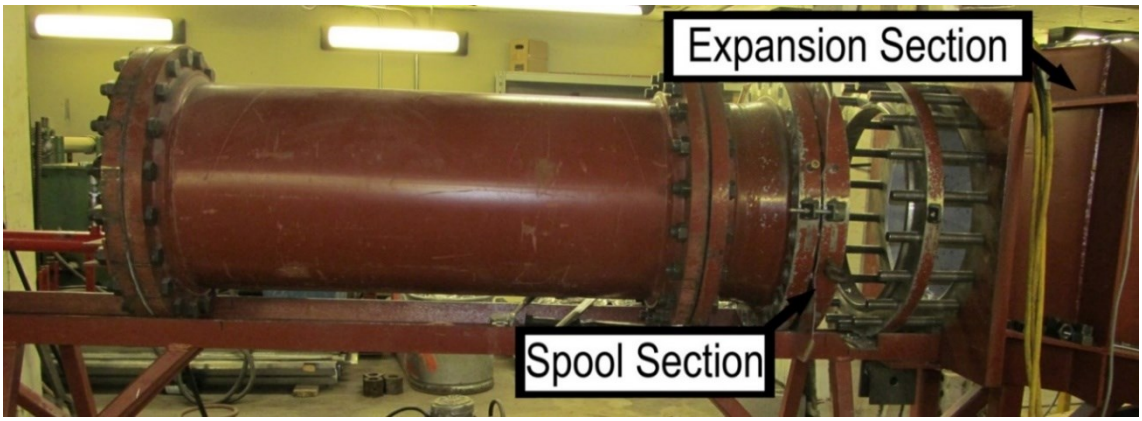

Figure 3-16 Shock-tube's spool section

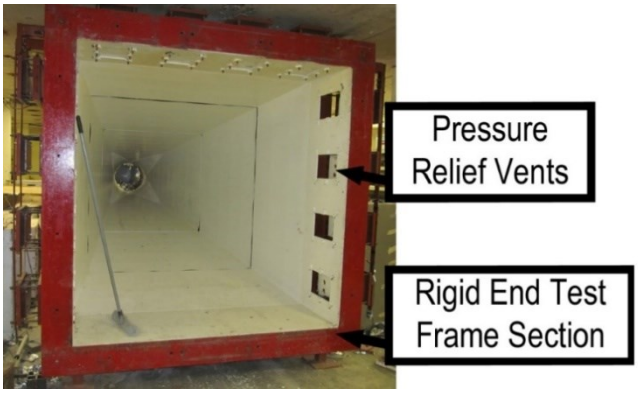

Figure 3-17 Shock-tube's rigid end test frame section

3.5.2. LATERAL LOAD TRANSFER DEVICE

The lateral load transfer device (LTD) was used to redirect the blast pressure generated by the shock-tube to two concentrated loads which were then applied on the beams. The LTD can be seen in Figure 3-18 in detail with the rigid end test frame. The test fixture closely replicates the load and support conditions used for the static tests. The lateral load transfer device is composed of two side-by-side rigid steel panels (2032 mm x 1000 mm), which are used to cover the entire 2 m x 2 m opening. Two I-steel load-transfer beams with dimensions of 160 mm x 165 mm x 1200 mm are attached to the LTD to transfer the blast loads as two concentrated point loads. Sliding hinges are provided near the top and bottom supports, allowing free lateral movement of the middle portion of the LTD without causing reactions at the hinge locations (Jacques, 2016), as can be seen in Figure 3-19.

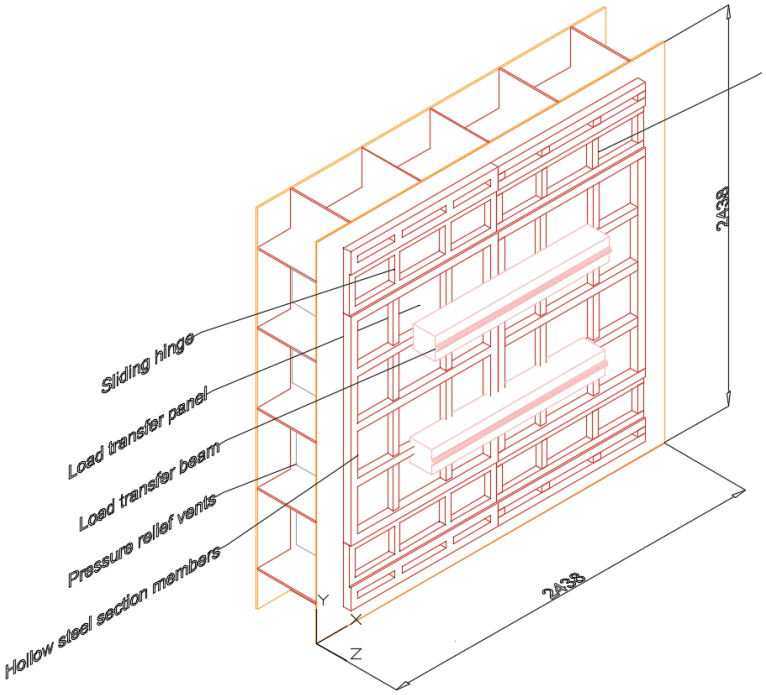

Figure 3-18 Isotropic view of lateral load transfer device

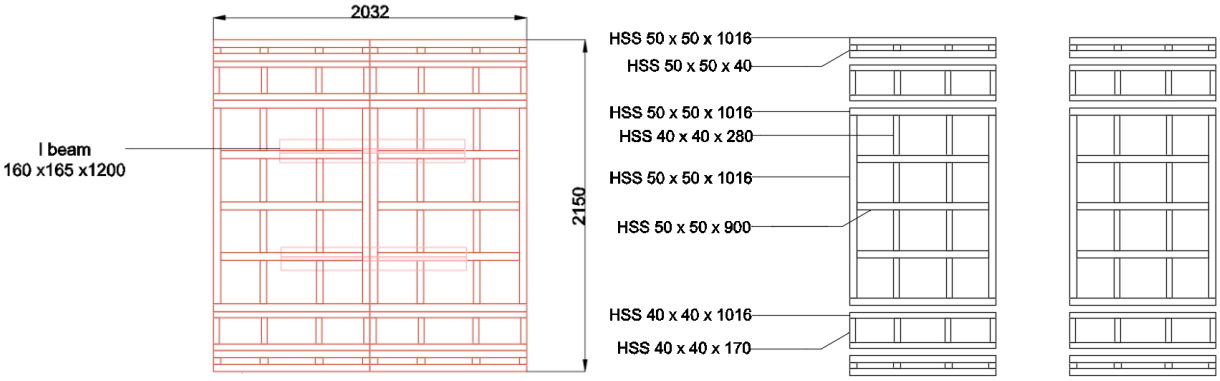

Figure 3-19 Lateral load transfer device section details

3.5.3. SUPPORTS

The boundary conditions in the setup simulate simply supported conditions with loads applied as two point loads over a constant moment region of 750 mm and two shear spans of 741 mm. The setup for both the top support and bottom support was the same, and consist of front and rear support components. The front portion of the supports consists of a 1000 mm long square 152 x 152 mm square HSS section welded with a circular load cell, and is tightened using four 19 mm diameter threaded steel rods. The rear supports consist of 500 mm long 51 mm x 51 mm square HSS and a smaller 440 mm long HSS section which simulates a roller condition. The load cells recorded the reaction load histories during each blast. Figure 3-20 shows a photograph at the test setup and the details of the support setup. Figure 3-21 shows the shape of the lateral load transfer device before and after testing.

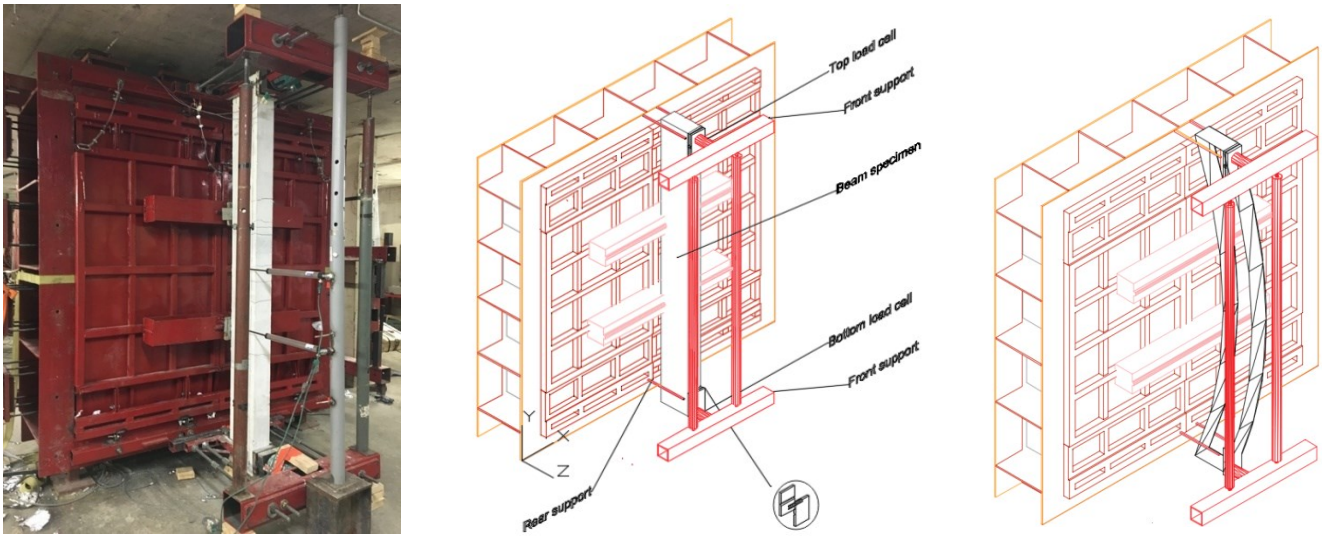

Figure 3-20 Lateral load transfer device

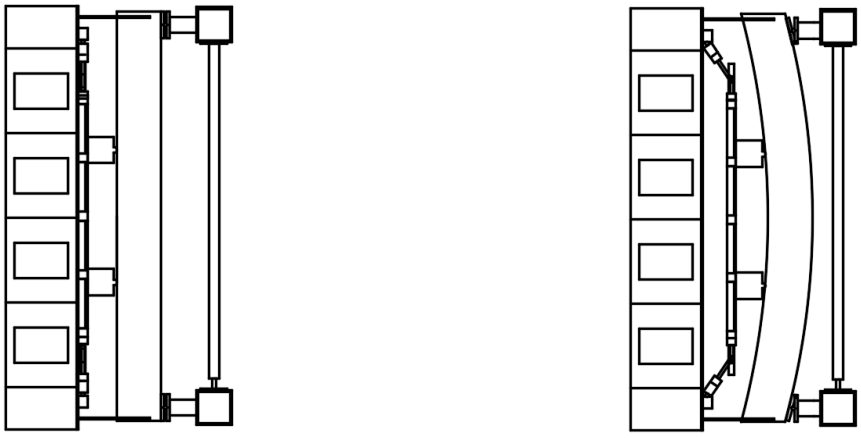

a) Before testing b) During testing

Figure 3-21 Lateral load transfer device

3.5.4. LINEAR VARIABLE DISPLACEMENT TRANSDUCERS (LVDT)

Two Celesco CLWF-300 linear variable displacement transducers (LVDT) with a stroke length of 300 mm were installed at mid-span and at 1/3 of the distance along the clear span of the beam specimens to measure the displacement time histories of the beams under dynamic loading. The LVDT at the mid-span was generally used to report the maximum and residual displacement of the beams. The displacements recorded at the 1/3 span provided a back-up in case of malfunction of the mid-span LVDT (in case of failure, the data collected by the LVDT at the 1/3 span could be used to estimate the mid-span displacements using geometric scaling relationships obtained using stills from the high-speed videos). Another LVDT was placed at the bottom of the shock-tube to measure the displacement of the shock-tube.

3.5.5. STRAIN GAUGES

One strain gauge was installed at the mid-span of one reinforcing tensile bar in each specimen. The FLA-6-350-11 strain gauges had a length of 6 mm and a resistance of 350 ohms. Figure 3-22 shows the location of the strain gauge in each beam specimen.

Side view:

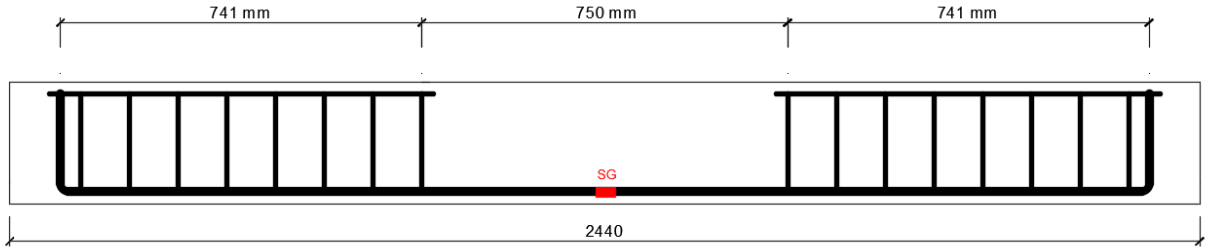

Top view:

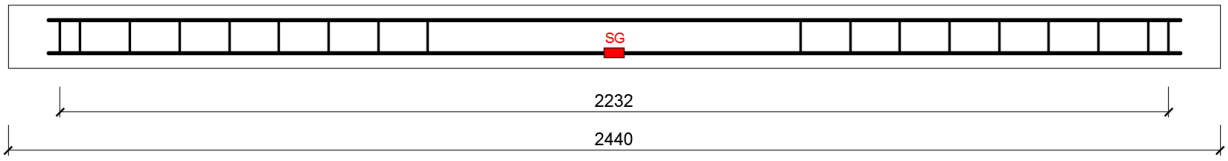

Figure 3-22 Strain gauge location

3.5.6. DATA ACQUISITION SYSTEM

A Yokogawa SL 1000 High-speed Data Acquisition system was used to record the data at 100,000 Hz (100,000 data items per second) during the dynamic testing. The data acquisition machine, together with the LVTDs and pressure sensors allow for continuous recording of the pressure, strains, and displacement time histories.

Two pressure measurement devices were installed at the side and bottom of the shock-tube end frame and connected to the data acquisition system. This instrumentation was used to record pressure-time histories for each simulated blast wave and to send a trigger signal to record the data.

An AOS Technology X-PRI high-speed camera was used to record videos of the behaviour of the beams during the testing. The camera is capable of recording 500 frames per second with an 800 x 600 resolution. During the testing the camera was placed on the side of the beam specimens.

3.5.7. SETUP FOR STATIC TEST

The four-point bending load setup shown in Figure 3-23 was used to test all the three companion static beams in this study, which include the HSC-F0-#4-S, HSC-F0-#5-S and HSC-F0-#6-S specimens. The setup is similar to the load setup used in the dynamic tests. As shown in Figure 3-24, all the beams were simply supported over a length of 2232 mm. The distance between the two concentrated loads was 750 mm, resulting in a central constant moment region of 750 mm and shear spans of 741 mm. The load was applied using a hydraulic jack connected to a circular load cell. A linear variable displacement transducer (LVDT) and a displacement cable transducer (DCT) were placed at the center of the beam to measure the mid-span deflection. One strain gauge was installed at the mid-span of one reinforcing bar in each beam specimen. The load cell, strain gauge, LVDT and the DCT were connected to a data acquisition system to record the load, the mid-span deflection, and the strains in the reinforcement.

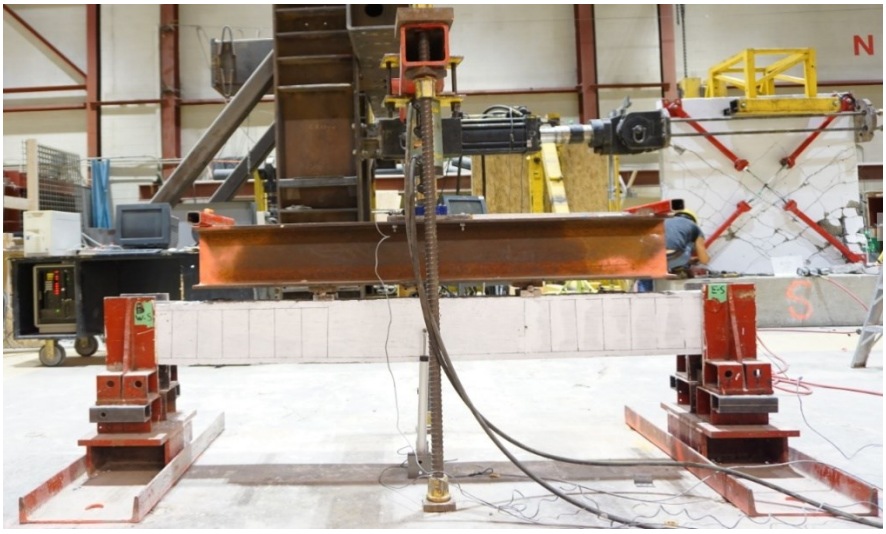

Figure 3-23 Beam specimen prior to static testing

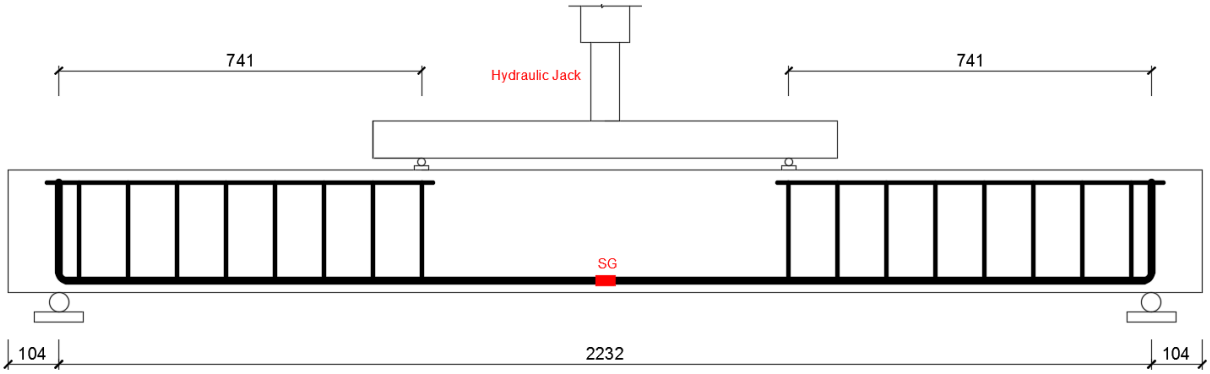

Figure 3-24 Loading device and support details

3.6. EXPERIMENTAL PROCEDURE

For the dynamic tests, each beam was subjected to a series of simulated blast loads until failure. Failure of the beam included flexural failure, shear failure, severe concrete spalling, severe concrete crushing, and tension bar rupture. The driver pressure and driver length as well as the average shock wave properties for each blast test (reflected pressure, reflected impulse and positive phase duration) can be seen in Table 3-9. Typical pressure-time histories for each blast are shown in Figure 3-25. For all tests, the driver length was kept constant at 2745mm (9 ft) with driver pressure increased in increments of 10 to 20 psi. For specimens reinforced with No.4 bars, the magnitude of blasts was increased using the following sequence: Blast 1 (17 psi), Blast 2 (30 psi), Blast 3a (40 psi), Blast 3b (50 psi) and Blast 4 (70 psi). This progression was similar for the specimens reinforced with No.5 and No.6 bars, except that Blast 3a was skipped with pressures applied in accordance with Blast 1 (17 psi), Blast 2 (30 psi), Blast 3b (50 psi) and subsequent blasts up to Blast 6 (100 psi). It is noted that Blast 1 and 2 were meant to keep the specimens within the elastic range (with Blast 2 intended to bring the #4 control specimens to yielding).

For the static tests, all the specimens followed the same loading procedure. Initially, the beams were tested under load–control with load increased by increments of 6 kN up to 30 kN in order to observe the first hairline crack. Then the load interval was increased to 12 kN and testing continued until yielding was detected. After yielding, loading was switched to displacement–control. For each load stage, mid-span deflection was increased in 5 mm increments and testing continued in this manner until beam failure (which was concrete crushing for all beams).

In terms of measuring cracking, a crack-width comparator gauge card was used in the initial stages of loading (crack width $\leq$ 1 mm), while larger cracks were measured using a digital calliper.

Table 3-9 Blast test properties

Test #	Driver Pressure kPa (psi)	Driver Length mm (ft)	Avg. Reflected Pressure (P_r) kPa	Avg. Reflected Impulse (I_r) kPa-ms	Avg. Positive Phase Duration (t_p) ms
Blast 1	117.3(17psi)	2745(9)	24.47	240.04	21.48
Blast 2	207(30psi)	2745(9)	40.98	379.68	21.27
Blast 3a	276(40psi)	2745(9)	49.57	461.84	21.48
Blast 3b	345(50psi)	2745(9)	57.71	547.75	21.76
Blast 4	483(70psi)	2745(9)	75.93	744.44	22.78
Blast 5	621(90psi)	2745(9)	88.24	891.42	25.03
Blast 6	690(100psi)	2745(9)	84.46	921.06	24.41

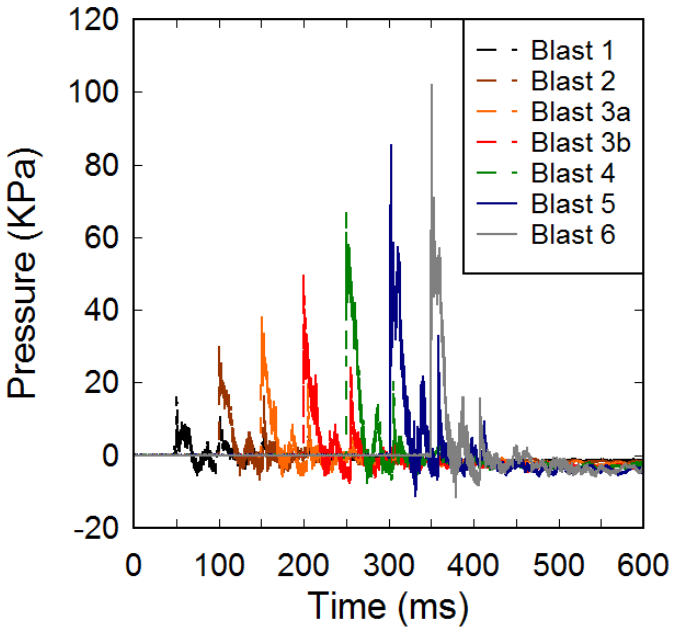

Figure 3-25 Typical pressure-time histories for Blasts 1-6

CHAPTER 4. RESULTS AND DISCUSSION - STATIC BEAM TESTS

4.1. EXPERIMENTAL RESULTS OF STATIC BEAMS

In this section, the results of the three high-strength concrete beams which were tested under static loads are discussed. The load versus displacement response, longitudinal reinforcement strains, crack widths, major events during the tests and failure modes are included for each specimen. All the specimens were subjected to the same loading protocol. The beams were first tested under load control, with an increase of 6 kN between stages up to the formation of the first hairline crack, followed by increments of 12 kN between load stages until yielding was detected After yielding, the loading protocol was switched to displacement control with intervals of 5 mm between stages. Testing continued in this manner until the beam showed signs of failure.

4.1.1. BEAM WITH HIGH-STRENGTH CONCRETE AND NO.4 BARS (HSC-F0-#4-S)

This beam was constructed with high-strength concrete and reinforced with No. 4 MMFX bars as well as transverse shear reinforcement. Figure 4-1(a) shows a plot of the applied load versus the mid-span deflection. Figure 4-1(b) shows a plot of the measured reinforcement strains. Figure 4-1(c) and Figure 4-1(d) show the growth of flexural and shear crack widths. Figure 4-2 shows major events during the tests.

The first hairline cracks were observed at the center of the beam in the flexural zone at an applied load value of approximately 11.9 kN. With an increase in the applied load, more flexural hairline cracks occurred along the beam length. Two major cracks were found to have formed at the mid-span when the load reached 65.5 kN. During the next load stage, diagonal flexural–shear cracks began to form on the west side shear-span of the beam at a load of 77.4 kN. Thereafter, further flexural and shear cracks were observed over the beam span until the beam showed signs of yielding at a load of 112.8 kN. When examining the beam response, the near-linear load-displacement curve eventually showed rounding indicating yielding of the high-strength steel bars was occurring (also confirmed from the measured steel strain data). The flexural cracks eventually inclined towards the top compressive zone of the beam and shear cracks propagated towards the top loading plate. After this loading stage, loading continued under deflection–control, the beam suddenly failed due to concrete crushing of the concrete at the top flexural zone at a load of 126.7 kN and a mid-span deflection of 35.2 mm. The beam response showed no clear yield plateau although a rounding of the load-deflection curve is observed prior to beam failure.

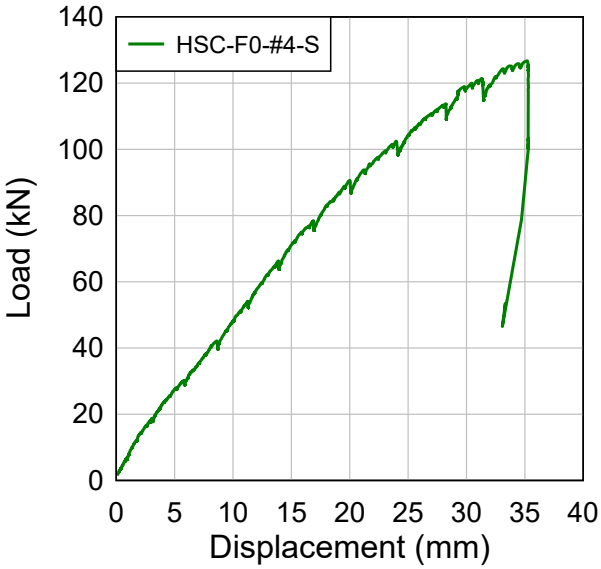

a) Load – mid-span deflection

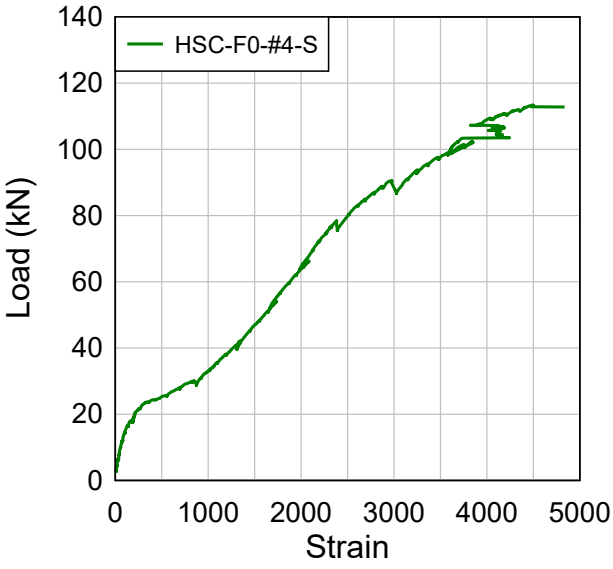

b) Tensile strains in longitudinal steel bars

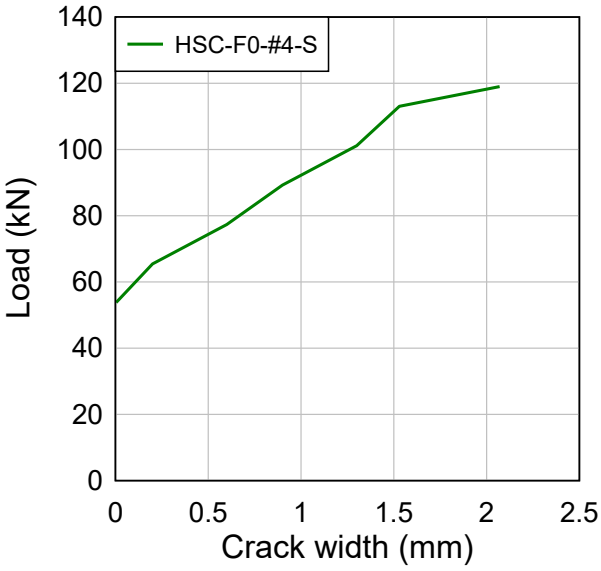

c) Maximum crack width (flexure)

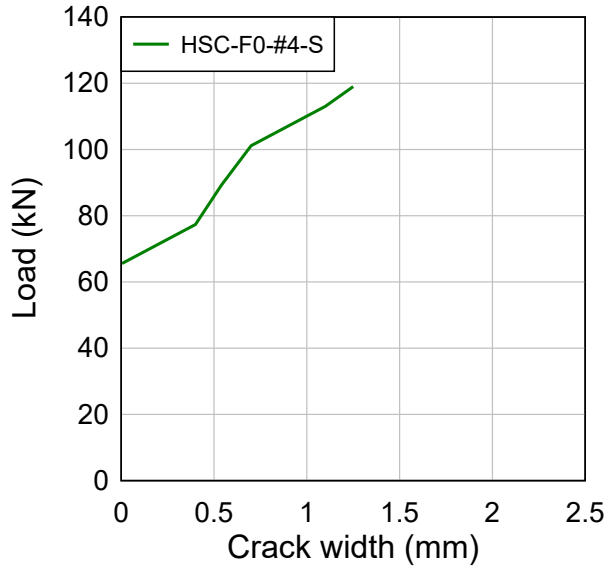

d) Maximum crack width (shear)

Figure 4-1 Experiment results for beam HSC-F0-#4-S

<table>
<tr><td>Load stage</td><td>2P (kN)</td><td>Mid-span deflection (mm)</td><td rowspan="3">- First hairline crack appeared in the flexure zone</td></tr>
<tr><td>L1</td><td>6.0</td><td>0.89</td></tr>
<tr><td colspan="3">  </td></tr>
<tr><td>Load stage</td><td>2P (kN)</td><td>Mid-span deflection (mm)</td><td rowspan="3">- Major crack appeared in the flexure zone</td></tr>
<tr><td>L8</td><td>65.5</td><td>13.78</td></tr>
<tr><td colspan="3">  </td></tr>
<tr><td>Load stage</td><td>2P (kN)</td><td>Mid-span deflection (mm)</td><td rowspan="3">- Flexure-shear crack began to form on the west side shear span
- Crack width in the flexure zone reached 0.6mm</td></tr>
<tr><td>L9</td><td>77.4</td><td>16.77</td></tr>
<tr><td colspan="3">  </td></tr>
<tr><td>Load stage</td><td>2P (kN)</td><td>Mid-span deflection (mm)</td><td rowspan="3">- Steel reinforcement yielding</td></tr>
<tr><td>L13</td><td>119.0</td><td>31.8</td></tr>
<tr><td colspan="3"> 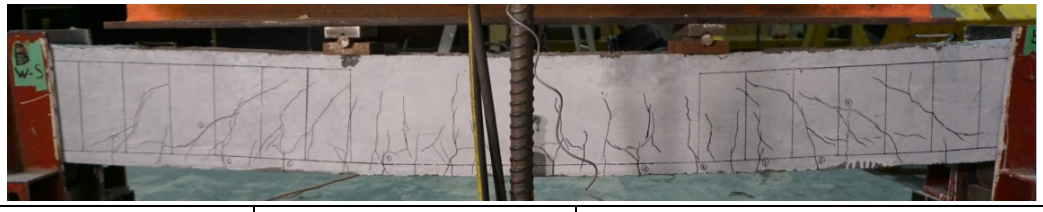 </td></tr>
<tr><td>Load stage</td><td>2P (kN)</td><td>Mid-span deflection (mm)</td><td rowspan="3">- Failure of the specimen with sudden crushing of concrete in the compression zone</td></tr>
<tr><td>L14</td><td>126.7</td><td>35.2</td></tr>
<tr><td colspan="3">  </td></tr>
</table>

Figure 4-2 Major events for specimen HSC-F0-#4-S

4.1.2.BEAM WITH HIGH-STRENGTH CONCRETE AND NO.5 BARS (HSC-F0-#5-S)

The HSC-F0-#5-S beam was constructed with high-strength concrete and reinforced with 2 - No. 5 MMFX bars and stirrups. Figure 4-3(a) shows a plot of the applied load versus the mid-span deflection. Figure 4-3(b) shows a plot of the measured reinforcement strains. Figure 4-3(c) and Figure 4-3(d) show the growth of flexural and shear crack widths during testing. Figure 4-4 shows major events during the tests.

The first hairline crack was observed in this beam in the mid-span region at a load of 11.9 kN. Thereafter, multiple hairline cracks were found over the span as the load increased. Several flexural cracks started to emerge in the flexural zone when the load reached 65.5 kN with the initiation of diagonal cracks near the load points. Flexural–shear cracks became more prominent in the west shear span at a load of 77.4 kN. The cracks in both the flexural region and the shear span continued to propagate over the span until the beam suddenly failed due to concrete crushing at the top of the flexural zone at a load of 194.7 kN. During the stages of load increase, it was noted that the longitudinal reinforced bars yielded at a load of 148.3 kN. It was also observed that, after the rebar yielded, the strain gauges failed. The maximum displacement was 33.96 mm at failure. Severe crushing was observing in the flexural zone with the formation of diagonal cracks which propagated towards the compressive zone and the top loading plates. Longitudinal cracking at the mid-span was also observed at the level of the tension steel. It is noted that the load-deflection response for this beam shows near-linear behaviour up to failure, with only limited rounding of the load-deflection response just prior to failure.

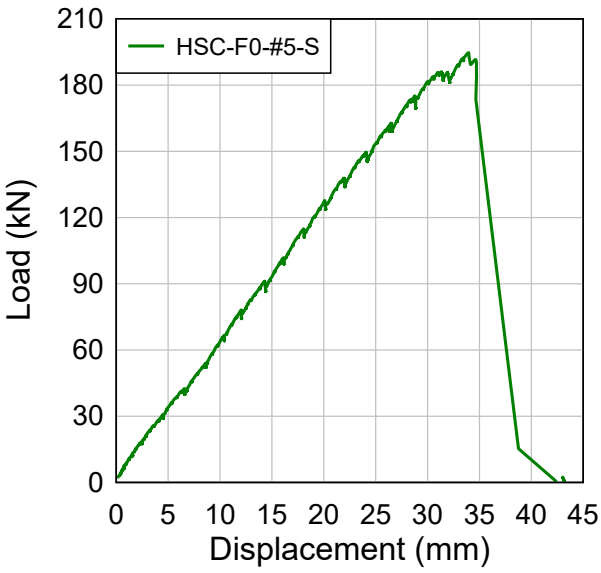

a) Load – mid-span deflection

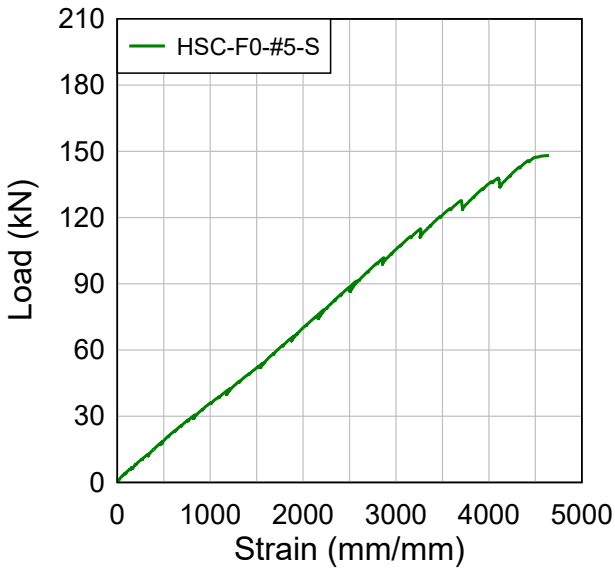

b) Tensile strains in longitude steel bars

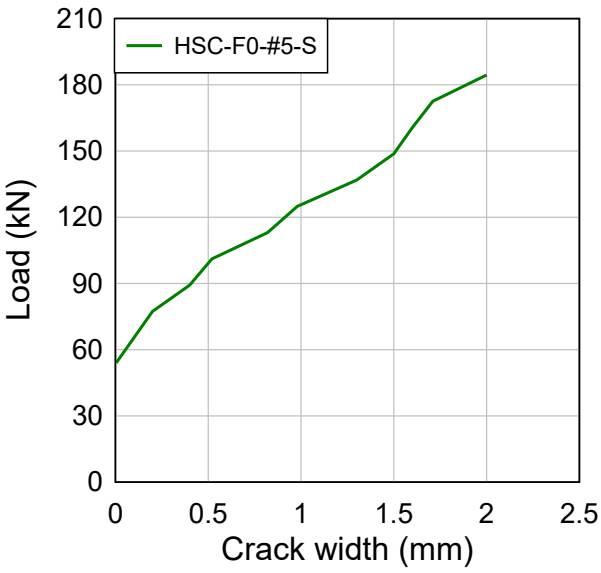

c) Maximum crack width (flexure)

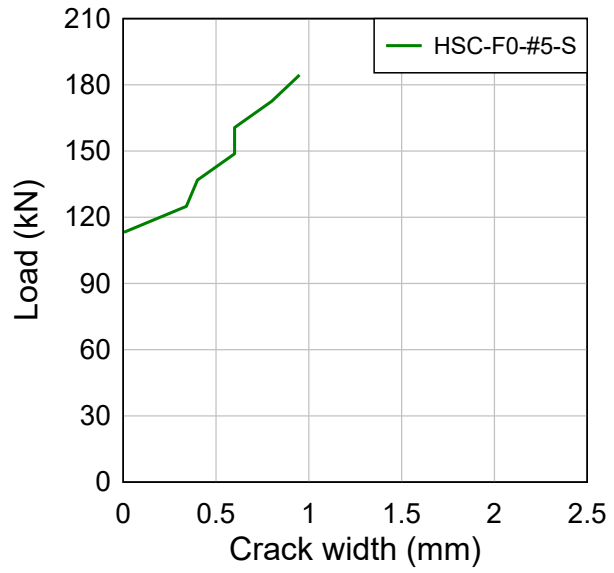

d) Maximum crack width (shear)

Figure 4-3 Experimental results for beam HSC-F0-#5-S

<table>
<tr><td>
<table>
<tr><td>Load stage</td><td>2P (kN)</td><td>Mid-span deflection (mm)</td></tr>
<tr><td>L2</td><td>11.9</td><td>1.58</td></tr>
</table>

</td><td>- First hairline crack appeared in the flexure zone</td></tr>
<tr><td>
<table>
<tr><td>Load stage</td><td>2P (kN)</td><td>Mid-span deflection (mm)</td></tr>
<tr><td>L8</td><td>65.5</td><td>10.38</td></tr>
</table>

</td><td>- Major crack appeared in the flexure zone</td></tr>
<tr><td>
<table>
<tr><td>Load stage</td><td>2P (kN)</td><td>Mid-span deflection (mm)</td></tr>
<tr><td>L9</td><td>77.4</td><td>12.05</td></tr>
</table>

</td><td>- Flexure-shear crack started to form on the west side shear span
- The major crack in the flexure zone reached 0.2mm</td></tr>
<tr><td>
<table>
<tr><td>Load stage</td><td>2P (kN)</td><td>Mid-span deflection (mm)</td></tr>
<tr><td>L19</td><td>194.7</td><td>33.96</td></tr>
</table>
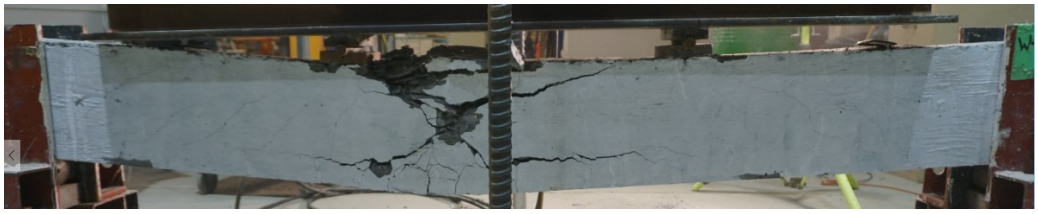
</td><td>- Failure of the specimen: severe concrete crushing, formation of diagonal cracks and longitudinal crack at level of steel</td></tr>
</table>

Figure 4-4 Major events for specimen HSC-F0-#5-S

4.1.3. BEAM WITH HIGH-STRENGTH CONCRETE AND NO.6 BARS (HSC-F0-#6-S)

This beam was the last specimen tested in the HSC series. The specimen was constructed with high-strength concrete and No. 6 MMFX bars for reinforcement. Stirrups were also provided in this specimen to avoid shear failure. Figure 4-5(a) shows a plot of the applied load versus the mid-span deflection. Figure 4-5(b) shows a plot of the measured reinforcement strains. Figure 4-5(c) and Figure 4-5(d) show the growth of flexural and shear crack widths. Figure 4-6 shows major events during the tests.

The first hairline cracks in the beam were observed when the load reached 11.9 kN in the flexural span. The first major cracks occurred in the constant moment region at a load of 77.4 kN. During the load stage, more hairline cracks were also observed. Thereafter, diagonal shear cracks formed on the west shear span of the beam when the applied load reached 89.3 kN. As loading continued to be applied, flexural and inclined shear cracks kept expanding. At a load of 172.6 kN, the concrete in the compression zone started to show signs of crushing. At this stage, the flexural crack width was 1.01 mm compared to 1.02 mm for the shear crack width. After reaching a maximum capacity of 199.0 kN and a mid-span deflection of 26.17 mm, the concrete in the compression zone suddenly crushed. The beam shows a similar crack pattern at failure when compared to the beams with No. 5 bars, with formation of diagonal cracks which propagated to the compression zone of the beam toward the top loading plates.

As seen in Figure 4-5, both flexural and diagonal crack widths gradually increased with applied loading, however the crack widths did not exceed 1.5 mm before failure. This beam showed a linear load-deflection response with no signs of yielding prior to the sudden failure. The strain data would seem to show a "yield" plateau at an applied load of 135.7 kN, however this reading is inconsistent with the beam response and is due to malfunction of the strain gauge. Indeed, it is noted that the beam reached a maximum capacity which was only slightly higher when compared to the companion HSC beam with No. 5 bars, an indicator that the use of larger reinforcement in this beam resulted in over-reinforced conditions which lead to a concrete-controlled failure prior to yielding of the tension reinforcement.

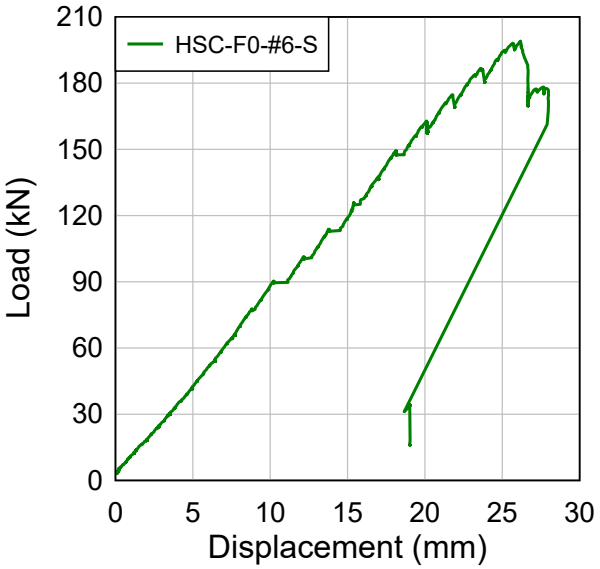

a) Shear load – mid-span deflection

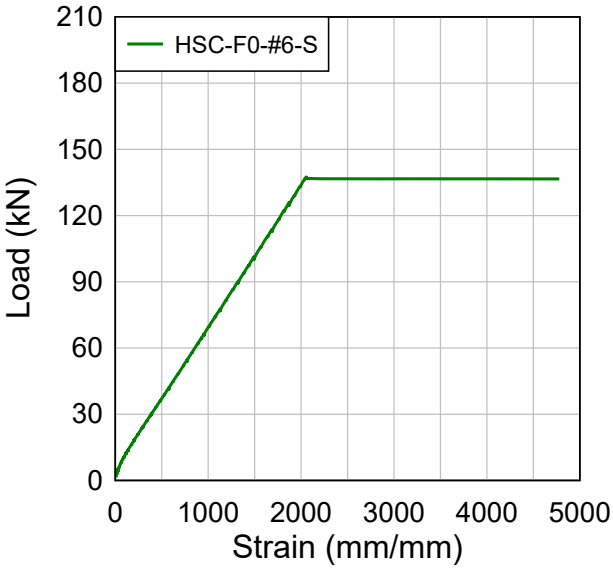

b) Tensile strains in longitudinal steel bars

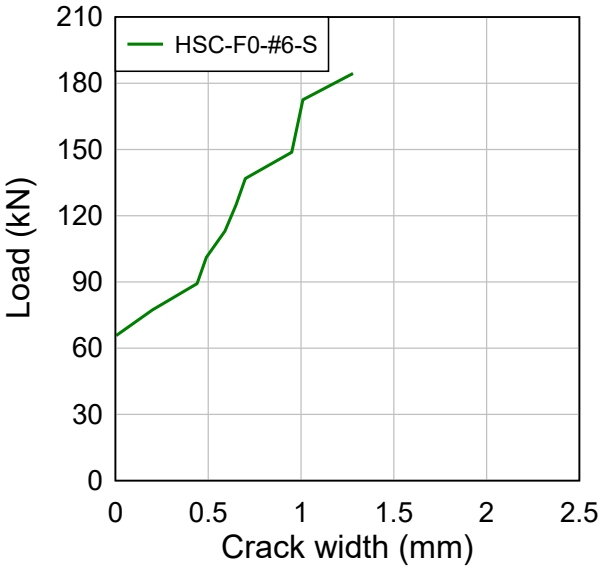

c) Maximum crack width (flexure)

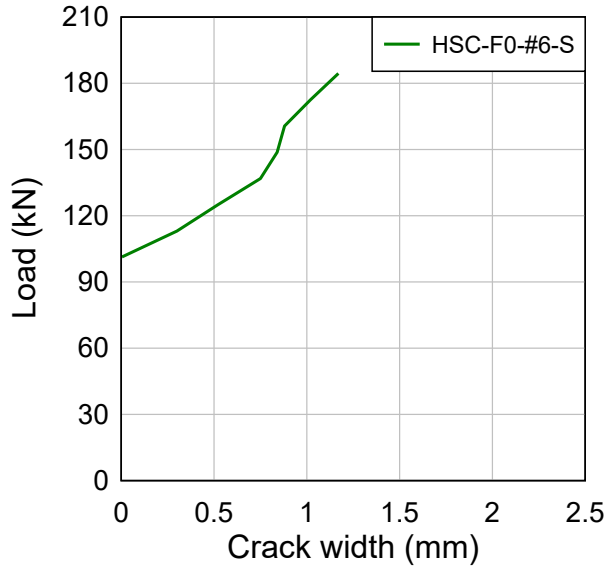

d) Maximum crack width (shear)

Figure 4-5 Experiment results for beam HSC-F0-#6-S

<table>
<tr><td>Load stage</td><td>2P (kN)</td><td>Mid-span deflection (mm)</td><td rowspan="3">- First hairline crack appeared in the flexure zone</td></tr>
<tr><td>L2</td><td>11.9</td><td>0.87</td></tr>
<tr><td colspan="3">  </td></tr>
<tr><td>Load stage</td><td>2P (kN)</td><td>Mid-span deflection (mm)</td><td rowspan="3">- Major crack appeared in the flexure zone</td></tr>
<tr><td>L9</td><td>77.4</td><td>9.04</td></tr>
<tr><td colspan="3"> 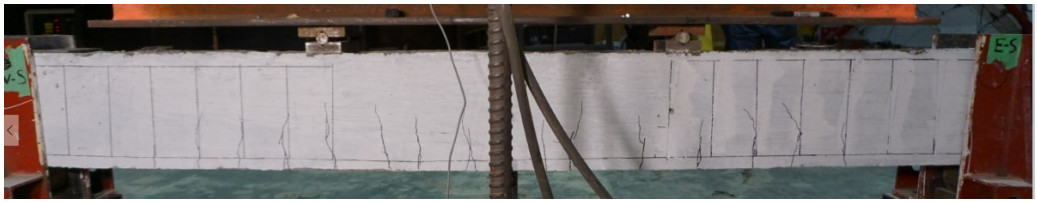 </td></tr>
<tr><td>Load stage</td><td>2P (kN)</td><td>Mid-span deflection (mm)</td><td rowspan="3">- Flexure-shear crack began to form on the west side shear span
- Major crack in the flexure zone reached 0.44mm</td></tr>
<tr><td>L10</td><td>89.3</td><td>10.54</td></tr>
<tr><td colspan="3">  </td></tr>
<tr><td>Load stage</td><td>2P (kN)</td><td>Mid-span deflection (mm)</td><td rowspan="3">- Top concrete started to crush
- Major crack in the flexure zone reached 1.01mm and shear cracks reached 1.02mm</td></tr>
<tr><td>L17</td><td>172.6</td><td>18.59</td></tr>
<tr><td colspan="3">  </td></tr>
<tr><td>Load stage</td><td>2P (kN)</td><td>Mid-span deflection (mm)</td><td rowspan="3">- Failure of the specimen: concrete crushing and formation of diagonal cracks in the central beam region</td></tr>
<tr><td>L20</td><td>199.0</td><td>26.17</td></tr>
<tr><td colspan="3">  </td></tr>
</table>

Figure 4-6 Major events for specimen HSC-F0-#6-S

4.2. DISCUSSION OF STATIC BEAM RESULTS

4.2.1. EFFECTS OF THE REINFORCEMENT RATIO IN THE HSC SERIES

The HSC series included three beams that were constructed with high-strength concrete, MMFX bars, and stirrups. These three beams were reinforced with No. 4, No. 5, and No. 6 high-strength bars, resulting in reinforcement ratios of ρ =1%, 1.5% and 2.2%, respectively. Maximum applied load, deflection at peak load and deflection at failure are summarized in Table 4-1. Figure 4-7 shows plots of load versus displacement, flexural cracks versus displacement, and shear cracks versus displacement for the three beams.

As shown in Figure 4-7(a), beam stiffness increased as the reinforcement ratio became higher with values of 4500 N/mm, 5733 N/mm and 7604 N/mm for the HSC-F0-#4-S, HSC-F0-#5-S and HSC-F0-#6-S specimens. An improvement in load resistance is also evident when comparing the No. 4 and No. 5 beams (ρ = 1% vs. 1.5%), with a 54% increase in capacity recorded for the HSC-F0-#5-S specimen. However, increasing the reinforcement ratio from 1.5% to 2.2% in the HSC-F0-#6-S beam (No. 6 bars) did not lead to a further increase in capacity, an indicator that this beam was over-reinforced. Indeed, the balanced reinforcement ratio was calculated to be 1.7%, which confirms that the No. 6 beam ($\rho = 2.2\%$) was over-reinforced. As a result, failure of the concrete occurred prior to yielding of the high-strength bars, which led to minimal increase in load carrying capacity since the strength of the bars was not fully utilized.

All three specimens showed nearly linear ascending load-deflection response, with no distinct yield points. In fact, only the HSC-F0-#4-S specimen showed signs of yielding with rounding of the load-deflection curve before failure. The other two specimens failed suddenly prior to the development of large plastic deformations. The failure displacements were also found to decrease with the use of larger diameter bars, an indicator of reduced ductility as the reinforcement ratio is increased from 1.0% to 2.2% (Δ_f = 35, 34 and 26 mm for the HSC-F0-#4-S, HSC-F0-#5-S and HSC-F0-#6-S specimens).

Figure 4-7 (b) shows that the use of larger diameter bars enhanced the crack control of the beams at equivalent load stages, with flexural crack widths reduced for the No. 5 and No. 6 specimens when compared to the beam with No. 4 bars. The trend is not as clear when examining the effect of reinforcement ratio on shear crack widths, although the crack widths of the HSC-F0-#5-S specimen are less than those of the HSC-F0-#4-S specimen at equivalent load stages.

All three specimens failed in flexure due to concrete crushing in the compression zone; however, the failure became more severe as the reinforcement ratio was increased. The specimen with No. 6 bars experienced a concrete-controlled failure, with sudden and severe crushing of compression concrete at failure.

In summary it can be concluded that increasing the reinforcement ratio of high-strength steel from No.4 to No.5 bars increased the load capacity and stiffness of the HSC beams. The use of larger size bars also reduced flexural crack widths at equivalent load stages. Increasing the amount of

reinforcement beyond the balanced conditions to 2 - No. 6 bars led to an over-reinforced (concrete-controlled) beam response, with failure prior to yielding of the high-strength bars. Increasing the reinforcement ratio also led to more brittle failures in the HSC beams.

Table 4-1 Summary of results for beams in the HSC series

Beam specimen	ρ (long.)	Max Load P_{max} (kN)	Deflection at peak Δ_{max} (mm)	Deflection at failure Δ_f (mm)	Stiffness (N/mm)
HSC-F0-#4-S	1.0%	126.7	35.21	35.21	4500
HSC-F0-#5-S	1.5%	194.7	33.96	33.96	5733
HSC-F0-#6-S	2.2%	199.0	26.17	27.23	7604

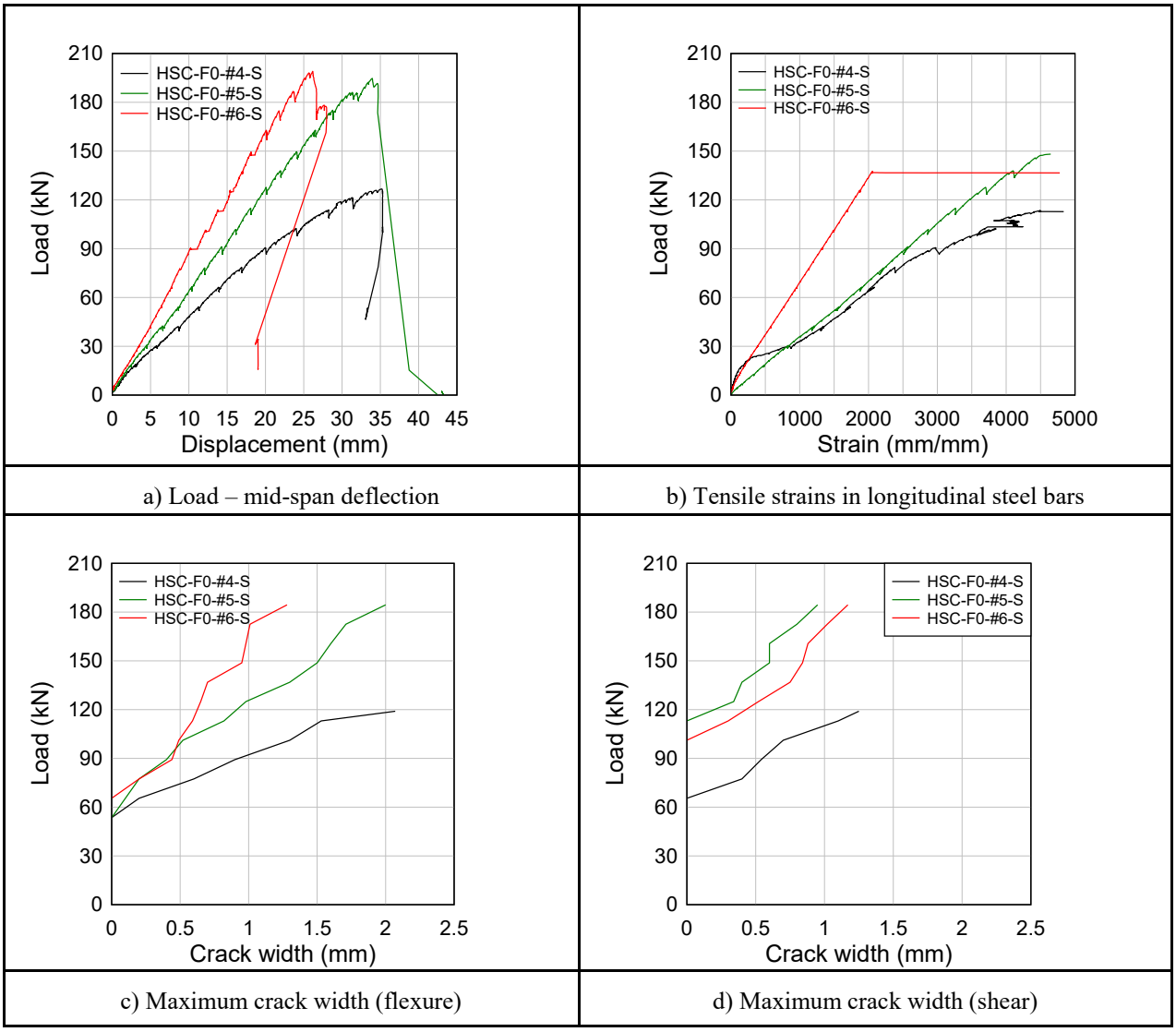

a) Load – mid-span deflection

b) Tensile strains in longitudinal steel bars

c) Maximum crack width (flexure)

d) Maximum crack width (shear)

Figure 4-7 Comparison of beam response in the HSC series

4.2.2. EFFECTS OF REINFORCEMENT TYPES IN THE HSC SERIES

In this sub-section, the performance of the high-strength concrete (HSC) beams with high-strength (HS) reinforcement are compared to a companion set of beams tested by Algassem (2016) which were built with HSC and normal-strength (NS) bars. Figure 4-8 compares the load-deflection response of the beams HSC-F0-#4-S, HSC-F0-#5-S and HSC-F0-#6-S from the current study, with companion beams HSC-F0-#4-S-400, HSC-F0-15M-S-400 and HSC-F0-20M-S, which had No. 4, 15M and 20M normal-strength (400 MPa) steel bars. It is noted that the beams in the #4 and #5/15M sets had the same bar size, while the beams in the #6/20M set have slightly different bar sizes (d_b = 19 vs. 19.5 mm, and A_s = 284 vs. 300 mm2, respectively). All other beam properties (dimensions, concrete type and transverse reinforcement) were identical with the exception of the reinforcement type. Maximum load and deflections for the beams in both sets are summarized in Table 4-2. Photos of the beams at failure can be seen in Figure 4-9.

The comparisons show that the beams reinforced with #4, #5, and #6 high-strength bars have load capacities which are increased by 67.8%, 86.2%, and 46.5% when compared to the companion beams with normal strength No. 4, 15M and 20M bars. However, the HSC beams with normal-strength steel proved to be more ductile when compared to the companions with high-strength reinforcement. The use of normal vs. high-strength steel did not have a significant effect on beam stiffness (this is to be expected since both steel types have the same elastic modulus).

Figure 4-8 shows that steel type affected the shape of the load-deflection curves. While the NS steel specimens show a clear yield plateau with large plastic deformations before failure, the HS steel specimens show a nearly linear ascending response, with slight rounding of the load-deflection curve, but no distinct yield plateau before failure. The beams with HS steel also showed lower failure deflections and lower ductility ratio (Δ_{max}/Δ_y) when compared to companion beams with conventional steel reinforcement. The maximum deflections of No. 4, No. 5 and No. 6 HS steel specimens are 35 mm, 34 mm and 27 mm respectively, compared to 59 mm, 39 mm and 30 mm for the companion beams with No. 4, 15M and 20M conventional steel bars. Similarly, the ductility ratio (Δ_{max}/Δ_y) were 1.34 and 1.37 for the beams with No. 4 and 5 HS steel, which compare to values of 5.12 and 2.28 for the companions with No. 4 and 15M normal-strength bars. Moreover, while the beam with normal-strength 20M bars showed a ductile failure (steel-controlled), the companion beam with high-strength No. 6 bars was over-reinforced and showed a brittle (concrete-controlled) failure, with concrete crushing prior to the development of yielding in the bars. Figure 4-9 compares the photos of the companion HSC beams at failure.

While the crack patterns and damage states are similar, the failures are somewhat more severe in the HS specimens, with greater damage in the midspan compression. Figure 4-8 shows that the use of high-strength reinforcement improved the cracking behaviour of the HSC beams. Nonetheless, the reduced crack widths near ultimate were associated with more brittle failures with lower deflections when compared to the specimens with normal-strength steel reinforcement.

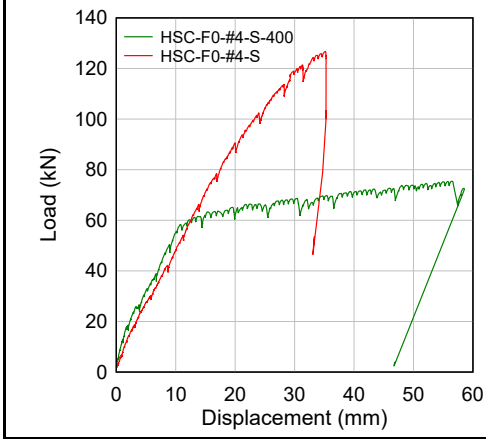

a) Load – mid-span deflection of No. 4 bars

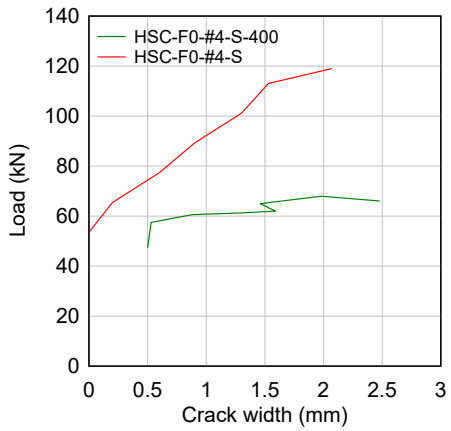

b) Maximum crack width (flexure) of No. 4 bars

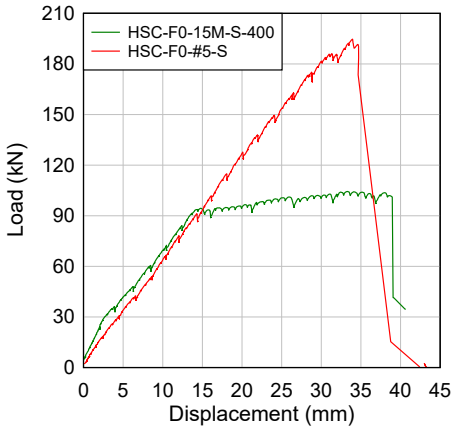

c) Load – mid-span deflection of No. 5/15M bars

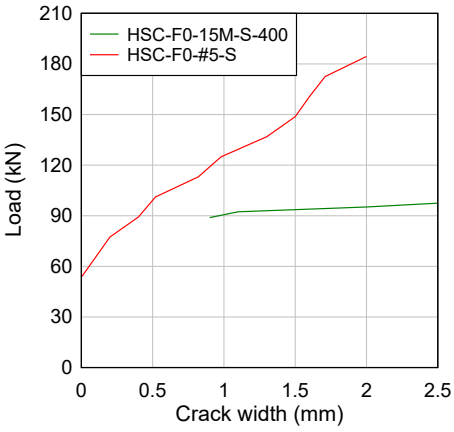

d) Maximum crack width (flexure) of No. 5/15M bars

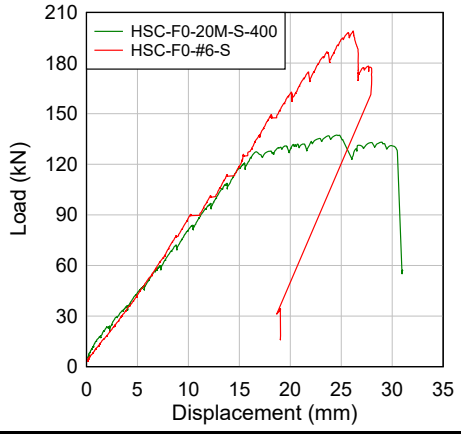

e) Load – mid-span deflection of No. 6/20M bars

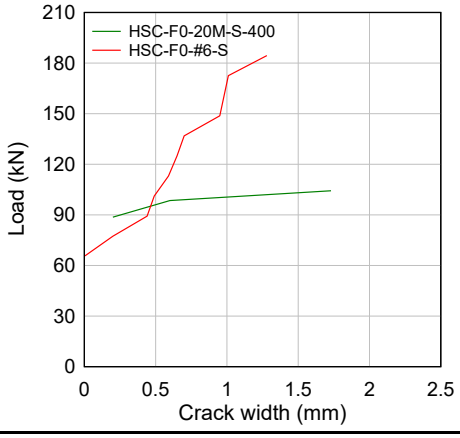

f) Maximum crack width (flexure) of No. 6/20M bars

Figure 4-8 Comparison of HSC beams reinforced with MMFX and normal bars

Table 4-2 Summary of results for HSC beams with NS and HS bars

Beam specimen	ρ (longitude)	Maximum Load P_{max} (kN)	Deflection at peak Δ_{max} (mm)	Deflection at failure Δ_f (mm)	Δ_{max}/Δ_y	Toughness up to peak
HSC-F0-#4-S	1.0%	126.7	35.21	35.21	1.34	2655
HSC-F0-#4-S-400	1.0%	75.4	55.76	58.76	5.12	3180
HSC-F0-#5-S	1.5%	194.7	33.96	35.21	1.37	3686
HSC-F0-15M-S-400	1.5%	104.4	33.28	38.96	2.28	3272
HSC-F0-#6-S	2.2%	199.0	26.17	27.26	-	3096
HSC-F0-20M-S-400	2.2%	137.3	24.52	30.51	1.63	2998

HSC-F0-#4-S-400: 75.4 kN	HSC-F0-#4-S: 126.7 kN
	
HSC-F0-15M-S-400: 104.4 kN	HSC-F0-#5-S: 194.7 kN
	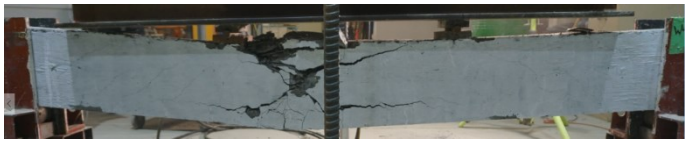
HSC-F0-20M-S-400: 137.3 kN	HSC-F0-#6-S: 199.0 kN
	

Figure 4-9 Failure mode for HSC specimens reinforced with normal-strength bars

CHAPTER 5. EXPERIMENTAL RESULTS OF THE DYNAMIC TESTS

5.1. CHAPTER OVERVIEW

In this chapter, the data collected from the dynamic experiments are presented. For each of the eight beams, recorded data included: reflected pressure and reflected impulse, maximum and residual displacements at mid-span, and photographic record of damage with identification of failure mode. Section 5.2 provides a general summary of the results. Further details and explanations for each beam are given in Section 5.3, including reflected pressure and impulse time histories, mid-span displacement time histories and photographs of damage and description of failure modes. Discussion of the results is presented in Chapter 6.

5.2. SUMMARY OF RESULTS OF EXPERIMENTS

The overall results for the self-consolidating concrete (SCC), high-strength concrete (HSC), and HSFRC beams are given in Table 5-1 and Table 5-2. These tables summarize the shockwave properties for each blast, including the driver length (L), driver pressure (P_d), reflected pressure (P_r), positive phase duration (t_p) and reflected impulse (I_r). The tables also summarize the response of the beams after each blast in terms of maximum displacement (δ_{max}), residual displacement (δ_{res}), and maximum rotation at the supports (θ_{max}).

For the specimens with No. 4 reinforcement, five blasts with variable magnitudes corresponding to driver pressures of 17 psi, 30 psi, 40 psi, 50 psi and 70 psi were applied until failure of the specimens. Whereas, six blasts with driver pressure values of 17 psi, 30 psi, 50 psi, 70 psi, 90 psi and 100 psi were applied to the specimens with No. 5 and No. 6 reinforcement. The dynamic load magnitude was increased gradually until the specimens failed. The specimens with a higher reinforcement ratio and those containing fibres were able to generally withstand larger blasts prior to failure.

The reflected pressure values presented in Table 5-1 and Table 5-2 were recorded from a pressure transducer on the interior of the shock-tube expansion section and measured the pressure acting on the load transfer device. The impulse-time history curves were obtained by integrating the pressure-time history curves using software DPlot. The impulse values listed in the tables correspond to the area under the positive phase of the pressure-time history curves (first peak in the impulse-time history curves).

The maximum displacements and residual displacements were recorded by an LVDT at the mid-span of the beams. The maximum/residual displacements and support rotation values reported in the tables are not cumulative. The sections that follow present the detailed results for each beam.

Table 5-1 Blast data summary (1/2)

Name		Driver Length	Approximate Driver Pressure	Reflected Pressure	Reflected Impulse	Positive Phase Duration	Max Deflection	Max Support Rotation	Residual Deflection
Specimen ID	***Blast #***	L_d mm	P_d kPa	P_r kPa	I_r kPa-ms	t_P ms	δ_{max} mm	θ_{max} degree	δ_{res} mm
SCC-F0-#4-S	-1	2745	117.3	22.94	231.66	22.60	13.44	0.61	2.60
	-2	2745	207	38.51	357.54	19.40	24.32	1.11	1.40
	-3a	2745	276	50.12	443.22	22.31	37.30	1.70	6.60
	-3b	2745	345	60.26	515.28	21.43	64.52	2.95	20.20
SCC-F0-#5-S	-1	2745	117.3	22.14	258.45	22.77	13.04	0.60	3.67
	-2	2745	207	41.73	394.06	22.03	20.13	0.92	1.22
	-3b	2745	345	61.07	568.03	22.85	33.97	1.55	0.78
	-4	2745	483	78.03	743.72	21.77	77.17	3.53	39.81
HSC-F0-#4-S	-1	2745	117.3	27.57	281.13	21.88	10.17	0.46	1.01
	-2	2745	207	40.37	403.62	21.14	22.39	1.02	1.28
	-3a	2745	276	51.95	479.62	21.09	33.78	1.54	3.89
	-3b	2745	345	58.21	540.28	22.56	52.74	2.41	8.69
HSC-F0-#5-S	-1	2745	117.3	22.33	216.41	19.96	9.08	0.41	3.63
	-2	2745	207	43.8	377.63	21.78	17.72	0.81	3.13
	-3b	2745	345	59.11	547.47	21.18	26.77	1.22	1.16
	-4	2745	483	77.63	749.71	24.38	64.71	2.96	19.96
HSC-F0-#6-S	-1	2745	117.3	24.7	222.82	22.35	10.91	0.50	2.05
	-2	2745	207	39.7	334.57	21.56	16.59	0.76	0.95
	-3b	2745	345	55.47	539.23	21.97	26.15	1.19	1.86
	-4	2745	483	/	/	/	/	/	25.22

Table 5-2 Blast data summary (2/2)

Name		Driver Length	Approximate Driver Pressure	Reflected Pressure	Reflected Impulse	Positive Phase Duration	Max Deflection	Max Support Rotation	Residual Deflection
Specimen ID	*Blast* #	L_d mm	P_d kPa	P_r kPa	I_r kPa-ms	t_P ms	δ_{max} mm	θ_{max} degree	δ_{res} mm
HSC-F1-#4-S	-1	2745	117.3	22.21	229.3	22.35	9.06	0.41	1.31
	-2	2745	207	39.38	381.21	21.95	19.18	0.88	3.00
	-3a	2745	276	46.64	462.68	21.27	26.02	1.19	1.53
	-3b	2745	345	54.96	526.24	20.59	37.65	1.72	12.16
	-4	2745	483	70.21	717.58	20.94	61.79	2.82	35.01
HSC-F1-#5-S	-1	2745	117.3	28.6	267.2	20.75	9.20	0.42	4.12
	-2	2745	207	43.09	408.46	20.66	14.60	0.67	2.66
	-3b	2745	345	58.75	572.35	21.01	22.51	1.03	0.60
	-4	2745	483	74.33	747.75	23.66	39.47	1.80	7.70
	-5	2745	621	79.42	845.02	24.65	63.11	2.88	37.36
	-6	2745	690	85.77	885.24	23.97	/	/	/
HSC-F1-#6-S	-1	2745	117.3	25.29	213.36	19.21	6.11	0.28	1.31
	-2	2745	207	41.23	380.31	21.62	14.76	0.67	2.41
	-3b	2745	345	53.87	573.1	21.70	22.33	1.02	1.19
	-4	2745	483	79.46	763.46	23.13	35.99	1.64	5.35
	-5	2745	621	97.06	937.81	25.4	66.84	3.05	38.86
	-6	2745	690	83.14	956.87	24.85	/	/	/

5.3. DESCRIPTION OF EXPERIMENTAL RESULTS – SCC SERIES

5.3.1. BEAM WITH NORMAL-STRENGTH CONCRETE & NO. 4 BARS (SCC – F0 – #4 – S)

This specimen was a normal-strength concrete beam with plain SCC (no fibres) and reinforced with 2 - No. 4 MMFX steel bars. The shockwave and displacement data for this beam can be found in Table 5-1. Complete reflected pressure and impulse histories, as well as reflected pressure and mid-span displacement histories for each blast are shown in Figure 5-1 and Figure 5-2. Figure 5-3 includes photographs detailing the effects of each blast on this beam.

Blast 1 (17 psi) was meant to test the beam within the elastic range. The maximum and residual displacements at mid-span were 13.44 mm and 2.60 mm respectively. The tensile strain gauge recorded a maximum strain of 0.0020 mm/mm (ε_{res}=0.0005 mm/mm). Eight hairline cracks could be found in the flexural zone in the central region of the beam.

Blast 2 (30 psi) was meant to test the beam to yielding. The maximum and residual displacements at mid-span were 24.32 mm and 1.4 mm respectively. The cumulative residual displacement reached 4.0 mm after this test. The tensile strain gauge recorded a maximum strain of 0.0055 mm/mm (ε_{res}=0.0015 mm/mm) during this test, which is slightly below the yield strain (ε_y =0.0067 mm/mm).. This blast resulted in the formation of further hairlines that appeared in the flexural and shear zones, but no major crack openings were visible.

Blast 3a (40 psi) was meant to test the beam within the plastic range. The maximum and residual displacements at mid-span were 37.3 mm and 6.6 mm respectively. The cumulative residual displacement reached 10.6 mm after this test. The tensile strain gauge recorded a maximum strain of 0.0105 mm/mm (ε_{res}=0.0049 mm/mm), which means the steel bars were in the post yield range. It was observed that further hairline cracks appeared along the beam length, with some cracks connecting together in the mid-span region. Some longitudinal cracks also formed in the tensile zone at the level of the longitudinal steel. Two major cracks were found in the flexural zone, and the maximum crack was measured as 1.78 mm.

The specimen failed in flexure after Blast 3b (50 psi). The maximum and residual displacements at mid-span were 64.52 mm and 20.2 mm respectively. The cumulative residual displacement reached 30.8 mm after this test. The tensile strain gauge recorded a maximum strain of 0.02 mm/mm before failure, which means the steel bars yielded. This blast caused the concrete in the compression zone at mid-span to crush, with significant spalling of tension concrete at mid-span. High-speed video shows the formation of secondary fragments and the projection of six main blocks of cover concrete from the beam at failure. The distance between the beam and the blocks varied from 2 meters to 5.5 meters. The reinforcing steel bars were exposed over a distance of 700 mm in the flexural zone.

5.3.2. BEAM WITH NORMAL-STRENGTH CONCRETE & NO. 5 BARS (SCC – F0 – #5 – S)

This beam was constructed with plain SCC (without fibres), and was reinforced with No. 5 MMFX steel bars. The shockwave and displacement data for this beam can be found in Table 5-1. Complete reflected pressure and impulse histories, as well as reflected pressure and mid-span displacement histories for each blast are shown in Figure 5-4 and Figure 5-5. Figure 5-6 includes photographs detailing the effects of each blast on this specimen.

For this beam, the maximum displacements for Blast 1 (17 psi), Blast 2 (30 psi), Blast 3b (50 psi), and Blast 4 (70 psi) were measured as 13.0 mm, 20.13 mm, 33.97 mm and 77.17 mm respectively. The residual displacements for Blast 1 (17 psi), Blast 2 (30 psi), Blast 3b (50 psi), and Blast 4 (70 psi) were recorded as 3.67 mm, 1.22 mm (4.89 mm cumulative), 0.78 mm (5.67 mm cumulative), and 39.81 mm (45.48 mm cumulative) respectively. The strain gauges were not considered to be reliable for this beam.

Similar to the previous specimen, Blast 1 (17 psi) was meant to test the beam within the elastic range. A couple of hairline cracks were visible over the central span, but no major cracks were detected after this test. Blast 2 (30 psi) was meant to bring the beam to just before yielding. More flexural hairline cracking occurred over the central span, with the formation of some diagonal cracks in the shear spans, but no major crack was observed.

For Blast 3b (50 psi), four major cracks were observed at 350 mm, 450 mm, 600 mm, and 1200 mm from the top support, with crack widths of 0.98 mm, 2.2 mm, 0.84 mm and 0.46 mm respectively. It was also observed that the concrete in the compression zone at the top support began to crush. In addition, a long piece of concrete cover (30 mm x 70 mm) detached after this test, however no steel bars were exposed, as seen in Figure 5-6 (e).

Blast 4 (70 psi) was the final test for this specimen, with the beam failing in shear. Two major cracks with nearly 45-degree angles were observed in the shear region at the top of the beam, spaced at 300 mm from each other. Figure 5-6 (f) shows spalling of the side and bottom concrete covers, exposure of stirrups and reinforcement bars and buckling of the top reinforcement bars in the shear spans. The chunks released from the beam were scattered over the floor, and the farthest chunk was 5.5 meters away from the beam. High-speed video shows the formation of significant debris during the test. The results of this test demonstrate the importance of shear reinforcement detailing in beams containing high-strength steel reinforcement. For this beam with SCC, the balanced reinforcement ratio was estimated to be $\rho = 0.9\%$; thus, the SCC-F0-#5-S specimen ($\rho = 1.6\%$) can be considered to have been over-reinforced.

5.4. DESCRIPTION OF EXPERIMENT RESULTS – HSC SERIES

5.4.1. BEAM WITH HIGH-STRENGTH CONCRETE & NO. 4 BARS (HSC – F0 – #4 – S)

The HSC-F0-#4-S specimen was a high-strength concrete beam without fibres, and was reinforced with No. 4 MMFX steel bars. This beam was the first specimen tested in the HSC series. The shockwave and displacement data for this beam can be found in Table 5-1. Complete reflected pressure and impulse histories, as well as reflected pressure and mid-span displacement histories for each blast are shown in Figure 5-7 and Figure 5-8. Figure 5-9 includes photographs detailing the effects of each blast on this beam.

Blast 1 (17 psi) was meant to test the beam within the elastic range. The maximum and residual displacements in the middle span were recorded as 10.17 mm and 1.01 mm respectively. The tensile strain gauge recorded a maximum strain to be 0.0022 mm/mm (ε_{res}=0.0001 mm/mm). Several hairline cracks could be observed over the beam span, but major cracking was considered to be negligible.

Blast 2 (30 psi) was meant to bring the beam to yielding. The maximum and residual displacements in the middle span were 22.39 mm and 1.28 mm respectively. The cumulative residual displacement reached 2.29 mm after this test. The tensile strain gauge recorded a maximum strain of 0.0055 mm/mm (ε_{res}=0.0012 mm/mm) during this test. More hairline cracks appeared in the flexural and shear region after this blast. A major crack with a width of 2.31 mm could be observed in the beam mid-span, and a longitudinal crack with a 0.14 mm width formed at the level of the steel reinforcement in the mid-span tensile region.

Blast 3a (40 psi) was meant to test the beam within the plastic range. The maximum and residual displacements in the mid-span were 37.3 mm and 6.6 mm respectively. The cumulative residual displacement reached 10.6 mm. The tensile strain gauge recorded the maximum strain to be 0.019 mm/mm (ε_{res}=0.007 mm/mm), which means the steel bars were in post-yield range. Figure 5-9 (e) shows further growth of the longitudinal which reached a crack width of 4.09 mm. The flexural cracks in the mid-span region also grew in width, with crack widths which varied between 1.33 mm and 2.95 mm.

The failure mechanism of this beam was associated with significant spalling of concrete in the tensile region and crushing of the concrete in the compression region at mid-span as a result of Blast 3b (50 psi). The maximum and residual displacements at mid-span were 52.74 mm and 8.69 mm respectively. The cumulative residual displacement reached 19.3 mm. The tensile strain gauge recorded the maximum strain to be 0.02 mm/mm (ε_{res}=0.02 mm/mm) during this blast. As shown in Figure 5-9 (f), the reinforcing bars were exposed over a length of 500 mm at mid-span as a result of the concrete spalling. The chunks of the cover concrete released from the beam and were scattered over distances of 1.7 meters to 3.3 meters from the beam. The high-speed video footage

showed the formation of additional secondary fragmentation during the test due to the crushing of concrete, as shown in Figure 5-9 (g).

5.4.2. BEAM WITH HIGH-STRENGTH CONCRETE & NO. 5 BARS (HSC – F0 – #5 – S)

Beam HSC-F0-#5-S had the same properties as the HSC-F0-#4-S specimen, except that it was reinforced with No. 5 instead of No. 4 MMFX steel bars. The shockwave and displacement data for this beam can be found in Table 5-1. Complete reflected pressure and impulse histories, as well as reflected pressure and mid-span displacement histories for each blast are shown in Figure 5-10 and Figure 5-11. Figure 5-12 includes photographs detailing the effects of each blast on this beam.

Blast 1 (17 psi) was meant to test the beam within the elastic range. The maximum and residual displacements at mid-span were 9.63 mm and 3.63 mm respectively. The tensile strain gauge recorded a maximum strain of 0.0014 mm/mm (ε_{res}=0.0003 mm/mm). A few hairline cracks in the flexure zone were observed along the beam span, however no major crack was visible.

Blast 2 (30 psi) was meant to test the beam at larger strains prior to yielding. The maximum and residual displacements at mid-span were 17.72 mm and 3.13 mm respectively. The cumulative residual displacement reached 6.76 mm after this test. The strain gauge recorded the maximum strain to be 0.0039 mm/mm (ε_{res}=0.0007 mm/mm) which is below yield (ε_y=0.007 mm/mm). After this test, a major crack was visible at the mid-span (width of 0.3 mm), with the formation of further cracks in the flexural and shear spans.

Blast 3b (50 psi) was meant to test the beam in the post-yield range. The maximum and residual displacements at mid-span were 26.77 mm and 1.16 mm respectively. The cumulative residual displacement reached 7.92 mm after this blast. The tensile strain gauge recorded the maximum strain to be 0.0073 mm/mm (ε_{res}=0.0021 mm/mm), which means the steel bars were in post-yield range. The major crack found at the midsection expanded to a width of 0.41 mm as a result of this blast. A longitudinal crack with a length of 500 mm was observed in the compression region of the flexural zone. The cracks width measured 2.1 mm in this zone, as seen in Figure 5-12 (e).

This beam failed in the flexural zone after Blast 4 (70 psi). The maximum and residual displacements in the middle span were 64.71 mm and 19.96 mm respectively. The cumulative residual displacement reached 27.88 mm after this test. The tensile strain gauge recorded the maximum strain to be 0.027 mm/mm (ε_{res}=0.027 mm/mm). As seen in Figure 5-12 (f), the concrete in the compression zone showed significant crushing, and the concrete in the tensile zone spalled into several chunks which ejected from the beam at failure. The distance between the chunks and the beam ranged from 0.7 meters to 2.6 meters. The reinforced steel bars on the tensile face were exposed over a distance of 500 mm. The high-speed video showed the formation of secondary fragmentation due to concrete crushing in the compression zone and spalling of the concrete in the tensile zone, as shown in Figure 5-12 (g).

5.4.3. BEAM WITH HIGH-STRENGTH CONCRETE & NO. 6 BARS (HSC – F0 – #6 – S)

This specimen was the third beam tested in the HSC series and differed from the HSC-F0-#4-S and HSC-F0-#5-S specimens only in terms of the use of No. 6 MMFX steel bars. The shockwave and displacement data for this beam can be found in Table 5-1. Complete reflected pressure and impulse histories, as well as mid-span displacement histories for each blast for this beam are shown in Figure 5-13 and Figure 5-14. Figure 5-15 includes photographs detailing the effects of each blast on this beam. The results recorded by the strain gauge were deemed to be unreliable since the values were too large.

Blast 1 (17 psi) was meant to test the beam within the elastic range. The maximum and residual displacements at mid-span were 10.91 mm and 2.05 mm respectively. Several hairline cracks were observed in the mid-span, and no major crack was visible.

After Blast 2 (30 psi) the maximum and residual displacements at mid-span were 16.59 mm and 0.95 mm respectively. The low residual displacement indicates that the #6 bars did not reach yielding after this test. The cumulative residual displacement reached 3.0 mm. A major crack with a width of 0.61 mm near the bottom load application point was observed and further hairline cracks were observed to have formed when compared with that of the previous blast.

Blast 3b (50 psi) resulted in maximum and residual displacements at mid-span of 26.15 mm and 1.86 mm respectively. The cumulative residual displacement reached 4.86 mm after this test. As a result of this blast, the crack on the bottom load point increased in width to 1.04 mm and a new major crack near the top load point was visible and was measured to be 1.07 mm in width. A crack in the longitudinal direction with a length of 500 mm was also noted near the bottom load point at the level of the tension steel. The crack widths varied between 0.2 mm and 0.59 mm in this region.

Blast 4 (70 psi) can be considered to be the failure blast for this beam. No data were collected during this test except for the residual displacement, which was measured to be 25.22 mm. The cumulative residual displacement reached 30.08 mm after this test. Figure 5-15 (g) shows the failure mechanism of this beam, with failure due to crushing of compression concrete in the mid-span region as a result of Blast 4 (70 psi). The cover concrete in the tensile zone also showed signs of spalling with the formation of large longitudinal cracks at the level of the tension steel. However, unlike beams HSC-F0-#4-S and HSC-F0-#5-S, the tension concrete in the HSC-F0-#6-S beam stayed in place and did not eject from the tension zone. Nonetheless, the crack width in this zone was measured to be 15 mm such that the reinforcing steel bars were partially exposed.

5.5. DESCRIPTION OF EXPERIMENTAL RESULTS – HSFRC SERIES

5.5.1. BEAM WITH HSFRC & NO. 4 BARS (HSC – F1 – #4 – S)

The HSC-F1-#4-S beam was the first beam of the high-strength fibre-reinforced concrete (HSFRC) series. It was constructed using HSC containing 1% steel fibres, and reinforced with No. 4 MMFX steel bars. The shockwave and displacement data for this beam can be found in Table 5-1. Complete reflected pressure and impulse histories, as well as mid-span displacement histories for each blast are shown in Figure 5-16 and Figure 5-17. Figure 5-18 includes photographs detailing the effects of each blast on this beam.

For this beam, the maximum displacements for Blast 1 (17 psi), Blast 2 (30 psi), Blast 3a (40 psi), Blast 3b (50 psi) and Blast 4 (70 psi) were measured as 9.06 mm, 19.18 mm, 26.02 mm, 37.65 mm and 61.79 mm respectively. The residual displacements for Blast 1 (17 psi), Blast 2 (30 psi), Blast 3a (40 psi), Blast 3b (50 psi) and Blast 4 (70 psi) were recorded as 1.31 mm, 3.0 mm (4.31 mm cumulative), 1.53 mm (5.84 mm cumulative), 12.39 mm (16.69 mm cumulative), and 35.01 mm (48.7 mm cumulative) respectively.

Blast 1 (17 psi) was meant to test the beam within the elastic range. The strain gauge data in the mid-span showed the maximum strain to be 0.0010 mm/mm (ε_{res}=0.0002 mm/mm). Several hairline cracks could be seen at mid-span.

Blast 2 (30 psi) was meant to test the beam to just before yielding. The strain gauge data in the mid-span showed that the maximum strain was 0.0036 mm/mm (ε_{res}=0.0008 mm/mm), which indicates that the MMFX bars were still in the elastic range. It is noted that the strains are lower when compared to the companion beam without fibres. The number of hairline cracks increased compared with Blast 1 (17 psi), but no major cracks were observed.

For Blast 3a (40 psi), the strain gauge data in the mid-span showed the maximum strain to be 0.027 mm/mm (ε_{res}=0.004 mm/mm), which indicated the MMFX bars enters the plastic range. More hairline cracks were observed over the span and a principal crack with width of 2.43 mm could be seen in the mid-span region.

The provision of fibres allowed this beam to survive Blast 3b (50 psi). the strain gauge data shows maximum and residual strains in the exceeded ε=0.027 mm/mm. Figure 5-18 (g) shows that the previous principal crack at mid-span increased to a width of 3.18 mm in width. A crack with a length of 250 mm also formed in the longitudinal direction on the tensile face in the mid-span at the level of the steel reinforcement, and the maximum width of the crack in this zone measured 1.92 mm.

Blast 4 (70 psi) can be considered the failure blast for this beam due to fibre pull-out. The principal crack found in Blast 3b (50 psi) expanded to a maximum width of 9.64 mm with some fibres pulling out at this location. Although the cover concrete stayed in place, the longitudinal crack increased to 3.30 mm in width, and the length of the crack increased to 350 mm. The maximum dimension crack opening when considering all cracks was 15.87 mm which was deemed too large

for the beam to resist another blast since the steel fibres had pulled out at this location with their residual contribution to blast resistance deemed limited for any further blast testing. The concrete on the compression face showed signs of crushing near the bottom load application point, however unlike like the plain HSC, crushing was controlled. From the high-speed camera, only some fine powder was observed during the failure of the specimen, an indicator of the improved fragmentation resistance of the HSFRC concrete.

5.5.2. BEAM WITH HSFRC AND NO. 5 bars (HSC – F1 – #5 – S)

This beam was constructed with HSC containing 1% and was reinforced with No. 5 MMFX steel bars. The shockwave and displacement data for this beam can be found in Table 5-1. Complete reflected pressure and impulse histories, as well as mid-span displacement histories for each blast are shown in Figure 5-19, Figure 5-20, and Figure 5-21. Figure 5-22 includes photographs detailing the effects of each blast on this beam.

The provision of steel fibres allowed this beam to survive up to Blast 6 (100 psi). The maximum displacements for Blast 1 (17 psi), Blast 2 (30 psi), Blast 3b (50 psi), Blast 4 (70 psi) and Blast 5 (90 psi) were measured as 9.2 mm, 14.6 mm, 22.51 mm, 39.47 mm, and 52.33 mm respectively. The residual displacements for Blast 1 (17 psi), Blast 2 (30 psi), Blast 3b (50 psi), Blast 4 (70 psi) and Blast 5 (90 psi) were recorded as 4.13 mm, 2.66 mm (6.78 mm cumulative), 0.6mm (7.38 mm cumulative), 7.7 mm (16.69 mm cumulative), and 15.18 mm (48.7 mm cumulative) respectively. No displacement data were recorded for Blast 6 (100 psi).

Blast 1 (17 psi) kept the beam within the elastic range. The strain gauge data in the mid-span show the maximum strain was 0.0010 mm/mm (ε_{res}=0.0002 mm/mm). No damage was observed after the blast.

Blast 2 (30 psi) also tested the beam within the elastic range. The strain gauge data in the mid-span showed the maximum strain to be 0.0028 mm/mm (ε_{res}=0.0006 mm/mm), which is evidence of the elastic behaviour of the longitudinal MMFX bars. Some hairline cracks appeared over the beam span when compared with Blast 1 (17 psi), and no major crack was visible.

For Blast 3b (50 psi), the strain gauge data showed that the strain gauge reached a value ε=0.02 mm/mm before failure, which indicates yielding of the steel reinforcement. A principal flexural crack, with a maximum width of 0.78 mm, was found to have formed after Blast 3b (50 psi). This crack was located 1000 mm from the top load application point.

For Blast 4 (70 psi), two major cracks were observed at distances of 1000 mm and 1200 mm from the top load point. The major crack detected in Blast 3b (50 psi) continued growing to a width of 1.8 mm and several new cracks with widths which varied between 1.63 mm and 2.59 mm formed on the bottom tension face of the beam. Longitudinal cracks with a length of 200 mm at the level of the steel reinforcement appeared after this blast and reached a width of 0.69 mm, as shown in Figure 5-22 (h). Limited crushing of compression concrete was also observed at mid-span.

Figure 5-22 (i) shows the condition of the beam after Blast 5 (90 psi). The concrete on the compression face at mid-span showed signs of crushing after this blast. The high-speed video footage showed limited secondary fragmentation in terms of the production of some fine powder due to the crushing of the concrete. The major cracks found in the last blast expanded to 6.67 mm and 9.35 mm in width respectively leading to partial pullout of the steel fibres at this location. The longitudinal crack also increased to 300 mm in length with a maximum width of 3.38 mm.

Blast 6 (100 psi) can be regarded as the final test for this beam since the longitudinal bars ruptured after the test, as seen in Figure 5-22 (j). A chunk of concrete with a length of 150 mm flew out during the test. As a result of the rupture of the bars, the beam split into two parts. The top part of the beam collapsed and both parts released from the supports.

5.5.3. BEAM WITH HSFRC AND NO. 6 BARS (HSC – F1 – #6 – S)

The HSC-F1-#6-S beam was the last beam of the HSFRC series. The only difference in the composition of this beam from that of the HSC-F1-#4-S and HSC-F1-#5-S specimens was the use of No. 6 bars instead of No. 4 or No. 5 bars. The shockwave and displacement data for this specimen can be found in Table 5-1. Complete reflected pressure and impulse histories, as well as mid-span displacement histories for each blast on this beam are shown in Figure 5-23, Figure 5-24 and Figure 5-25. Figure 5-26 includes photographs detailing the effects of each blast on this specimen.

For this beam, the maximum displacements for Blast 1 (17 psi), Blast 2 (30 psi), Blast 3b (50 psi), Blast 4 (70 psi), and Blast 5 (90 psi) were measured as 6.11 mm, 14.76 mm, 22.33 mm, 35.99 mm, and 66.84 mm respectively. The residual displacements for Blast 1 (17 psi), Blast 2 (30 psi), Blast 3b (50 psi), Blast 4 (70 psi) and Blast 5 (90 psi) were recorded as 1.31 mm, 2.41 mm (3.72 mm cumulative), 1.19 mm (4.91 mm cumulative), 5.35 mm (10.26 mm cumulative), and 38.86 mm (49.12 mm cumulative) respectively. No data was recorded for displacement during Blast 6 (100 psi).

The strain gauge data in the mid-span showed a maximum strain of 0.0007 mm/mm (ε_{res}=0.0002 mm/mm) which indicated that the beam was tested in the elastic range at Blast 1 (17 psi). No observed damage was detected as a result of this test.

At Blast 2 (30 psi) the strain gauge at mid-span recorded a maximum strain of 0.0024 mm/mm (ε_{res}=0.0005 mm/mm), which indicates elastic behaviour of the beam. Some hairline cracks appeared after this test, but no major crack was visible.

For Blast 3b (50 psi), the maximum strain measured by the strain gauge at mid-span reached 0.0042 mm/mm (ε_{res}=0.0009 mm/mm), which means the beam was still in the elastic range. A major flexural crack was found in the mid-span region located 1200 mm from the top load point with a width of 1.08 mm. This crack extended to the top of the beam. Some diagonal cracks also began to form in the shear spans.

After Blast 4 (70 psi), the strain gauge data reached an extreme value of 0.027 mm/mm and continued to keep this value until the beam failed. The larger strain capacity of HSFRC when compared to HSC allowed the steel reinforcement to reach yielding prior to crushing of the concrete. The crack that was observed in Blast 3b (50 psi) expanded to 4.5 mm. A vertical crack in the longitudinal direction also appeared after Blast 4 (70 psi) with a length of 250 mm and a maximum width of 1.39 mm. Further diagonal cracks were also observed in the shear spans.

For Blast 5 (90 psi), Figure 5-26 (h) shows the concrete on the compression face began to crush after the test. A new diagonal crack with a length of 400 mm was observed in the mid-span region, with a width of 4.51 mm. The two cracks resulting from Blast 4 (70 psi) continued growing after application of this blast; the flexural crack had a width of 4.39 mm and the length of the longitudinal crack increased to 600 mm with a maximum width of 5.7 mm. Two new flexural cracks with maximum widths of 1.27 mm and 1.75 mm were observed on the tensile face located 800 mm and 1250 mm from the top load point. Some fine powder could be observed in the high-speed video footage due to the concrete crushing on the compression face.

Blast 6 (100 psi) was the last blast for this beam. This test resulted in brittle failure of the beam, with the specimen releasing from the supports and falling to the ground due to the large intensity of this blast. A large chunk of concrete showed signs of major failure at mid-span, although it was held in place by a limited number of fibres. It was noted that the steel bars did not rupture after the test, as shown in Figure 5-26 (i).

5.6. PRESSURE, IMPULSE, AND DISPLACEMENT TIME HISTORIES & SELECTED PHOTOGRAPHS – SCC SERIES

5.6.1. SCC – F0 – #4 – S

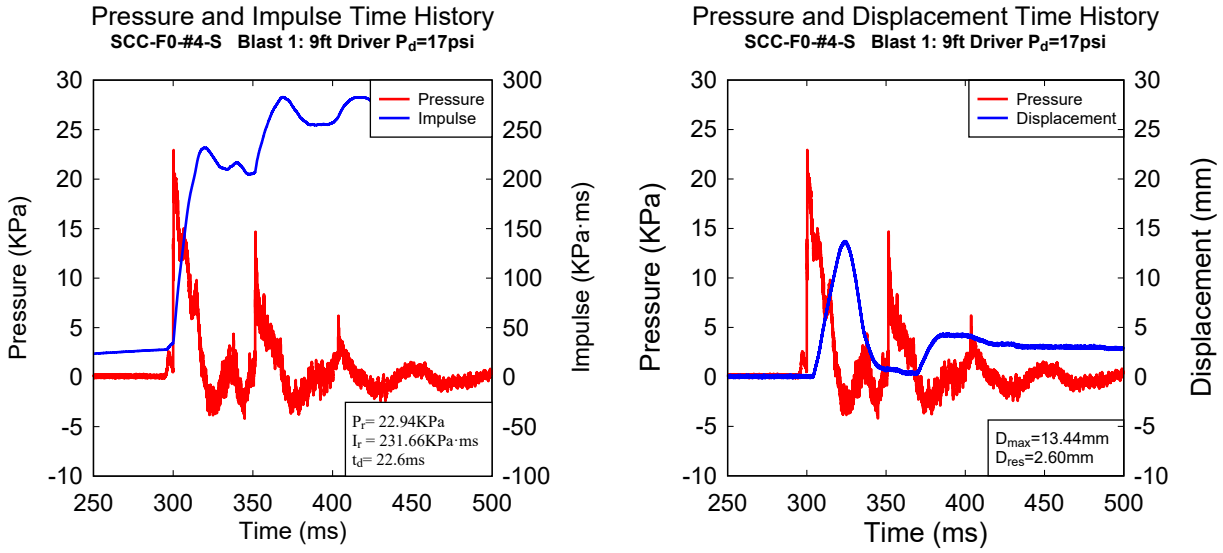

a) Blast 1: Reflected pressure, impulse, and displacement time histories.

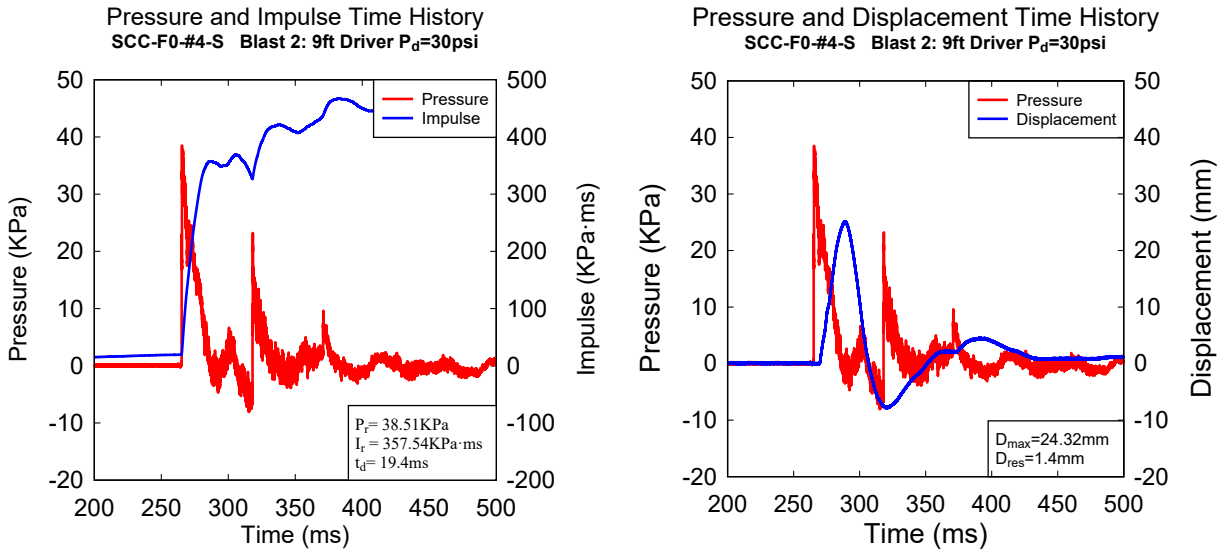

b) Blast 2: Reflected pressure, impulse, and displacement time histories.

Figure 5-1 SCC-F0-#4-S, recorded reflected pressure, impulse and displacement for Blasts 1 and 2

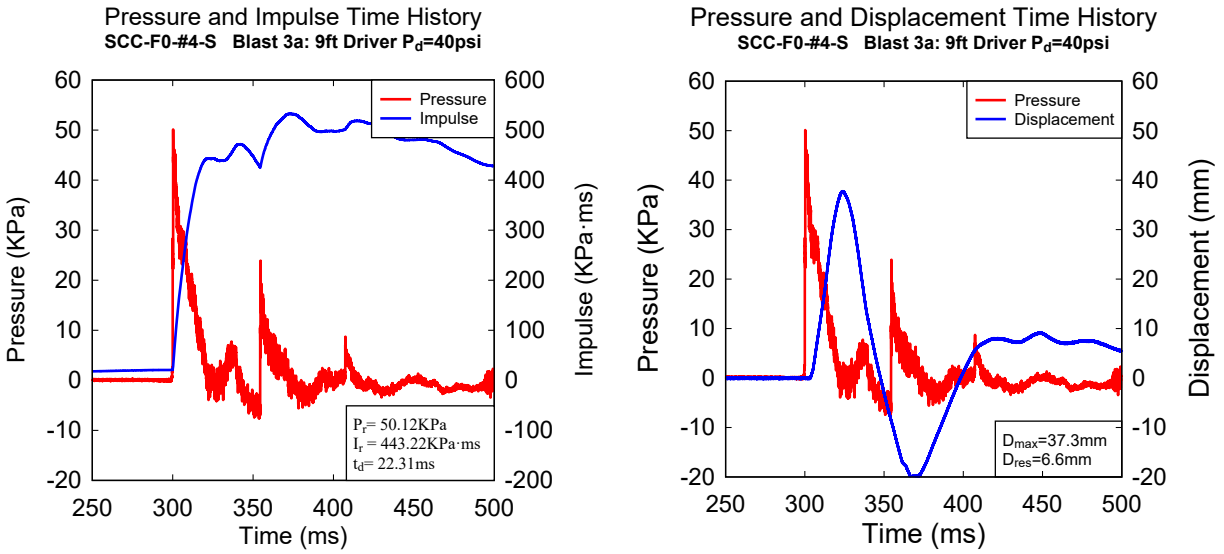

c) Blast 3a: Reflected pressure, impulse, and displacement time histories.

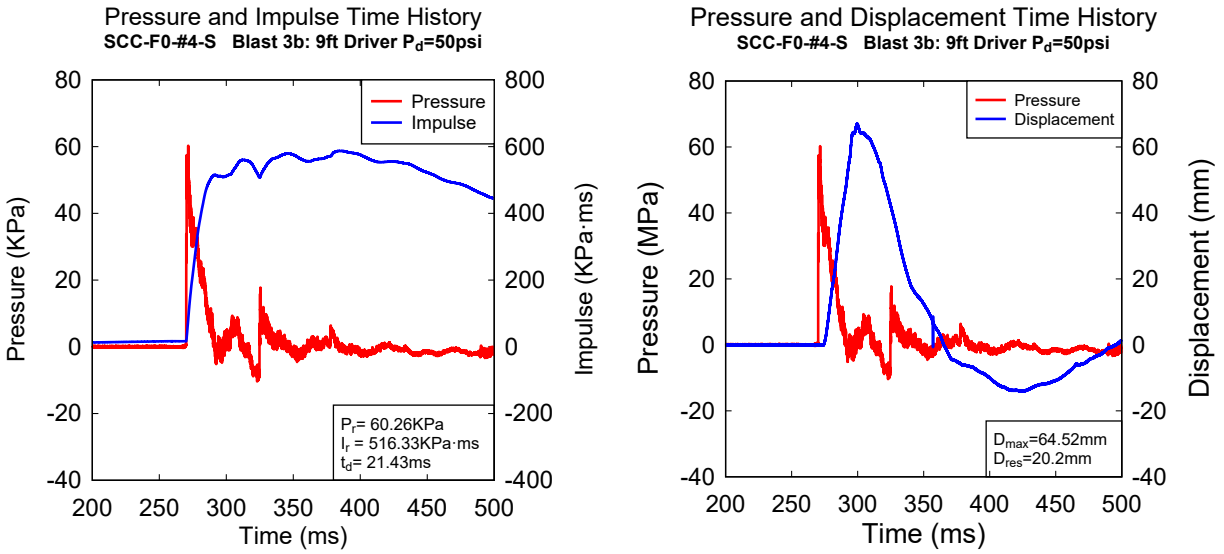

d) Blast 3b: Reflected pressure, impulse, and displacement time histories.

Figure 5-2 SCC-F0-#4-S, recorded reflected pressure, impulse and displacement for Blast 3a-3b

a) Blast 1
(17 PSI)

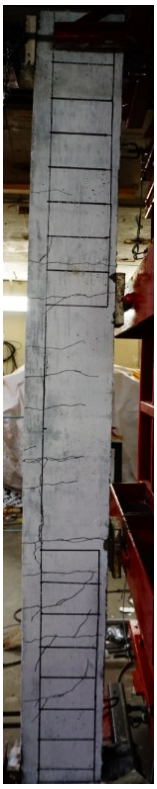

b) Blast 2
(30 PSI)

c) Blast 3a
(40 PSI)

d) Blast 3b
(50 PSI)

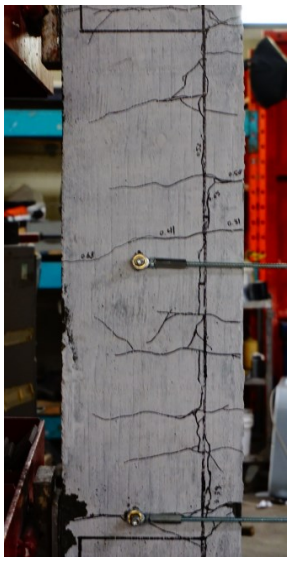

e) Mid-span cracking at Blast 3a

f) Mid-span crushing at Blast 3b

g) Concrete split out during blast 3b

Figure 5-3 SCC-F0-#4-S, photographs showing results of Blasts 1 - 4

5.6.2. SCC – F0 - #5 – S

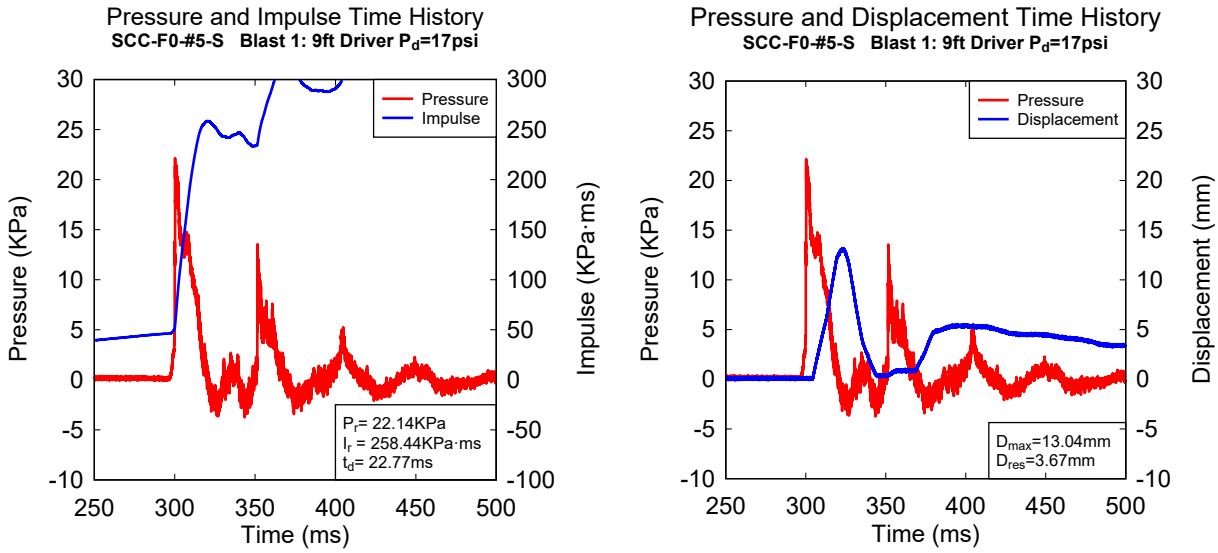

a) Blast 1: Reflected pressure, impulse, and displacement time histories.

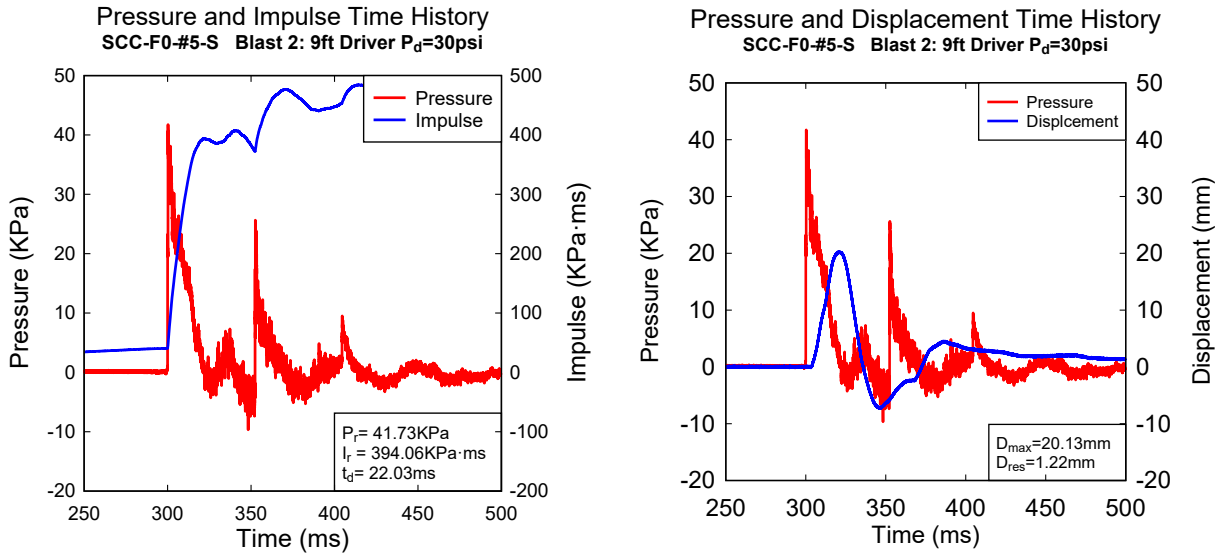

b) Blast 2: Reflected pressure, impulse, and displacement time histories.

Figure 5-4 SCC-F0-#5-S, recorded reflected pressure, impulse and displacement for Blasts 1 and 2

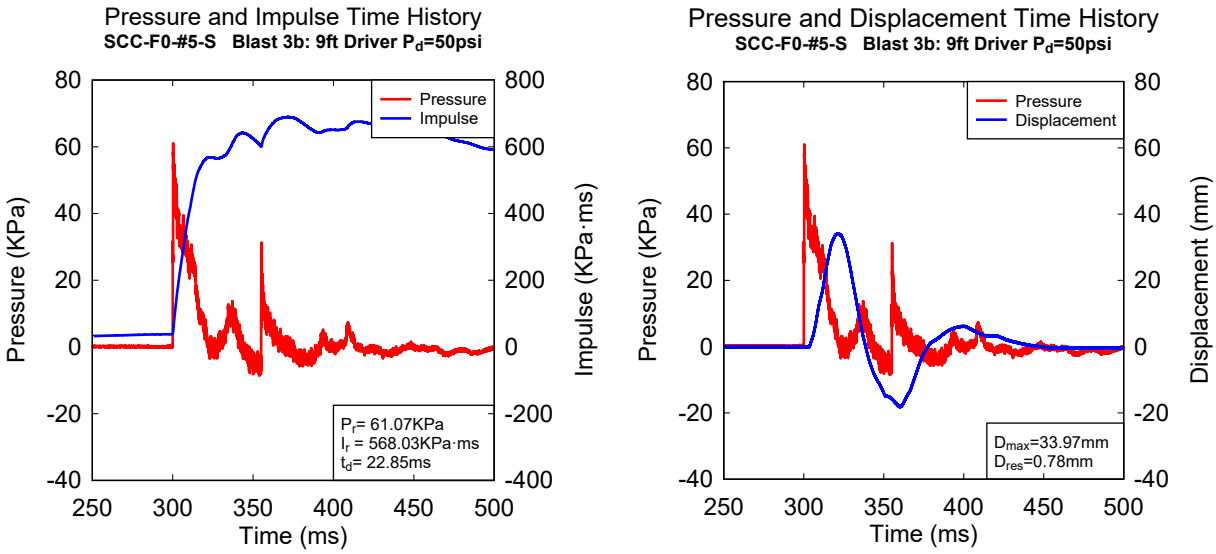

c) Blast 3b: Reflected pressure, impulse, and displacement time histories.

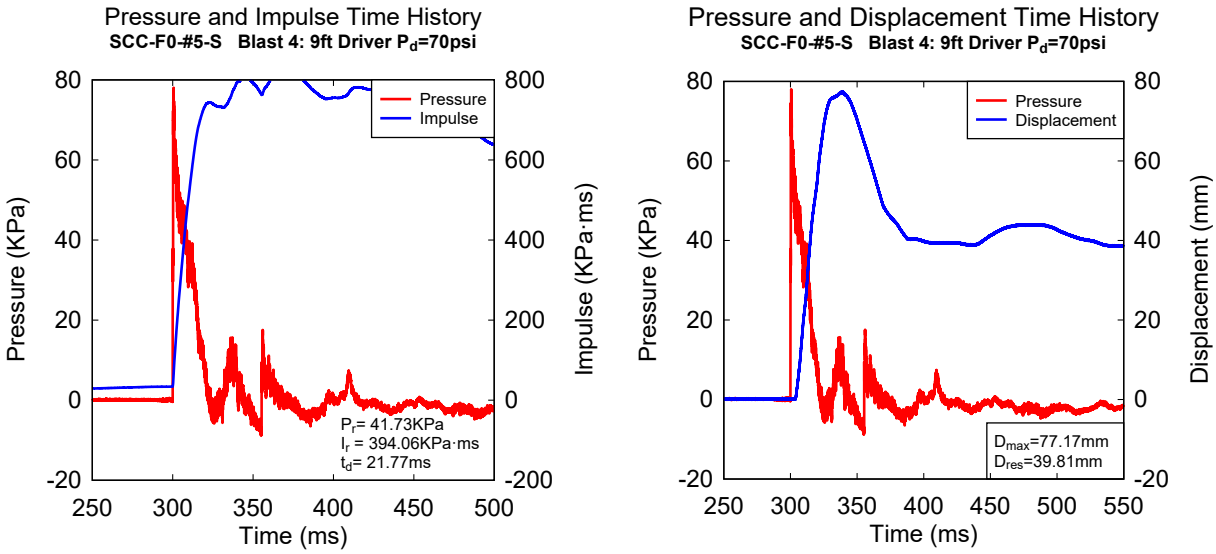

d) Blast 4: Reflected pressure, impulse, and displacement time histories.

Figure 5-5 SCC-F0-#5-S, recorded reflected pressure, impulse and displacement for Blasts 3b and 4

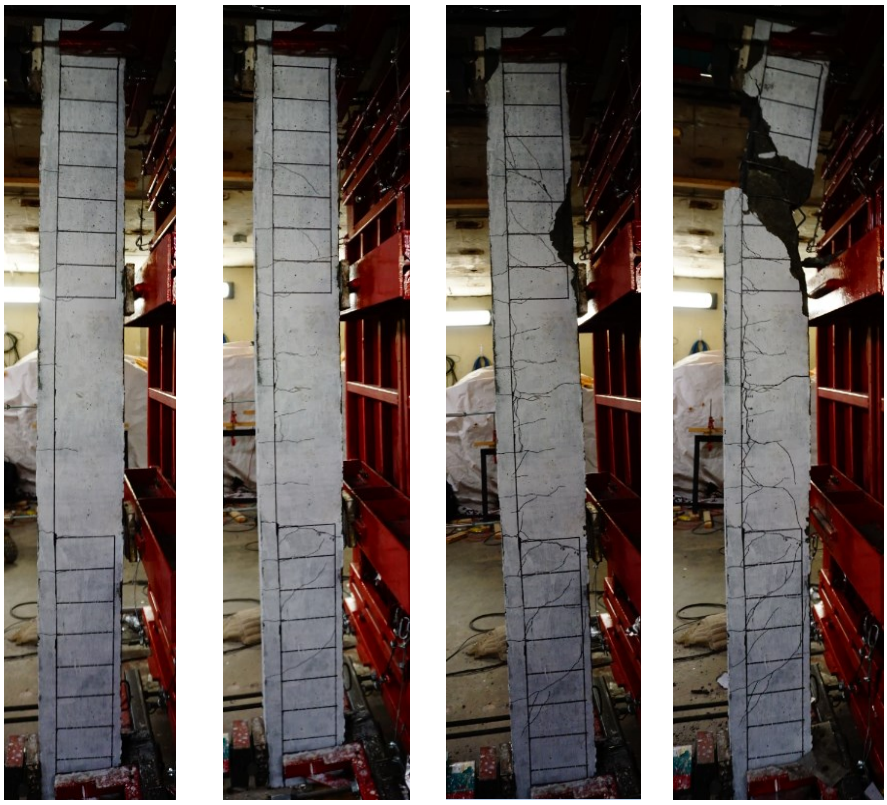

a) Blast 1 (17 PSI) b) Blast 2 (30 PSI) c) Blast 3b (50 PSI) d) Blast 4 (70 PSI)

e) Top-span cracking at Blast 3b f) Top-span cracking at Blast 4 g) Secondary fragmentation during blast 4

Figure 5-6 SCC-F0-#5-S, photographs at the end of Blasts 1 - 4

5.7. PRESSURE, IMPULSE, AND DISPLACEMENT TIME HISTORIES & SELECTED PHOTOGRAPHS – HSC SERIES

5.7.1. HSC – F0 - #4 – S

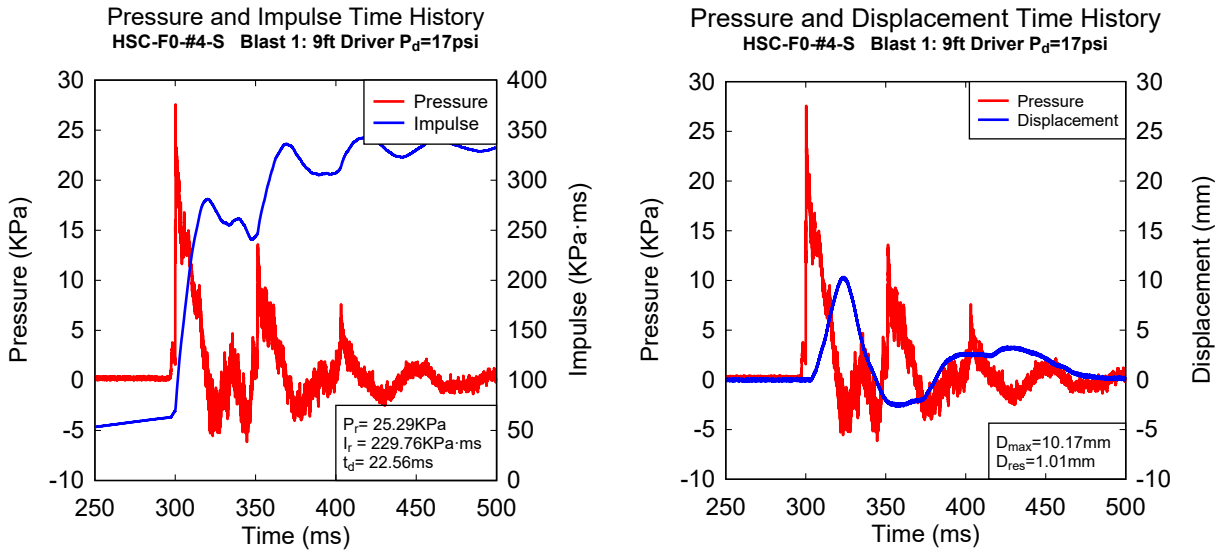

a) Blast 1: Reflected pressure, impulse, and displacement time histories.

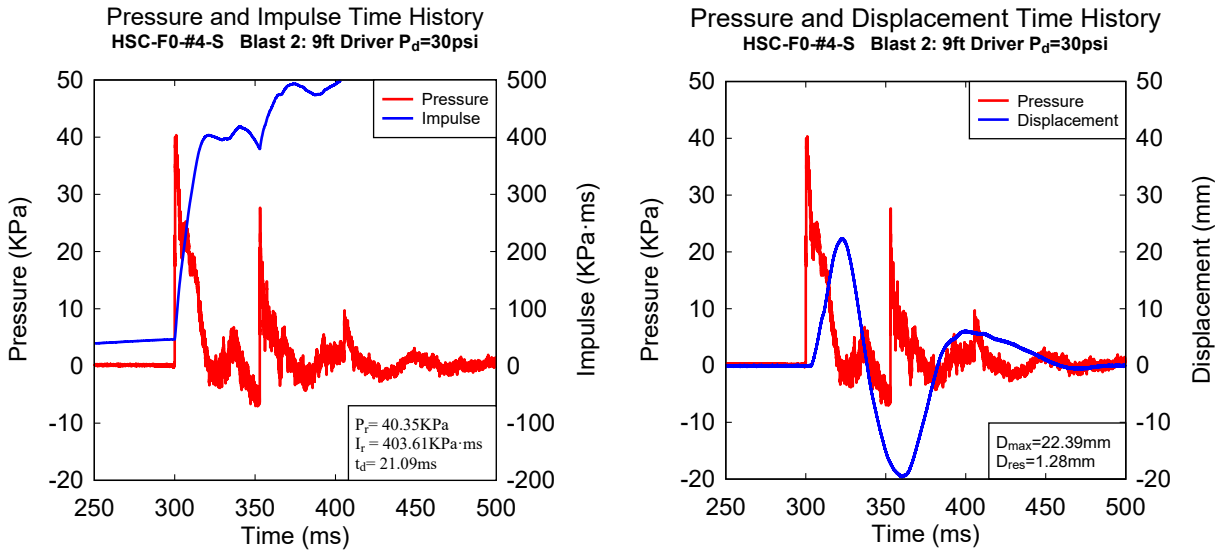

b) Blast 2: Reflected pressure, impulse, and displacement time histories.

Figure 5-7 HSC-F0-#4-S, recorded reflected pressure, impulse and displacement for Blasts 1 and 2

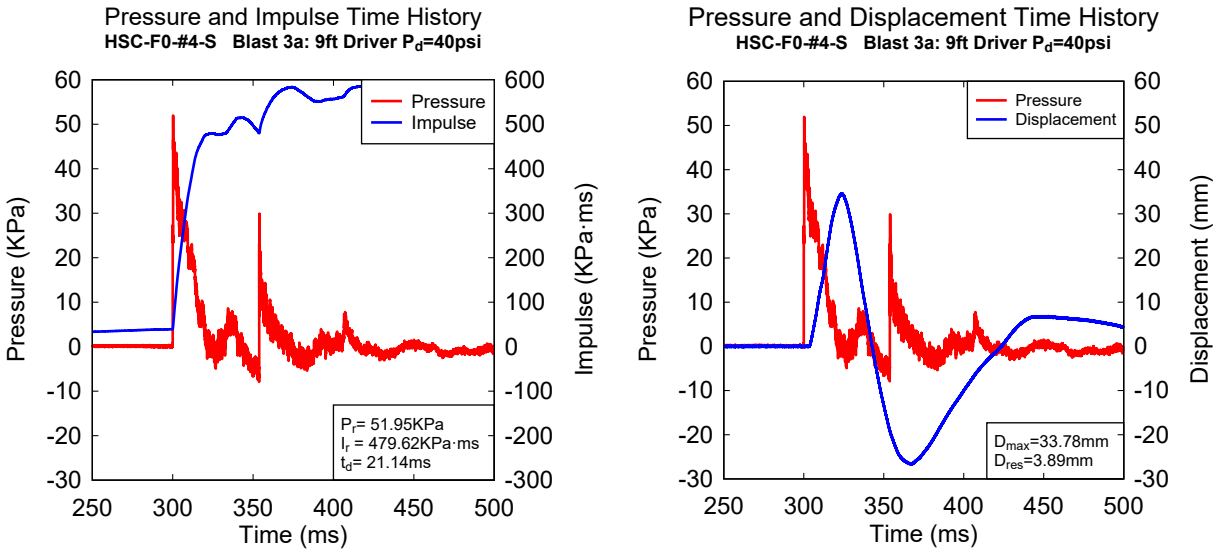

c) Blast 3a: Reflected pressure, impulse, and displacement time histories.

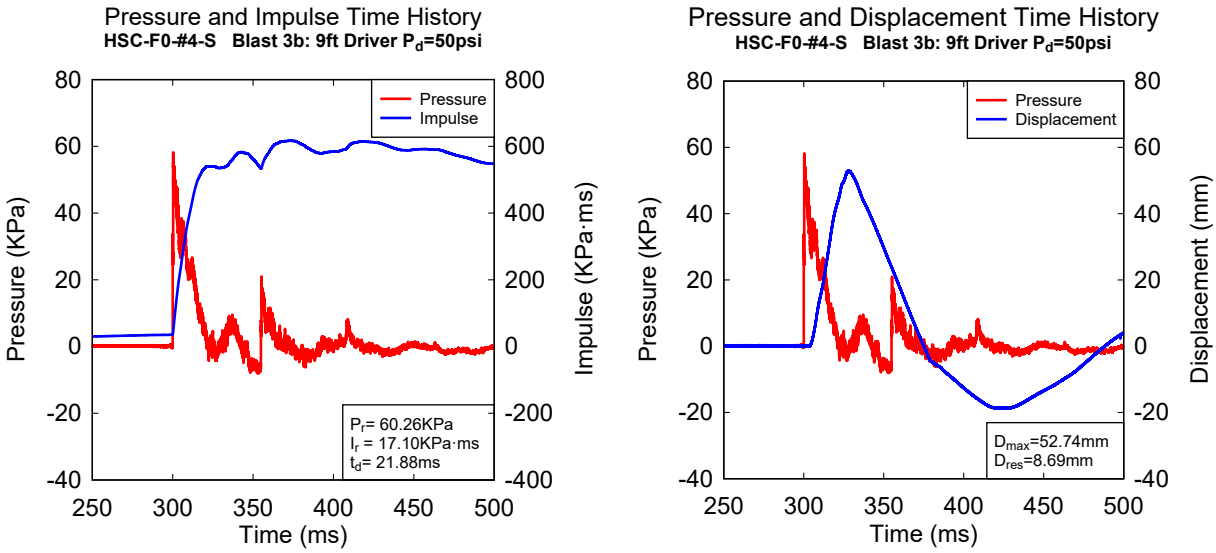

d) Blast 3b: Reflected pressure, impulse, and displacement time histories.

Figure 5-8 HSC-F0-#4-S, recorded reflected pressure, impulse and displacement for Blasts 3a and 3b

a) Blast 1
(17 PSI)

b) Blast 2
(30 PSI)

c) Blast 3a
(40 PSI)

d) Blast 3b
(50 PSI)

e) Mid-span cracking at Blast 3a

f) Mid-span cracking at Blast 3b

g) Concrete split out and secondary fragmentation during blast 3b

Figure 5-9 HSC-F0-#4-S, photographs at the end of Blasts 1 - 3b

5.7.2. HSC – F0 - #5 – S

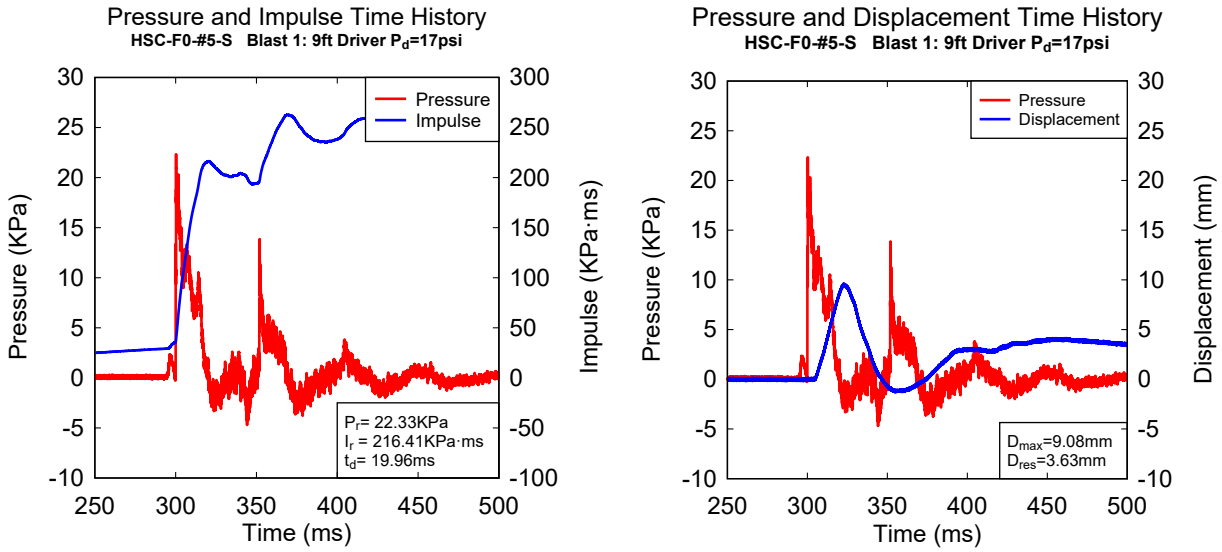

a) Blast 1: Reflected pressure, impulse, and displacement time histories.

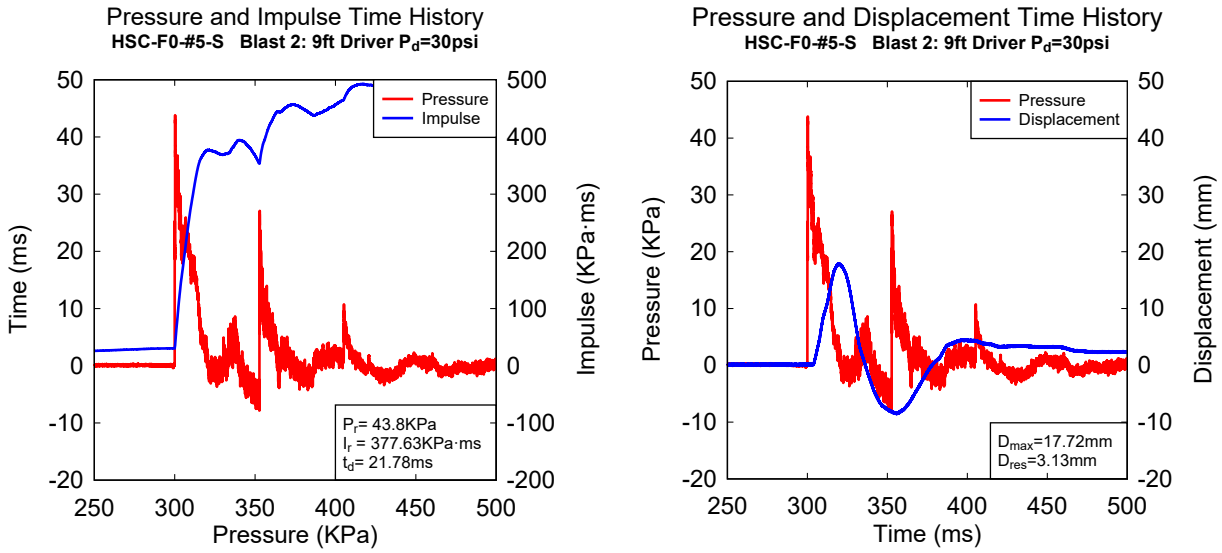

b) Blast 2: Reflected pressure, impulse, and displacement time histories.

Figure 5-10 HSC-F0-#5-S, recorded reflected pressure, impulse and displacement for Blasts 1 and 2

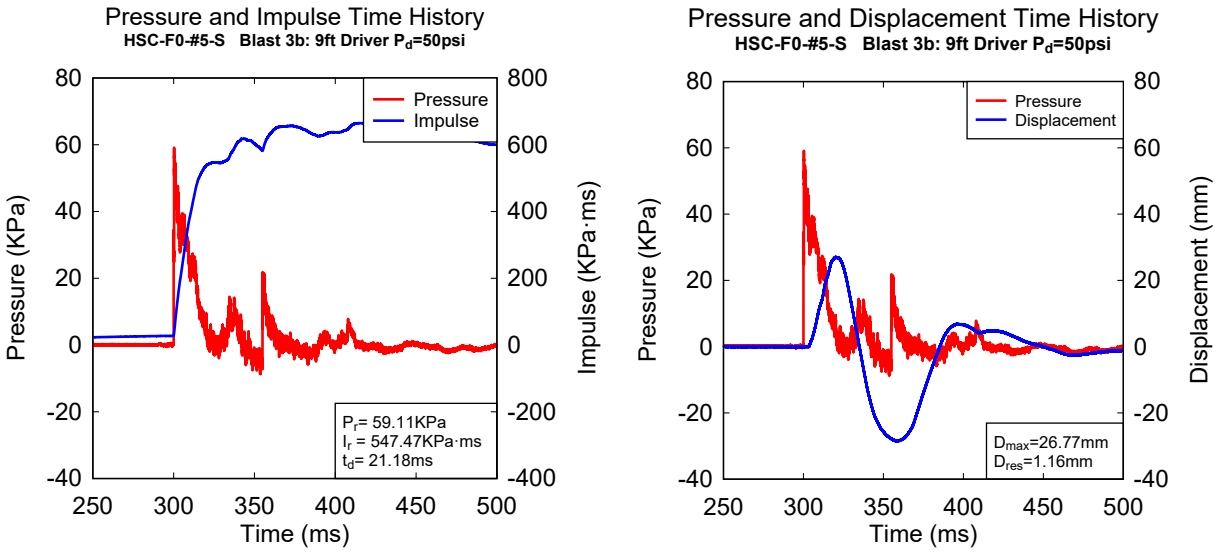

c) Blast 3b: Reflected pressure, impulse, and displacement time histories.

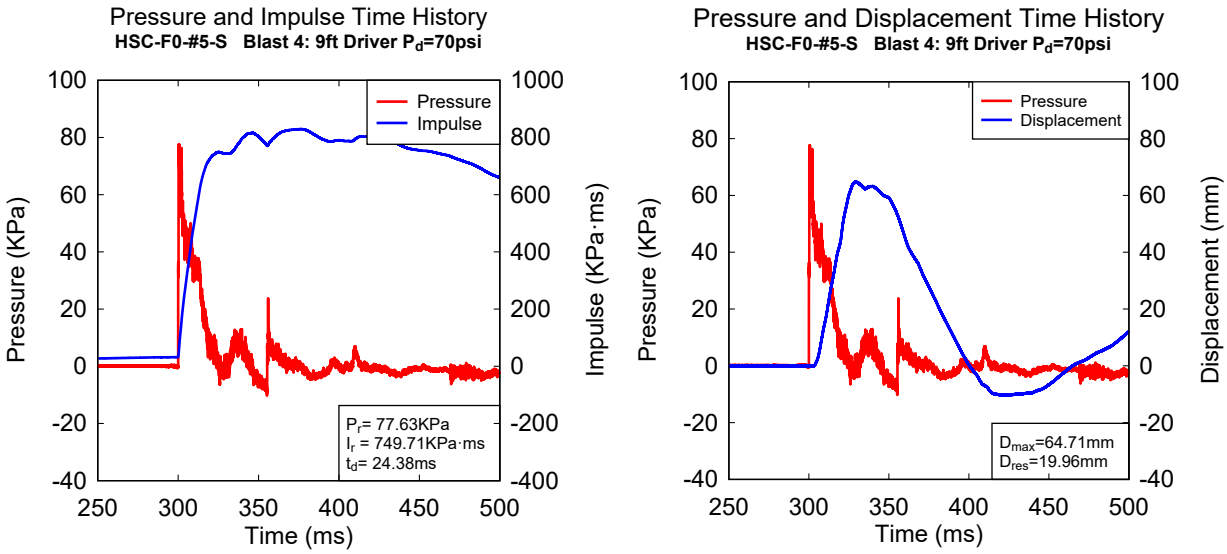

d) Blast 4: Reflected pressure, impulse, and displacement time histories.

Figure 5-11 HSC-F0-#5-S, recorded reflected pressure, impulse and displacement for Blasts 3b and 4

a) Blast 1 (17 PSI)

b) Blast 2 (30 PSI)

c) Blast 3b (50 PSI)

d) Blast 4 (70 PSI)

e) Mid-span cracking at Blast 3b

f) Mid-span cracking at Blast 4

g) Concrete split out and secondary fragmentation during blast 4

Figure 5-12 HSC-F0-#5-S, photographs at the end of Blasts 1 - 4

5.7.3. HSC – F0 - #6 – S

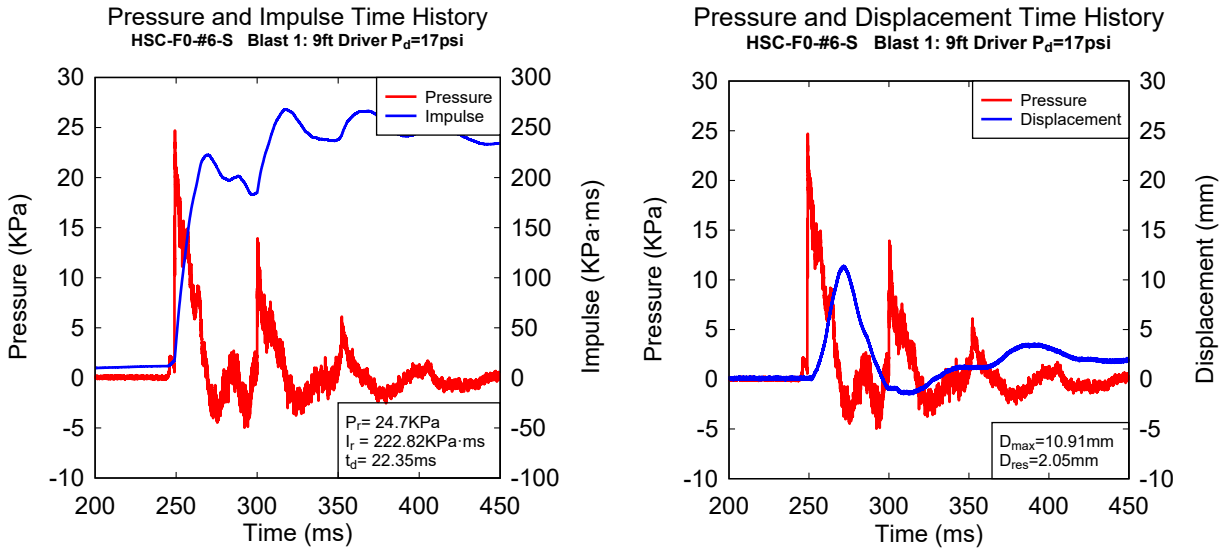

a) Blast 1: Reflected pressure, impulse, and displacement time histories.

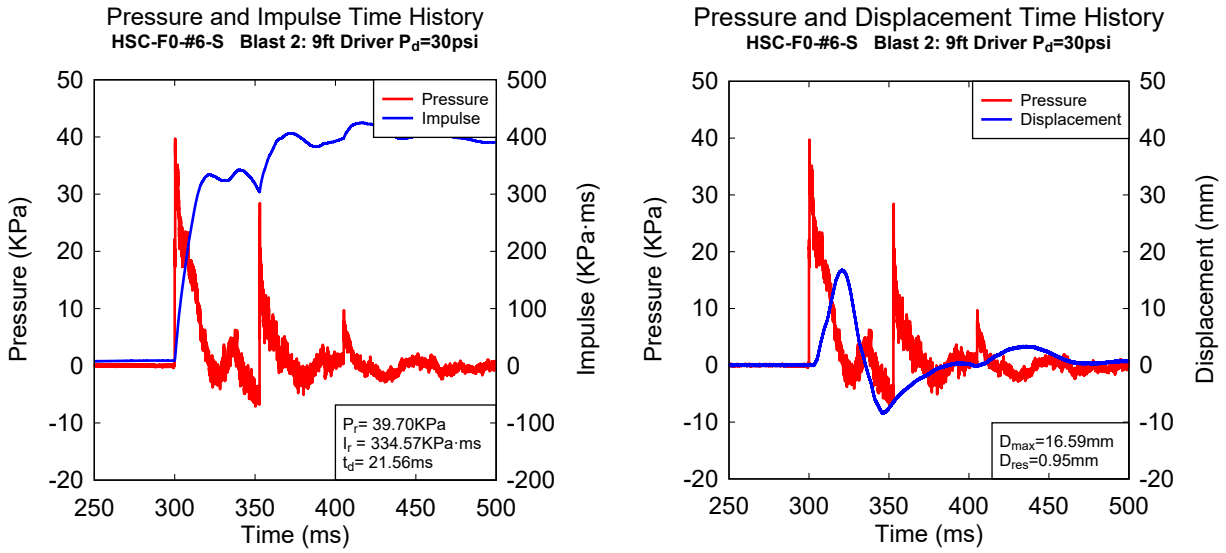

b) Blast 2: Reflected pressure, impulse, and displacement time histories.

Figure 5-13 HSC-F0-#6-S, recorded reflected pressure, impulse and displacement for Blasts 1 and 2

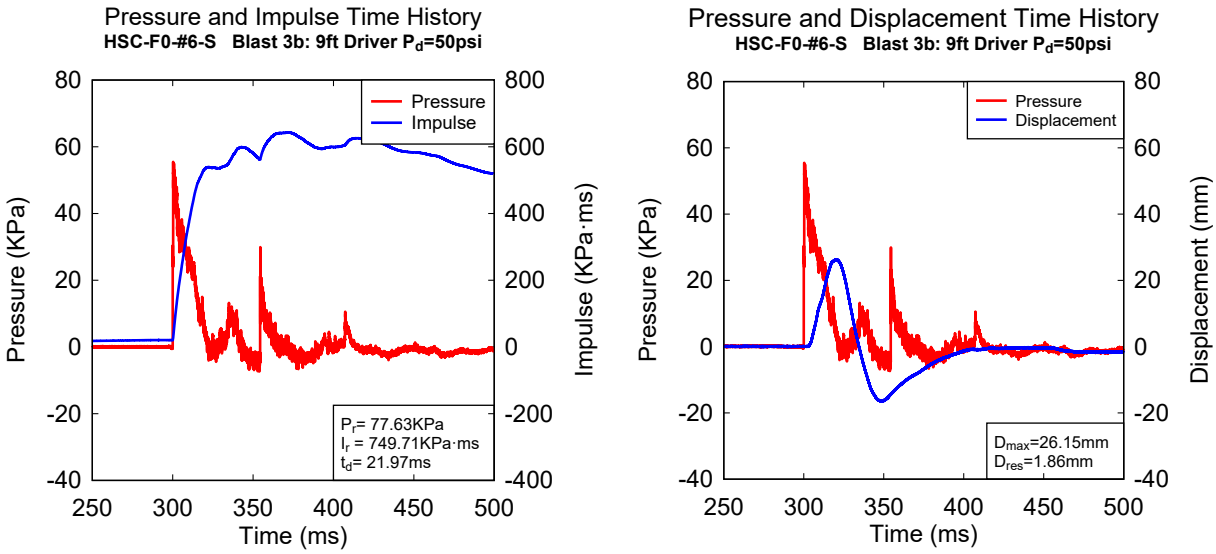

c) Blast 3b: Reflected pressure, impulse, and displacement time histories.

Figure 5-14 HSC-F0-#6-S, recorded reflected pressure, impulse and displacement for Blast 3b

a) Blast 1 (17 PSI) b) Blast 2 (30 PSI) c) Blast 3b (50 PSI) d) Blast 4 (70 PSI)

e) Mid-span cracking at Blast 2 f) Mid-span cracking at Blast 3b g) Mid-span crushing at Blast 4

Figure 5-15 HSC-F0-#6-S, photographs at the end of Blasts 1 - 4

5.8. PRESSURE, IMPULSE, AND DISPLACEMENT TIME HISTORIES & SELECTED PHOTOGRAPHS – HSFRC SERIES

5.8.1. HSC – F1 - #4 – S

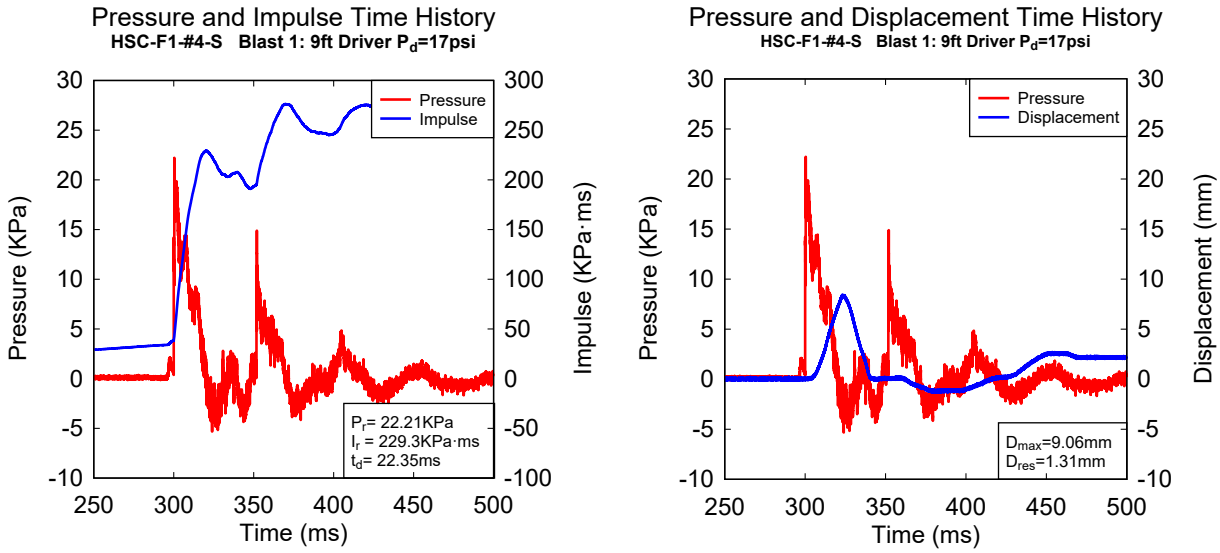

a) Blast 1: Reflected pressure, impulse, and displacement time histories.

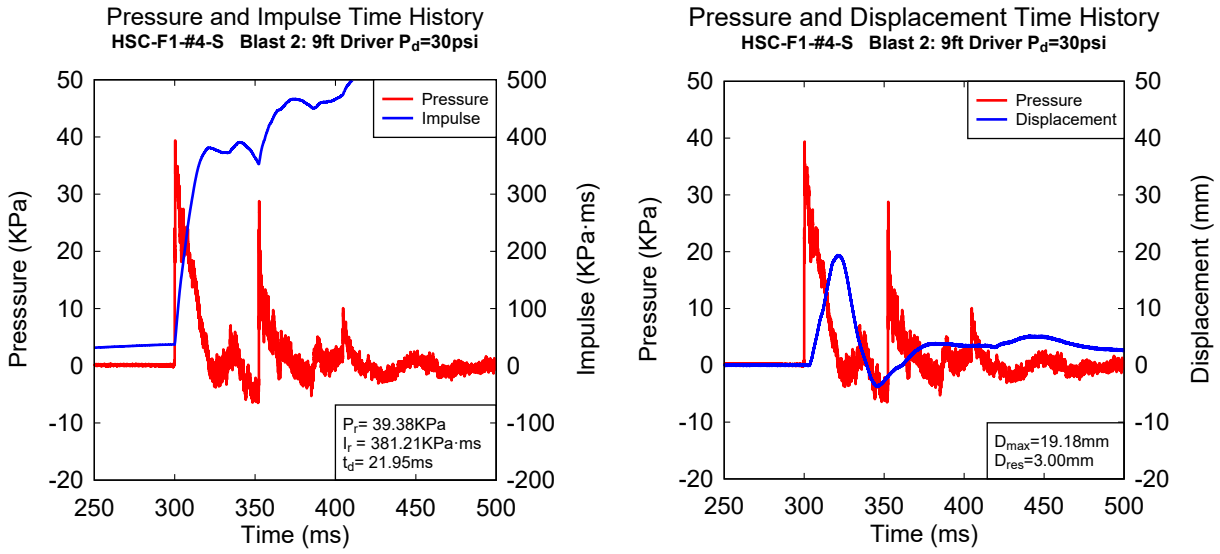

b) Blast 2: Reflected pressure, impulse, and displacement time histories.

Figure 5-16 HSC-F1-#4-S, recorded reflected pressure, impulse and displacement for Blasts 1 and 2

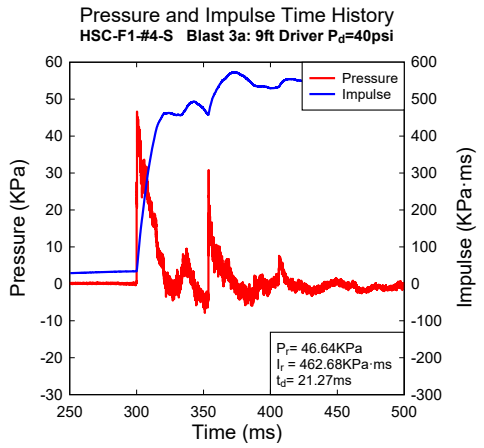

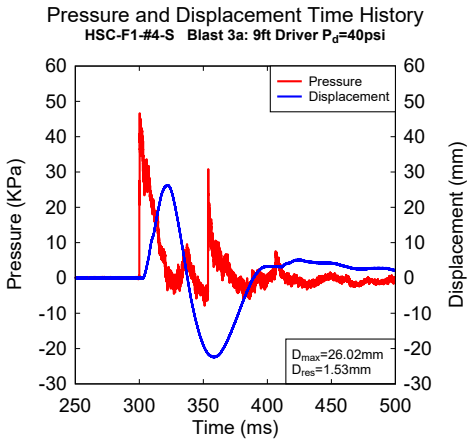

c) Blast 3a: Reflected pressure, impulse, and displacement time histories.

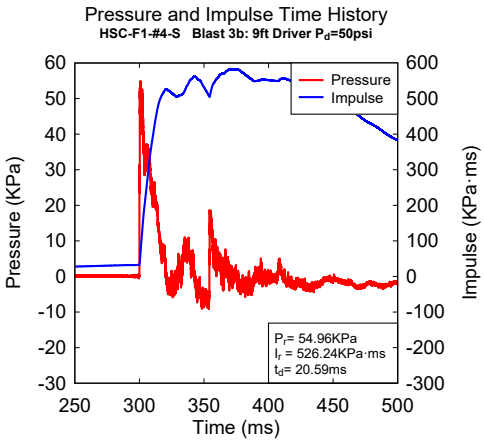

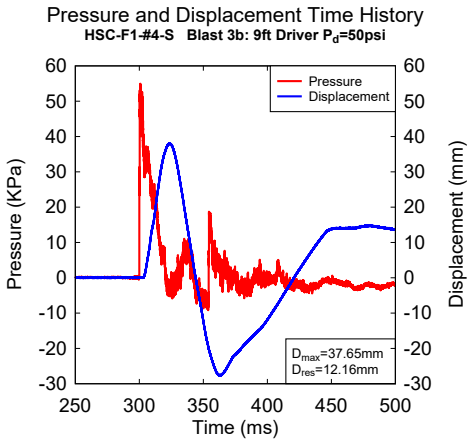

d) Blast 3b: Reflected pressure, impulse, and displacement time histories.

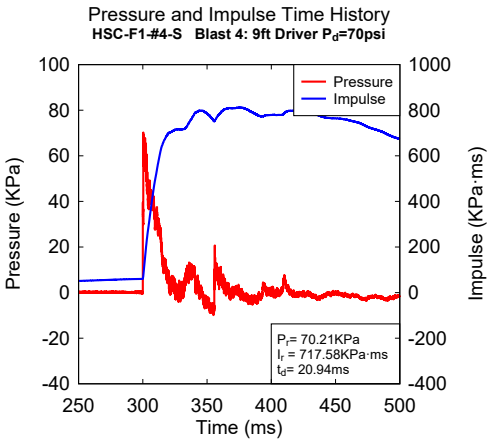

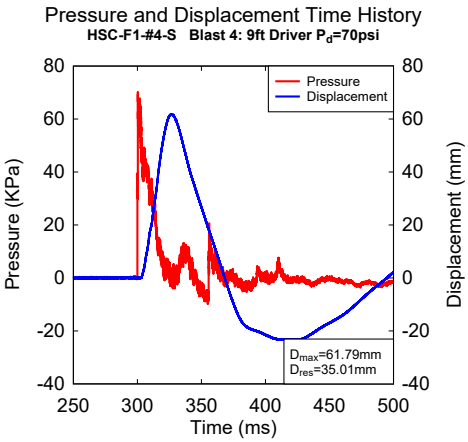

e) Blast 4: Reflected pressure, impulse, and displacement time histories.

Figure 5-17 HSC-F1-#4-S, recorded reflected pressure, impulse and displacement for Blasts 3a and 4

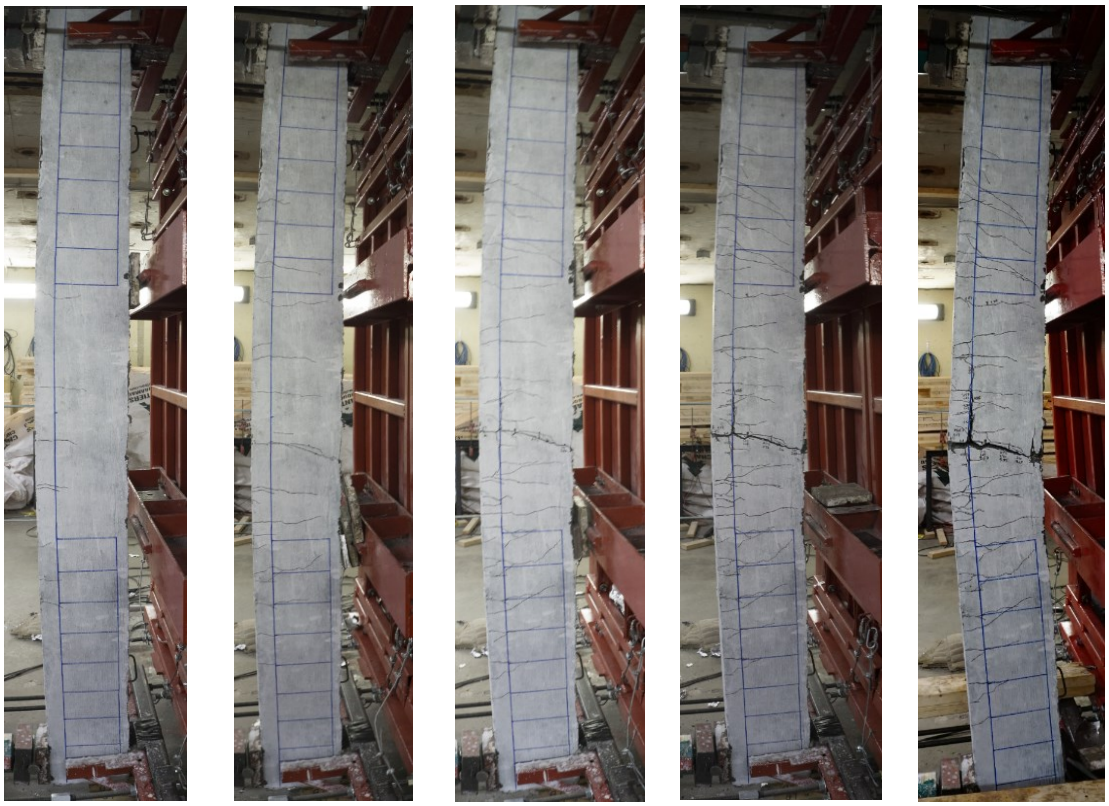

a) Blast 1 (17 PSI) b) Blast 2 (30 PSI) c) Blast 3a (40 PSI) d) Blast 3b (50 PSI) e) Blast 4 (70 PSI)

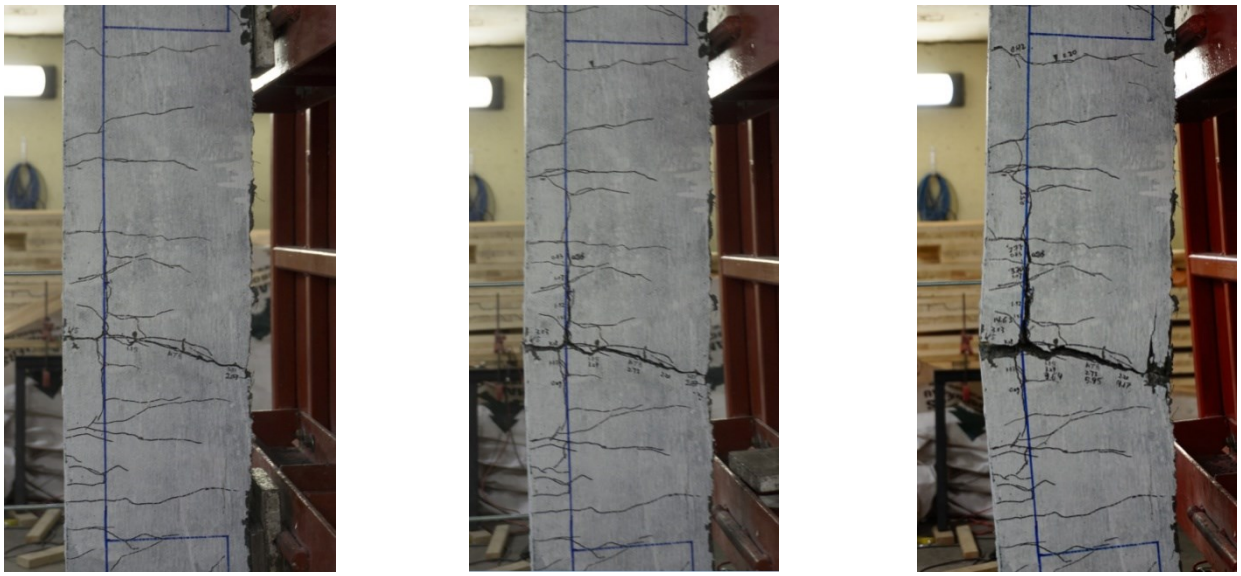

f) Mid-span cracking at Blast 3a g) Mid-span cracking at Blast 3b h) Mid-span crushing at blast 4

Figure 5-18 HSC-F1-#4-S, photographs at the end of Blasts 1 - 4

5.8.2. HSC – F1 - #5 – S

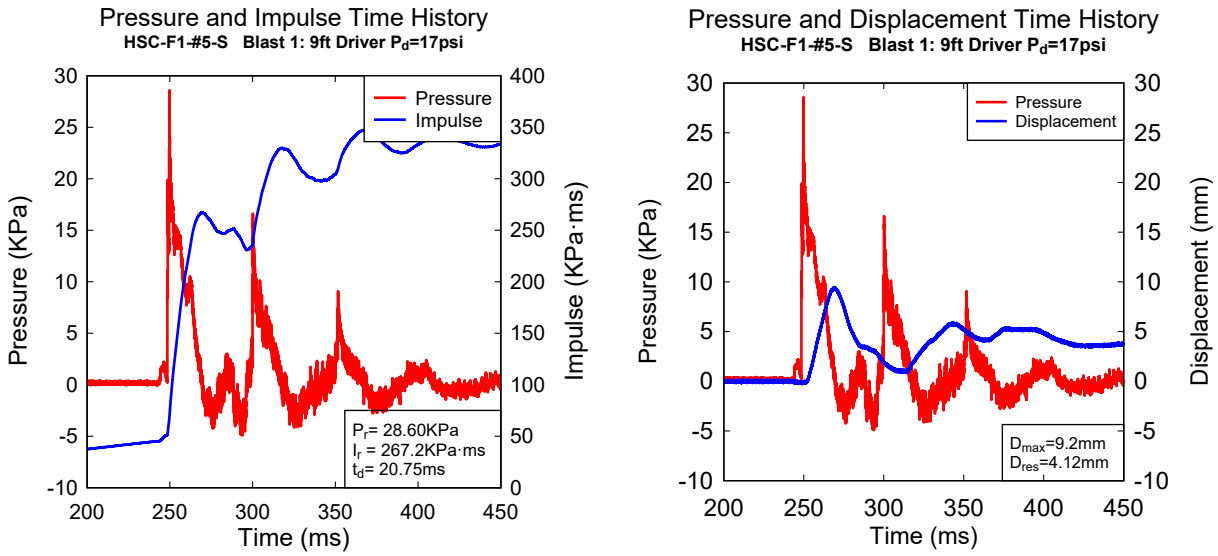

a) Blast 1: Reflected pressure, impulse, and displacement time histories.

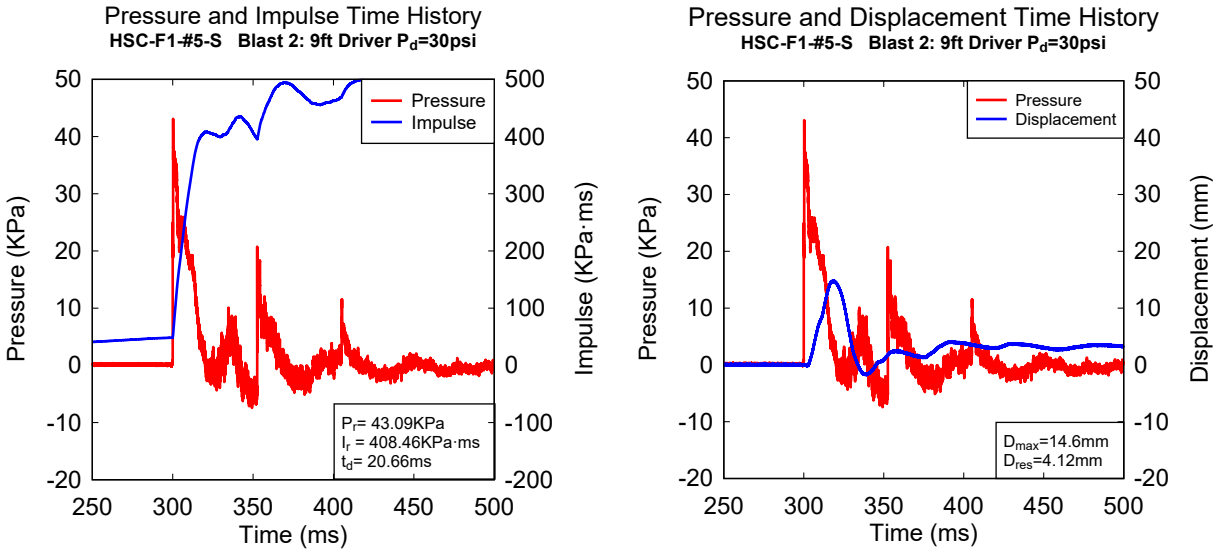

b) Blast 2: Reflected pressure, impulse, and displacement time histories.

Figure 5-19 HSC-F1-#5-S, recorded reflected pressure, impulse and displacement for Blasts 1 and 2

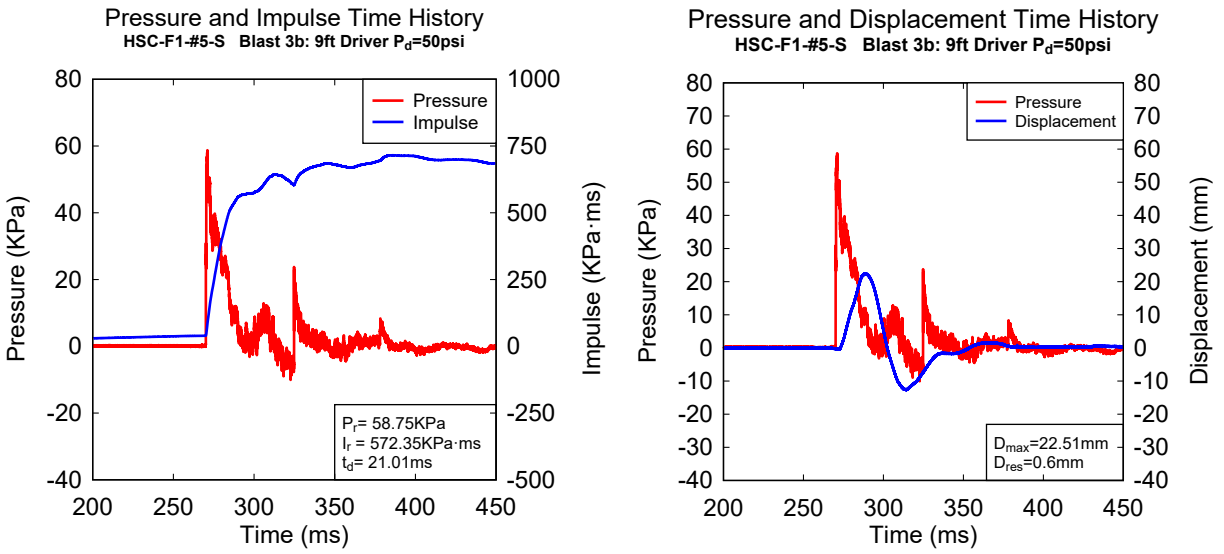

c) Blast 3b: Reflected pressure, impulse, and displacement time histories.

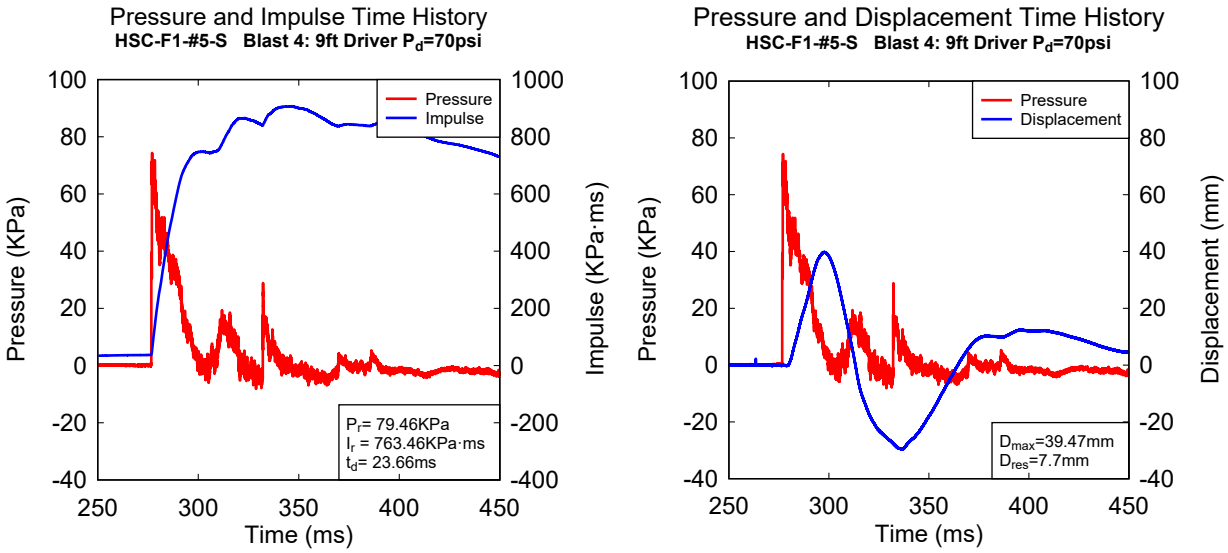

d) Blast 4: Reflected pressure, impulse, and displacement time histories.

Figure 5-20 HSC-F1-#5-S, recorded reflected pressure, impulse and displacement for Blasts 3b and 4

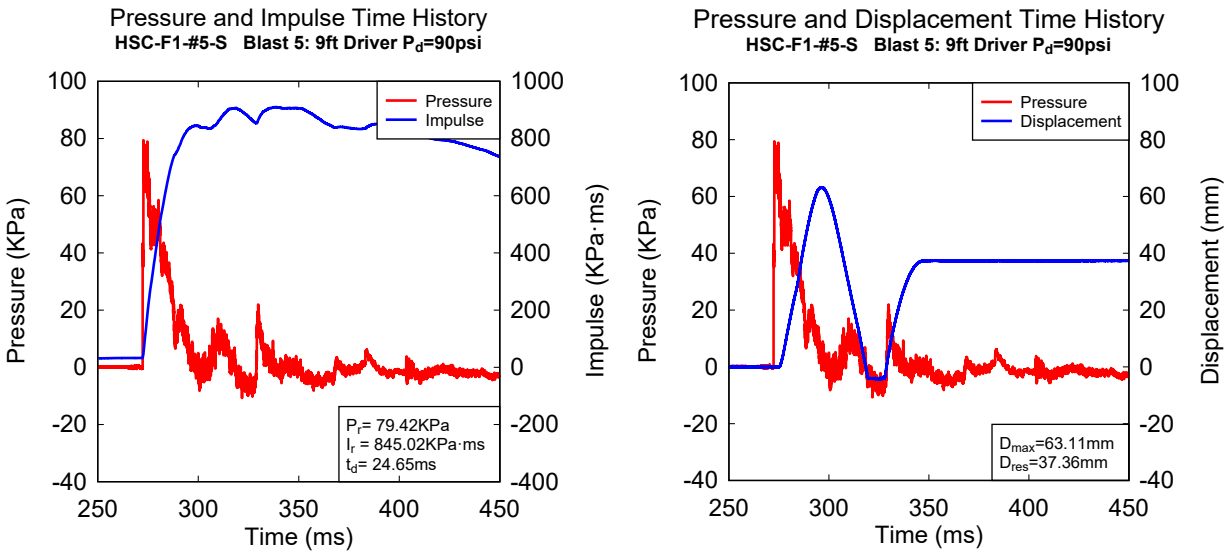

e) Blast 5: Reflected pressure, impulse, and displacement time histories.

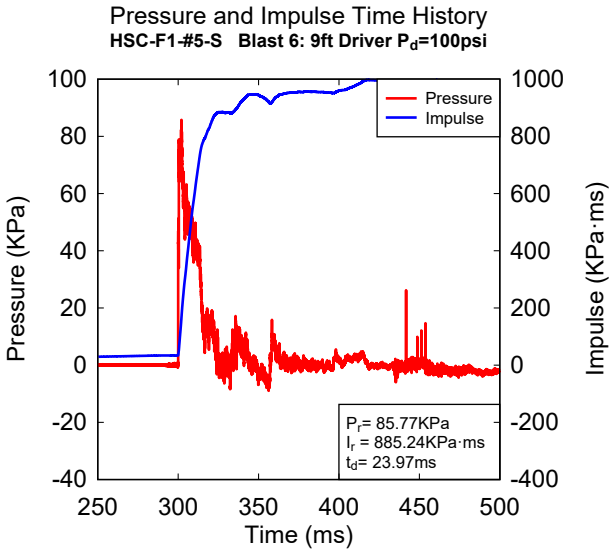

f) Blast 6: Reflected pressure, impulse, and displacement time histories.

Figure 5-21 HSC-F1-#5-S, recorded reflected pressure, impulse and displacement for Blasts 5 and 6

a) Blast 1 (17 PSI)

b) Blast 2 (30 PSI)

c) Blast 3b (50 PSI)

d) Blast 4 (70 PSI)

e) Blast 5 (90 PSI)

f) Blast 6 (100 PSI)

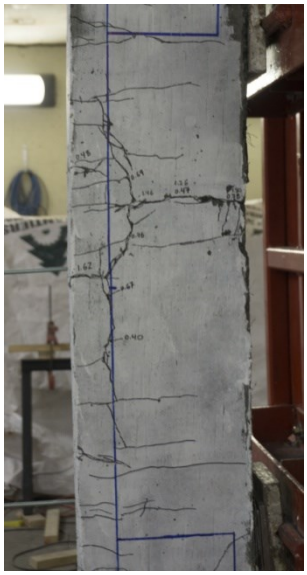

g) Mid-span cracking at Blast 4

h) Mid-span cracking at Blast 5

i) Tensile Reinforcement bar ruptured at blast 6

Figure 5-22 HSC-F1-#5-S, photographs at the end of Blasts 1 - 6

5.8.3. HSC – F1 - #6 – S

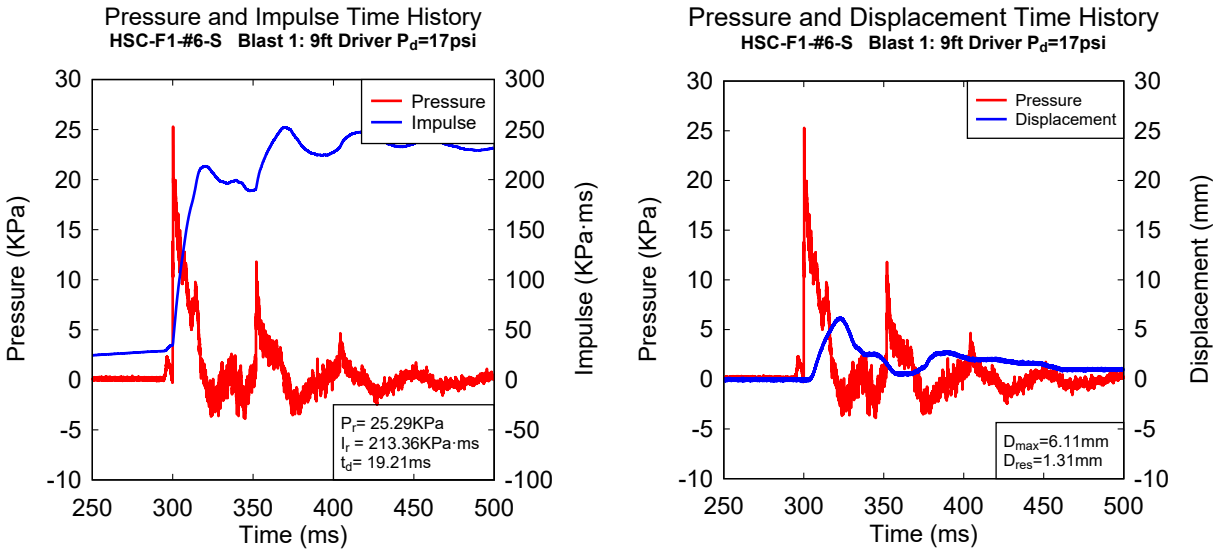

a) Blast 1: Reflected pressure, impulse, and displacement time histories.

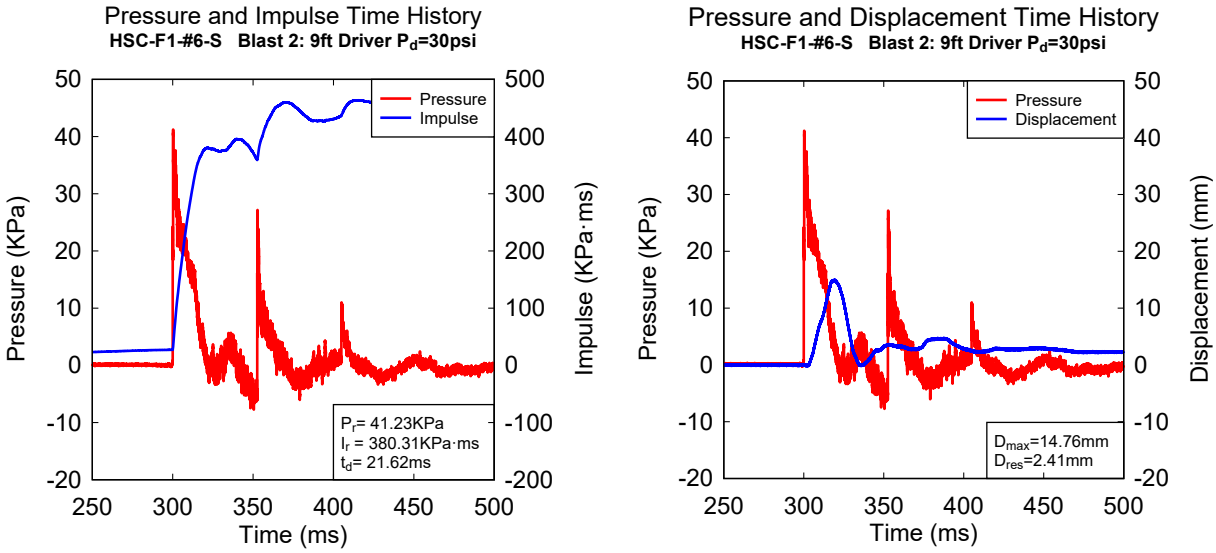

b) Blast 2: Reflected pressure, impulse, and displacement time histories.

Figure 5-23 HSC-F1-#6-S, recorded reflected pressure, impulse and displacement for Blasts 1 and 2

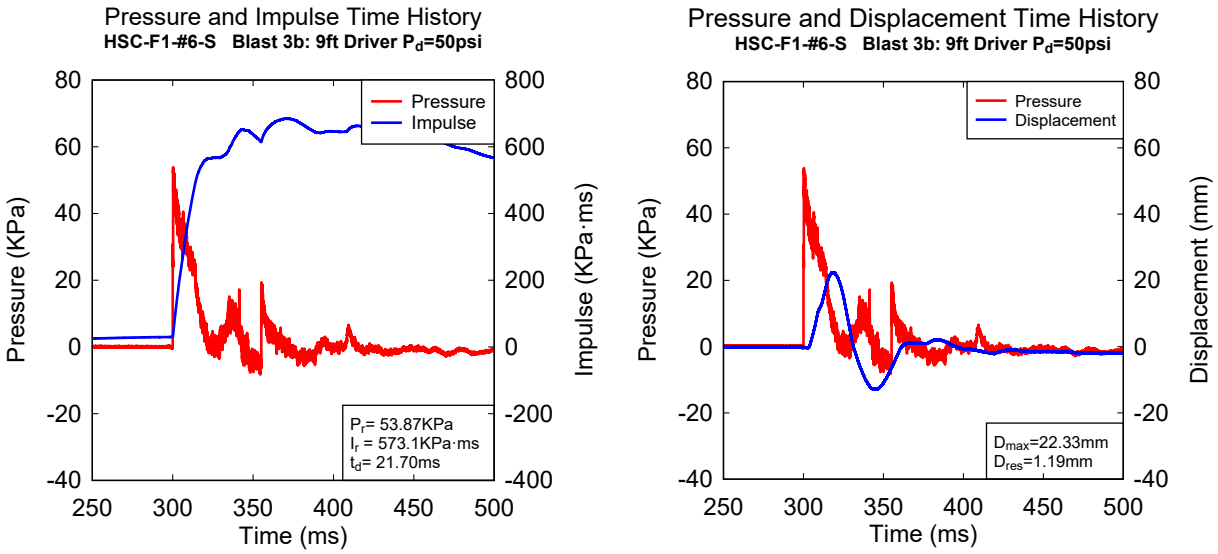

c) Blast 3b: Reflected pressure, impulse, and displacement time histories.

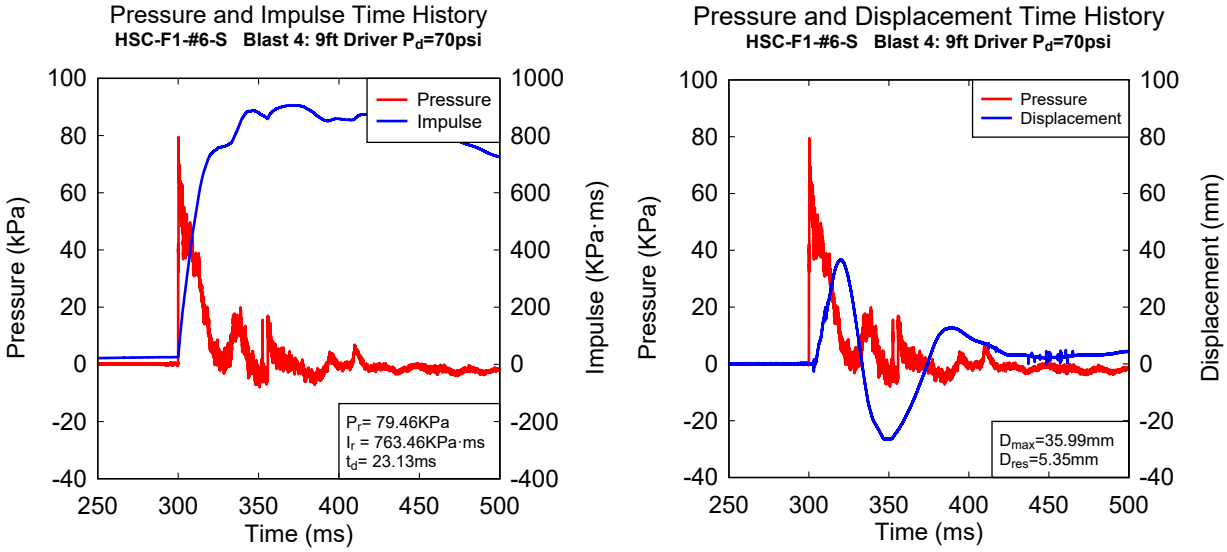

d) Blast 4: Reflected pressure, impulse, and displacement time histories.

Figure 5-24 HSC-F1-#6-S, recorded reflected pressure, impulse and displacement for Blast 3-4

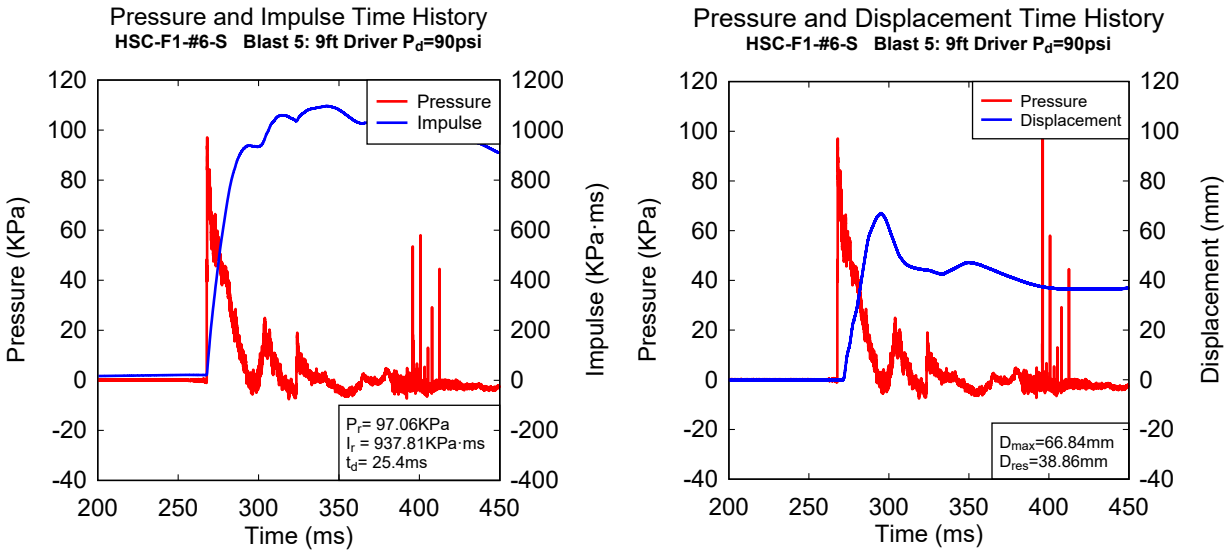

e) Blast 5: Reflected pressure, impulse, and displacement time histories.

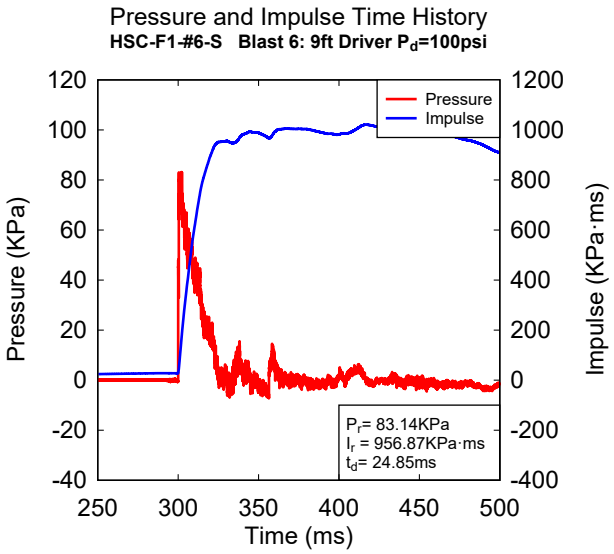

f) Blast 6: Reflected pressure, impulse, and displacement time histories.

Figure 5-25 HSC-F1-#6-S, recorded reflected pressure, impulse and displacement for Blasts 5 and 6

a) Blast 1 (17 PSI)

b) Blast 2 (30 PSI)

c) Blast 3b (50 PSI)

d) Blast 4 (70 PSI)

e) Blast 5 (90 PSI)

f) Blast 6 (100 PSI)

g) Mid-span cracking at Blast 4

h) Mid-span cracking at Blast 5

i) Mid-span crushing at blast 6

Figure 5-26 HSC-F1-#6-S, photographs at the end of Blasts 1 - 6

CHAPTER 6. DISCUSSION OF DYNAMIC TEST RESULTS

6.1. CHAPTER OVERVIEW

This chapter compares and discusses the experimental results from the blast tests. The effect of the various parameters on the response of the beams is investigated, including the effect of: high-strength steel longitudinal reinforcement ratio, steel fibres, concrete strength, and steel reinforcement type. The performance criteria include: maximum and residual displacements, failure mode, the magnitude of blast failure load, damage tolerance and secondary fragmentation. With regard to the effects of the steel reinforcement type, the performance of the beams with high-strength bars is compared to a companion set of beams reinforced with normal-strength bars tested by Al-gassem (2016). The chapter is divided into several sections, discussing the following effects:

The effects of the high-strength steel reinforcement ratio:

- in SCC beams
    - SCC-F0-#4-S vs. SCC-F0-#5-S
- in HSC beams
    - HSC-F0-#4-S vs. HSC-F0-#5-S vs. HSC-F0-#6-S
- in HSFRC beams
    - HSC-F1-#4-S vs. HSC-F1-#5-S vs. HSC-F1-#6-S

The effects of steel fibres:

- in HSC beams with No. 4 MMFX steel bars
    - HSC-F0-#4-S vs. HSC-F1-#4-S
- in HSC beams with No. 5 MMFX steel bars
    - HSC-F0-#5-S vs. HSC-F1-#5-S
- in HSC beams with No. 6 MMFX steel bars
    - HSC-F0-#6-S vs. HSC-F1-#6-S

The effects of concrete type:

- in beams with No. 4 MMFX steel bars
    - SCC-F0-#4-S vs. HSC-F0-#4-S
- in beams with No. 5 MMFX steel bars
    - SCC-F0-#5-S vs. HSC-F0-#5-S

The effects of steel reinforcement type:

- in SCC beams with No. 4 steel bars
    - SCC-F0-#4-S-400 vs. SCC-F0-#4-S
- in HSC beams with No. 4 steel bars
    - HSC-F0-#4-S-400 vs. HSC-F0-#4-S

- in HSC beams with No. 5 steel bars
    - HSC-F0-15M-S-400 vs. HSC-F0-#5-S
- in HSC beams with No. 6 steel bars
    - HSC-F0-20M-S-400 vs. HSC-F0-#6-S
- in HSC beams with No. 4 steel bars and fibres
    - HSC-F1-#4-0-400 vs. HSC-F1-#4-S
- in HSC beams with No. 5 steel bars and fibres
    - HSC-F1-15M-0-400 vs. HSC-F1-#5-S
- in HSC beams with No. 6 steel bars and fibre
    - HSC-F1-20M-S-400 vs. HSC-F1-#6-S

6.2. GENERAL OBSERVATIONS

The experimental results are summarized in this section. Plots showing the maximum and residual mid-span displacements for each beam at the different blast intensities are summarized in Figure 6-1 to Figure 6-6. The failure blasts are also noted in the diagrams. Failure was caused by either one or a combination of the following mechanisms: shear failure, spalling of tension concrete, crushing of compression concrete, concrete splitting with fibre pullout, or rupture of tension steel reinforcement. In general, most of the HSC beams failed in flexure, with severe concrete spalling or crushing. The exception was beam SCC-F0-#4-S which failed in shear. The HSFRC beams generally failed in flexure, with failure associated with concrete splitting and fibre pullout or blowout failures at extreme blast pressures. Beam HSC-F1-#5-S failed due to rupture of tension steel reinforcement.

Table 6-1 also summarizes the maximum principal crack width for the beams after each blast. In this table, “HL” means hairline cracks, “-” means no test run at this blast load, and “F” means failure after the test, thus no maximum and residual displacements were recorded.

A brief examination of the displacements data and failure blasts shows improvements in performance with the increase in longitudinal reinforcement ratio. Beams cast with steel fibres also showed enhanced performance, with an ability to resist higher blast loads, when compared to companions cast with plain concrete. In general HSC beams show improved performance when compared to companions cast with normal-strength SCC. Further details on the effects of the various test parameters are discussed in the sections that follow.

Table 6-1 Summary of principal crack widths

Specimen	Principle Crack Width (mm)						
	Blast 1 (17 PSI)	Blast 2 (30 PSI)	Blast 3a (40 PSI)	Blast 3b (50 PSI)	Blast 4 (70 PSI)	Blast 5 (90 PSI)	Blast 6 (100 PSI)
SCC-F0-#4-S	HL	HL	1.78	F	-	-	-
SCC-F0-#5-S	HL	HL	-	2.20	2.78	-	-
HSC-F0-#4-S	HL	2.31	6.50	F	-	-	-
HSC-F0-#5-S	HL	0.3	-	1.39	F	-	-
HSC-F0-#6-S	HL	0.61	-	1.37	F	-	-
HSC-F1-#4-S	HL	HL	2.07	5.02	16.60	-	-
HSC-F1-#5-S	HL	HL	-	0.78	2.67	9.94	F
HSC-F1-#6-S	HL	HL	-	1.08	1.92	4.67	F

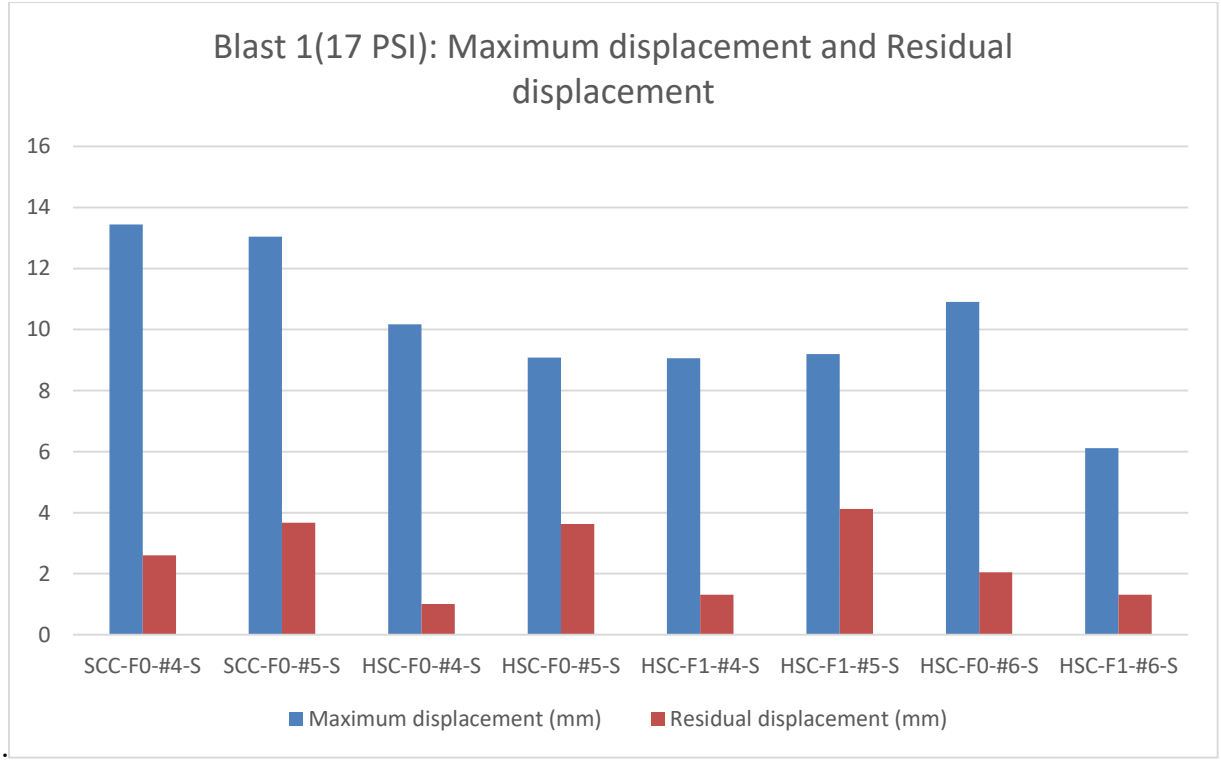

Figure 6-1 Maximum and residual displacements for Blast 1

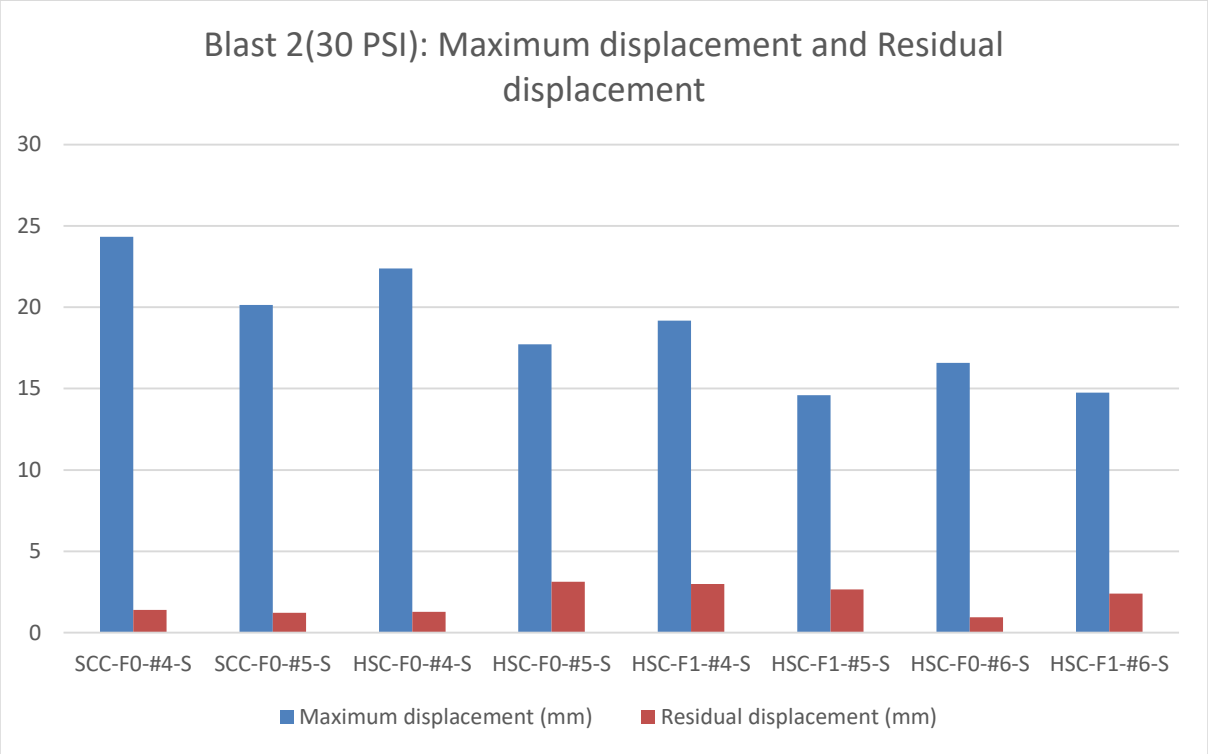

Figure 6-2 Maximum and residual displacements for Blast 2

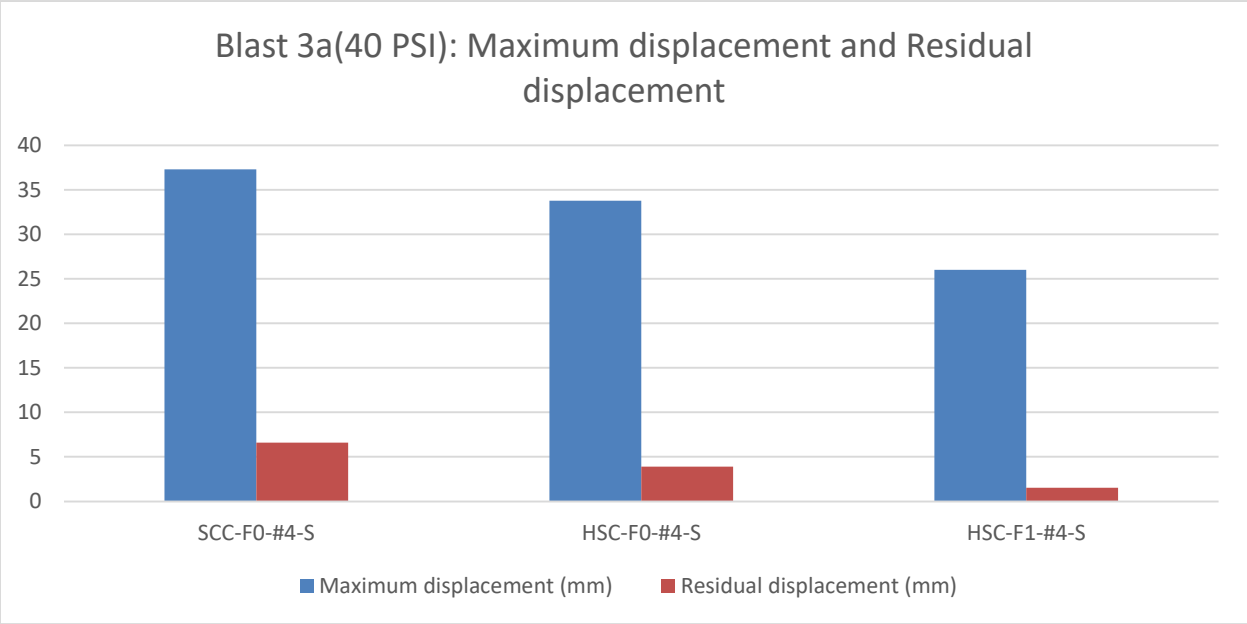

Figure 6-3 Maximum and residual displacement for Blast 3a

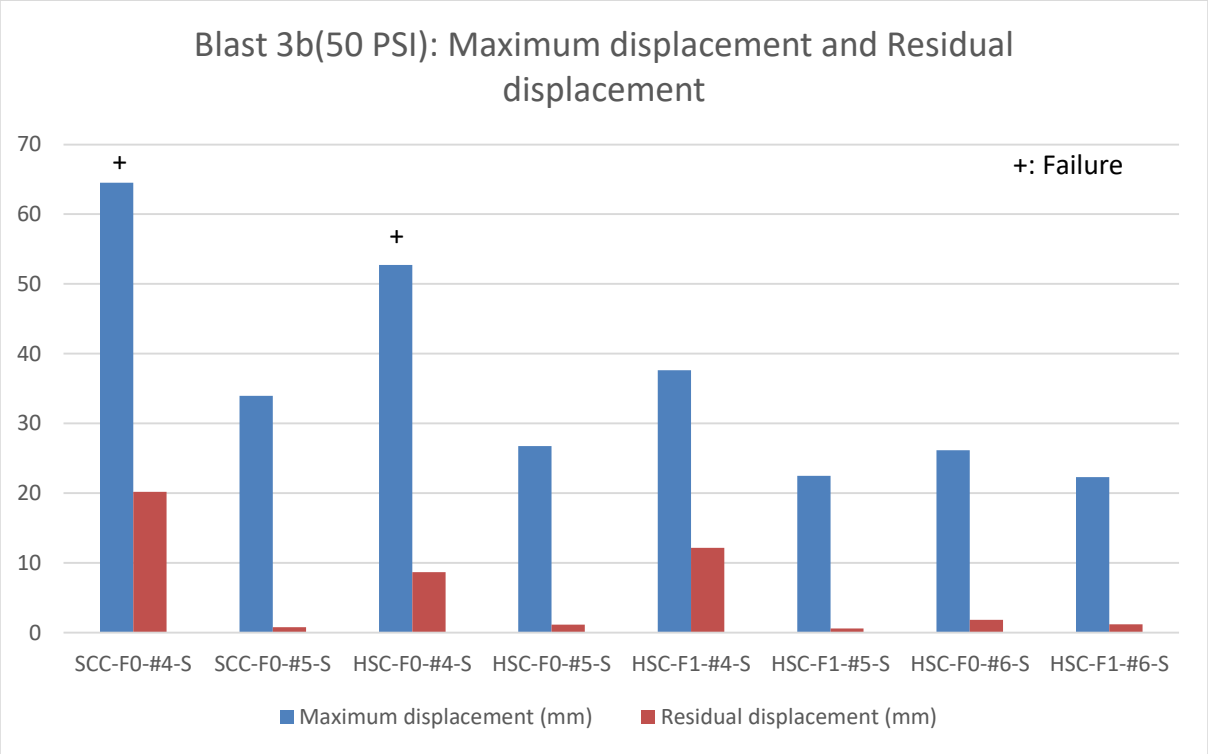

Figure 6-4 Maximum and residual displacements for Blast 3b

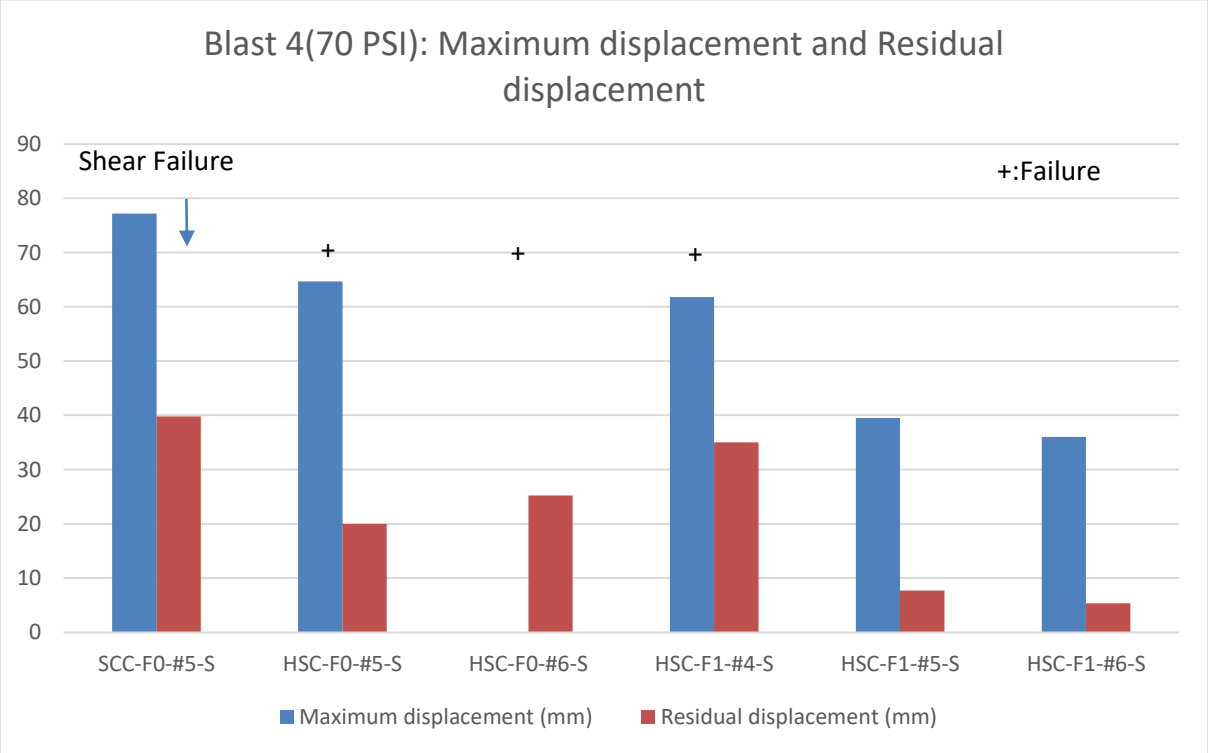

Figure 6-5 Maximum and residual displacements for Blast 4

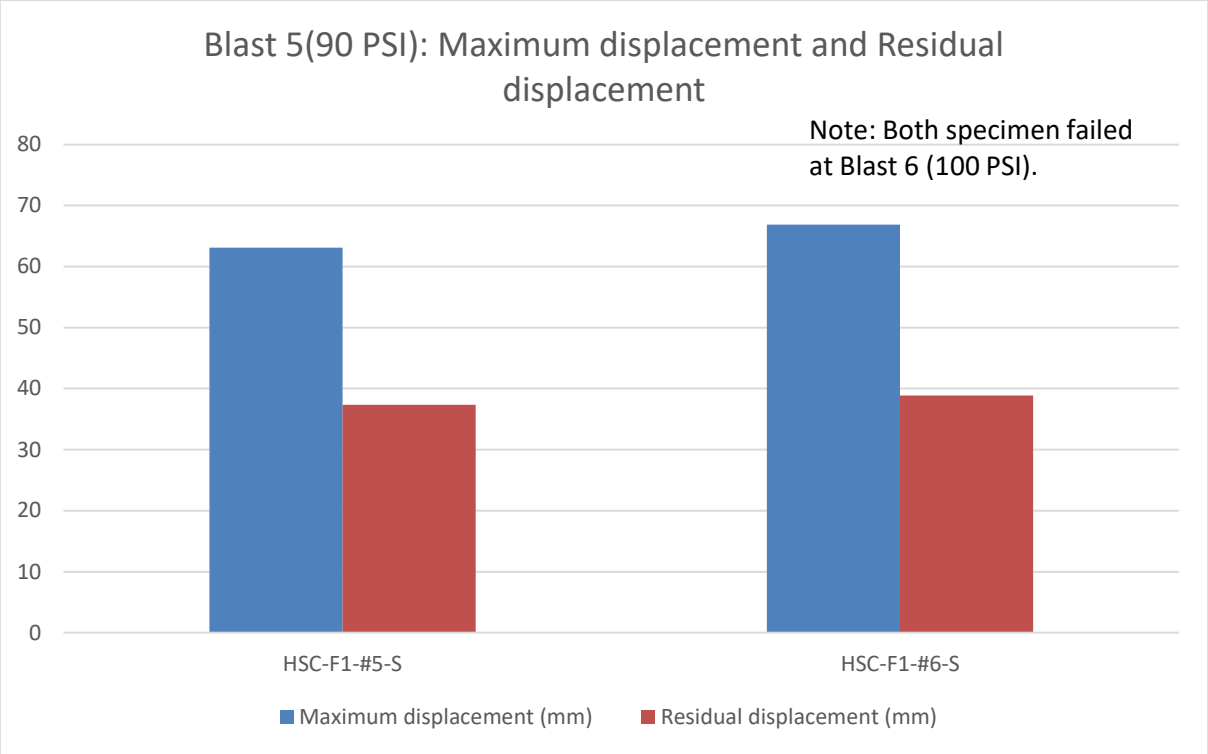

Figure 6-6 Maximum and residual displacements for Blast 5

6.3. EFFECTS OF THE STEEL REINFORCEMENT RATIO

The experimental results show significant improvement in the behaviour of the beams with the use of a higher steel reinforcement ratio. The effect of this parameter is investigated in three groups of specimens: SCC specimens reinforced with No. 4 and No. 5 bars, HSC specimens reinforced with No. 4, No. 5, and No. 6 bars and HSFRC specimens reinforced with No. 4, No. 5, and No. 6 bars. All beams contained high-strength steel reinforcement.

6.3.1. EFFECTS OF THE STEEL REINFORCEMENT RATIO: SCC SPECIMENS

The SCC-F0-#4-S and SCC-F0-#5-S specimens were both constructed with plain self-consolidating concrete and with high-strength ASTM A1035 MMFX longitudinal reinforcement. Beam SCC-F0-#4-S contained 2 - No. 4 bars and had a reinforcement ratio of 1%. In comparison Beam SCC-F0-#5-S contained 2 - No. 5 bars with a reinforcement ratio of 1.6%. Photographs showing the damage in the beams at failure are included in Figure 6-7. Comparative bar charts showing maximum/residual displacements and displacement-time history diagrams are shown in Figure 6-8 and Figure 6-9.

In comparing the mid-span displacements and residual displacements, there was no obvious difference between these two specimens after Blast 1. Blast 2 and Blast 3b were meant to test the beams within yield and post-yield ranges. Beam SCC-F0-#5-S, which had a higher reinforcement ratio showed maximum displacements δ_{max} = 20.13 mm and 33.97 mm at Blast 2 and Blast 3b, respectively, with residual displacements of δ_{res} = 1.22 mm and 0.78 mm, respectively. In comparison, maximum and residual displacements were higher for the SCC beam with No. 4 reinforcement, with δ_{max} = 24.32 mm and δ_{res} =1.4 mm at Blast 2, and δ_{max} = 64.52 mm and δ_{res} =20.2 mm under Blast 3b. Since the SCC-F0-#4-S beam failed at Blast 3b due to severe spalling of tension concrete at mid-span, no comparison was made for Blast 4.

The beam reinforced with No. 5 bars was able to resist one larger blast prior to failure when compared to the companion specimen with No.4 reinforcement. Although transverse reinforcement was provided, failure of the SCC-F0-#5-S beam at Blast 4 was brittle, with shear failure in the top shear span. The results indicate that an insufficient amount of transverse shear reinforcement was provided in this beam. The increased ratio of high-strength reinforcement resulted in increased shear demand, and therefore required a greater amount of shear reinforcement to prevent shear failure.

Examination of the high-speed video indicates that both the SCC-F0-#4-S and SCC-F0-#5-S specimens, showed high amount of secondary fragmentation during the failure blasts. It is also noted in Table 6-1 that there was no significant reduction of principal crack widths between the two beams during the tests. For example, the major crack width of 1.78 mm in the SCC-F0-#4-S beam after Blast 3a was close to the crack width of 2.20 mm in the SCC-F0-#4-S specimen after Blast 3b.

In summary, the increase in the high-strength reinforcement ratio in the normal-strength SCC beams resulted in reduced displacements at equivalent blasts, and an ability to resist greater impulsive loads before failure. However, the results also indicate the importance of providing sufficient shear reinforcement in beams containing high-strength bars. Because of the increased shear demand, the failure mode may be changed from flexure to shear when using large amounts of high-strength reinforcement, and therefore special attention should be paid to the detailing of the transverse reinforcement in such beams.

a) SCC-F0-#4-S (50 psi)

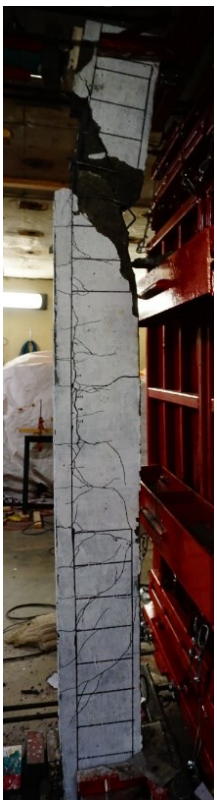

b) SCC-F0-#5-S (70 psi)

c) SCC-F0-#4-S

Mid-span spalling at Blast 3b (50 psi)

d) SCC-F0-#5-S

Top-span shear failure at Blast 4 (70 psi)

Figure 6-7 Photographs; effects of the steel reinforcement ratio on SCC specimens

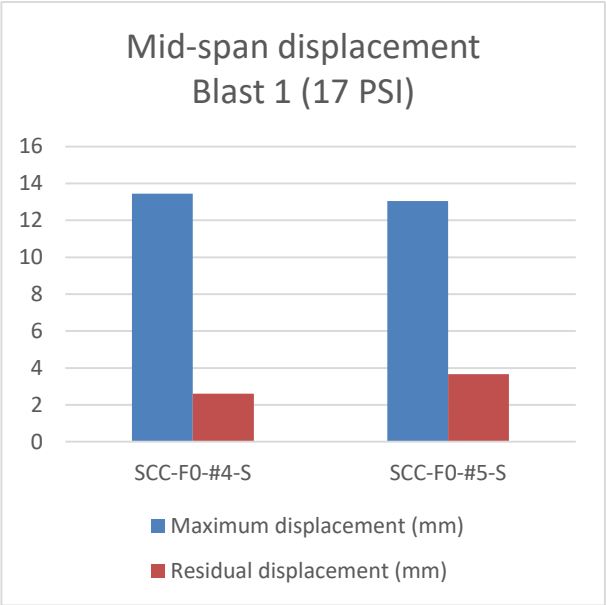

a) Blast 1

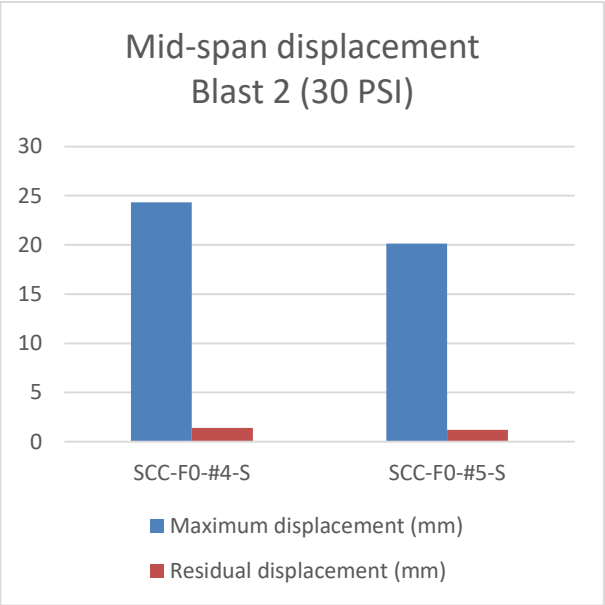

b) Blast 2

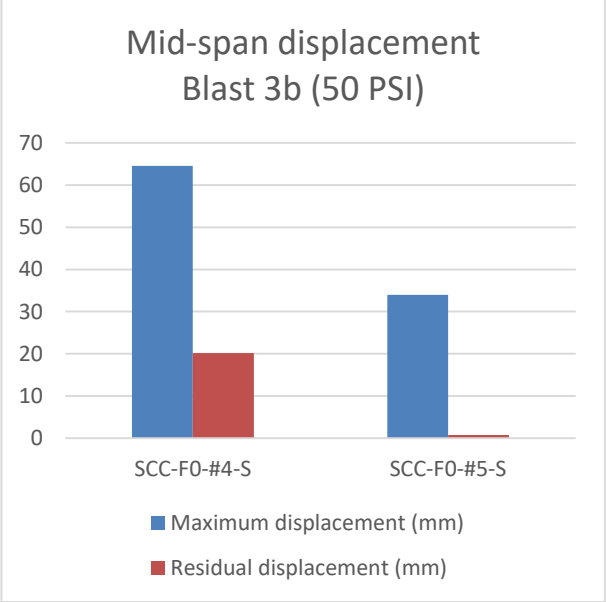

c) Blast 3b

Figure 6-8 Maximum and residual displacements; effects of the steel reinforcement ratio on SCC specimens

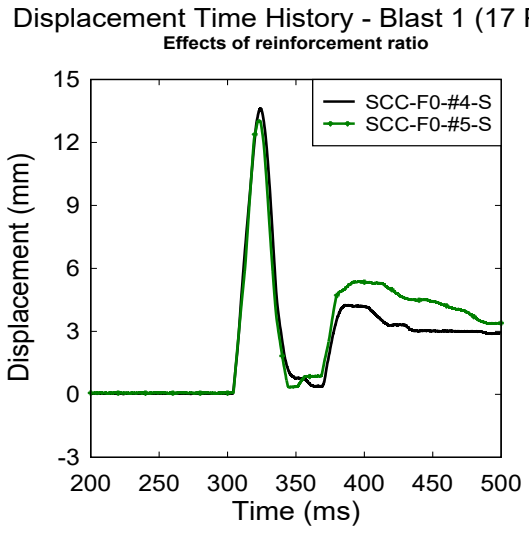

a) Blast 1

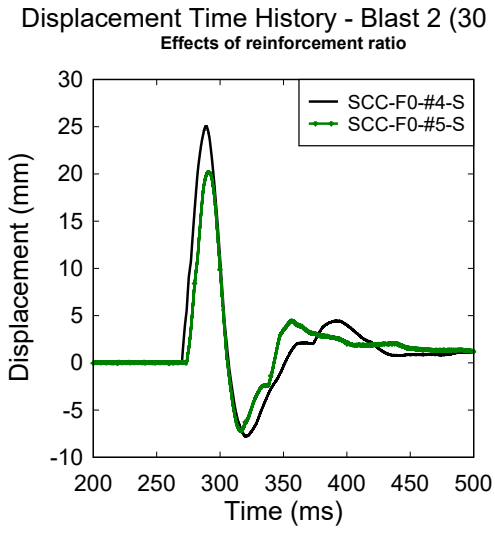

b) Blast 2

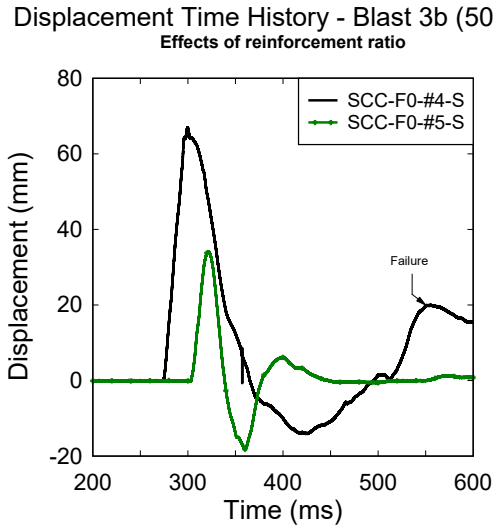

c) Blast 3b

Figure 6-9 Displacement time histories; effects of the steel reinforcement ratio on SCC specimens

6.3.2. EFFECTS OF THE STEEL REINFORCEMENT RATIO: HSC SPECIMENS

The response of specimens HSC-F0-#4-S, HSC-F0-#5-S, and HSC-F0-#6-S, are compared in this sub-section. These three beams were cast with plain high-strength concrete and reinforced with different amounts of ASTM A1035 high-strength steel reinforcement, with 2 - No. 4 (ρ = 1%), 2 - No. 5 (ρ = 1.6%), and 2 - No. 6 (ρ = 2.3%) bars, respectively. It is noted that the balanced reinforcement ratio for the HSC beam sections is estimated as being 1.7%, thus the HSC-F0-#6-S is over-reinforced. Photographs showing the beams at failure are included in Figure 6-10. Comparative bar charts showing maximum and residual displacements can be seen in Figure 6-11, and displacement-time history diagrams are shown in Figure 6-12.

The mid-span displacements for HSC-F0-#4-S, HSC-F0-#5-S, and HSC-F0-#6-S were similar after Blast 1. After Blast 2, the maximum displacements for the specimens with #5 and #6 bars were similar and recorded as 17.72 mm and 16.59 mm. These values are reduced from that of the No. 4 specimen (δ_{max} = 22.39 mm). The residual displacements for these three specimens at this blast were close (δ_{res} = 3.13 mm for No. 4, 0.95 mm for No. 5, and 1.28 mm for No. 6). The HSC-F0-#4-S specimen failed after Blast 3b; in comparison the HSC-F0-#5-S and HSC-F0-#6-S beams withstood the impulse of this blast load. As a result, the maximum displacements of No. 5 and No. 6 specimens (δ_{max} = 17.72 mm for No. 5, 16.59 mm for No. 6) were reduced by 49.2% and 50.4% respectively, when compared with the HSC-F0-#4-S specimen (δ_{max} = 22.39 mm). The specimens reinforced with #5 and #6 bars failed at Blast 4. Although no maximum displacement data was collected at this shot, the residual displacement of the No. 6 specimen (δ_{res} = 25.22 mm) was higher by 20.9% when compared to the No. 5 specimen (δ_{res} = 19.96 mm). The result is not unexpected since the No. 6 beam was over-reinforced.

In terms of crack control, the beams with larger amounts of reinforcement tended to show narrower crack widths at equivalent blasts. The crack widths of the HSC-F0-#5-S and HSC-F0-#6-S specimens (0.3 mm and 0.61 mm) decreased 87% and 73.6%, respectively, compared to the width of the HSC-F0-#4-S specimen (2.31 mm) at Blast 2. The No. 4 specimen failed after Blast 3b, therefore, no major crack was measured for this beam at this blast level. Major crack widths of specimens reinforced with No. 5 and No. 6 bars were similar at this blast (1.39 mm and 1.37 mm). In terms of failure mode, the HSC-F0-#4-S and HSC-F0-#5-S beams failed in flexure with crushing of concrete and severe spalling (and ejection) of concrete cover at failure. The failure mode of the HSC-F0-#6-S specimen was also in flexure, although chunk remained in place. Concrete crushing in the compression zone tended to be more severe as the reinforcement ratio increased. The high-speed video shows significant formation of secondary fragments for all specimens at the failure blasts.

In summary the results indicate improvements in HSC beam performance as the ratio of high-strength steel reinforcement was increased. The performance improvements included better control of maximum displacements and an ability to sustain greater blast pressures before failure. The No. 5 and No. 6 specimens performed better than the specimen with No. 4 bars; however both specimens showed similar behaviour with no improvement when increasing the bar size from No.

5 to No. 6. As noted previously the specimen with No. 6 bars can be considered to be over-reinforced (also confirmed in the static testing). The result points to the importance of properly designing HSC beams containing high-strength reinforcement in order to prevent over-reinforced behaviour.

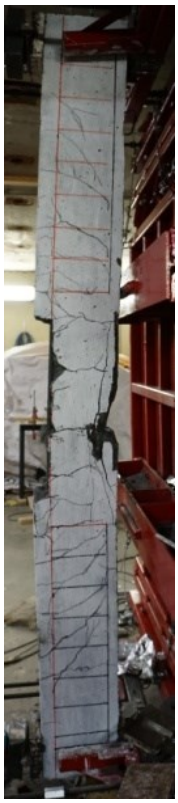

a) HSC-F0-#4-S (50 psi)

b) HSC-F0-#5-S (70 psi)

c) HSC-F0-#6-S (70 psi)

d) HSC-F0-#4-S

Mid-span spalling at Blast 3b (50 psi)

e) HSC-F0-#5-S

Mid-span spalling at Blast 4 (70 psi)

f) HSC-F0-#6-S

Mid-span crushing at Blast 4 (70 psi)

Figure 6-10 Photographs; effects of the steel reinforcement ratio on HSC specimens

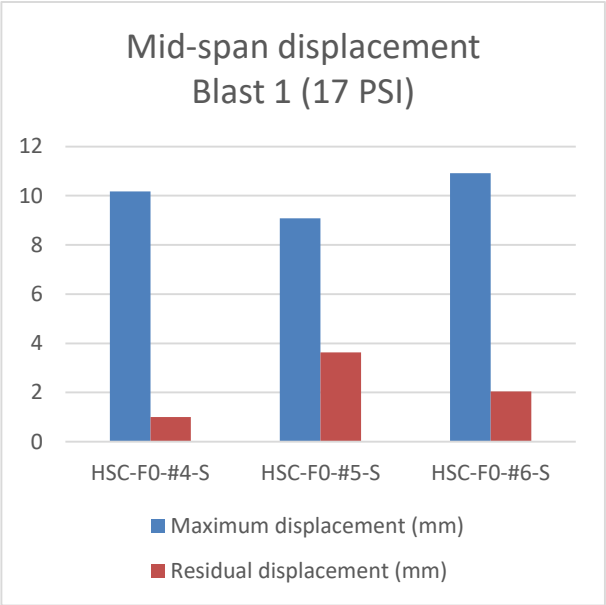

a) Blast 1

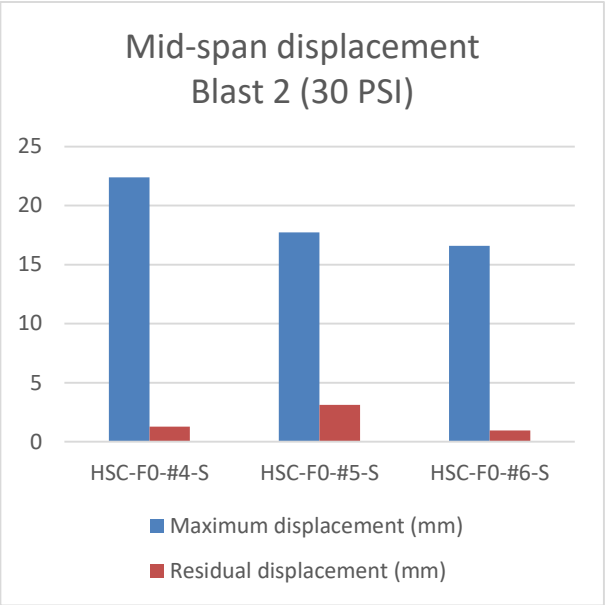

b) Blast 2

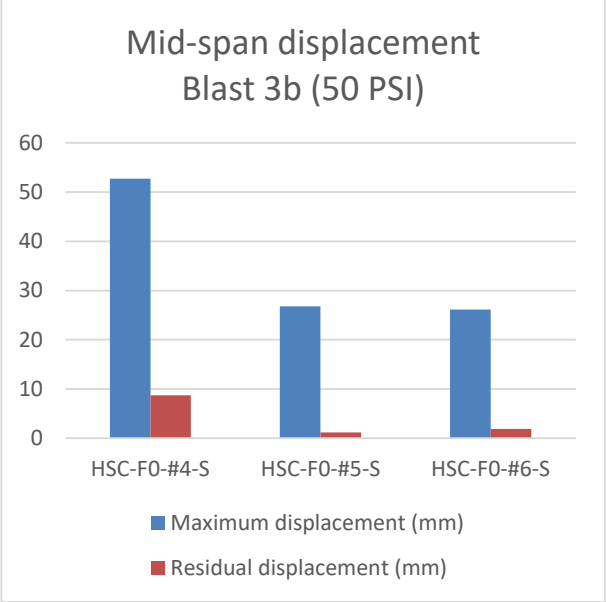

c) Blast 3b

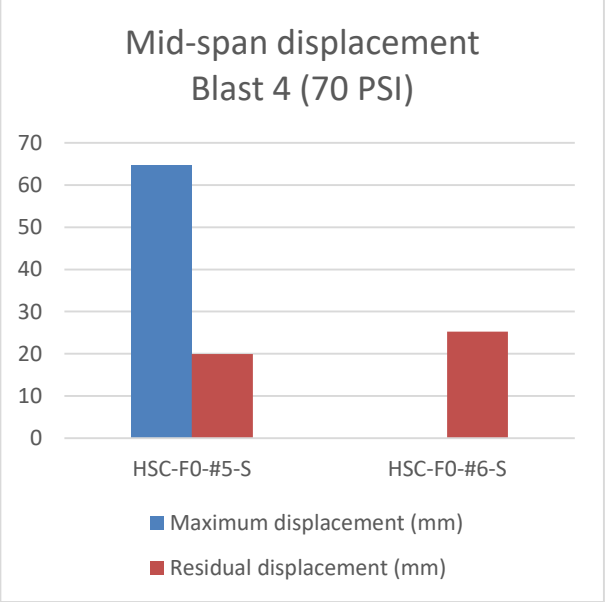

d) Blast 4

Figure 6-11 Maximum and residual displacements; effects of the steel reinforcement ratio on HSC specimens

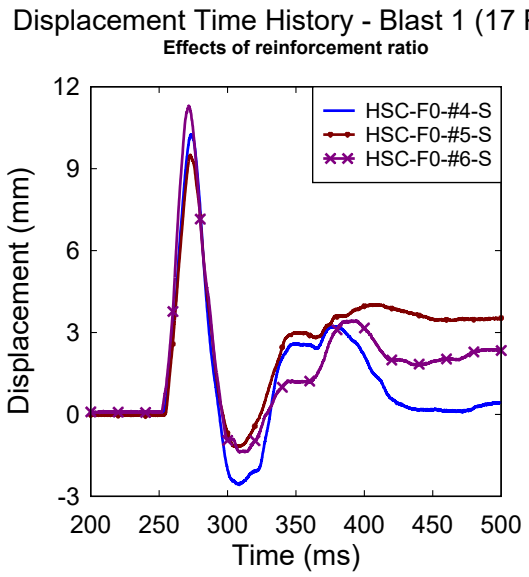

a) Blast 1

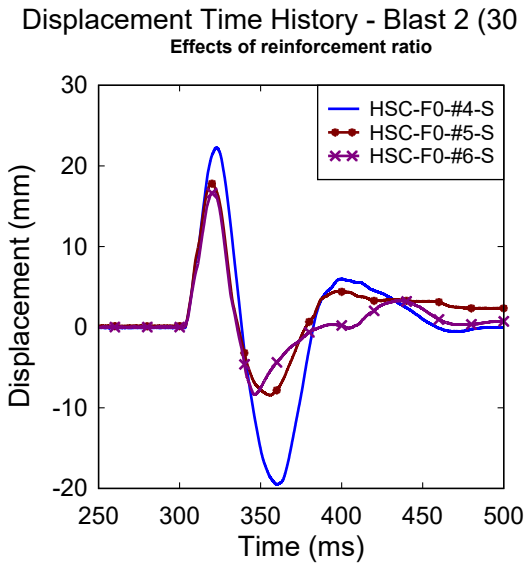

b) Blast 2

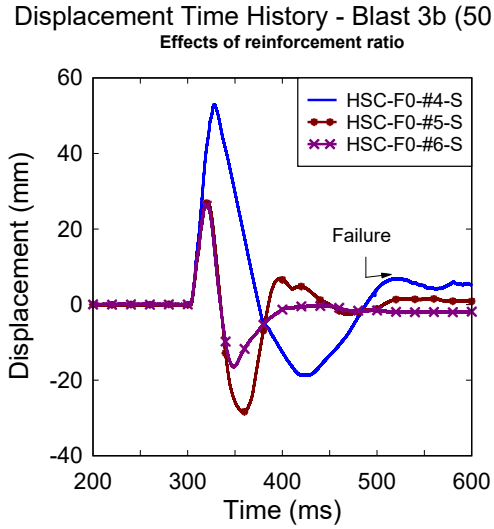

c) Blast 3b

Figure 6-12 Displacement time histories; effects of the steel reinforcement ratio in HSC specimens

6.3.3. EFFECTS OF THE STEEL REINFORCEMENT RATIO: HSFRC SPECIMENS

The HSC-F1-#4-S, HSC-F1-#5-S, and HSC-F1-#6-S specimens were designed to examine the effects of different high-strength steel reinforcement ratios on the performance of the HSFRC beams. These three beams were constructed with high-strength concrete containing 1% steel fibres and were reinforced with No. 4, No. 5, and No. 6. ASTM A1035 MMFX bars (ρ = 1%, 1.6% and 2.3%). Relevant photographs of the beams at failure are included in Figure 6-13. Comparative displacement bar charts and displacement-time history diagrams can be seen in Figure 6-14 and Figure 6-15.

In comparing the HSC-F1-#4-S and HSC-F1-#5-S specimens, significant improvements were seen in different aspects; the specimen reinforced with No. 5 bars had the capacity to resist higher blast loads, to reduce maximum and residual displacements and to better control crack widths. Since the two specimens were in the elastic range for Blast 1, the displacements were close. From Blast 2 to Blast 4, the maximum and residual displacements of the No. 4 reinforced specimen (δ_{max} = 19.18 mm, 37.65 mm, 61.79 mm; δ_{res} = 3.5 mm, 12.16 mm, 35.01 mm for Blast 2 to 4) were greater than those in the No. 5 reinforced specimen (δ_{max} = 14.6 mm, 22.51 mm, 39.47 mm; δ_{res} = 2.66 mm, 0.6 mm, 7.7 mm for Blast 2 to 4). The maximum displacements of the No. 5 reinforced specimen were lower by 23.9%, 40.2%, and 36.1% and the residual displacements were reduced by 11.3%, 95.1% and 78% for Blast 2, Blast 3b and Blast 4, respectively. In comparing the mid-span displacements and residual displacements of HSC-F1-#5-S and HSC-F1-#6-S (δ_{max} = 14.76 mm, 22.33 mm, 35.99 mm; δ_{res} = 2.41 mm, 1.19 mm, 5.35 mm for Blast 2 to 4) from Blast 1 to Blast 5, the differences between these two specimens are in the 5% range at most shots. Thus, the displacement control for both specimens was similar.

The use of larger reinforcement ratio also had an effect of reducing crack widths at equivalent blasts. No major cracks were observed after Blast 1 or Blast 2 for any of the specimens due to the presence of fibres. The major crack widths in the HSC-F1-#5-S and HSC-F1-#6-S specimens were reduced by 84.5% and 78.5% (0.78 mm and 1.08 mm) for Blast 3b and 84.9% and 88.4% (2.67 mm and 1.92 mm) for Blast 4 when compared to the crack widths in the HSC-F1-#4-S beam (5.02 mm for Blast 3b and 16.60 mm for Blast 4). At Blast 5, the maximum crack width measured 9.94 mm compared to 4.67 mm for the No. 5 and No. 6 beams, respectively. It can be concluded that the use higher reinforcement ratio improved crack width control in the HSFRC series.

The variation in reinforcement ratio in the HSFRC specimens also had an effect on failure mode. The HSC-F1-#4-S beam failed at Blast 4 due to concrete splitting in the tension zone with fibre pullout at the major crack location. The HSC-F1-#5-S beam failed at Blast 6 due to the rupture of tensile reinforcing bars at extreme blast pressures. The use of larger bars prevented rupture of the reinforcement in the HSC-F1-#6-S specimen, however the extreme loading combined with the over-reinforcement resulted in disintegration of compression concrete and blow-out failure at Blast 6. Secondary concrete fragments for the beams reinforced with steel fibres was minimal and in the form of fine powder, even at failure.

In general, the results show improved HSFRC beam performance under blast loading as the reinforcement ratio is increased. The combined use of steel fibres and high-strength steel reinforcement allowed the beams to withstand very high blast pressures before failure.

a) HSC-F1-#4-S (70 psi)

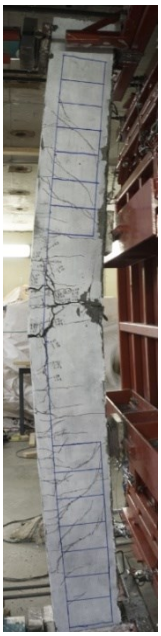

b) HSC-F1-#5-S (90 psi)

c) HSC-F1-#6-S (90 psi)

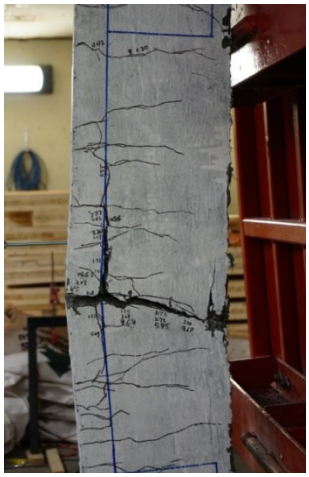

d) HSC-F1-#4-S

Mid-span fibre pull out at Blast 4 (70 psi)

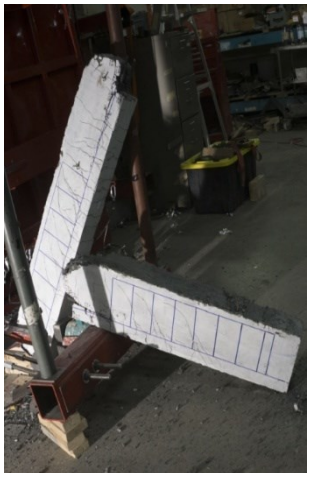

e) HSC-F1-#5-S

Steel bar rupture at Blast 6 (100 psi)

f) HSC-F1-#6-S

Failure with ejection of beam at Blast 6 (100 psi)

Figure 6-13 Photographs; effects of the steel reinforcement ratio on HSC specimens with fibres

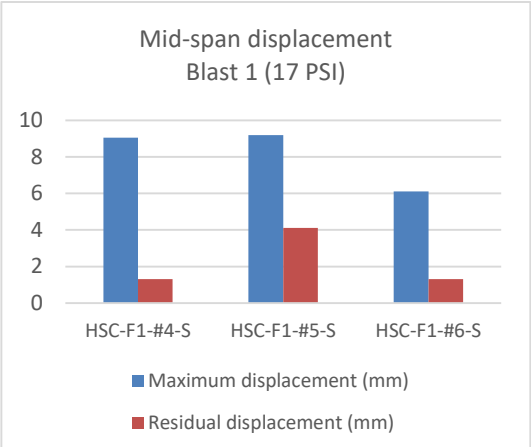

a) Blast 1

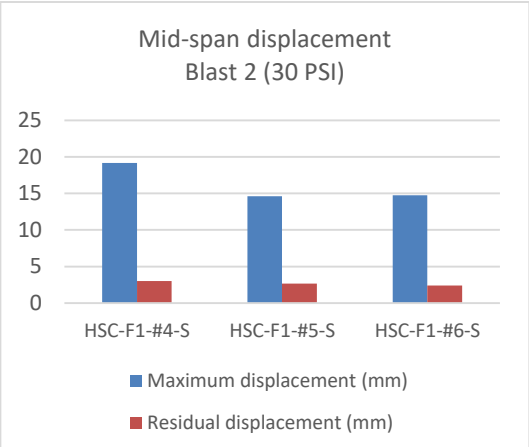

b) Blast 2

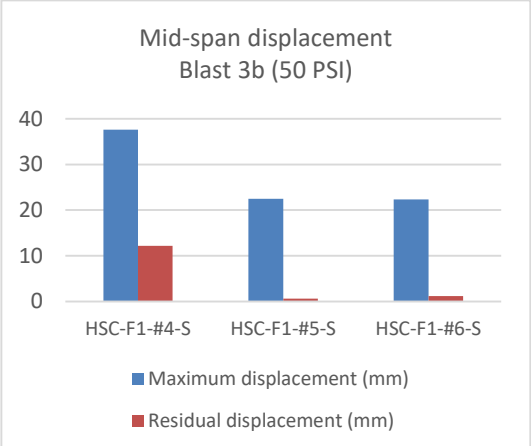

c) Blast 3b

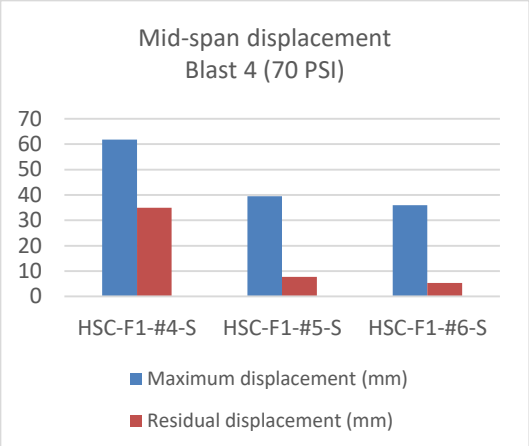

d) Blast 4

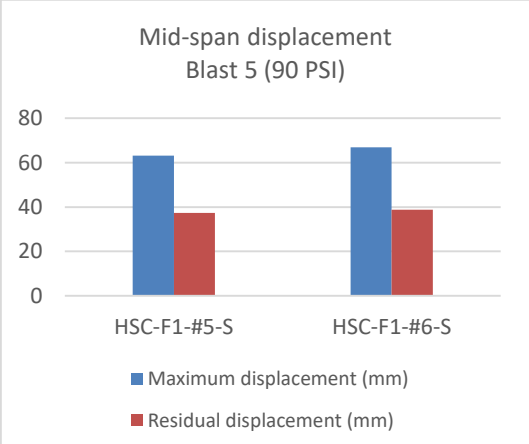

e) Blast 5

Figure 6-14 Maximum and residual displacements; effects of the steel reinforcement ratio on HSC specimens with fibres

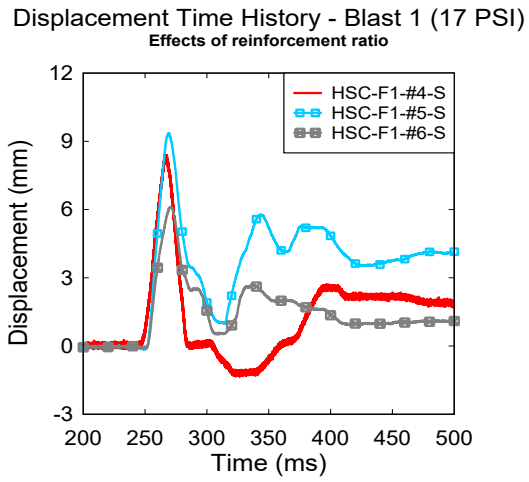

a) Blast 1

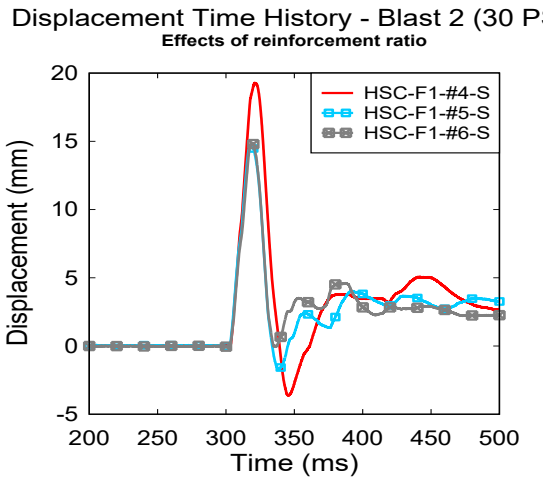

b) Blast 2

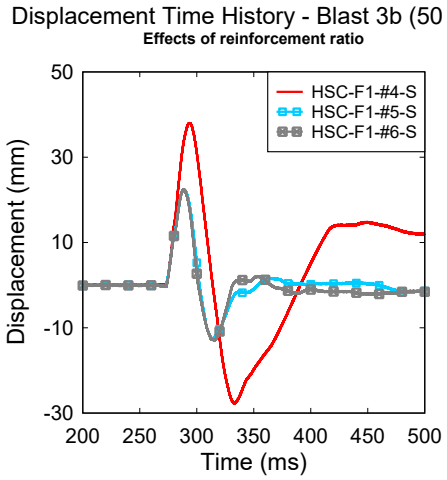

c) Blast 3b

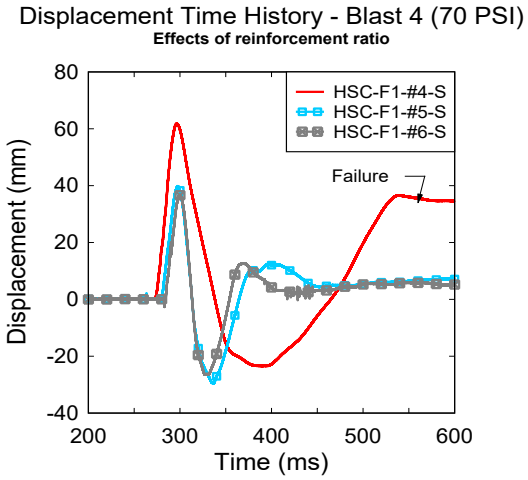

d) Blast 4

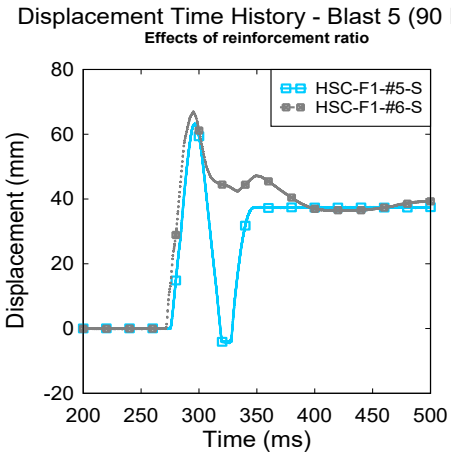

e) Blast 5

Figure 6-15 Displacement time histories; effects of the steel reinforcement ratio on HSC specimens with fibres

6.4. EFFECTS OF STEEL FIBRE REINFORCEMENT

The results from this research program indicate that the provision of steel fibres in high-strength concrete beams allows for significant improvements in blast performance such as an ability to resist higher magnitude blast loads, an ability to better control maximum and residual displacements, and improved damage tolerance and control of cracking. In this section, the effect of fibres is examined by comparing three groups of companion specimens constructed with HSC, with and without steel fibres.

6.4.1. EFFECTS OF STEEL FIBRES – HSC beams with NO. 4 MMFX STEEL BARS

The performance of specimens HSC-F0-#4-S and HSC-F1-#4-S are discussed in this sub-section. The specimens were both constructed with high-strength concrete and No. 4 MMFX bars, but one beam was reinforced with 1% of steel fibres, while the other did not contain fibres. Photographs of the specimens at failure are included in Figure 6-16. Comparative displacement bar charts and displacement-time history diagrams can be seen in Figure 6-17 and Figure 6-18.

In comparing the maximum mid-span displacements, the HSC-F1-#4-S specimen which contained fibres performed better, both in terms of control of displacements and overall blast resistance. The improvement in displacement control was present at all blast intensities. For Blasts 1, 2, 3a and 3b, this specimen showed reduced maximum displacements by margins of 10.9%, 14.3%, 23.0% and 28.6%, when compared to the HSC-F0-#4-S specimen, which contained no fibres (Blast 1: δ_{max} = 9.06 mm vs. 10.17 mm, Blast 2: 19.18 mm vs. 22.39 mm, Blast 3a: 26.02 mm vs. 33.78 mm, and Blast 3b: 37.65 mm vs. and 52.74 mm). In terms of residual displacements, the HSC-F1-#4-S specimen showed similar displacement results when compared to the HSC-F0-#4-S beam. However, at the failure blast of beam HSC-F0-#4-S, the cumulative residual displacement was 14.87 mm, which compares to 18.00 mm for the HSC-F1-#4-S specimen. However, in general the effect of fibres on maximum displacements was more important than on residual displacements for this series which had No. 4 bars.

As shown in the summary of principal crack widths in Table 6-1, steel fibres were effective in improving crack control. For specimens without fibres, the first major crack appeared during Blast 2, while the formation of major cracking was not observed until one blast later in the specimen with fibres. Similarly, at Blast 3a, the HSC-F1-#4-S beam's major crack was 2.07 mm in width, which compares to 6.50 mm for the HSC-F0-#4-S beam.

The provision of fibres also had an important effect on failure mode. The HSC-F0-#4-S specimen failed at Blast 3b due to the severe spalling of concrete cover in the mid-span tension region. The addition of fibres eliminated this mechanism, with failure of the HSC-F1-#4-S beam delayed until Blast 4. While the specimen had residual blast capacity after this blast, it was deemed to have failed because of the significant opening of a major crack at mid-span, with associated fibre pulled out. Another clear benefit of using steel fibres was the reduction of secondary fragmentation.

During the last shot (Blast 4) the high-speed video shows limited fragmentation for beam HSC-F1-#4-S, with only a small amount of fine powder generated at failure. In contrast, significant fragmentation and ejection of large concrete cover fragments was observed in the case of the companion beam with plain HSC. In conclusion, the specimen with steel fibres showed improved blast performance with reduction in major cracking, prevention of concrete cover loss, increased blast resistance, and improved control of maximum displacements.

a) HSC-F0-#4-S (50 psi)

b) HSC-F1-#4-S (70 psi)

c) HSC-F0-#4-S

Mid-span spalling at Blast 3b (50 psi)

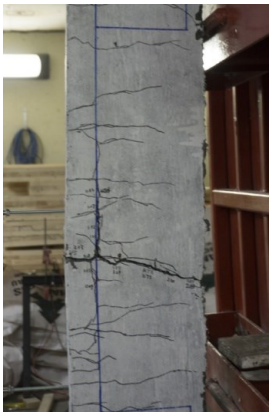

d) HSC-F1-#4-S

Mid-span damage at Blast 3b (50 psi)

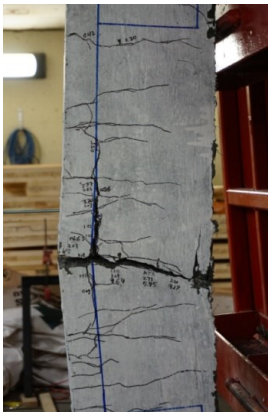

e) HSC-F1-#4-S

Mid-span fibre pull out at Blast 4 (70 psi)

Figure 6-16 Photographs; effects of steel fibres on HSC specimens with No. 4 bars

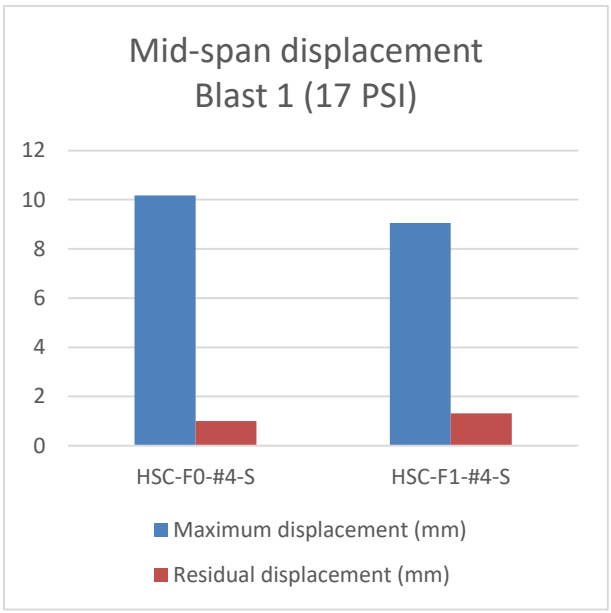

a) Blast 1

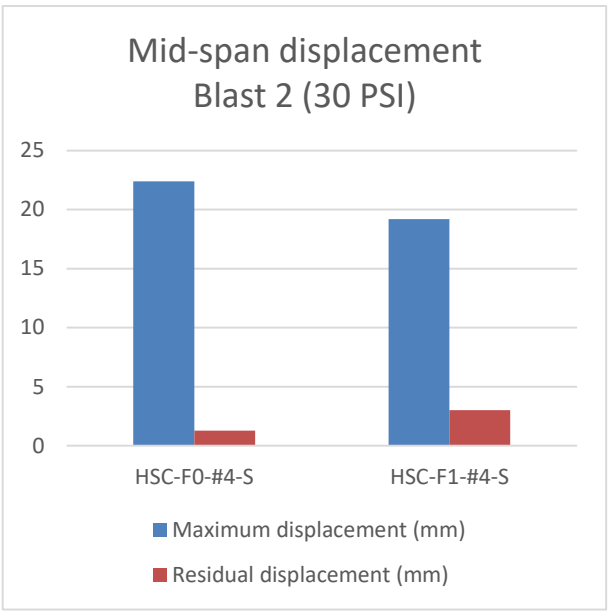

b) Blast 2

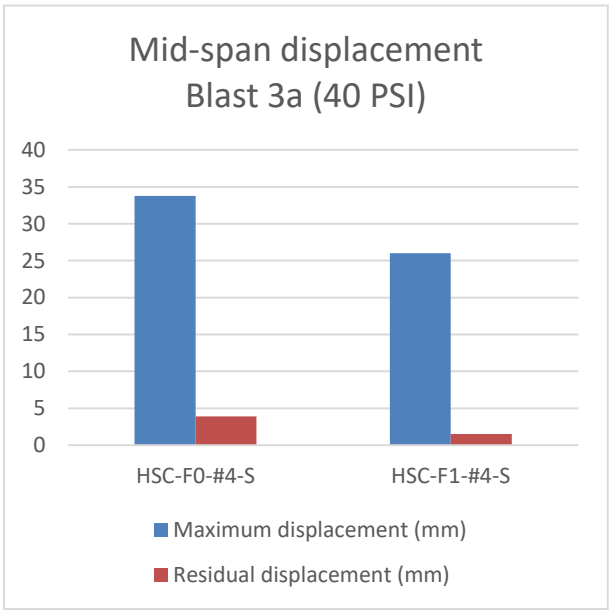

c) Blast 3a

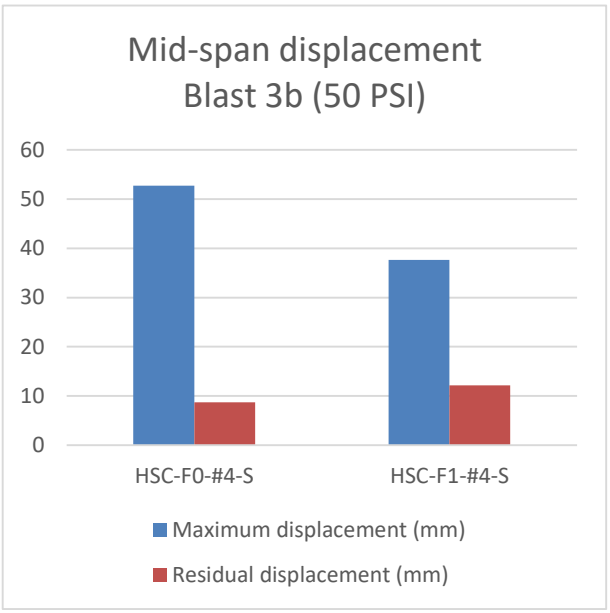

d) Blast 3b

Figure 6-17 Maximum and residual displacements; effects of steel fibres on HSC specimens with No. 4 bars

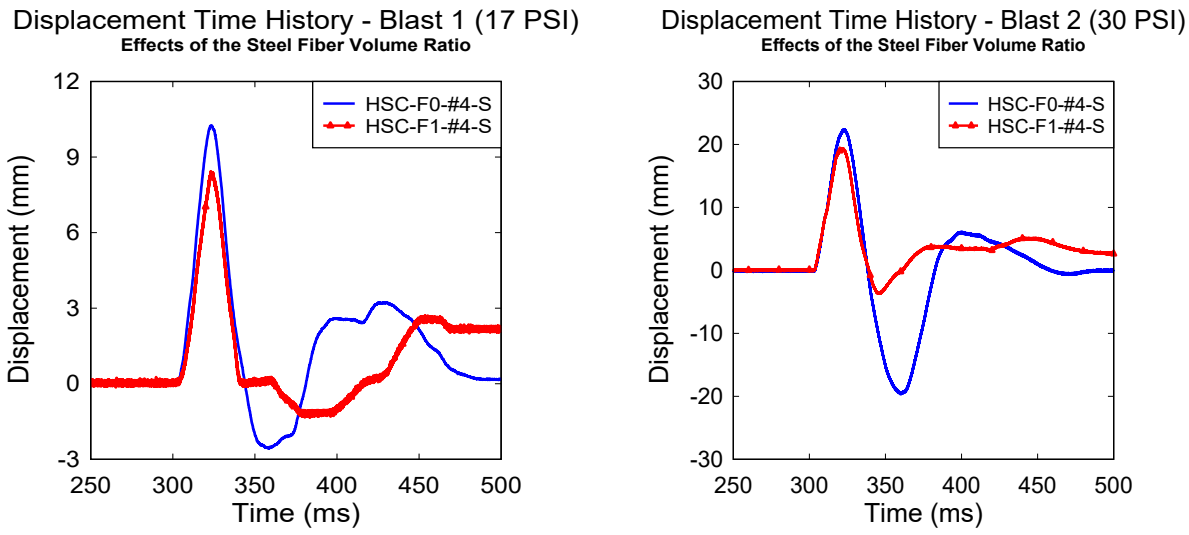

a) Blast 1

b) Blast 2

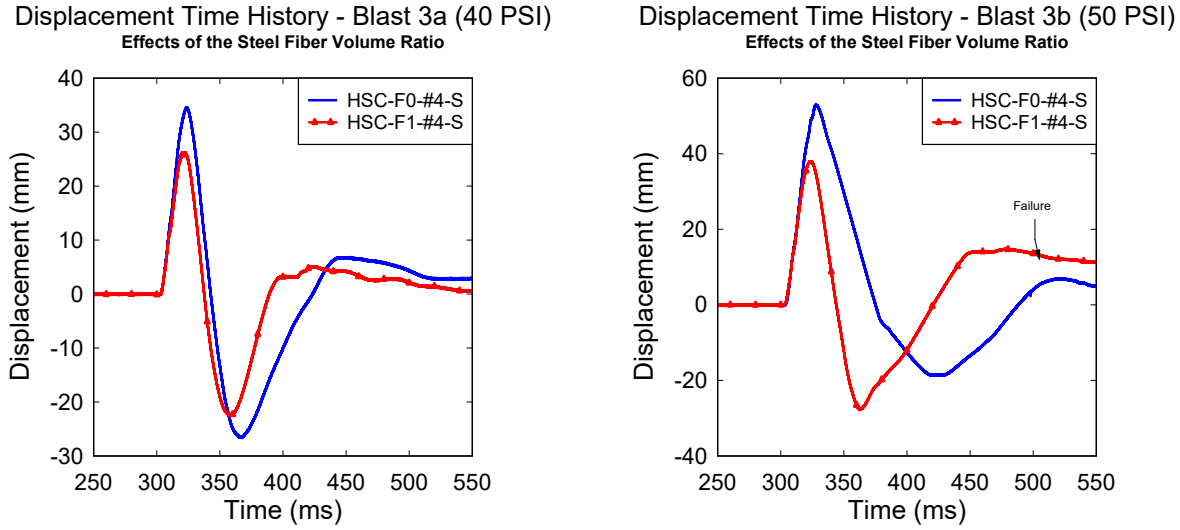

c) Blast 3a

d) Blast 3b

Figure 6-18 Displacement time histories; effects of steel fibres on HSC specimens with No. 4 bars

6.4.2. EFFECTS OF STEEL FIBRES – HSC beams with NO. 5 MMFX STEEL BARS

Companion beams HSC-F1-#5-S and HSC-F0-#5-S were constructed with high-strength concrete, and No. 5 MMFX bars but contained plain and fiber-reinforced HSC, respectively. Photographs showing the beams at failure are included in Figure 6-19, comparative displacement bar charts are included in Figure 6-20, and displacement-time history diagrams can be seen in Figure 6-21.

In terms of maximum displacements, specimen HSC-F1-#5-S which contained 1% steel fibres had maximum displacements δ_{max} = 9.2 mm, 14.6 mm, 22.51 mm, and 39.47 mm, at Blasts 1, 2, 3b, and 4, respectively. In comparison the corresponding maximum displacements were δ_{max} = 9.63 mm, 17.72 mm, 26.77 mm and 64.71 mm, for the specimen with plain HSC. This comparison shows that the fibres in beam HSC-F1-#5-S resulted in reductions in maximum displacements by 5.9%, 17.6%, 15.9% and 39.0% at these four blasts. The residual displacement values were similar for these two specimens from Blast 1 to Blast 3b, although the displacements are slightly less for the specimen with fibres. At Blast 4, the residual displacement of the HSC-F1-#5-S beam was 7.7 mm compared to 19.96 mm for HSC-F0-#5-S, which failed at this blast intensity. It can be concluded that use of steel fibres reduced maximum displacements, with moderate effects on residual displacements in this series which had No. 5 bars.

The previous companion set showed steel fibres are effective in improving crack control under blast loading, and this trend continued in this series. As with the previous set, the first major cracking was delayed by one blast when compared to the beam with plain HSC. As shown in Table 6-1, the specimen with fibres had smaller major crack widths at the various blast pressures. For example, at Blast 3b crack widths were reduced by 43.9% (1.39 mm vs. 0.78 mm). The HSC-F0-#5-S specimen failed at Blast 4, therefore no comparison was made for crack widths after Blast 3b.

The HSC-F1-#5-S specimen withstood two more blasts when compared to the HSC-F0-#5-S specimen. At Blast 4, the specimen without fibres failed due to concrete spalling (with complete loss of concrete cover in the mid-span region) and crushing of concrete in the compression zone. In contrast spalling was eliminated in the HSC-F1-#5-S specimen and failure was prevented at this blast intensity. At Blast 5, the specimen with fibres was considered to have successfully resisted the blast load, although some fibres were observed to have pulled out. Subsequent testing under Blast 6 pressures resulted in rupture of the tensile bars in this specimen. Despite the severe blowout failure caused by the loss of tension reinforcement, the concrete did not disintegrate and the amount of secondary fragmentation observed during the final shot (Blast 6) was limited. In contrast significant fragmentation can be seen in the high-speed video at Blast 4 for the HSC-F0-#5-S specimen (see Figure 6-52).

a) HSC-F0-#5-S (70 psi)

b) HSC-F1-#5-S (90 psi)

c) HSC-F0-#5-S

Mid-span spalling at Blast 4 (70 psi)

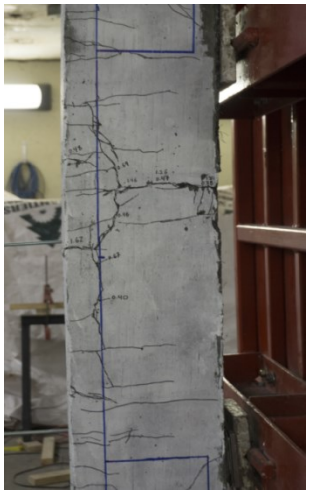

d) HSC-F1-#5-S

Mid-span damage at Blast 4 (70 psi)

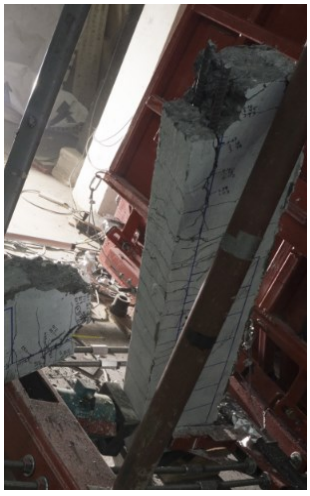

e) HSC-F1-#5-S

Tensile reinforcement bars rupture at Blast 6 (100 psi)

Figure 6-19 Photographs; effects of steel fibres in HSC specimens with No. 5 bars

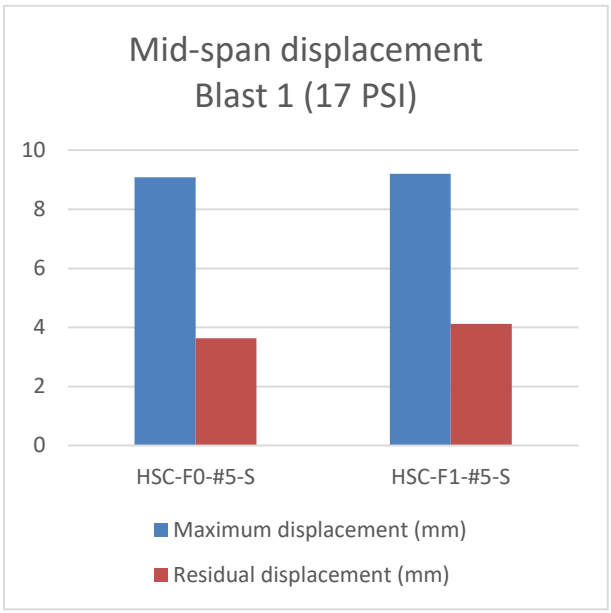

a) Blast 1

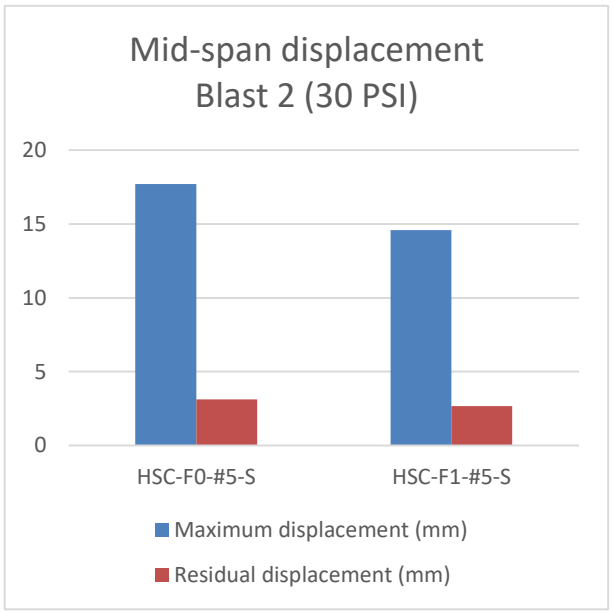

b) Blast 2

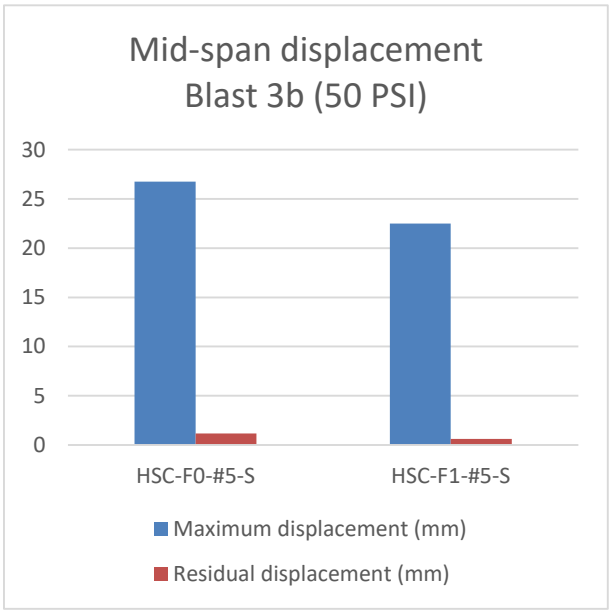

c) Blast 3b

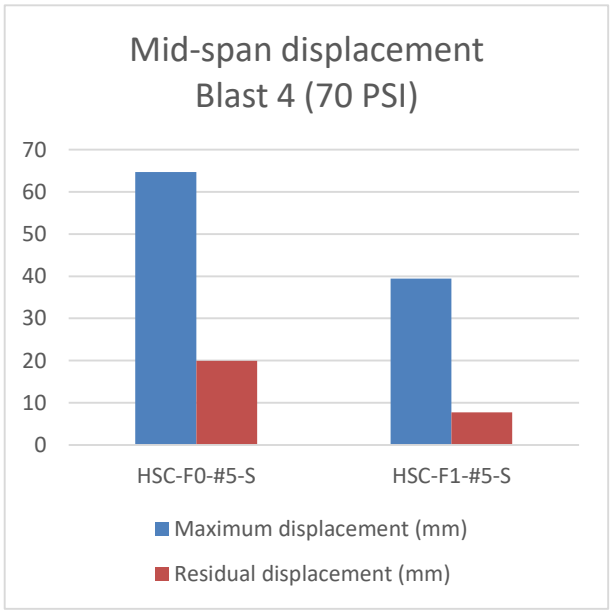

d) Blast 4

Figure 6-20 Maximum and residual displacements; effects of steel fibres in HSC specimens with No. 5 bars

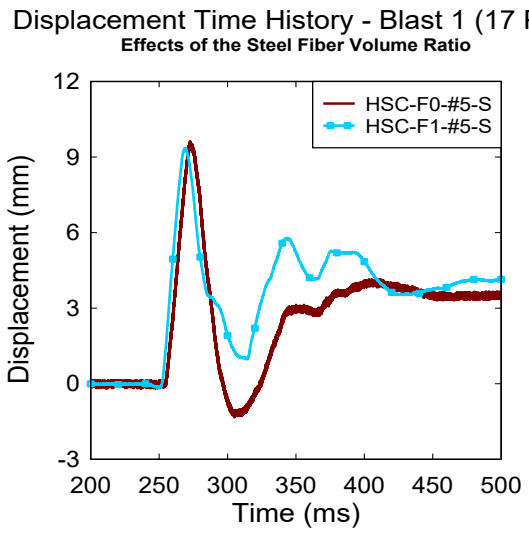

a) Blast 1

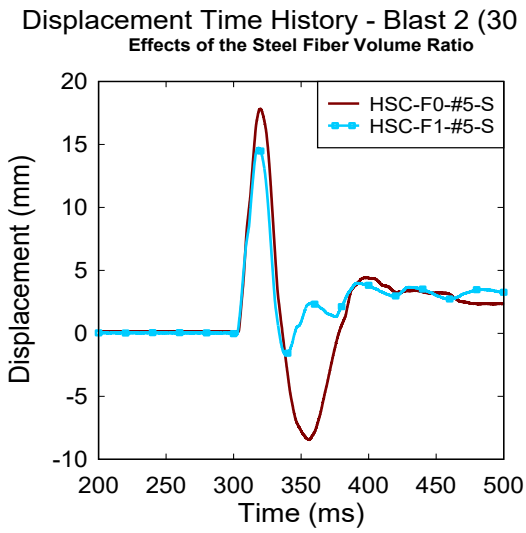

b) Blast 2

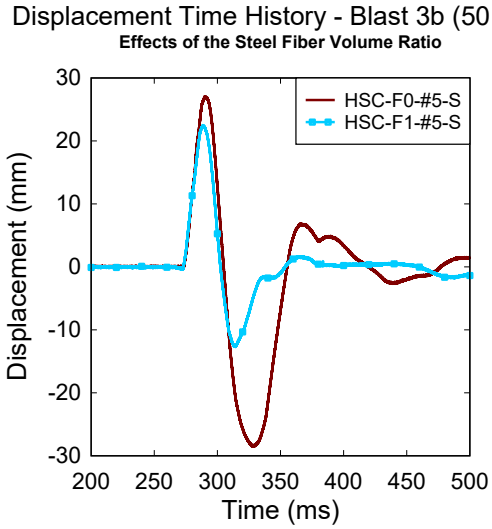

c) Blast 3b

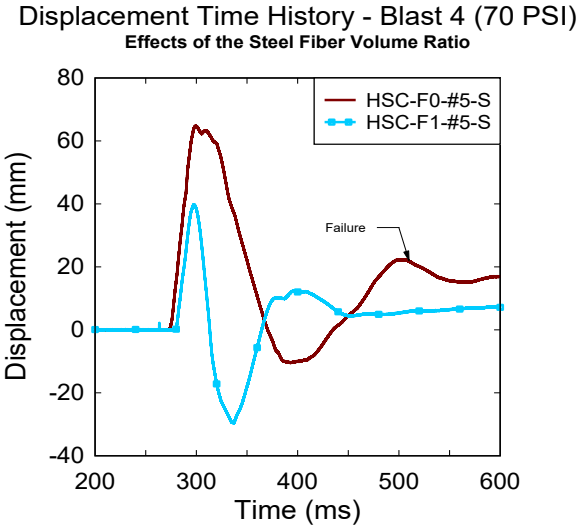

d) Blast 4

Figure 6-21 Displacement time histories; effects of steel fibres in HSC specimens with No. 5 bars

6.4.3. EFFECTS OF STEEL FIBRES – HSC beams with NO. 6 MMFX STEEL BARS

This is the final comparison in this sub-section. Specimens HSC-F1-#6-S and HSC-F0-#6-S were constructed with high-strength concrete, No. 6 MMFX bars, but contained 1% and 0% fibres, respectively. Photographs of the specimens at failure are included in Figure 6-22, comparative displacement bar charts are displayed in Figure 6-23, and displacement-time history diagrams can be seen in Figure 6-24.

Comparing the maximum displacements for each blast, the HSC-F1-#6-S specimen had a slightly improved response when compared to the HSC-F0-#6-S specimen. For the specimen reinforced with fibres, the maximum displacements are 6.11 mm, 14.76 mm, and 22.33 mm for Blasts 1, 2 and 3b, respectively, which are lower by 44.0%, 11.0%, 14.6% when compared to the specimen without fibres which had displacements of 10.91 mm, 16.59 mm, and 26.15 mm for Blasts 1, 2 and 3b, respectively. No maximum displacement data was recorded at Blast 4, therefore no comparison is possible at this shot. The cumulative residual displacement of beam HSC-F1-#6-S was 4.91 mm, compared to 4.86 mm for HSC-F0-#6-S at Blast 3b. The specimen without fibres failed at Blast 4, and the associated residual displacement was 25.22 mm, compared to 5.35 mm for the specimen with fibres. It can be concluded that steel fibres improved the control of maximum displacements at mid-span, and decreased residual displacements.

In terms of major crack widths, the same findings which were summarized for the specimens with No. 4 and No. 5 bars were observed for the beam with No. 6 bars. Major crack in the HSC-F1-#6-S specimen was found at Blast 3b, which was one blast later than for the HSC-F1-#6-S specimen (Blast 2). The maximum crack width for HSC-F1-#6-S specimen was 1.08 mm compared to 1.37 mm for the HSC-F0-#6-S specimen at Blast 3b. The HSC-F0-#6-S specimen failed at Blast 4; therefore, no comparison was made after Blast 4.

In addition to reducing maximum displacements, the use of fibres in the No. 6 specimen allowed the beam to resist two more blasts when compared to the No. 6 specimen with plain HSC. The HSC-F1-#6-S failed after application of Blast 6 pressures due to concrete crushing. While rupture of tension steel was prevented at this blast, the large impulse resulted in the beam being released from the setup, with loss of concrete in the compression zone (although the large blocks of fragmented concrete did not disintegrate). No video was recorded for the HSC-F0-#6-S specimen during the last blast; however, examination of the test floor area in front of the beam showed no ejection of major blast fragments at failure, which contrasts with the fragmentation observed in the high-speed video of the beam with plain HSC at failure.

In summary, from the three companion sets of HSC and HSFRC beams, it can be concluded that the provision of fibres results in important improvements in blast performance in high-strength concrete beams reinforced with high-strength steel bars. In particular, the use of fibres leads to increased blast capacity (larger failure blasts), reduced maximum displacements and improved damage tolerance and crack control.

a) HSC-F0-#6-S (70 psi)

b) HSC-F1-#6-S (90 psi)

c) HSC-F0-#6-S

Mid-span crushing at Blast 4 (70 psi)

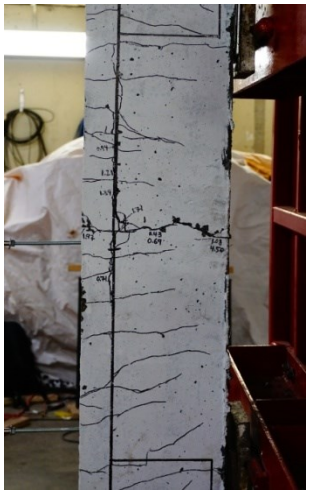

d) HSC-F1-#6-S

Mid-span damage at Blast 4 (70 psi)

e) HSC-F1-#6-S

Mid-span crushing at Blast 6 (100 psi)

Figure 6-22 Photographs; effects of the steel fibre on HSC specimens with No. 6 bars

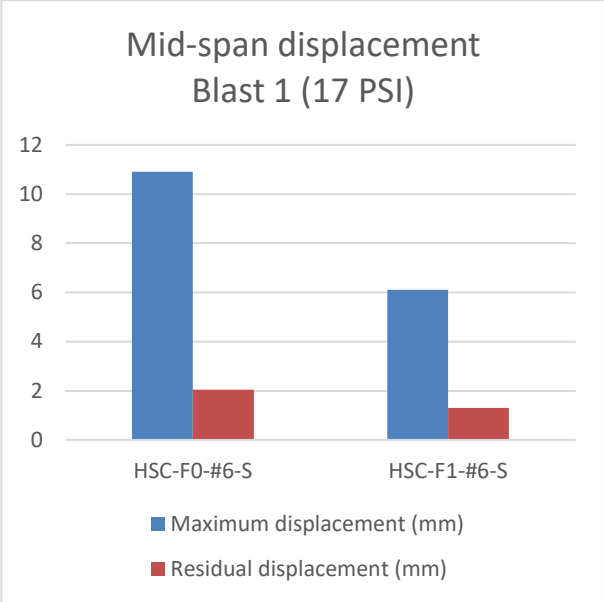

a) Blast 1

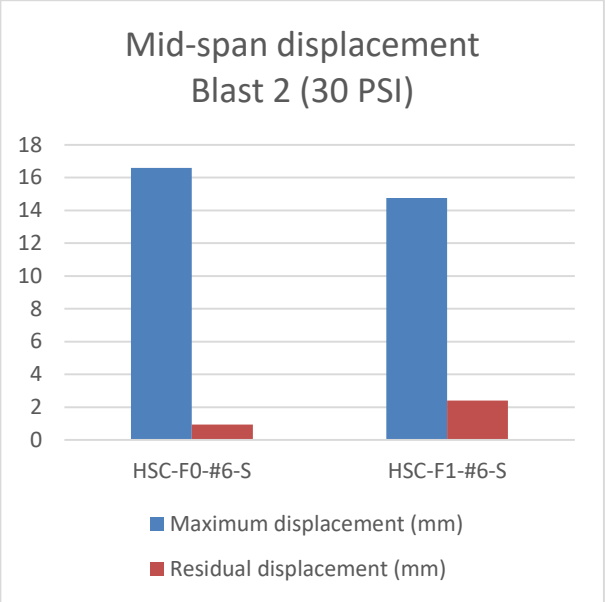

b) Blast 2

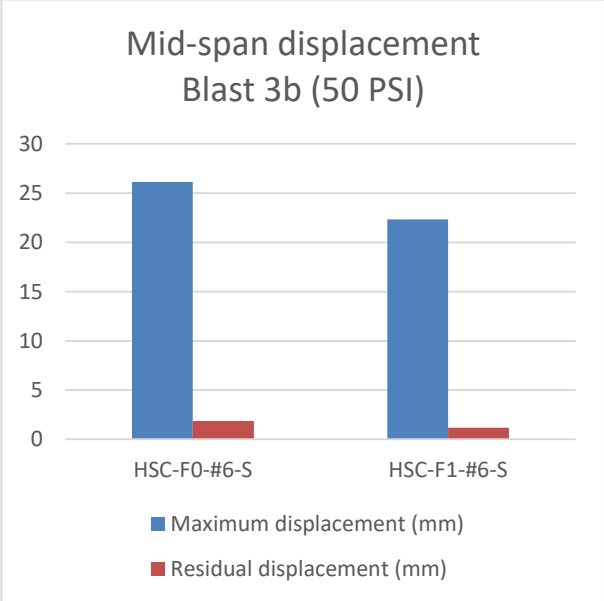

c) Blast 3b

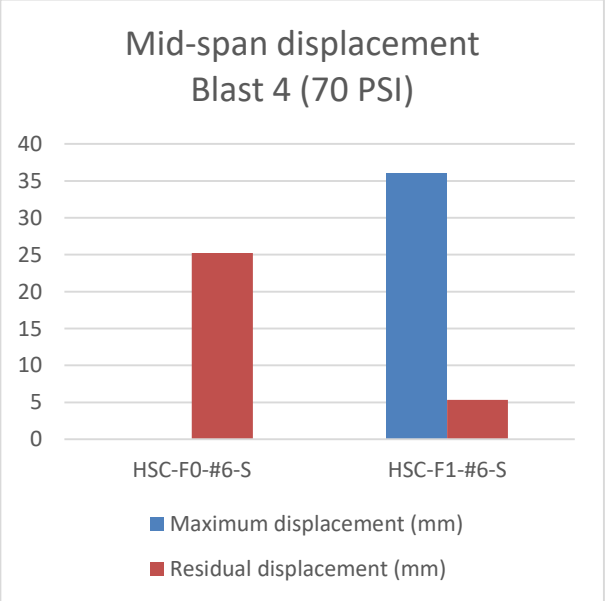

d) Blast 4

Figure 6-23 Maximum and residual displacements; effects of steel fibres on HSC specimens with No. 6 bars

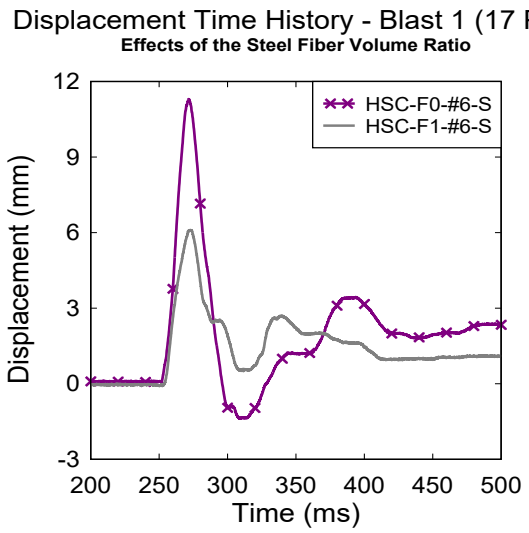

a) Blast 1

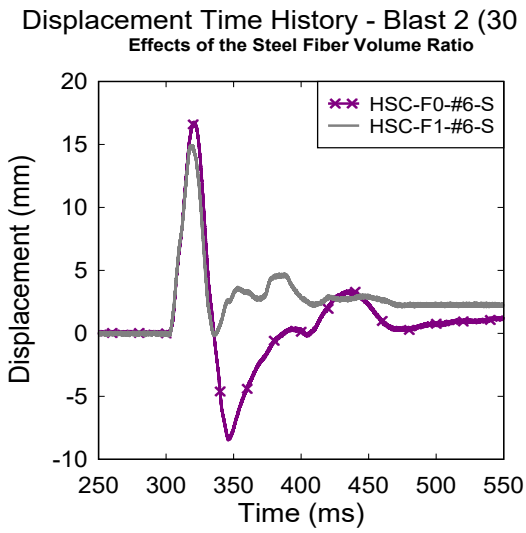

b) Blast 2

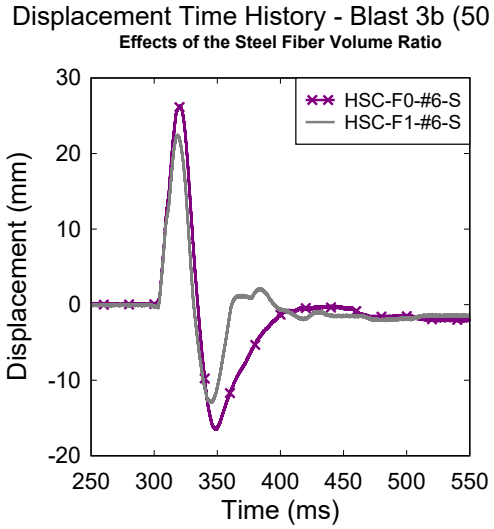

c) Blast 3b

Figure 6-24 Displacement time histories; effects of steel fibres on HSC specimens with No. 6 bars

6.5. EFFECTS OF CONCRETE STRENGTH

One of the parameters investigated in this study was concrete strength in beams built with high-strength steel reinforcement. The sections that follow examine the effect of this parameter in beams built with No. 4 and No. 5 MMFX steel bars.

6.5.1. EFFECTS OF CONCRETE STRENGTH – SPECIMENS with NO. 4 MMFX STEEL BARS

The SCC-F0-#4-S and HSC-F0-#4-S specimens were both designed with No. 4 MMFX bars and did not contain fibres. The only difference between them was the use of normal-strength self-consolidating concrete in the SCC-F0-#4-S beam and high-strength concrete in the HSC-F0-#4-S beam. Photographs of the specimens at failure are included in Figure 6-25, comparative displacement bar charts are depicted in Figure 6-26 and displacement-time history diagrams can be seen in Figure 6-27.

The use of high-strength concrete had some limited effects on the behaviour of the beams in this set. In general, maximum and residual displacements were better controlled when using HSC. At Blasts 1, 2, 3a and 3b, the maximum displacements of the high-strength concrete specimen were 10.17 mm, 22.39 mm, 33.78 mm, and 52.74 mm, which are decreased by 24.3%, 7.9%, 9.4% and 18.3%, when compared to the companion beam with normal-strength concrete (δ_{max} = 13.44 mm, 24.32 mm, 37.3 mm and 64.52 mm). Similarly, residual displacements were reduced for the HSC specimen when compared to the companion SCC-F0-#4-S specimen, with reduction of 61.1%, 8.6%, 41.1% and 57.0% at Blasts 1, 2, 3a and 3b, respectively (Blast 1: 1.01 mm vs. 2.6 mm, Blast 2: 1.28 mm vs. 1.4 mm, Blast 3a: 3.89 mm vs. 6.6 mm, and Blast 3b: 8.69 mm vs. 20.2 mm). It can be concluded that the use of high-strength concrete has effects on decreasing maximum and residual displacements at equivalent blast loads.

Figure 6-25 shows the failure mode of the SCC-F0-#4-S and the HSC-F0-#4-S specimens; both specimens failed at Blast 3b due to severe spalling of the concrete in the tensile mid-span region, with crushing of concrete in the compression zone. Both specimens showed significant amounts of secondary fragmentation when examining the high-speed videos at this failure blast.

In terms of crack control, the specimen with SCC showed narrower crack widths at equivalent blasts when compared to the companion beam with high-strength concrete. Major cracking in the HSC specimen was observed at Blast 2, which was one blast prior to the cracking of the SCC specimen, which occurred at Blast 3a. At Blast 3b, the crack width of the HSC-F0-#4-S beam was 6.5 mm compared to 1.78 mm for the SCC-F0-#4-S beam.

It can be concluded that the high-strength specimen allowed for better control of maximum and residual displacements under blast loading. However, the use of HSC did not improve cracking and did not allow for greater blast capacity, an indicator that the blast performance of reinforced concrete flexural members is more greatly affected by the properties of the tension steel reinforcement.

a) SCC-F0-#4-S (50 psi)

b) HSC-F0-#4-S (50 psi)

c) SCC-F0-#4-S
Mid-span failure at Blast 3b (50 psi)

d) HSC-F0-#4-S
Mid-span failure at Blast 3b (50 psi)

Figure 6-25 Photographs; effects of concrete strength on specimens with No. 4 bars

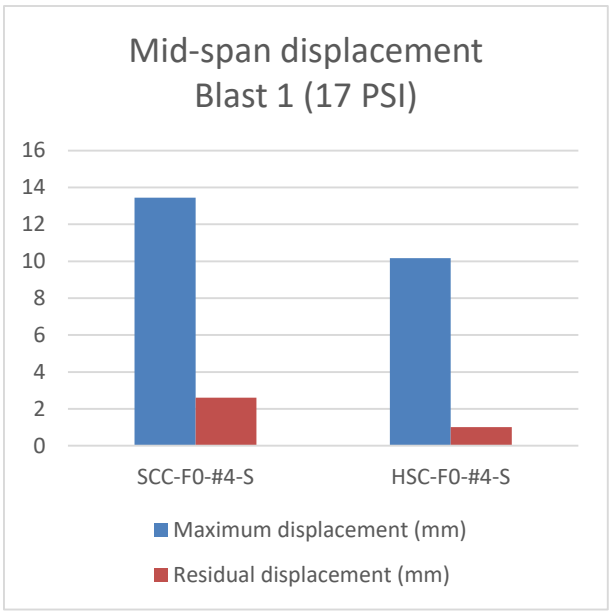

a) Blast 1

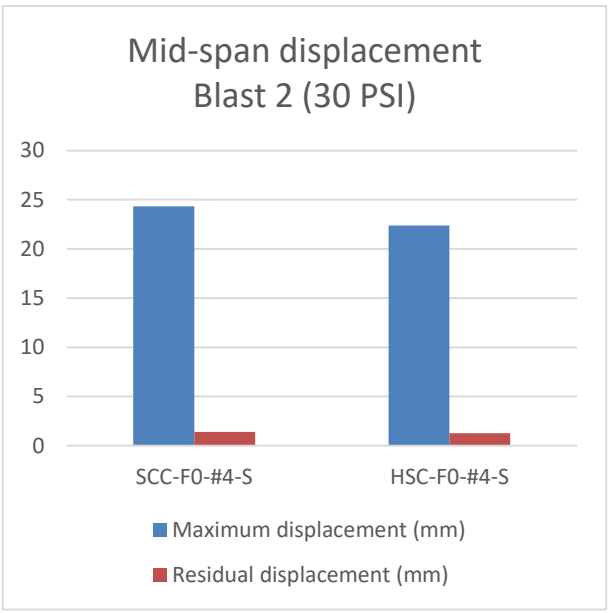

b) Blast 2

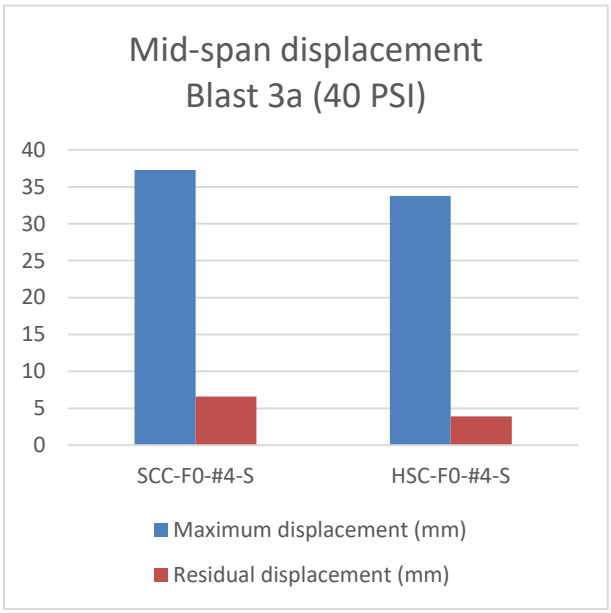

c) Blast 3a

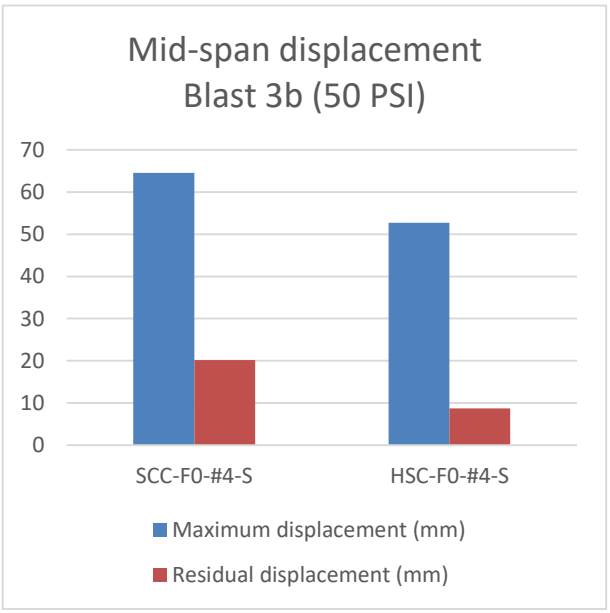

d) Blast 3b

Figure 6-26 Maximum and residual displacements; effects of concrete strength on specimens with No. 4 bars

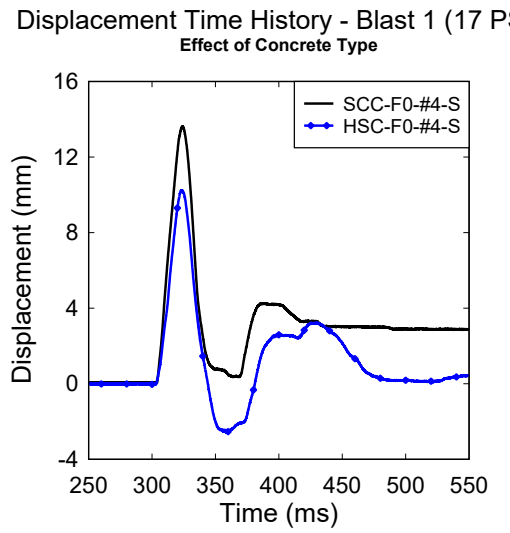

a) Blast 1

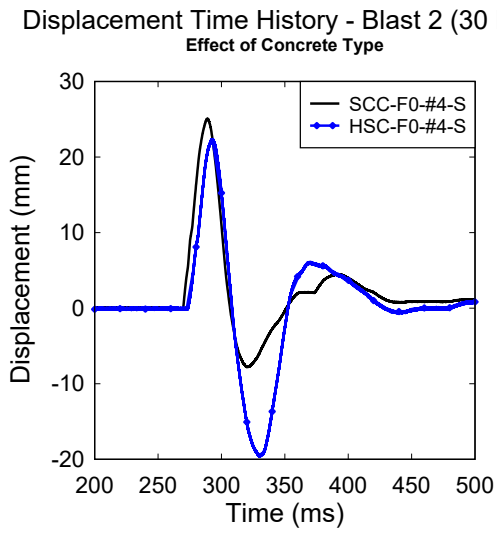

b) Blast 2

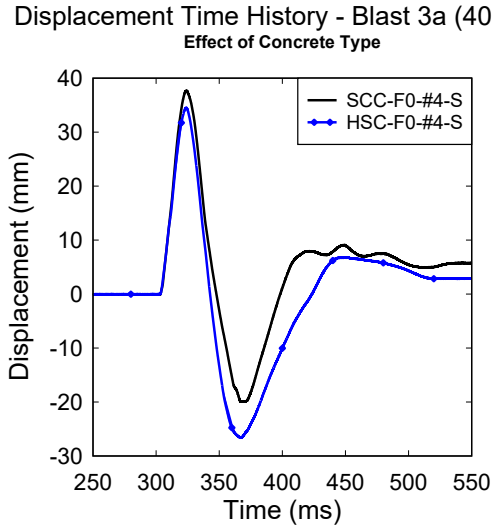

c) Blast 3a

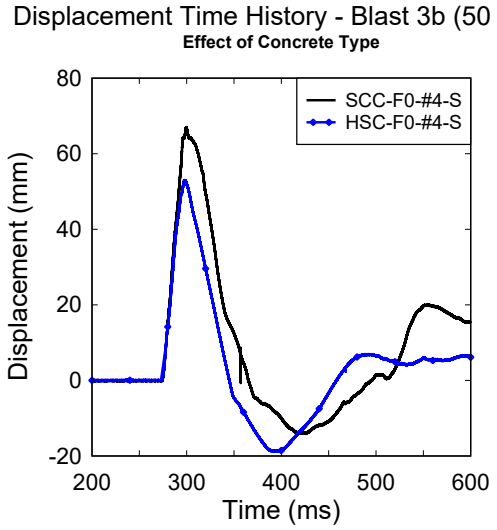

d) Blast 3b

Figure 6-27 Displacement time histories; effects of concrete strength on specimens with No. 4 bars

6.5.2. EFFECTS OF CONCRETE STRENGTH – SPECIMENS with NO. 5 MMFX STEEL BARS

The SCC-F0-#5-S and HSC-F0-#5-S specimens were designed with MMFX No. 5 steel bars but were constructed with normal and high-strength concrete, respectively. Both specimens did not contain fibres and had 6 mm stirrups at s = 100 mm in the shear spans. Photographs of the beams at failure are included in Figure 6-28, comparative displacement bar charts are included in Figure 6-29, and displacement-time history diagrams can be seen in Figure 6-30.

Concrete strength had a more important effect on the behaviour of the beams in this companion set. As with the previous set, the HSC specimen showed reduced mid-span displacements when compared to the SCC beam. At blast 1, the maximum and residual mid-span displacements for the HSC-F0-#5-S specimen (δ_{max} = 9.63 mm and δ_{res} = 3.63 mm) dropped by 26.2% and 1.1% respectively when compared to the SCC-F0-#4-S specimen (δ_{max} = 13.04 mm and δ_{res} = 3.67 mm). At blast 2, the reduction for the HSC-F0-#5-S specimen (δ_{max} = 17.72 mm and δ_{res} = 3.13 mm) reached 12% for the maximum displacement when compared to the HSC-F1-#4-0 specimen (δ_{max} = 20.13 mm and δ_{res} = 1.22 mm). At Blast 3b, the HSC-F0-#5-S specimen (δ_{max} = 26.77 mm and δ_{res} = 1.16 mm) showed a reduction by 21.2% for maximum displacement when compared to the SCC-F0-#5-S specimen (δ_{max} = 33.97 mm and δ_{res} = 0.78 mm). At the failure shot (Blast 4), the maximum and residual displacements for the HSC-F0-#5-S specimen were recorded as 64.71 mm and 19.96 mm, which reduced 16.1% and 49.9% from those of the companion SCC specimen (δ_{max} = 77.17 mm and δ_{res} = 39.81 mm).

Both specimens failed at Blast 4, but with different failure modes. The HSC-F0-#5-S beam failed in flexure with crushing and concrete spalling in the tension zone. In contrast, the SCC-F0-#5-S beam failed in a brittle manner in shear, an indicator that the amount of transverse reinforcement was insufficient in the SCC specimen. Shear resistance is the sum of concrete and transverse steel contributions, with the concrete contribution being proportional to the square root of compressive strength ($\sqrt{f_c'}$). Since the beams had the same stirrup spacing, the shear failure in the SCC specimen can be attributed to the reduced compressive strength of SCC vs. HSC.

The results from this set demonstrate the need to carefully design shear reinforcement in beams which contain high-strength steel bars. The increased flexural strength provided by high-strength bars results in increased shear demand which requires greater shear resistance. The results also show that the combined use of HSC and high-strength reinforcement may be better suited in flexural members subjected to blast loading when compared to normal-strength concrete and high-strength steel reinforcement.

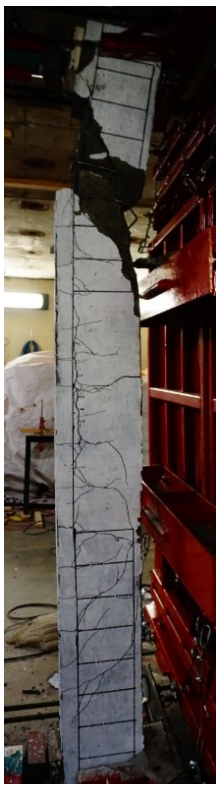

a) SCC-F0-#5-S (70 psi)

b) HSC-F0-#5-S (70 psi)

c) SCC-F0-#5-S

Top-span shear failure at Blast 4 (70 PSI)

d) HSC-F0-#5-S

Mid-span spalling at Blast 4 (70 PSI)

Figure 6-28 Photographs; effects of concrete strength on specimens with No. 5 bars

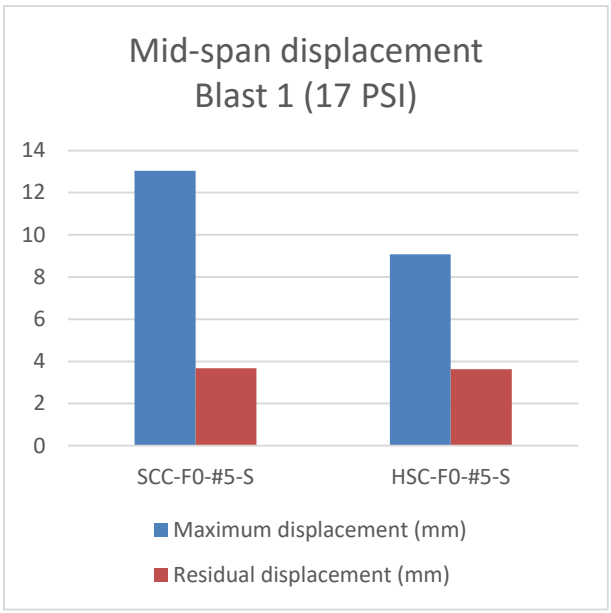

a) Blast 1

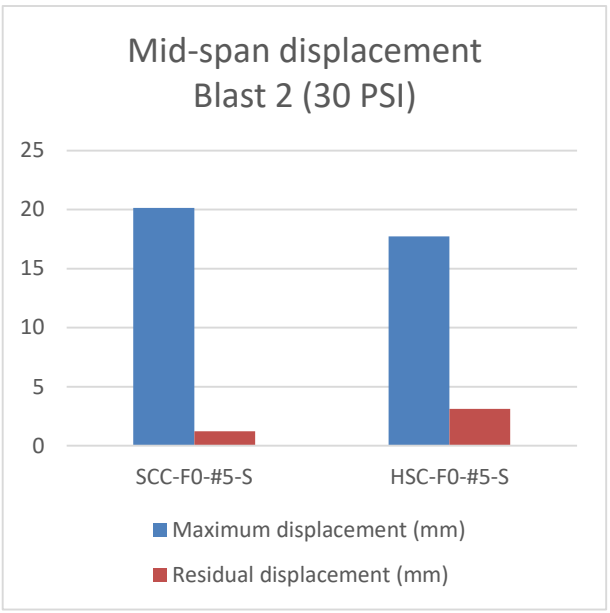

b) Blast 2

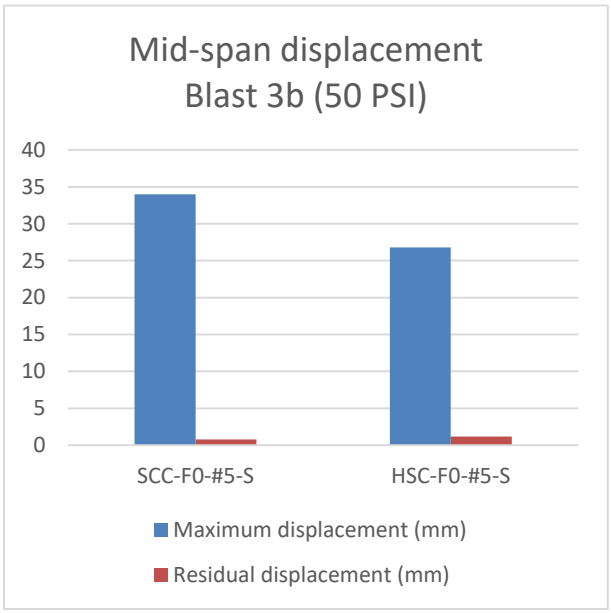

c) Blast 3b

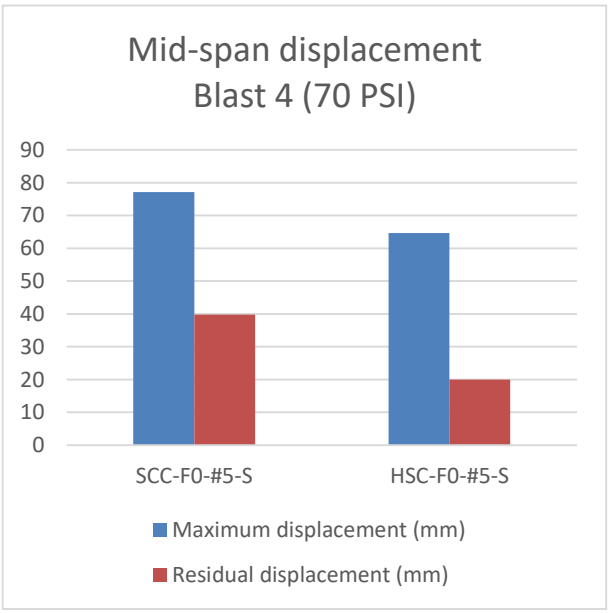

d) Blast 4

Figure 6-29 Maximum and residual displacements; effects of concrete strength on specimens with No. 5 bars

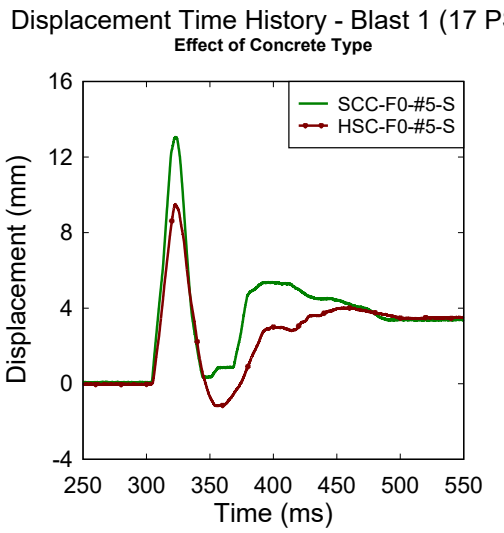

a) Blast 1

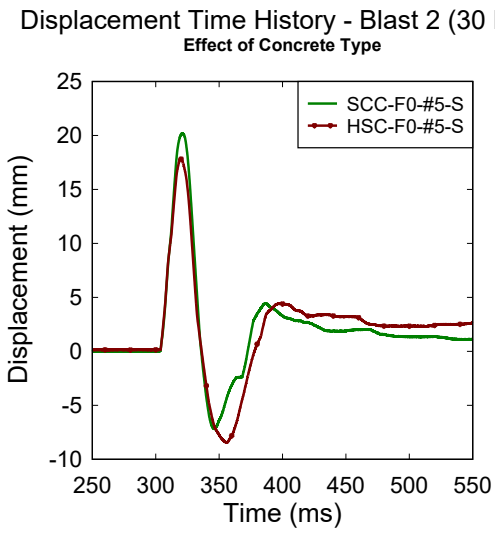

b) Blast 2

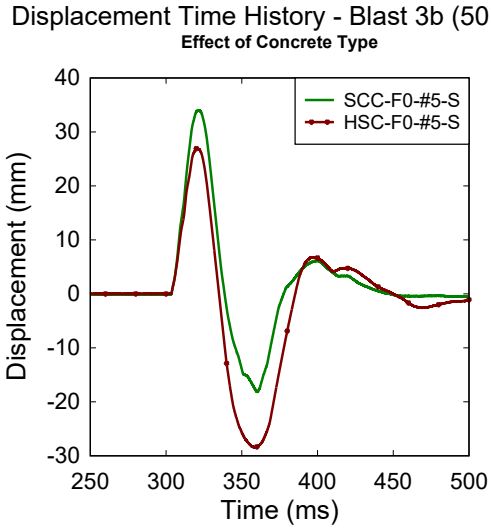

c) Blast 3b

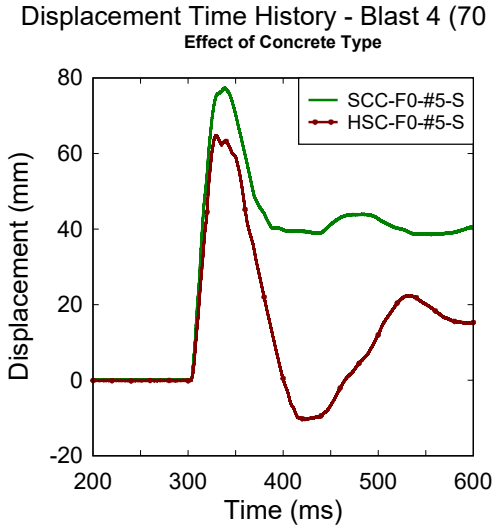

d) Blast 4

Figure 6-30 Displacement time histories; effects of concrete strength on specimens with No. 5 bars

6.6. EFFECTS OF STEEL REINFORCEMENT TYPE

One of the objectives of this research study was to examine the effect of high-strength reinforcement on the blast performance of reinforced concrete beams. In this section the performance of the beams from this study are compared to a companion set of HSC and HSFRC beams tested by Al-gassem (2016), which were built with conventional normal-strength reinforcement.

The comparisons in the sections that follow demonstrate that the use of high-strength reinforcement is beneficial in reinforced concrete beams subjected to blast loading. This reinforcement generally led to increased blast resistance (magnitudes of failure blasts) and decreased maximum and residual displacements at equivalent blast loads. The combined use of steel fibres and high-strength steel reinforcement was particularly beneficial in improving the blast performance of the beams.

The properties of the seven companion beams in Al-gassem (2016)'s study are summarized in Table 6-3. Relevant displacement data from the shock-tube testing of these beams are summarized in Table 6-4. Also included are the blast properties (reflected pressure, impulse and positive phase duration) for each test. Table 6-3 also summarizes maximum crack width data for each beam at the various blasts.

The beams in Al-gassem (2016)'s study had identical geometry and cross-sectional properties as the beams in the current study. The nomenclature follows the same methodology as in the current study (HSC or SCC for concrete type; F0 and F1 for 0% and 1% fibres; No. 4, 15M or 20M for reinforcement size; and S or 0 for beams built with and without stirrups at 100 mm, respectively). The "400" in the nomenclature indicated the use of normal-strength, 400 MPa, bars. The 15M beams had the same reinforcement ratio as the #5 beams in the current study. However, the 20M beams in Al-gassem's study are built with Canadian size 20M bars (A_s = 300 mm^2) resulting in slightly larger reinforcement ratio when compared to the #6 beams in the current study (A_s = 284 mm^2 for the #6 bars). In addition, since the HSFRC beams with No. 4 and 15M normal-strength bars were expected to have sufficient shear reinforcement, these beams were built without stirrups.

Table 6-2 Matrix of normal-strength steel specimens (Al-gassem, 2016)

Specimen ID	Concrete Type	Fibre content V_f(%)	Longitudinal Reinforcing Bars	Type of Longitudinal Reinforcing Bars	Transverse Reinforcement
SCC-F0-#4-S-400	SCC	0	2 – No. 4	Grade 400 with average yield strengths of: No. 4: 449 MPa 15M: 471 MPa 20M: 460 MPa	6.3 mm stirrups @ s = 100 mm
HSC-F0-#4-S-400	HSC		2 – No. 4		
HSC-F0-15M-S-400			2 - 15M		
HSC-F0-20M-S-400			2 - 20M		
HSC-F1-#4-0-400	HSFRC	1%	2 – No .4		n/a
HSC-F1-15M-0-400			2 - 15M		
HSC-F1-20M-S-400			2 - 20M		6.3 mm stirrups @ s = 100 mm

Table 6-3 Summary of principal crack widths for normal-strength steel specimens (Al-gassem, 2016)

Specimen	Principle Crack Width (mm)						
	Blast 1 (17 PSI)	Blast 2 (30 PSI)	Blast 3a (40 PSI)	Blast 3b (50 PSI)	Blast 4x (60 PSI)	Blast 4 (70 PSI)	Blast 5x (80 PSI)
HSC-F0-20M-S-400	HL	0.5	/	1.79	/	F	-
HSC-F1-20M-S-400	HL	HL	/	1.48	/	8.01	F
HSC-F1-15M-0-400	HL	HL	/	3.81	/	19.32 (F)	-
HSC-F0-15M-S-400	HL	1.54	/	F	-	-	-
HSC-F0-#4-S-400	0.2	1.5	F	-	-	-	-
HSC-F1-#4-0-400	HL	0.4	3.84	9.14	F	-	-
SCC-F0-#4-S-400	HL	1.78	3.93 (F)	-	-	-	-

Table 6-4 Blast data summary for companion normal-strength reinforcement specimens (Al-gassem, 2016)

		Driver Length	Approximate Driver Pressure	Reflected Impulse	Reflected Pressure	Positive Phase Duration	Max Deflection	Residual Deflection	Max Support Rotation
Specimen ID	***Blast #***	L_d mm	P_d psi	I_r kPa-ms	P_r kPa	t_P ms	δ_{max} mm	δ_{res} mm	θ_{max} degree
HSC-F0-20M-S-400	-1	2745	17	244.28	23.58	20.72	10.44	1.98	0.54
	-2	2745	30	360.00	39.22	18.36	15.12	0.15	0.78
	-3b	2745	50	538.18	57.40	18.75	32.91	12.43	1.69
	-4	2745	70	702.59	68.83	20.42	118.06	71.69	6.06
HSC-F1-20M-S-400	-1	2745	17	260.4	23.8	21.87	9.21	2.29	0.47
	-2	2745	30	358.0	41.4	17.30	14.91	2.2	0.77
	-3b	2745	50	552.0	57.4	19.24	27.64	4.04	1.42
	-4	2745	70	732.7	71.1	20.60	67.03	41.84	3.44
	-5X	2745	80	774.0	79.1	19.56	153.01	79.22	7.86
HSC-F1-15M-0-400	-1	2745	17	213.70	24.49	17.45	10.05	3.91	0.52
	-2	2745	30	347.60	40.28	17.26	15.02	2.66	0.77
	-3b	2745	50	512.00	56.51	18.12	33.31	10.08	1.71
	-4	2745	70	657.00	69.48	18.91	78.91	54.68	4.05
HSC-F0-15M-S-400	-1	2745	17	223.00	23.89	18.67	11.50	2.66	0.59
	-2	2745	30	340.70	42.88	15.89	21.40	4.71	1.10
	-3b	2745	50	516.00	58.64	17.60	124.00	22.04	6.41
HSC-F1-#4-0-400	-1	2745	17	216.60	24.29	17.83	10.63	3.71	0.55
	-2	2745	30	344.00	41.50	16.58	18.47	4.10	0.95
	-3a	2745	40	428.95	48.21	17.80	35.18	15.61	1.81
	-3b	2745	50	512.00	55.50	18.45	55.10	32.26	2.83
	-4x	2745	60	562.62	68.75	16.37	61.0	38.89	3.13
HSC-F0-#4-S-400	-1	2745	17	229.00	24.42	18.76	13.15	3.62	0.64
	-2	2745	30	348.00	38.24	18.20	30.44	14.16	1.56
	-3a	2745	40	421.00	44.99	18.72	44.53	6.59	2.29
SCC-F0-#4-S-400	-1	2745	17	245.00	23.31	21.02	12.65	1.54	0.65
	-2	2745	30	373.00	40.82	18.28	29.53	13.04	1.52
	-3a	2745	40	448.50	45.24	19.83	47.96	25.11	2.46

6.6.1.EFFECTS OF STEEL REINFORCEMENT TYPE – PLAIN CONCRETE SPECIMENS

This section examines the effect of reinforcement type of the performance of companion beams built with plain normal and high-strength concrete. Included in the comparison sets are SCC beams built with #4 bars and HSC beams built with #4, #5/15M and #6/20M reinforcement.

6.6.1.1. SCC beams with No. 4 steel bars

The performance of the SCC-F0-#4-S-400 and SCC-F0-#4-S, are compared in this sub-section. The two specimens were constructed with the same plain SCC and contained stirrups, but were reinforced with 2 - #4 size conventional (400 MPa) and high-strength (MMFX) steel reinforcing bars, respectively. Photographs of the beams after application of failure blast loads are shown Figure 6-31. Comparative displacement bar charts and displacement-time history diagrams can be seen in Figure 6-32 and Figure 6-33, respectively.

The SCC specimen with high-strength reinforcement out-performed its comparison with conventional reinforcement in several aspects, including control of displacements and overall blast capacity. At Blast 1, the maximum and residual displacements for the two specimens were similar. At Blast 2, the maximum and residual displacements of the SCC-F0-#4-S specimen which had high-strength reinforcement (δ_{max} = 24.32 mm, δ_{res} = 1.4 mm) dropped by 17.6% and 89.3% when compared to the companion SCC-F0-#4-S-400 specimen (δ_{max} = 29.53 mm, δ_{res} = 13.04 mm). At Blast 3a, the SCC-F0-#4-S specimen had maximum and residual mid-span displacements of δ_{max} = 37.3 mm and δ_{res} = 6.6 mm, showing a decrease by 22.2% for maximum displacement and 73.7% for residual displacement when compared to the SCC-F0-#4-S-400 specimen (δ_{max} = 47.96 mm and δ_{res} = 25.11 mm).

The SCC specimen with high-strength reinforcement was also able to resist a higher blast load when compared to the companion the normal-strength reinforcement specimen. While beam SCC-F0-#4-S-400 failed at Blast 3a, failure of beam SCC-F0-#4-S was delayed until Blast 3b. Both specimens failed in a similar manner, with spalling of the concrete cover in the mid-span tension region; however, spalling was more extensive (with some crushing) in beam SCC-F0-#4-S which was subjected to greater blast pressures. From the high-speed video, the amount of secondary fragmentation was also slightly higher at failure for the specimen with high-strength rebar.

a) SCC-F0-#4-S-400
(40 psi)

b) SCC-F0-#4-S
(50 psi)

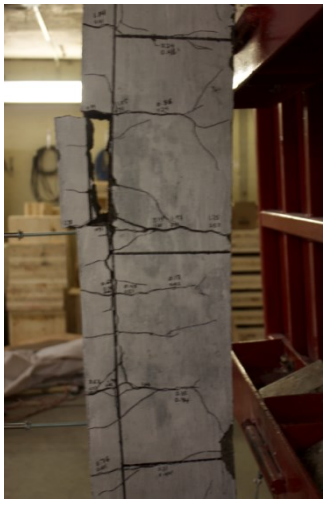

c) SCC-F0-#4-S-400

Mid-span spalling at Blast 3a
(40 psi)

d) SCC-F0-#4-S

Mid-span damage at Blast 3a
(40 psi)

e) SCC-F0-#4-S

Mid-span spalling at Blast 3b
(50 psi)

Figure 6-31 Photographs; effects of steel reinforcement type on SCC beams with No. 4 bars

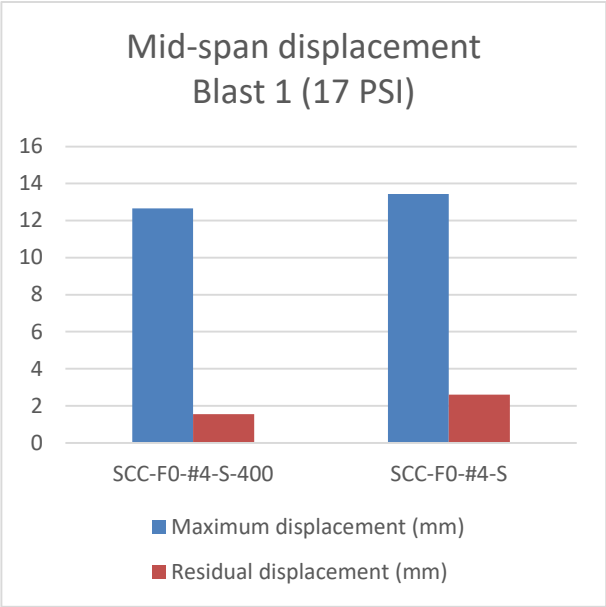

a) Blast 1

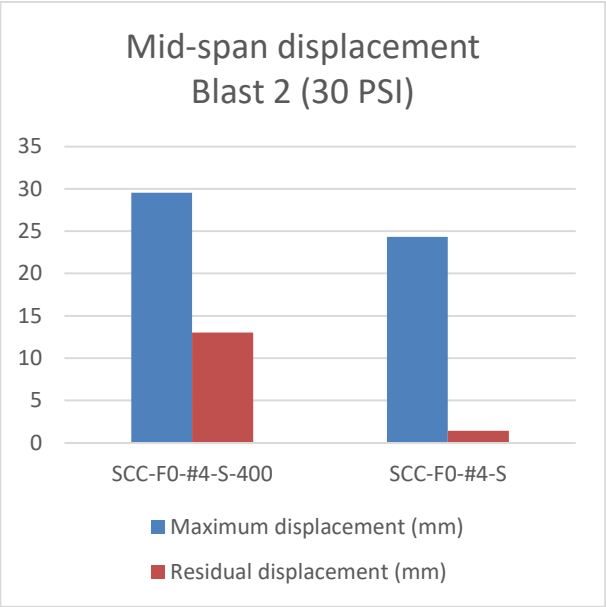

b) Blast 2

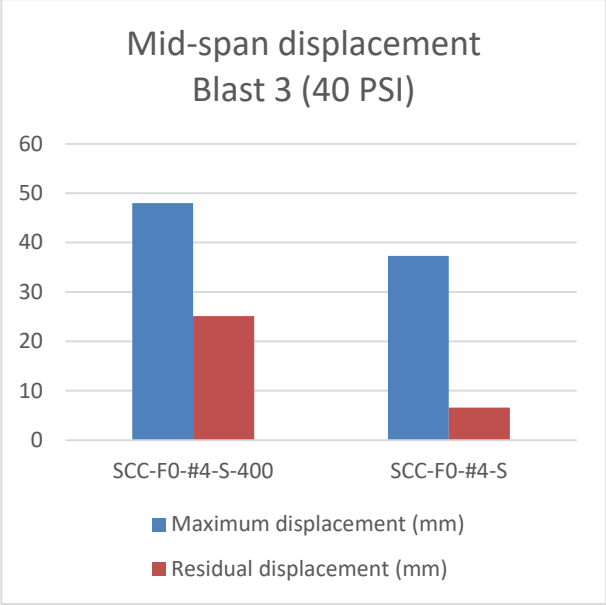

c) Blast 3a

Figure 6-32 Maximum and residual displacements; effects of steel reinforcement type on SCC beams with No. 4 bars

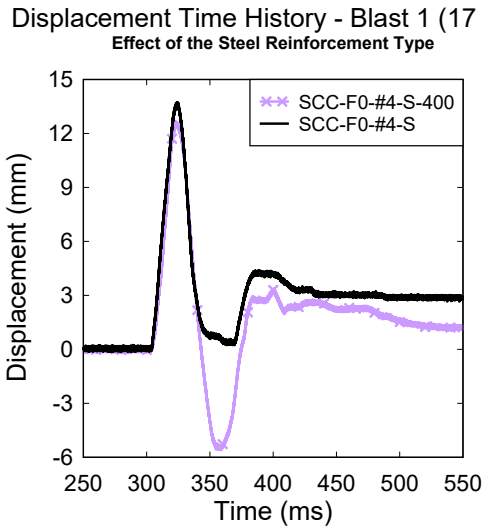

a) Blast 1

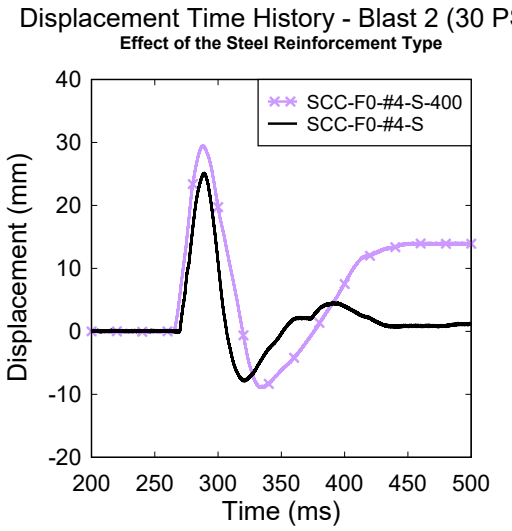

b) Blast 2

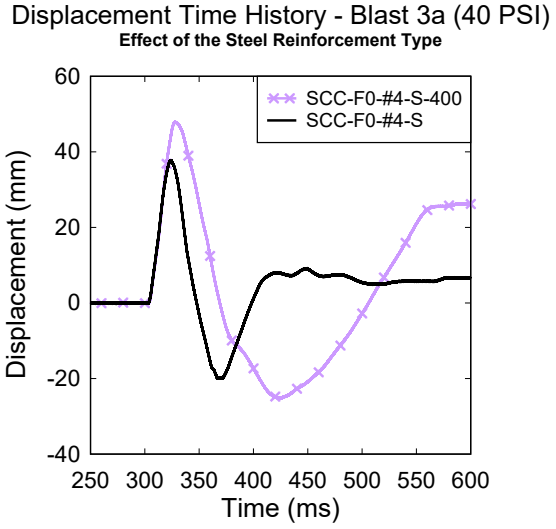

c) Blast 3a

Figure 6-33 Displacement time histories; effects of steel reinforcement type on SCC beams with No. 4 bars

6.6.1.2. HSC beams with No. 4 steel bars

This companion set is similar to previous one, with the exception being that beams HSC-F0-#4-S-400 and HSC-F0-#4-S were built with plain high-strength concrete. Both beams contained stirrups and were reinforced with #4 size normal and high-strength bars respectively. Photographs for the beams at failure blasts are included in Figure 6-34. Comparative displacement bar charts and displacement-time history diagrams can be seen in Figure 6-35 and Figure 6-36, respectively.

The provision of MMFX high-strength reinforcement in the high-strength concrete beams improved response under blast loading. At Blast 1, maximum and residual displacements of the beams with HSC and MMFX bars were 10.17 mm and 1.01 mm, which dropped 1.8% for maximum displacement and 72.1% for residual displacement compared to the companion beam with convention steel (δ_{max} = 12.50 mm, δ_{res} = 3.62 mm). At blast 2, the maximum and residual mid-span displacements dropped by 26.4% and 91% respectively when comparing the HSC-F0-#4-S specimen (δ_{max} = 22.39 mm and δ_{res} = 1.28 mm) to the HSC-F0-#4-S-400 specimen (δ_{max} = 30.44 mm and δ_{res} = 14.16 mm). Finally, comparing the HSC-F0-#4-S specimen (δ_{max} = 33.78 mm and δ_{res} = 3.89 mm) with the HSC-F0-#4-S-400 specimen (δ_{max} = 44.53 mm and δ_{res} = 6.59 mm) at Blast 3a, the MMFX specimen showed reductions of 24.1% and 41.0% in maximum and residual displacements.

The provision of high-strength steel in high-strength concrete also increased the blast capacity of the HSC beam. The normal-strength steel specimen (HSC-F0-#4-S-400) failed at Blast 3a, while the companion with high-strength steel failed in Blast 3b. Both specimens failed in flexure with spalling of the concrete cover in the mid-span region, however the failure mode of the high-strength steel HSC-F0-#4-S specimen was more severe, as shown in Figure 6-34. In both cases, high-speed video shows ejection of large blocks of concrete from the cover region at failure.

a) HSC-F0-#4-S-400
(40 psi)

b) HSC-F0-#4-S
(50 psi)

c) HSC-F0-#4-S-400

Mid-span spalling at Blast 3a
(40 psi)

d) HSC-F0-#4-S

Mid-span damage at Blast 3a
(40 psi)

e) HSC-F0-#4-S

Mid-span spalling at Blast 3b
(50 psi)

Figure 6-34 Photographs; effects of steel reinforcement type on HSC beams with No. 4 bars

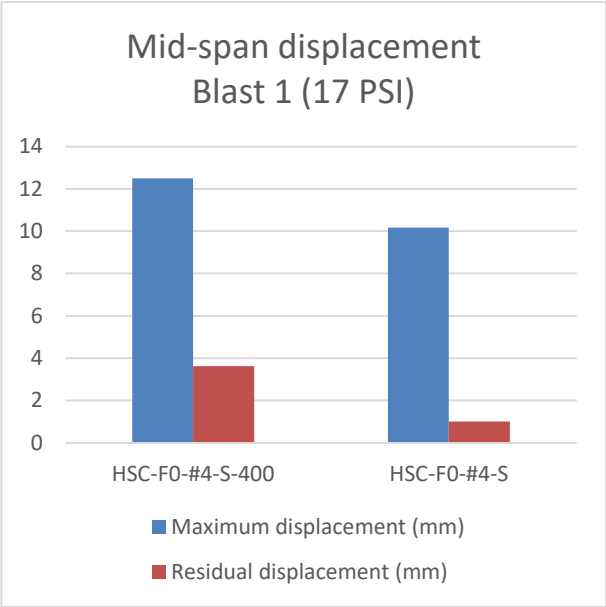

a) Blast 1

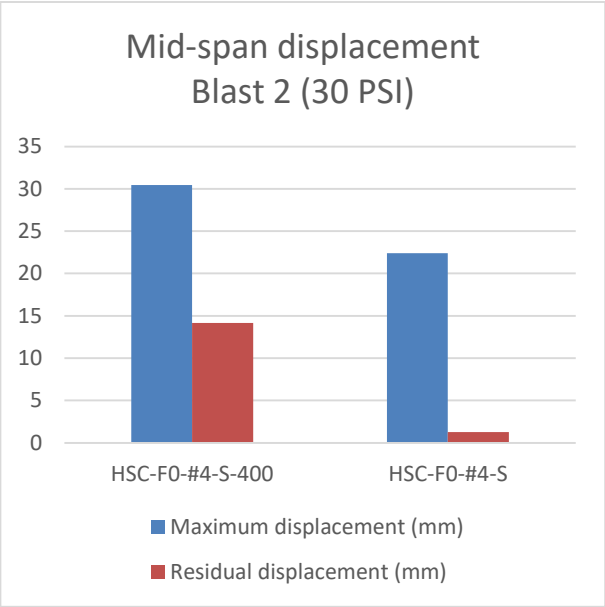

b) Blast 2

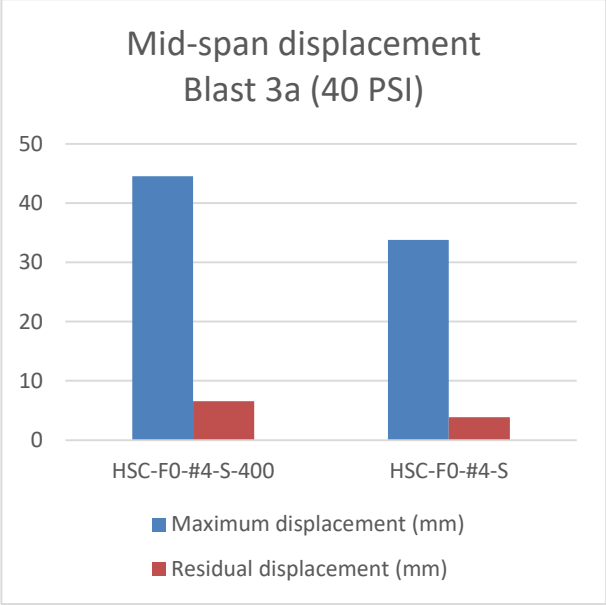

c) Blast 3a

Figure 6-35 Maximum and residual displacements; effects of steel reinforcement type on HSC beams with No. 4 bars

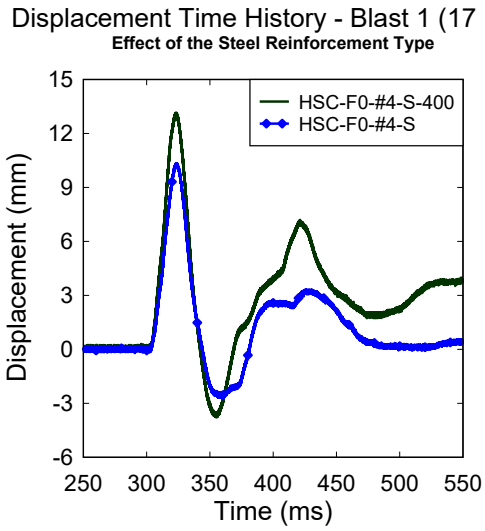

a) Blast 1

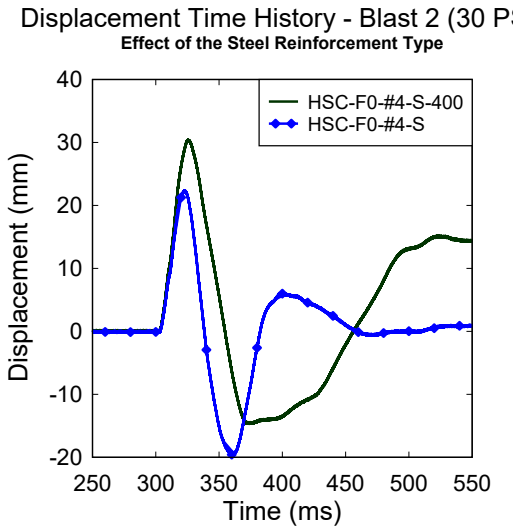

b) Blast 2

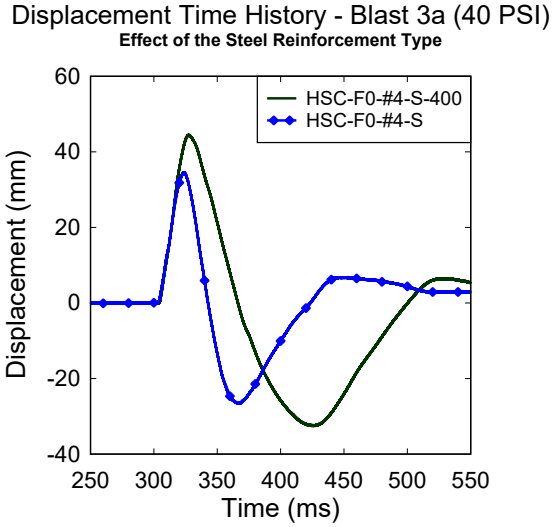

c) Blast 3a

Figure 6-36 Displacement time histories; effects of steel reinforcement type on HSC beams with No. 4 bars

6.6.1.3. HSC beams with No. 5/15M steel bars

The two specimens in this companion set, HSC-F0-15M-S-400 and HSC-F0-#5-S were constructed with high-strength concrete, stirrups, and no fibres. The only difference between the two specimens was that the HSC-F0-15M-S-400 beam was reinforced with normal-strength 15M bars, and the HSC-F0-#5-S beam was reinforced with #5 MMFX bars. Photographs are included in Figure 6-37. Comparative displacement bar charts and displacement-time history diagrams can be seen in Figure 6-38 and Figure 6-39, respectively.

In regard to mid-span displacements, combining the use of high-strength steel in high-strength concrete significantly improved the response of the beams. At Blast 1, the maximum and residual displacements for the high-strength steel specimen were 9.08 mm and 3.63 mm, which diminished 20.9% for maximum displacement compared to the normal-strength steel (δ_{max} = 11.48 mm, δ_{res} = 2.66 mm). At Blast 2, the HSC-F0-#5-S specimen (δ_{max} = 17.72 mm, δ_{res} = 3.13 mm) dropped by 17.2% and 94.7% for the HSC-F0-15M-S-400 specimen (δ_{max} = 21.4 mm, δ_{res} = 4.71 mm). At blast 3b, the HSC-F0-#5-S specimen had maximum and residual mid-span displacements of δ_{max} = 26.77 mm and δ_{res} = 1.16 mm, showing a decrease by 78.6% for maximum displacement and 94.7% for residual displacement when compared to the HSC-F0-15M-S-400 specimen (δ_{max} = 124.95 mm and δ_{res} = 22.04 mm).

In addition to reducing the magnitude of maximum and residual displacements, the high-strength reinforcement specimen was able to better control major crack widths at equivalent blast loads. Crushing also initiated at an earlier stage in the HSC specimen with conventional steel bars.

Reinforcing the HSC beam with high-strength reinforcement also had the effect of enabling it to resist a higher blast load prior to failure. The HSC-F0-#5-S specimen suffered failure at Blast 4, unlike the HSC-F0-15M-S-400 specimen which failed at Blast 3b. Both specimens failed due to concrete crushing in the top flexural region. The failure was somewhat more severe in the beam with high-strength reinforcement, which also suffered spalling in the tension zone. In both cases secondary fragmentation was observed at failure.

a) HSC-F0-15M-S-400
(50 psi)

b) HSC-F0-#5-S
(70 psi)

c) HSC-F0-15M-S-400
Mid-span failure at Blast 3b (50 PSI)

d) HSC-F0-#5-S
Mid-span damage at Blast 3b (50 PSI)

e) HSC-F0-#5-S
Mid-span failure at Blast 4 (70 PSI)

Figure 6-37 Photographs; effects of the steel reinforcement type on HSC with No. 5/15M bars

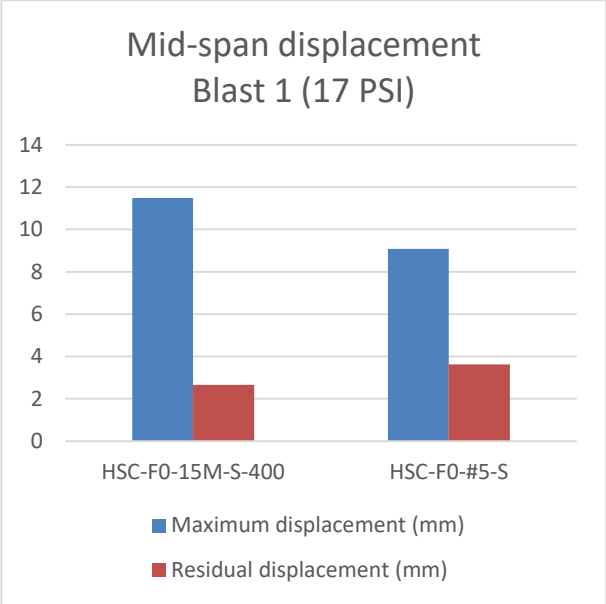

a) Blast 1

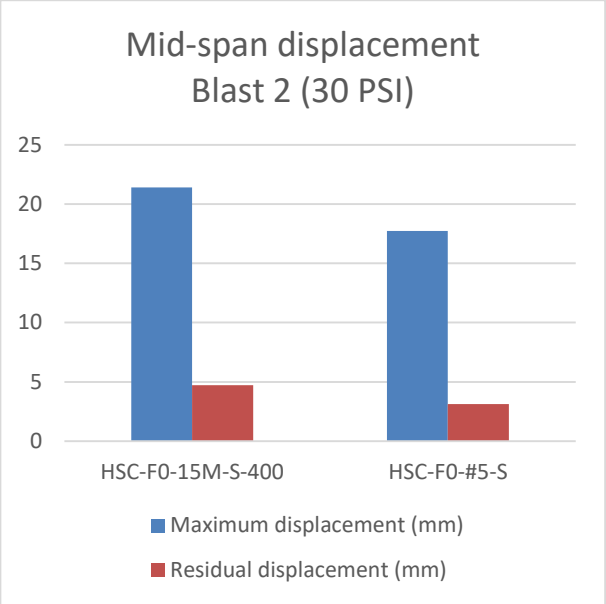

b) Blast 2

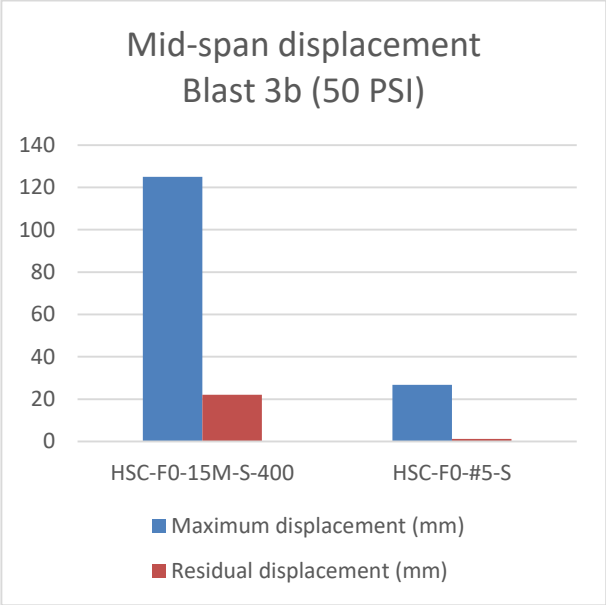

c) Blast 3b

Figure 6-38 Maximum and residual displacements; effects of steel reinforcement type on HSC beams with No. 5/15M bars

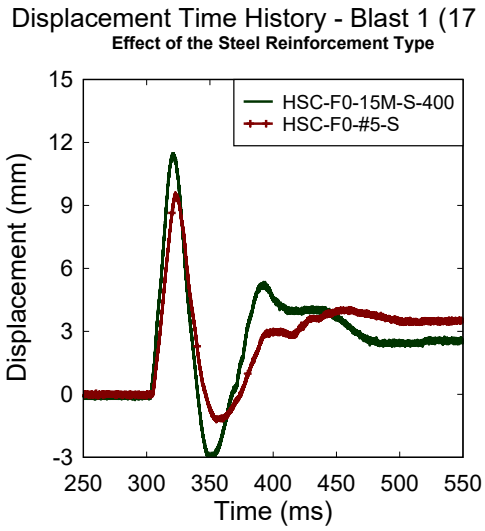

a) Blast 1

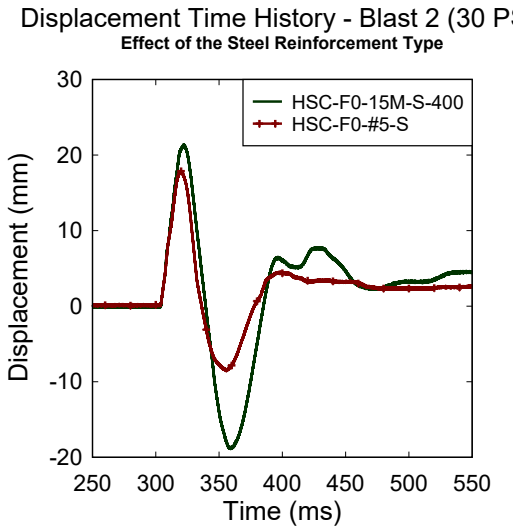

b) Blast 2

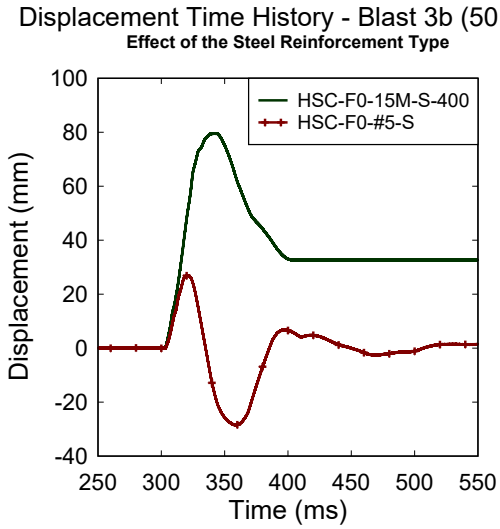

c) Blast 3b

Figure 6-39 Displacement time histories; effects of steel reinforcement type on HSC beams with No. 5/15M bars

6.6.1.4. HSC beams with No. 6/20M steel bars

The last companion set in the HSC series includes specimens HSC-F0-20M-S-400 and HSC-F0-#6-S. Both beams were built with plain high-strength concrete and stirrups. The specimens differed only by the type of steel bars: the HSC-F0-20M-S-400 specimen was built 20M normal-strength steel bars (A_s = 300 mm^2), while beam HSC-F0-#6-S was built No. 6 MMFX high-strength steel bars (A_s = 284 mm^2). Photographs of the beams at failure blast loads are included in Figure 6-40, comparative displacement bar charts can be found in Figure 6-41, and displacement-time history diagrams can be seen in Figure 6-42.

Unlike the previous beams in this series, the use of high-strength steel reinforcement in this set led to some limited improvements in HSC beam blast performance. Maximum and residual displacements at Blast 1 and Blast 2 for the two specimens were similar in magnitude (For the MMFX specimen, δ_{max} = 10.91 mm, 16.59 mm, δ_{res} = 2.05 mm, 0.95 mm; for the conventional steel specimen, δ_{max} = 10.44 mm, 15.12 mm, δ_{res} = 1.98 mm, 0.15 mm). To recall from Chapter 4, the static response of the companion beams was similar in the elastic (pre-yield) range, with similar stiffness recorded for both specimens, which can explain the similarity in maximum and residual displacements under Blast 1 and 2 loadings. Nonetheless, at Blast 3b, the maximum and residual mid-span displacements dropped by 9.7% and 85.0% respectively when comparing the HSC-F0-#6-S specimen (δ_{max} = 26.15 mm, δ_{res} = 1.86 mm) to the HSC-F0-20M-S-400 specimen (δ_{max} = 32.19 mm, δ_{res} = 12.43 mm). Finally, comparing the HSC-F0-#6-S specimen (δ_{res} = 25.22 mm) with the HSC-F0-20M-S-400 specimen (δ_{res} = 71.69 mm) at Blast 4, the MMFX specimen showed a reduction by 64.8% for residual displacement (no maximum displacement data was recorded at this blast).

Both specimens failed due to concrete crushing in the compression at Blast 4. The normal-strength specimen showed more severe crushing in the compression zone when compared to the specimen with high-strength steel reinforcement. A similar amount of secondary fragmentation was observed for both specimens from the high-speed video.

Despite the above it is noted that unlike the previous beams in the HSC series, the beam with No. 6 high-strength reinforcement did not show increased blast capacity (ability to withstand greater blast pressures) when compared to the companion with normal-strength steel bars. This can be explained by the fact that this HSC beam with high-strength bars was over-reinforced (ρ = 2.3% > ρ_{bal} = 1.7%), as also confirmed during the static tests.

The results from the SCC and HSC series clearly show that reinforced concrete beam response under blast loading can improve with the use of high-strength reinforcement. However, careful attention should be paid to ensure such beams are not over-reinforced ($\rho < \rho_{bal}$). In addition, such beams should be detailed with sufficient shear reinforcement to avoid brittle shear failures.

a) HSC-F0-20M-S-400 (70 psi)

b) HSC-F0-#6-S (70 psi)

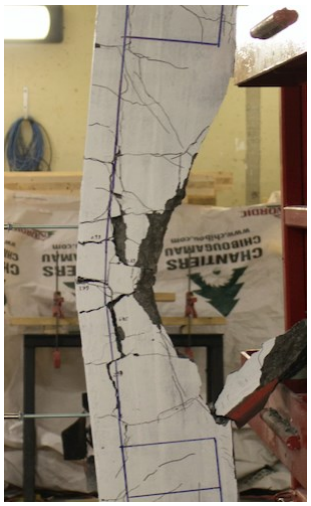

c) HSC-F0-20M-S-400

Mid-span failure at Blast 4 (70 PSI)

d) HSC-F0-#6-S

Mid-span damage at Blast 4 (70 PSI)

Figure 6-40 Photographs; effects of steel reinforcement type on HSC beams with No. 6/20M bars

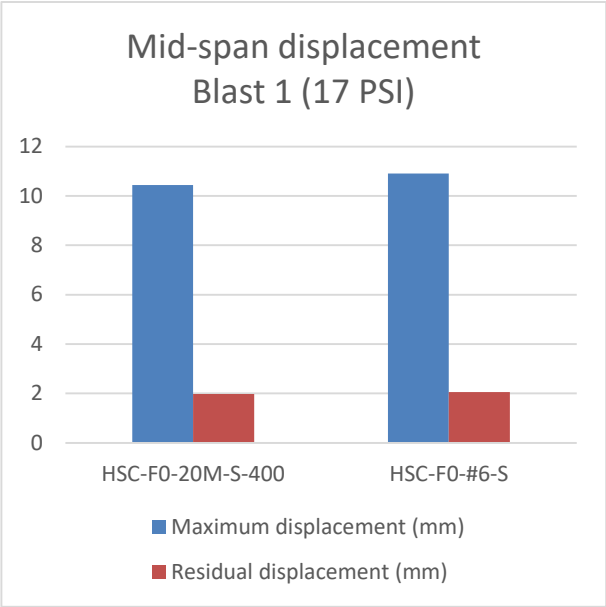

a) Blast 1

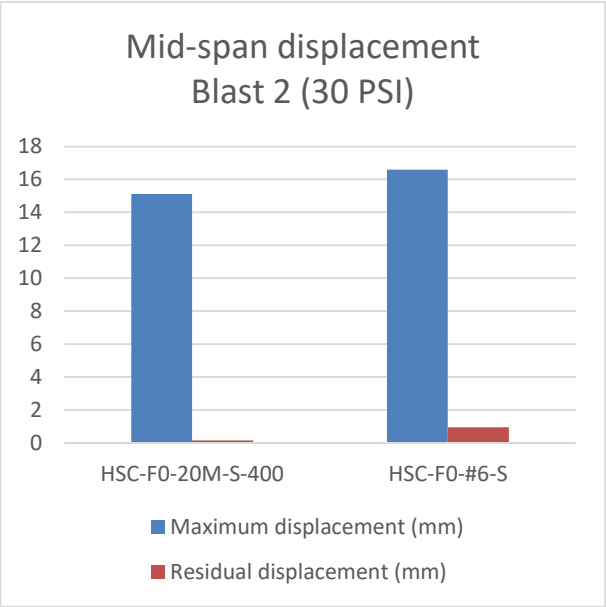

b) Blast 2

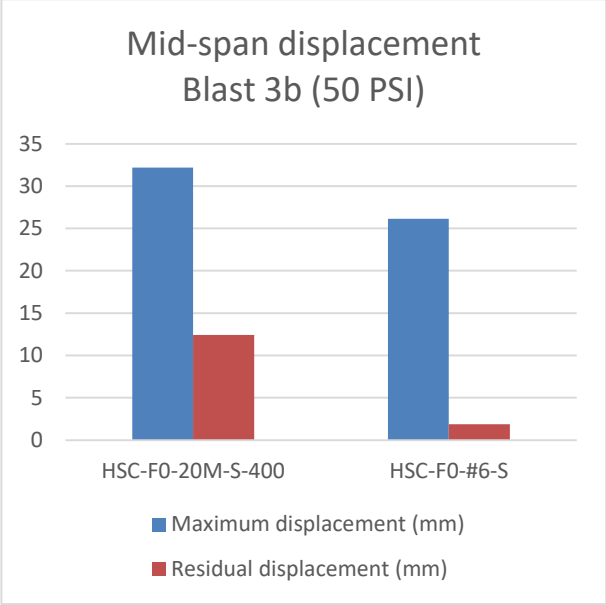

c) Blast 3b

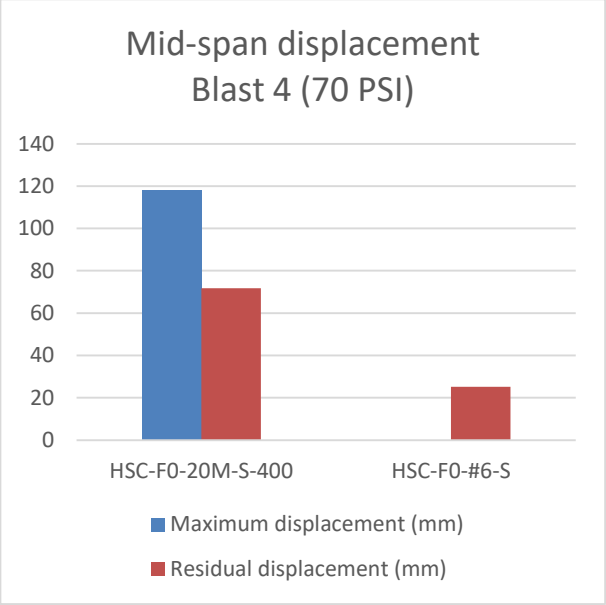

d) Blast 4

Figure 6-41 Maximum and residual displacements; effects of steel reinforcement type on HSC beams with No. 6/20M bars

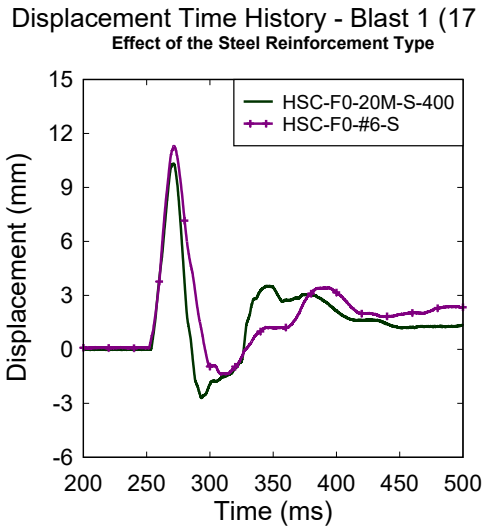

a) Blast 1

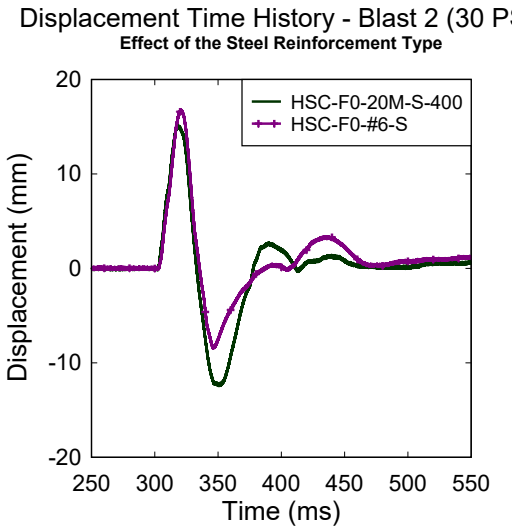

b) Blast 2

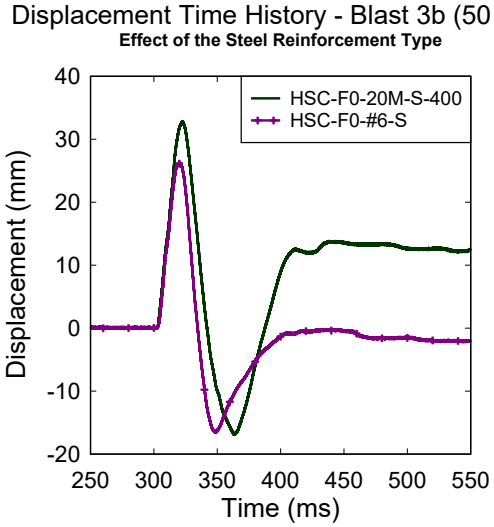

c) Blast 3b

Figure 6-42 Displacement time histories; effects of steel reinforcement type on HSC beams with No. 6/20M bars

6.6.2.EFFECTS OF STEEL REINFORCEMENT TYPE – HSFRC SPECIMENS

This next sub-section examines the effect of reinforcement type on the performance of companion beams built with HSFRC. The results clearly show benefits associated with the combined use of these two high-performance materials. Included in the comparison sets are HSFRC beams built with #4, #5/15M and #6/20M reinforcement.

6.6.2.1. HSCFRC beams with No. 4 steel bars

The first companion set in this series includes beams HSC-F1-#4-0-400 and HSC-F1-#4-S, which were both designed with high-strength concrete and 1% fibres. The differences include the use of high-strength steel and stirrups with 100 mm spacing in the shear span for the HSC-F1-#4-S specimen, while the HSC-F1-#4-0-400 specimen was built with conventional steel reinforcement and no stirrups. It is noted that despite the lack of shear reinforcement the HSC-F1-#4-0-400 failed in flexure due to the provision of fibres. Both specimens did not contain stirrups in the mid-span region, thus the main parameter affecting beam response is considered to be the longitudinal steel type. Photographs of the beams at failure are included in Figure 6-43. Comparative displacement bar charts and displacement-time history diagrams can be seen in Figure 6-44 and Figure 6-45, respectively.

Displacements of the two specimens at Blast 1 and Blast 2 are similar but slightly lower for the beam with high-strength steel (for HSC-F1-#4-S: δ_{max} = 9.06 mm & 19.18 mm, δ_{res} = 1.31 mm & 3.0 mm; for HSC-F1-#4-0-400: δ_{max} = 10.63 mm & 18.47 mm, δ_{res} = 3.71 mm & 4.1 mm). This is to be expected since the pre-yield stiffness of the two specimens is similar. Nonetheless, it is noted that the residual displacements of the high-strength specimen were lower by margins of 64.7% and 26.8% at these 2 blasts when compared to the companion with normal-strength steel bars. The effect on displacement control is more evident at subsequent blasts. At Blast 3a and Blast 3b, the maximum displacements for the HSC-F1-#4-0-400 specimen were 35.18 mm and 55.1 mm, which were significantly higher by 26.0% and 41.7% over those of the HSC-F1-#4-S specimen (δ_{max} = 26.02 mm and 37.65 mm) which had MMFX bars. The residual displacements of the HSC-F1-#4-0-400 specimen (δ_{res} = 15.61 mm and 32.26 mm) were 90.2% and 62.3% higher at these blasts when compared to beam HSC-F1-#4-S (δ_{res} = 1.53 mm and 12.16 mm).

As shown in Figure 6-43, cracking was also better distributed in the MMFX. Crack widths were also better controlled at equivalent blasts. Three major cracks were observed at Blast 2 for the normal-strength steel specimen, and the maximum crack width was measured at 0.4 mm. The high-strength specimen had several hairline cracks at Blast 2. At Blast 3a and Blast 3b, the maximum crack widths for the normal-strength steel specimen were 3.84 mm and 9.14 mm, respectively, and 2.07 mm and 5.02 mm for the high-strength steel specimen; increases of 46% and 45%, for the normal-strength steel HSFRC specimen.

The specimen reinforced with MMFX bars was also able to resist a higher magnitude of blast loading before failure. Whereas the HSC-F1-#4-0-400 specimen failed at Blast 4X (60 psi), the companion with high-strength steel survived up to Blast 4 (70 psi). Both specimens failed in flexure with concrete splitting in the tension zone and fibre pull-out at major crack locations. However, while three major cracks formed in the HSC-F1-#4-0-400 beam, only one major crack formed in the HSC-F1-#4-S beam (crack opening was also better controlled at the 60 psi blast). Due to the provision of fibres, both specimens did not exhibit significant amounts of secondary fragmentation at failure.

In summary the results demonstrate the benefit of combining HSFRC and high-strength reinforcement. The addition of fibres in HSC results in increased fragmentation resistance, improved tensile capacity and increased compressive toughness which allows the high-strength concrete beams to fully utilize the increased strength of the ASTM A1035 bars.

a) HSC-F1-#4-0-400 (60 psi)

b) HSC-F1-#4-S (70 psi)

c) HSC-F1-#4-0-400

Mid-span failure at Blast 3b (50 PSI)

d) HSC-F1-#4-0-400

Mid-span damage at Blast 4x (60 PSI)

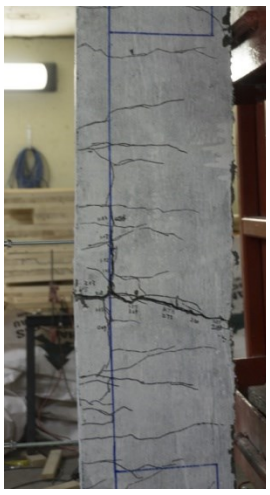

e) HSC-F1-#4-S

Mid-span failure at Blast 3b (50 PSI)

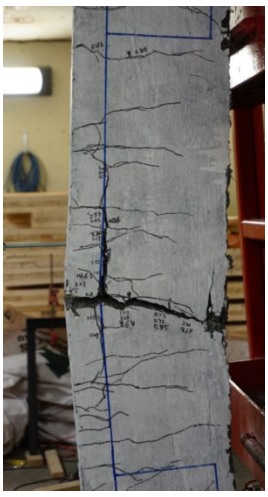

f) HSC-F1-#4-S

Mid-span damage at Blast 4 (70 PSI)

Figure 6-43 Photographs; effects of reinforcement type on HSFRC beams with No. 4 bars

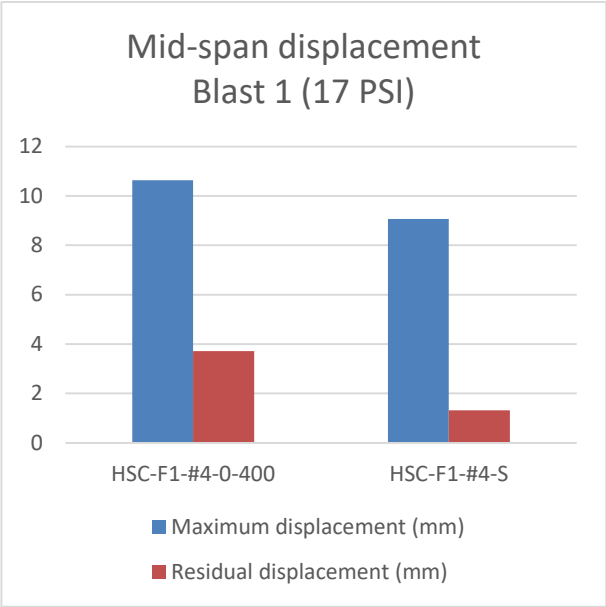

a) Blast 1

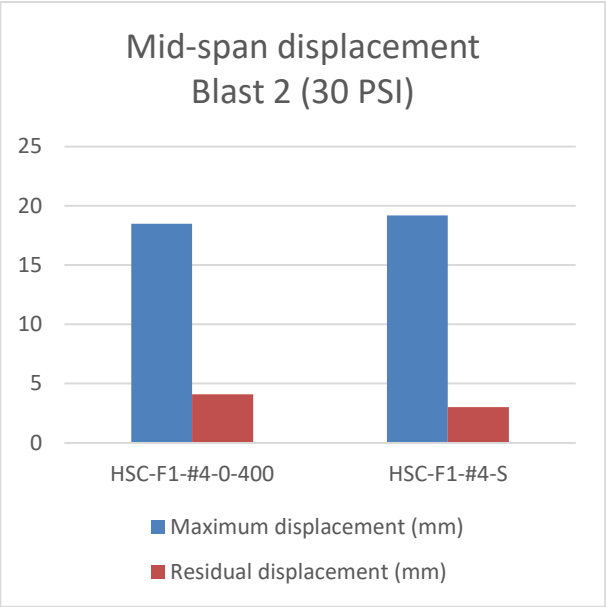

b) Blast 2

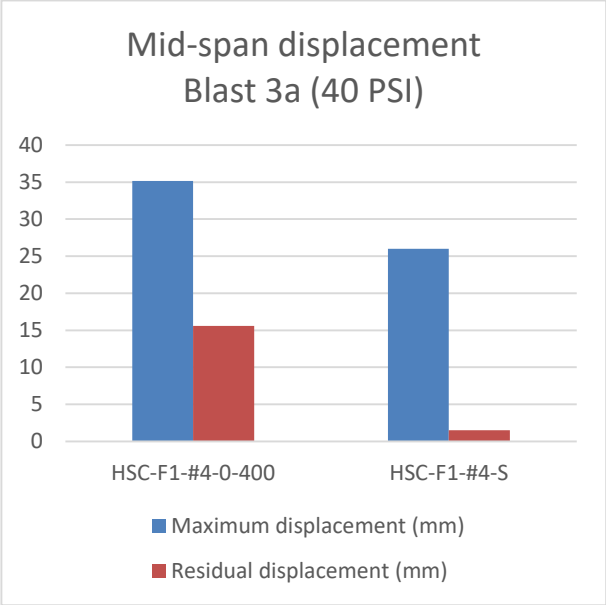

c) Blast 3a

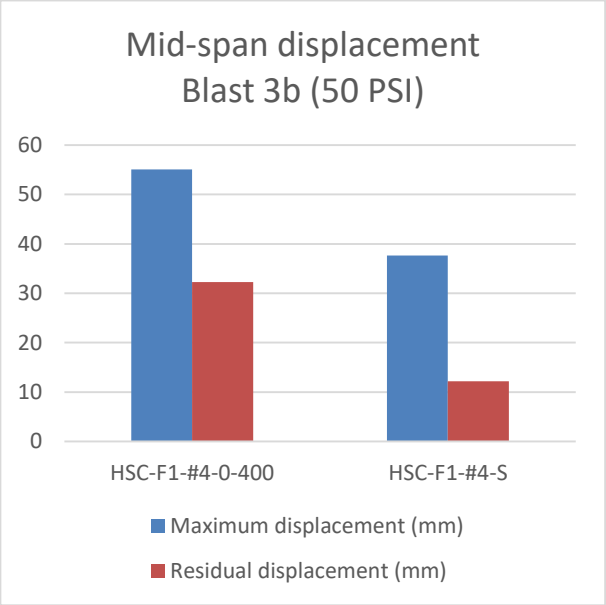

d) Blast 3b

Figure 6-44 Maximum and residual displacements; effects of reinforcement type on HSFRC beams with No. 4 bars

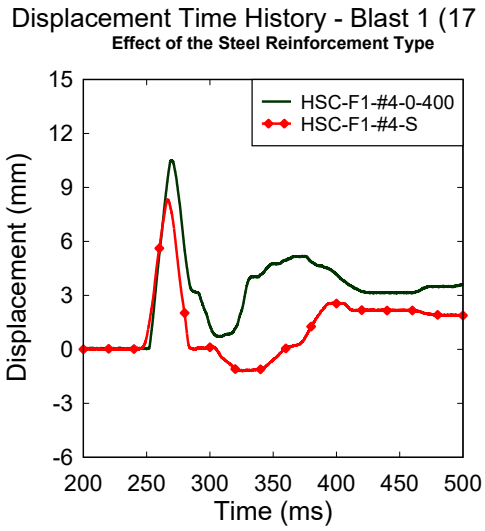

a) Blast 1

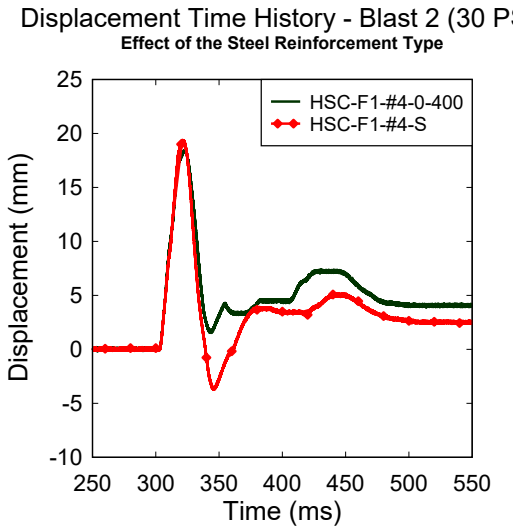

b) Blast 2

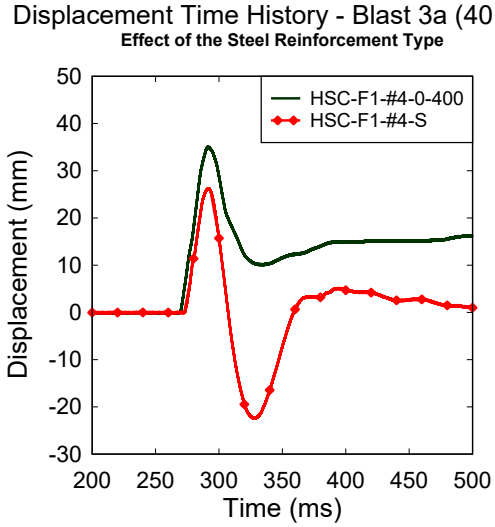

c) Blast 3a

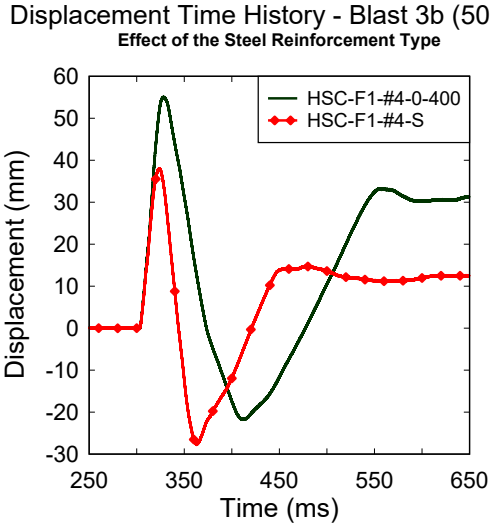

d) Blast 3b

Figure 6-45 Displacement time histories; effects of reinforcement type on HSFRC beams with No. 4 bars

6.6.2.2. HSFRC beams with No. 5/15M steel bars

Specimens HSC-F1-15M-0-400 and HSC-F1-#5-S were both constructed with high-strength concrete containing 1% steel fibres, but contained high-strength and normal-strength steel reinforcement, respectively. It is noted that no stirrups were provided in the HSC-F1-15M-0-400 beam, while stirrups with 100 mm spacing were provided in HSC-F1-#5-S (however as with the previous set, both specimens failed in flexure and did not contain stirrups in the midspan region). Photographs showing the specimens at failure are included in Figure 6-46. Comparative displacement bar charts and displacement-time history diagrams can be seen in Figure 6-47 and Figure 6-48, respectively.

The maximum and residual displacements of the HSC-F1-15M-0-400 and HSC-F1-#5-S specimens at Blast 1 and Blast 2, were similar with differences within margins of ±5% (HSC-F1-#5-S: δ_{max} = 9.2 mm & 14.6 mm, δ_{res} = 4.12 mm & 2.66 mm; HSC-F1-15M-0-400: δ_{max} = 10.05 mm & 15.02 mm, δ_{res} = 3.91 mm & 2.66 mm). When compared to the normal strength steel specimen, the high-strength steel specimen showed a reduction of 32.4% for maximum displacement (δ_{max} =22.51 mm vs. 33.31 mm) and 94.0% for residual displacement (δ_{res} = 0.6 mm vs. 10.08 mm), at Blast 3b. Similarly, at Blast 4, the MMFX specimen showed a reduction of 50% for maximum displacement (δ_{max} =39.47 mm vs. 78.91 mm) and 85.9% for residual displacement when compared to beam HSC-F1-15M-0-400 (δ_{res} = 7.7 mm vs. 54.68 mm).

In terms of major crack widths, the HSC-F1-#5-S specimen performed significantly better than the HSC-F1-15M-0-400 specimen. For both beams, the first major crack was observed after Blast 3b; it measured 3.81 mm for the normal-strength reinforced specimen and 0.78 mm for the high-strength reinforced specimen. The normal-strength reinforced specimen failed at Blast 4 since the fibre pulled out, with a maximum major crack width of 19.32 mm, compared to 2.67 mm for the high-strength steel specimen.

The HSC-F1-#5-S specimen was also able to withstand a larger blast before failure. This specimen failed at the maximum shock-tube driver pressure of 100 psi at Blast 6 due to rupture of the high-strength tensile bars, which corresponds to two additional blasts when compared to the companion HSFRC beam with normal-strength bars (failure at Blast 4). From the high-speed video it is evident that steel fibres were effective in controlling the formation of secondary fragments in both specimens.

As with the previous beam set in the HSFRC series, the results demonstrate important performance enhancements associated with the combined use of high-strength concrete, fibres and high-strength reinforcement. The beam in this series was able to larger blast pressures, fully utilizing the strength of the high-strength bars which ruptured in tension. The results also indicate the need to conservatively design HSFRC beams with high-strength bars in order to ensure sufficient reserve capacity to prevent brittle failures caused by rupture of steel reinforcement.

a) HSC-F1-15M-0-400
(70 psi)

b) HSC-F1-#5-S
(90 psi)

c) HSC-F1-15M-0-400

Mid-span failure at Blast 4 (70 psi)

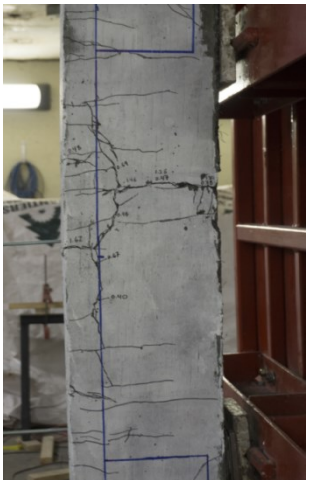

d) HSC-F1-#5-S

Mid-span damage at Blast 4 (70 psi)

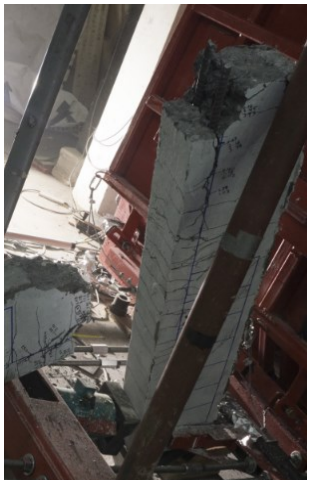

e) HSC-F1-#5-S

Mid-span failure at Blast 6 (100 psi)

Figure 6-46 Photographs; effects of reinforcement type on HSFRC beams with No. 5/15M bars

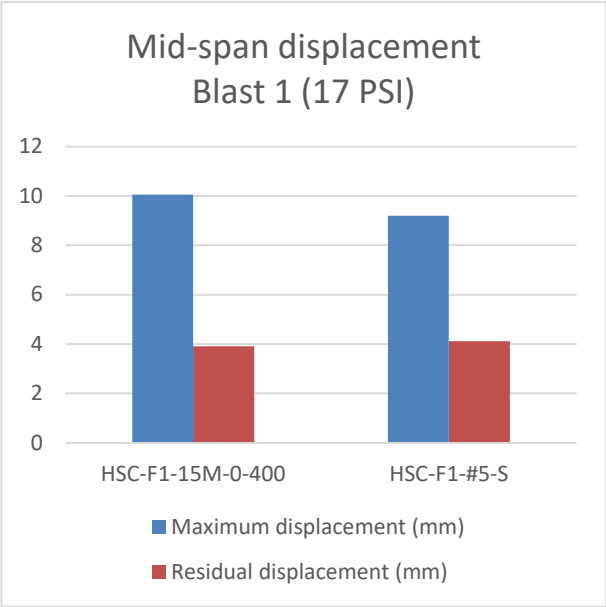

a) Blast 1

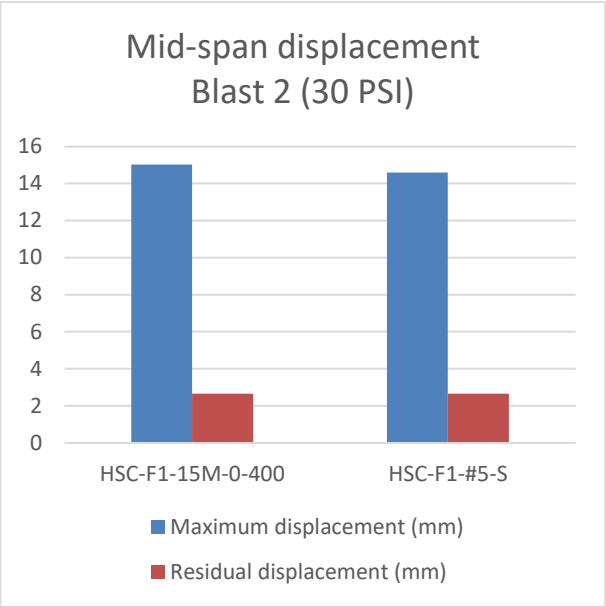

b) Blast 2

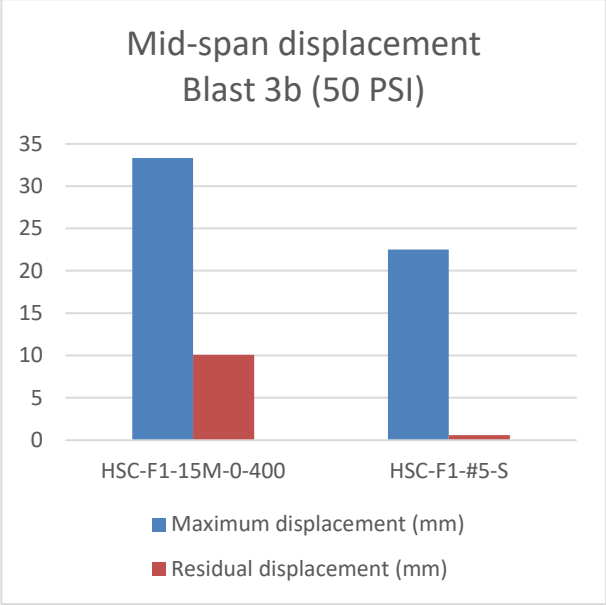

c) Blast 3b

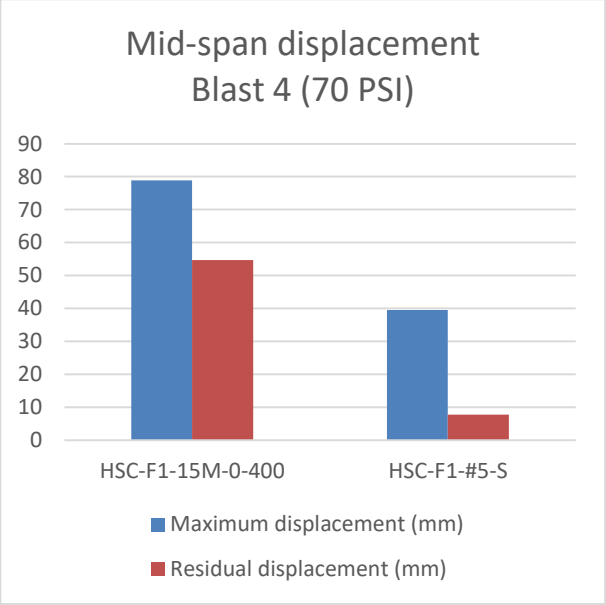

d) Blast 4

Figure 6-47 Maximum and residual displacements; effects of reinforcement type on HSFRC beams with No. 5/15M bars

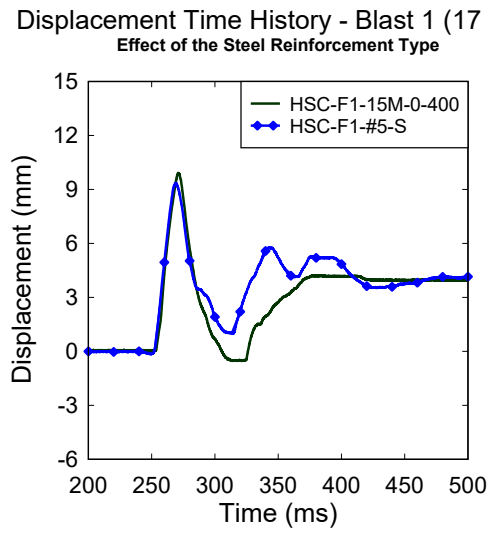

a) Blast 1

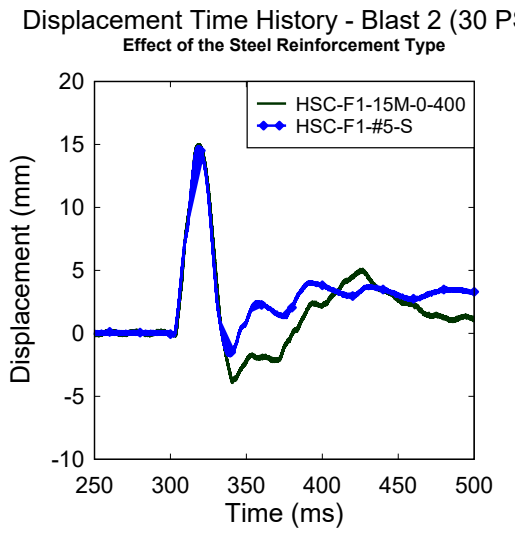

b) Blast 2

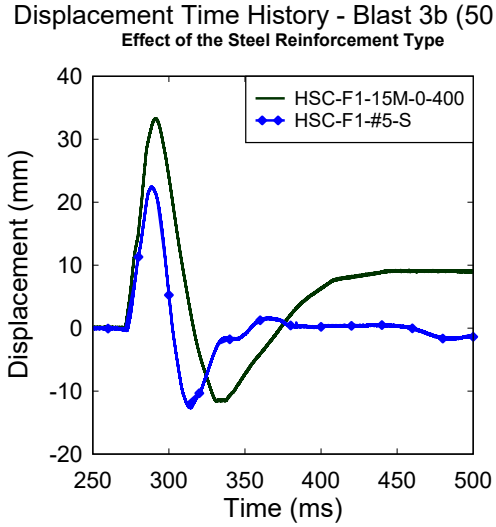

c) Blast 3b

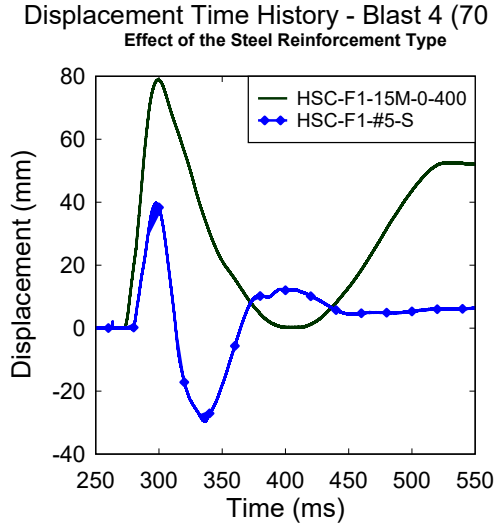

d) Blast 4

Figure 6-48 Displacement time histories; effects of reinforcement type on HSFRC beams with No. 5/15 M bars

6.6.2.3. HSFRC beams with No. 6/20M steel bars

The last companion set in the HSFRC beam series includes specimens HSC-F1-20M-S-400 and HSC-F1-#6-S, are discussed in this sub-section. Both beams were constructed with high-strength concrete containing 1% fibres and stirrups, but the former was reinforced with 20M (normal-strength bars A_s = 300 mm^2) and the latter was reinforced with #6 high-strength MMFX bars (A_s = 284 mm^2). Photographs of the beams at critical blast loadings are included in Figure 6-49. Comparative displacement bar charts and displacement-time history diagrams can be seen in Figure 6-50 and Figure 6-51, respectively.

The maximum and residual mid-span displacements for both specimens were quite similar after Blast 1 and Blast 2 (For the MMFX specimen: δ_{max} = 6.11 mm & 14.76 mm, δ_{res} = 1.31 mm & 2.41 mm; for the conventional steel specimen: δ_{max} = 9.21 mm & 14.91 mm, δ_{res} = 2.29 mm & 2.2 mm). At Blast 3b, the maximum and residual displacements of the high-strength specimen HSC-F1-#6-S (δ_{max} = 22.33 mm, δ_{res} = 1.19 mm) were lower than those of the normal-strength HSC-F1-20M-S-400 beam (δ_{max} = 27.64 mm, δ_{res} = 4.04 mm) by 19.2% and 70.5%, respectively. At Blast 4, maximum displacement was 46.3% lower (δ_{max} = 35.99 mm vs. 67.03 mm) and residual displacement was 87.2% lower (δ_{res} = 5.35 mm vs. 41.84 mm) for the high-strength steel specimen compared to the normal-strength steel specimen.

In terms of major crack width, the specimen reinforced with high-strength bars showed narrower crack widths than the other specimen with normal-strength bars. The major crack for both specimens was observed at Blast 3b, and the width measured 1.08 mm for the HSC-F1-#6-S beam and 1.48 mm for HSC-F1-20M-S-400 beam. At Blast 4, the maximum major crack was 1.92 mm for the high-strength reinforcement specimen compared to 8.01 mm for the normal-strength reinforcement specimen.

For the HSC-F1-20M-S-400 specimen, concrete began to crush at Blast 4 (70 psi), with failure at the next blast (80 psi; Blast 5) due to crushing of concrete in the compression zone, and fibre pullout in the tension zone. The HSC-F1-#6-S specimen withstood two additional blast applications after the 70 psi shot and failed at Blast 6 (100 psi). It is noted that unlike the specimen with #5 high-strength bars, rupture of the tension steel reinforcement was prevented when increasing the bar size to #6 in this specimen, however the impulse from Blast 6 was too large and resulted in the release of the beam from the supports.

The results show that the combined use of high-strength concrete, fibres and #6 high-strength bars resulted in significant improvements in blast performance when compared to the companion beam with normal-strength bars. The results also show that the use of HSFRC is better-suited for high-strength reinforcement when compared to plain HSC; while use of #6 high-strength bars resulted in over-reinforced behaviour in the HSC beam, the increased compressive strain capacity of HSFRC allowed for the use of the larger amount of high-strength bars without triggering over-reinforced conditions.

a) HSC-F1-20M-S-400
(80 psi)

b) HSC-F1-#6-S
(90 psi)

c) HSC-F1-20M-S-400

Mid-span damage at Blast 4 (70 psi)

d) HSC-F1-20M-S-400

Mid-span failure at Blast 5x (80 psi)

e) HSC-F1-#6-S

Mid-span damage at Blast 4 (70 psi)

f) HSC-F1-#6-S

Mid-span damage at Blast 5 (90 psi)

Figure 6-49 Photographs; effects of steel reinforcement type on HSFRC beams with No. 6/20M bars

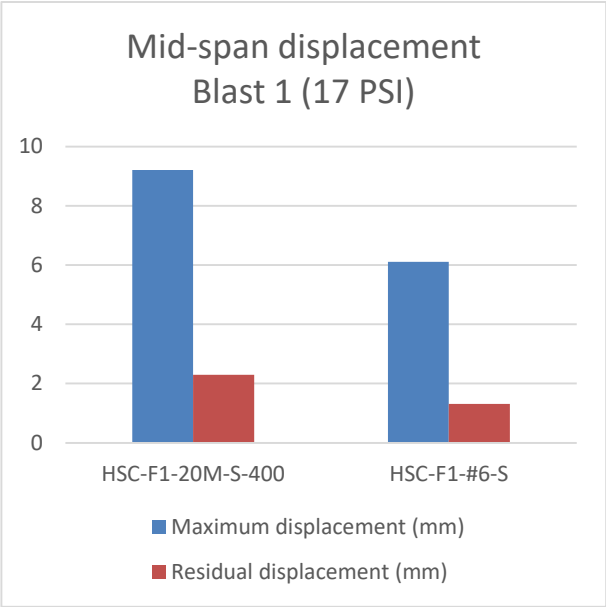

a) Blast 1

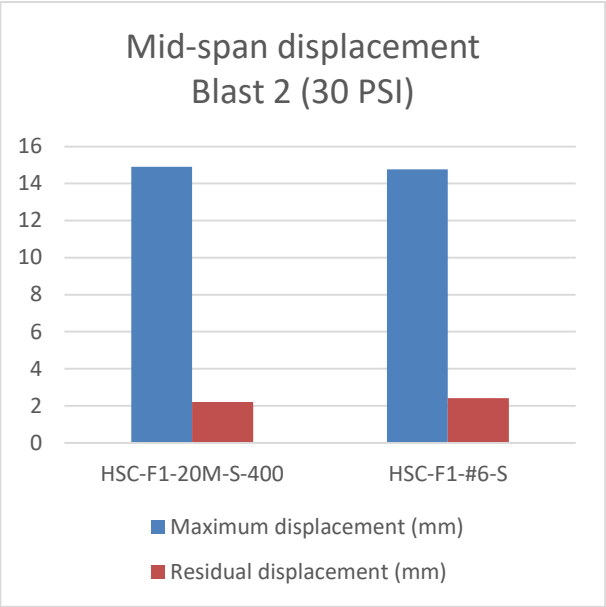

b) Blast 2

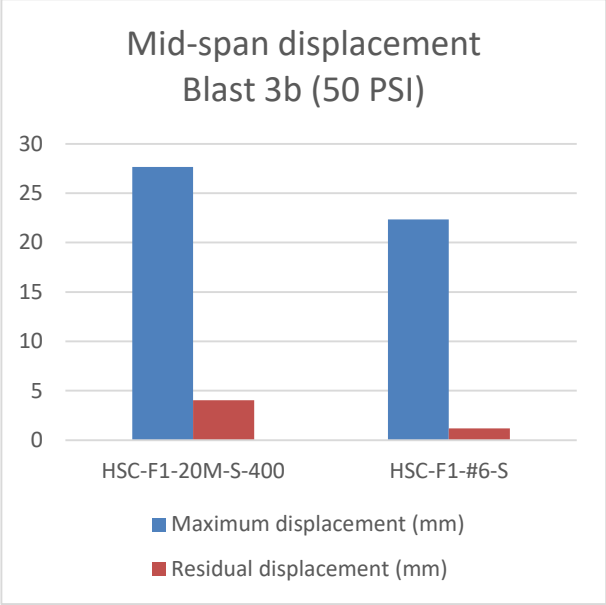

c) Blast 3b

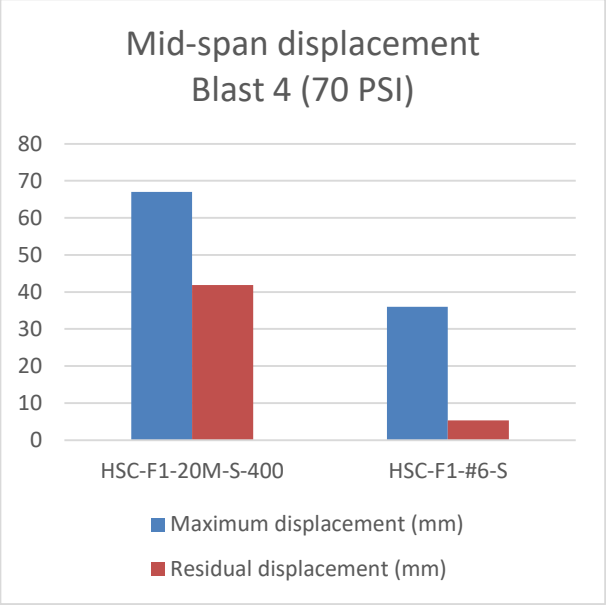

d) Blast 4

Figure 6-50 Maximum and residual displacements; effects of steel reinforcement type on HSFRC beams with No. 6/20M bars

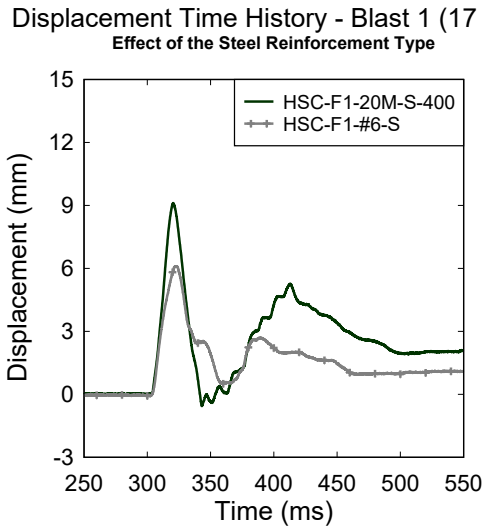

a) Blast 1

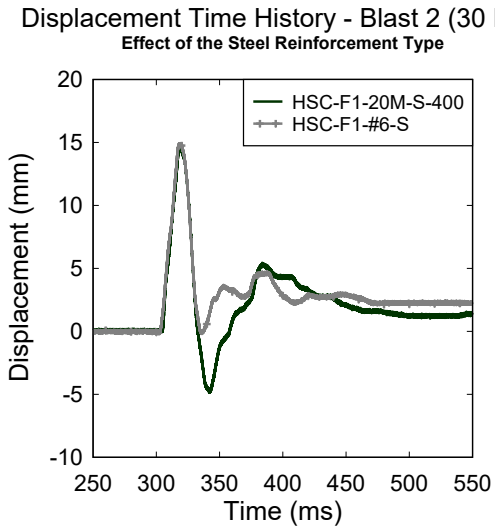

b) Blast 2

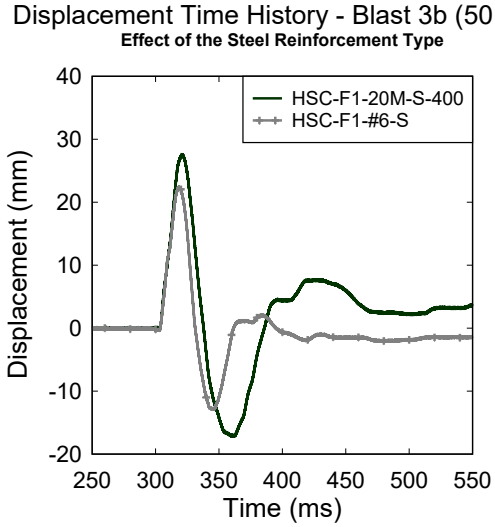

c) Blast 3b

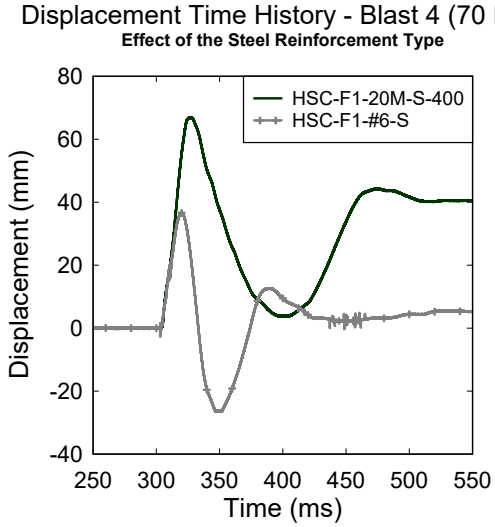

d) Blast 4

Figure 6-51 Displacement time histories; effects of steel reinforcement type on HSFRC beams with No. 6/20M bars

6.7.DAMAGE TOLERANCE AND FRAGMENTATION

The magnitude of blast load resistance and the ability to control mid-span displacements are the principal factors used to assess the blast performance of reinforced concrete beams. Secondary fragmentation and failure mode are also important criteria to be considered. Figure 6-53 shows stills from high-speed video showing secondary fragmentation formation in the plain concrete and HSFRC specimens. One can see the effect of concrete type, reinforcement ratio and fibre reinforcement by comparing the stills from companion beams.

As noted previously the use of plain HSC did not result in increased blast capacity when compared to plain normal-strength concrete (SCC), but resulted in reductions in maximum and residual displacements. Nonetheless, in both cases significant formation of secondary fragments was observed at failure for all beams in the plain SCC and HSC specimens.

The use of a larger reinforcement ratio generally improved blast resistance and displacement control of beams in the HSC series. However, as seen in the high-speed video stills, fragmentation at failure was high for all beams in this series, regardless of reinforcement ratio. For the HSC series, the No. 4 and No. 5 specimens failed due to severe spalling with complete loss of concrete cover, while concrete cover stayed in place for the No. 6 specimen.

The results from this study show that the use of steel fibre is effective in increasing blast resistance and controlling displacements in beams subjected to blast loading. Another important benefit was the ability of steel fibres to increase damage tolerance and reduce fragmentation. The use of 1% steel fibres increased the tensile resistance, toughness and fragmentation resistance of the high-strength concrete. This allowed the HSFRC beams to prevent failure mechanisms such as concrete spalling and sudden crushing. In addition, as clearly evidenced in the high-speed video stills, the provision of steel fibres was effective in reducing the amount of secondary fragmentation in the HSC beams, even at failure. Furthermore, the use of fibres resulted in a better control of cracking.

Reinforcing the beams with high-strength steel bars improved the blast performance of the beams by increasing blast capacity and enhancing control of displacements. However, in the HSC series, the use of high-strength reinforcement tended to increase brittleness when compared to companion beams with normal-strength bars. The combined use of fibres and high-strength reinforcement in the HSFRC series results in good fragmentation resistance, even as the reinforcement strength was increased.

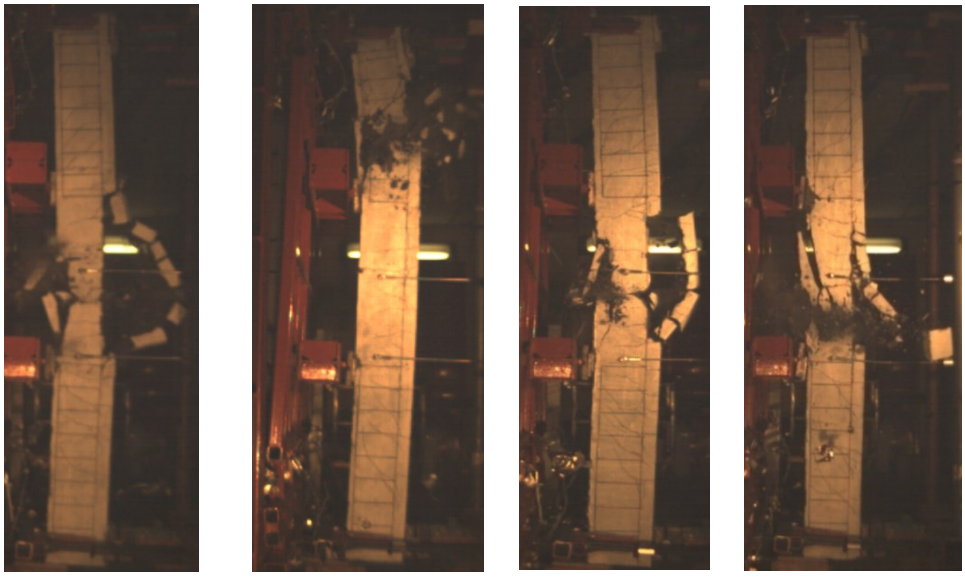

SCC-F0-#4-S SCC-F0-#5-S HSC-F0-#4-S HSC-F0-#5-S

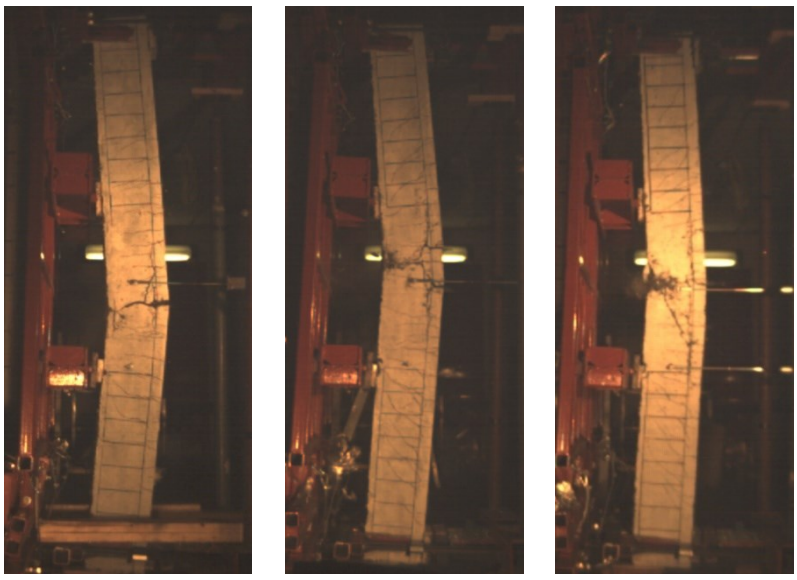

HSC-F1-#4-S HSC-F1-#5-S HSC-F1-#6-S

Figure 6-52 Secondary fragmentation formations in plain concrete and HSFRC from high-speed video

SCC-F0-#4-S

SCC-F0-#5-S：

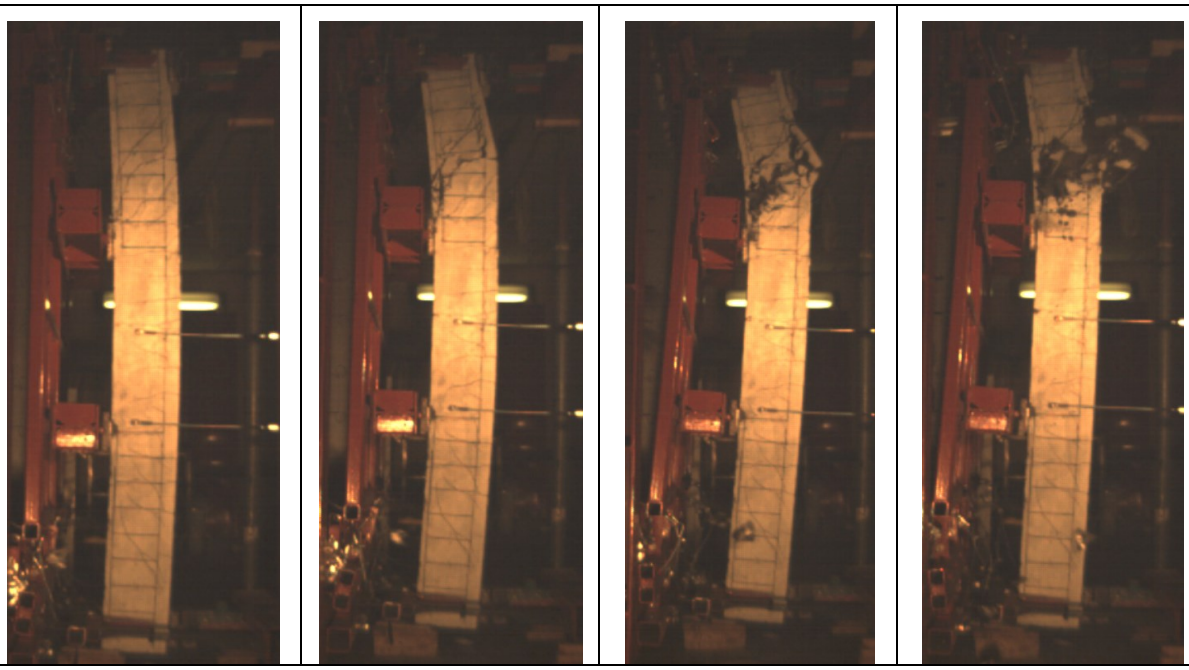

HSC-F0-#4-S：

HSC-F0-#5-S：

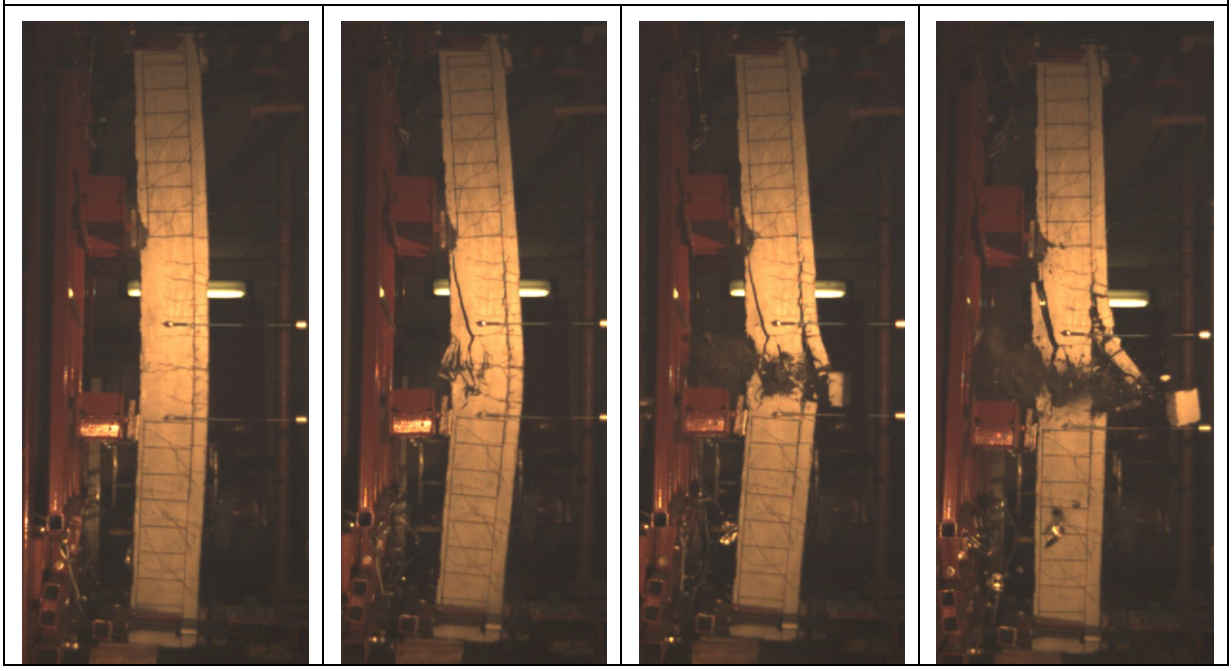

HSC-F1-#4-S：

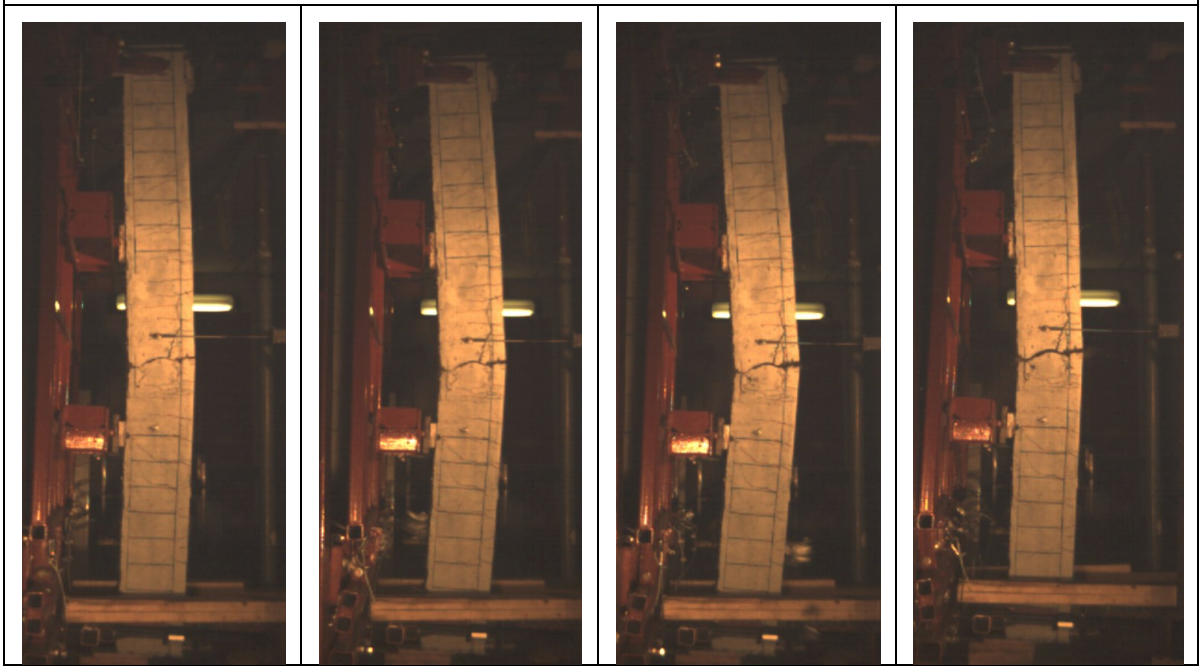

HSC-F1-#5-S：

HSC-F1-#6-S：

Figure 6-53 Failure sequence for plain concrete and HSFRC specimens from high-speed video

CHAPTER 7. ANALYSIS OF STATIC AND DYNAMIC TESTS

7.1. CHAPTER OVERVIEW

This section presents the analysis of the beams tested in the research program. The dynamic analysis is conducted by first developing resistance curves for each beam using dynamic material properties and a lumped inelasticity approach. Thereafter the response of the beams is predicted using single-degree-of-freedom (SDOF) analysis and software *RC-Blast* (Jacques 2014). For completeness, the analysis of the statically tested beams is also presented. Section 7.2 introduces the material models which are used in the sectional analysis. Various equations which are used to account for dynamic effects on material properties are summarized in Section 7.3. Section 7.4 presents the methodology used to develop the resistance curves, as well as an overview of the analysis procedure in software *RCBlast*. The static and dynamic analysis results are summarized in Sections 7.5 and 7.6. Finally, Section 7.7 presents a sensitivity analysis which examines the effect of modelling parameters (material and DIF model selection) on the analytical predictions.

7.2. MATERIAL MODELS

This section introduces the stress-strain models for concrete, HSFRC and steel which are used to develop the member resistance curves.

7.2.1. PLAIN CONCRETE MODELS

The unconfined compression models proposed by Popovics (1973) and Cusson and Paultre (1995) were selected to describe the stress-strain behaviour of plain concrete in the HSC and SCC beams. Concrete in tension was assumed to follow a linear-elastic response, with maximum tensile strength equal to $0.33\sqrt{f_c'}$ and a slope equal to the modulus of elasticity of plain concrete.

Popovics (1973)

The Popovics (1973) model is the default model considered for plain unconfined concrete in compression. In this model, equation (7–1) is used for both the ascending and descending branches of the stress-strain curve. The model is applicable for concrete with strengths ranging from 15 MPa to 125 MPa. The parameter k controls the slope of the descending branch and can be approximated using equation (7–2) as proposed by Collins and Mitchell (1990). Other parameters such as the curve-fitting factor n, initial tangent modulus E_c and strain at peak stress ϵ_0 can be computed using the relationships in equations (7–2), (7-3), (7-4) and (7–5).

$$f_c(\varepsilon_c) = \frac{n(\epsilon_c/\epsilon_0)}{n-1+(\epsilon_c/\epsilon_0)^{nk}} f_c' \tag{7–1}$$

$$k = \begin{cases} 1.0 & \epsilon_c/\epsilon_0 \leq 1.0 \\ 0.67 + \dfrac{f_c'}{62} & \epsilon_c/\epsilon_0 > 1.0 \end{cases} \tag{7–2}$$

$$n = 0.8 + \frac{f_c'}{17} \tag{7–3}$$

$$\epsilon_0 = \frac{f_c'}{E_c}\left(\frac{n}{n-1}\right) \tag{7–4}$$

$$E_c = 3300\sqrt{f_c'} + 6900 \tag{7–5}$$

Cusson & Paultre (1995)

The Cusson & Paultre (1995) confinement model can be adapted to predict the stress-strain response of normal and high-strength unconfined concrete. The model combines the same ascending branch used by Popovics (1973) and a descending branch which modifies an expression proposed by Fafitis and Shah (1985). The stress-strain relationships in this model are presented in equation (7–6). Coefficients n and k_{1u} can be obtained from equations (7–7) and (7–8). The curve-fitting factor n can be computed using equation (7–7), and for unconfined concrete, the coefficient k_{2u} can be taken as 1.5. The modulus of elasticity is estimated using equation (7–5). Finally, the strain at peak stress (ε_0) can be obtained using equation (7–9), while the strain ε_{50cu} can be taken as 0.004 mm/mm in the absence of test data.

$$f_c(\varepsilon_c) := \begin{cases} f_{cu}'\left[\dfrac{n(\varepsilon_c/\varepsilon_0)}{n-1+(\varepsilon_c/\varepsilon_0)^n}\right] & \text{for } \varepsilon_c \leq \varepsilon_0 \\ f_c' \cdot exp[k_{1u}(\varepsilon_c - \varepsilon_0)^{k_{2u}}] & \text{for } \varepsilon_c > \varepsilon_0 \end{cases} \tag{7–6}$$

$$n = \frac{E_c}{E_c - (f_c'/\varepsilon_0)} \tag{7–7}$$

$$k_{1u} = \frac{\ln(0.5)}{(\varepsilon_{50cu} - \varepsilon_0)^{k_{2u}}} \tag{7–8}$$

$$\varepsilon_0 = 0.001684 + 0.000016 f_c' \tag{7–9}$$

Sample plain unconfined concrete stress-strain curves

Figure 7-1 shows the stress-strain curves for normal and high-strength concretes with target strengths of 50 MPa and 100 MPa as predicted by both models. It can be seen that before reaching peak stress, the stiffness predicted by the Popovics model is higher when compared to the Cusson & Paultre model, while this model predicts a more gradual descending branch (stiffer post-peak response) when compared to the Popovics model.

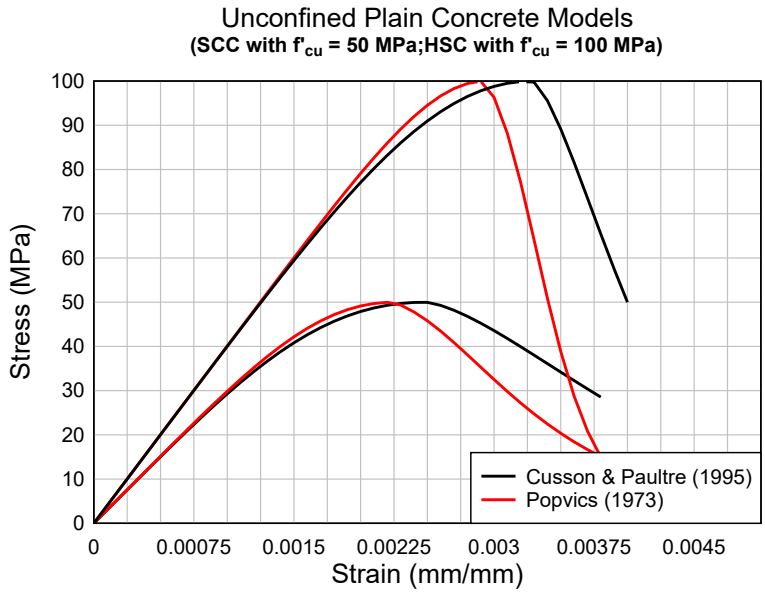

Figure 7-1 Unconfined plain concrete stress-strain models sample

7.2.2. STEEL FIBRE REINFORCED CONCRETE MODELS

Three models were considered to model the stress-strain behaviour of the high-strength fibre-reinforced concrete (HSFRC), including two compression models and one tension model. The behaviour of unconfined HSFRC in compression was taken into account using the models proposed by Ou et al. (2012) or Mansur et al. (1999). Tensile response is taken into account using the model proposed by Lok and Pei (1998). Figure 7-2 (b) shows typical stress-strain curves for HSFRC as obtained using these models.

Ou et al. (2012)

The stress-strain model proposed by Ou et al. (2012) modifies a model originally proposed by Carreira and Chu (1985), and can be used to predict the stress-strain response of normal and high-strength steel fibre-reinforced concrete in compression. In this model, Equation (7–10) is used for both the ascending and descending branches of the stress-strain curve. The ultimate compressive

strength (f'_{cuf}), the strain at peak stress (ε_{0f}) and the coefficient β are defined by equations (7–11), (7-12) and (7–13), where the variables v_f, L_f and d_f are the fibre content, the fibre length, and the fibre diameter, respectively.

$$f_{cf}(\varepsilon_c) := f'_{cf}\left[\frac{\beta\left(\frac{\varepsilon_c}{\varepsilon_{0f}}\right)}{\beta - 1 + \left(\frac{\varepsilon_c}{\varepsilon_{0f}}\right)^{\beta}}\right] \tag{7–10}$$

$$f'_{cuf} = f'_{cu} + 2.35\left(\frac{v_f L_f}{d_f}\right) \tag{7–11}$$

$$\varepsilon_{0f} = \varepsilon'_c + 0.0007\left(\frac{v_f L_f}{d_f}\right) \tag{7–12}$$

$$\beta = 0.71\left(\frac{v_f L_f}{d_f}\right)^2 - 2.00\left(\frac{v_f L_f}{d_f}\right) + 3.05 \tag{7–13}$$

Mansur et al. (1999)

The model proposed by Mansur et al. (1999) is the default model which is used to predict the stress-strain response of unconfined high-strength fibre-reinforced concrete in compression. The model is applicable for HSFRC with strengths ranging from 70 to 120 MPa. According to this model the ascending and descending branches of the stress-strain curve can be obtained using equation (7–14). The ascending branch follows the same form of the relationship proposed by Carreira and Chu (1985), with parameters n, E_c, f'_{cf}, and ε_{0f} defined by equations (7–15), (7–16) and (7–17). For the descending branch, the factors, k_{f1} and k_{f2} account for the effect of steel fibres on post-peak stress-strain response, and are obtained using equations (7–18) and (7–19). The variables v_f, L_f and d_f are the fibre content, the fibre length and the fibre diameter, respectively.

$$f_{cf}(\varepsilon_c) := \begin{cases} f'_{cf}\left[\dfrac{n(\varepsilon_c/\varepsilon_{0f})}{n - 1 + (\varepsilon_c/\varepsilon_{0f})^n}\right] & \text{for } \varepsilon_c \le \varepsilon_0 \\ f'_{cf}\left[\dfrac{k_{f1}n(\varepsilon_c/\varepsilon_{0f})}{k_{f1}n - 1 + (\varepsilon_c/\varepsilon_{0f})^{k_{f2}n}}\right] & \text{for } \varepsilon_c > \varepsilon_0 \end{cases} \tag{7–14}$$

$$n = \frac{E_c}{E_c - \left(f'_{cf}/\varepsilon_{0f}\right)} \tag{7–15}$$

$$E_c = \left(10300 - 400v_f\right) {f'_{cf}}^{1/3} \quad (7\text{–}16)$$

$$\varepsilon_{0f} = [0.00050 + 0.00000072(\frac{v_f L_f}{d_f})] {f'_{cf}}^{0.35} \quad (7\text{–}17)$$

$$k_{f1} = (\frac{50}{f'_{cf}})^{3.0}[1 + 2.5(\frac{v_f L_f}{d_f})^{2.5}] \quad (7\text{–}18)$$

$$k_{f2} = (\frac{50}{f'_{cf}})^{1.3}[1 - 0.11(\frac{v_f L_f}{d_f})^{-1.1}] \quad (7\text{–}19)$$

Lok & Pei (1998)

The model proposed by Lok & Pei (1998) is used to predict the tensile stress-strain response of HSFRC. The model consists of a tri-linear stress-strain curve. The first branch of the curve is linear with a peak stress equal to the cracking strength of HSFRC (estimated using equation (7–20)), and a slope equal to the modulus of elasticity of HSFRC (estimated using equation (7–5)). After reaching the cracking stress, the curve follows a bi-linear relationship which can either be ascending or descending. The first linear portion ends at stress and strain values ($f_2^* \; and \; \varepsilon_2^*$) defined using equations (7–21) and (7–22). In this thesis, the matrix bond strength τ_{bond} of HSFRC is taken as 6 MPa, which falls in the range of bond strength values suggested by Kutzing (2000). According to this study, if the concrete strength exceeds 70 MPa, the bond strength is estimated to be between 5-6 MPa (Grunewald 2004). The parameter E_{fp} is the modulus of the steel fibres and is taken as 200 GPa. The aspect ratio (L_f/d_f) and fibre content (v_f) are the other parameters which influence the stress f_2^* and strain ε_2^*. The second portion of the post-cracking curve is linearly descending and reaches zero stress at a strain of 0.02 (Lok and Pei, 1998).

$$f_{ctf} = 0.33\left(f'_{cf}\right)^{0.5} \quad (7\text{–}20)$$

$$f_2^* = \frac{1}{2} v_f \tau_{bond} \frac{L_f}{d_f} \quad (7\text{–}21)$$

$$\varepsilon_2^* = \tau_{bond} \frac{L_f}{d_f} \frac{1}{E_{fp}} \quad (7\text{–}22)$$

Sample HSFRC stress-strain curves

Figure 7-2 (a) shows the stress-strain curves for HSFRC with compressive strength of 100 MPa as predicted by the Ou et al. (2012), Mansur et al. (1999) and Lok and Pei (1998) models. It can be seen that the Ou and Mansur models show similar peak and post-peak stress-strain responses. At 1% fibre content, the Lok and Pei model predicts a tension softening response for the HSFRC.

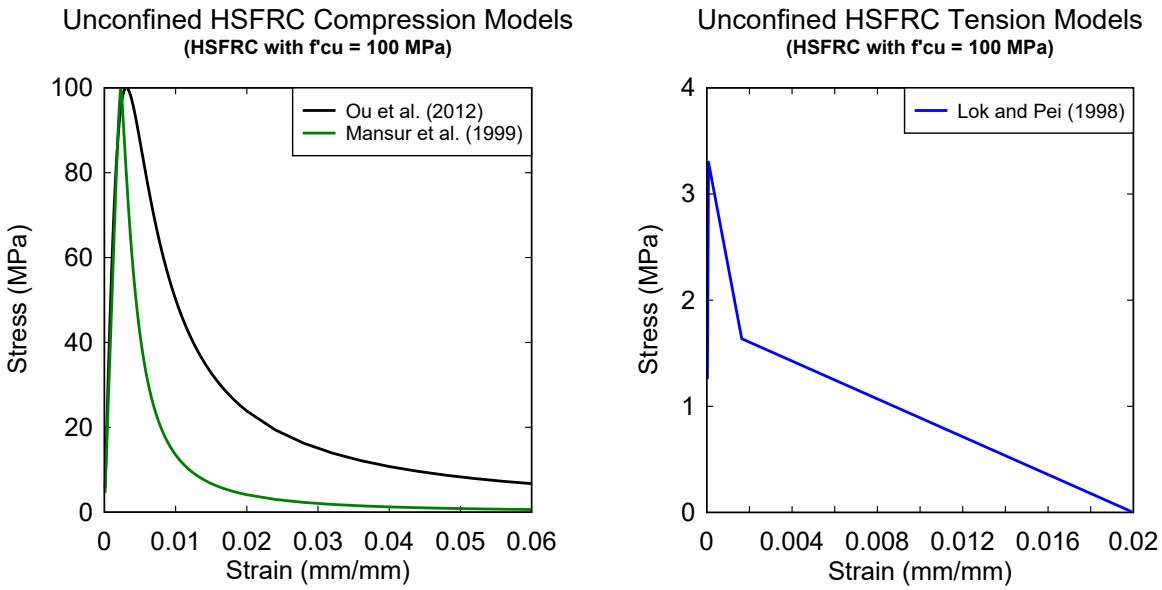

a) HSFRC unconfined compression models b) HSFRC unconfined tension model

Figure 7-2 Unconfined HSFRC stress-strain models sample

7.2.3. HIGH-STRENGTH STEEL (MMFX2) MODELS

The tensile response of the high-strength MMFX steel reinforcement was taken into account using either the experimental coupon data or a model proposed by the ACI Task Group ITG-6 (2010). Sample experimental coupon data for the No. 4, No. 5, and No. 6 steel reinforcement are shown in Figure 7-3. The three-part stress-strain relationship proposed by the ACI ITG-6R (2010) is presented in equation (7–23). The first portion of the curve is linear-elastic up to a strain, ε_s = 0.0024, with a slope corresponding to the modulus of elasticity of the high-strength steel (200,000 MPa). The second branch of the curve is non-linear and follows a parabolic response until reaching an ultimate stress of 1040 MPa at a strain of ε_s = 0.02. In the final branch, the stress remains constant at 1040 MPa until reaching the rupture strain of the high-strength steel (taken as ε_s = 0.06 in the model). Figure 7-3 compares the model prediction to the stress-strain data from the coupon tests; it can be seen that the ACI ITG-6R model closely matches the data obtained from the coupon tests, with conservative predictions of ultimate stress.

$$f_s(\varepsilon_s) := \begin{cases} 200{,}000\varepsilon_s(MPa) & \text{for } \varepsilon_s \le 0.0024 \\ 1170 - \dfrac{2.96}{\varepsilon_s + 0.0019}(MPa) & \text{for } 0.0024 < \varepsilon_s \le 0.02 \\ 1040(MPa) & \text{for } 0.02 < \varepsilon_s \le 0.06 \end{cases} \qquad (7\text{–}23)$$

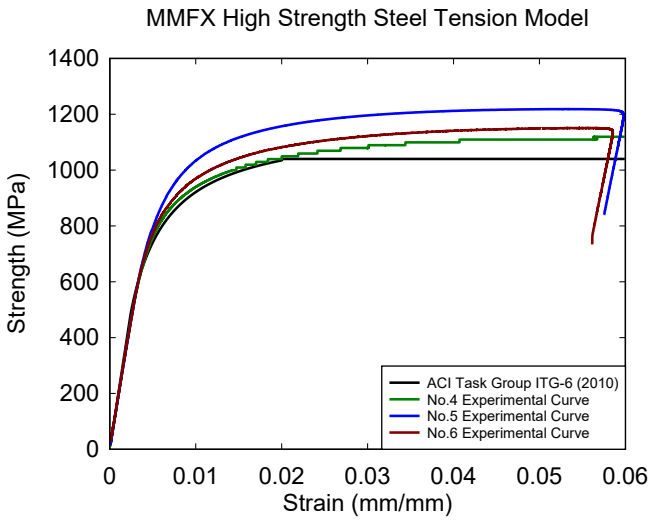

Figure 7-3 High strength steel reinforcement coupon data and ACI ITG-6R model

7.3. DYNAMIC INCREASE FACTORS

Concrete and steel properties are affected by strain-rate. This section presents several models which were used to account for dynamic effects in concrete, HSFRC and steel reinforcement.

7.3.1.UFC-3-340-02 (2008) Design Dynamic Increase Factors

Table 7-1 shows the dynamic increase factor proposed by UFC-3-340-02 (2008). The UFC-3-340-02 (2008) gives conservative DIF values which can be used in the blast-resistant design of reinforced concrete members. Unlike other models, these design values are not dependent on the strain rate. In this research, the beam specimens were primarily subjected to "bending" stresses and were tested under "far design range" blast loads, which results in DIF values of 1.17/1.05 at yield/ultimate for the reinforcing bars and 1.19 for concrete in compression.

Table 7-1 Dynamic increase factors for design of reinforced concrete elements (Adapted from UFC-3-340-02, 2008)

Type of stress	Far design range			Close-in design range		
	Reinforcing bars		Concrete	Reinforcing bars		Concrete
	f_{dy}/f_y	f_{du}/f_u	f'_{dc}/f'_c	f_{dy}/f_y	f_{du}/f_u	f'_{dc}/f'_c
Bending	1.17	1.05	1.19	1.23	1.05	1.25
Diagonal tension	1.00	-	1.00	1.10	1.00	1.00
Direct shear	1.10	1.00	1.10	1.10	1.00	1.10
Bond	1.17	1.05	1.00	1.23	1.05	1.00
Compression	1.10	-	1.12	1.13	-	1.16

7.3.2.DIF MODELS FOR CONCRETE

Under high-strain rate dynamic loading, the compressive and tensile strengths of concrete are increased. The apparent increase in strength can be taken into account using various strain rate-dependant dynamic increase factor (DIF) models. In this research two DIF models are considered for plain concrete in compression: CEB (1990) and the Saatcioglu et al. (2011). The DIF of HSFRC in compression is considered using the model proposed by Zhang and Mindness (2011). The dynamic response of concrete and HSFRC in tension is taken into account using the equations proposed by Malvar and Ross (1998). In addition, the design dynamic increase factors proposed by the UFC-3-340-02 (2008) were also considered for analysis.

CEB (1990)

The Euro-international Concrete Committee proposed the relationships shown in equations (7–24) and (7–25) to define the dynamic increase factor for plain concrete in compression (DIF_c). The parameter $\dot{\varepsilon}$ represents the dynamic strain rate while $\dot{\varepsilon}_s$ is a constant representing the quasi-static strain rate (30 x 10^{-6} s^{-1}). It is noted that the parameter α is function of the unconfined compressive strength of concrete (f'_{cu}), with the model predicting reduced strain-rate sensitivity for HSC when compared to NSC. Assuming a strain-rate of $\dot{\varepsilon}_s$= 1 s^{-1} for the beams tested in the shock-tube, this model predicts a DIF_c = 1.14 for unconfined concrete in compression.

$$DIF_c = \begin{cases} \left(\frac{\dot{\varepsilon}}{\dot{\varepsilon}_s}\right)^{1.026\alpha} & \text{for } \dot{\varepsilon} \le 30s^{-1} \\ \gamma\left(\frac{\dot{\varepsilon}}{\dot{\varepsilon}_s}\right)^{1/3} & \text{for } \dot{\varepsilon} > 30s^{-1} \end{cases} \quad (7\text{–}24)$$

$$\log\gamma = 6.156\alpha - 2, \;\; \alpha = 1/(5 + 9f'_{cu}/10), \;\; \dot{\varepsilon}_s = 30 \cdot 10^{-6}s^{-1} \quad (7\text{–}25)$$

Saatcioglu et al. (2011)

Equation (7–26), proposed by Saatcioglu et al. (2011), was also considered for the dynamic increase factor of plain concrete in compression. As with the CEB expressions, this model results in two linear segments with a sharp transition at a strain of 30 s^{-1}. Based on the large scatter of experimental results reported by other researchers, the DIF of concrete in compression is assumed to be independent of concrete strength. At a strain-rate of $\dot{\varepsilon}_s$= 1 s^{-1}, this model predicts a DIF_c = 1.3 for concrete in compression.

$$DIF_c = \begin{cases} 0.03ln(\dot{\varepsilon}) + 1.30 \ge 1.0 & \dot{\varepsilon} \le 30s^{-1} \\ 0.055ln(\dot{\varepsilon}) - 0.47 & \dot{\varepsilon} > 30s^{-1} \end{cases} \quad (7\text{–}26)$$

Zhang & Mindness (2011)

Research has shown that the properties of steel fibre-reinforced concrete (SFRC) are affected by strain-rate. Zhang and Mindness (2011) proposed the bilinear relationship shown in equations (7–27) and (7–28) to evaluate the dynamic increase factor for high-strength SFRC in compression. The variable $\dot{\varepsilon}_{BLT}$ is the transition point of the bi-linear relationship, while the parameter f'_{cuf} is the static compressive strength of SFRC. At a strain-rate of $\dot{\varepsilon}_s$= 1 s^{-1}, this model predicts a DIF_c = 1.28 for HSFRC in compression.

$$DIF_c = \begin{cases} (\phi\dot{\varepsilon})^{\alpha} & \text{for } \dot{\varepsilon} < \dot{\varepsilon}_{BLT} \\ \beta(\dot{\varepsilon})^{1/3} & \text{for } \dot{\varepsilon} \geq \dot{\varepsilon}_{BLT} \end{cases} \tag{7–27}$$

$$\alpha = \frac{\ln\left(\beta \cdot \dot{\varepsilon}_{BLT}{}^{1/3}\right)}{ln(\phi \cdot \dot{\varepsilon}_{BLT})}, \;\; \beta = \frac{5}{9} \cdot exp\left(\frac{-f'_{cuf}}{230}\right), \;\; \phi = 10^5, \dot{\varepsilon}_{BLT} = 25 \cdot exp\left(\frac{f'_{cuf}}{130}\right) \tag{7–28}$$

Malvar & Ross (1998)

Although typically ignored in the analysis of reinforced concrete elements, research has shown that the tensile strength of concrete is sensitive to dynamic loading. The bilinear relationship shown in equations (7–29) and (7–30), which was proposed by Malvar and Ross (1998), can be used to evaluate the dynamic increase factor DIF_t for concrete in tension:

$$DIF_t = \begin{cases} \left(\dfrac{\dot{\varepsilon}}{\dot{\varepsilon}_s}\right)^{\delta} & \text{for } \dot{\varepsilon} \leq 1s^{-1} \\ \beta^* \left(\dfrac{\dot{\varepsilon}}{\dot{\varepsilon}_s}\right)^{1/3} & \text{for } \dot{\varepsilon} > 1s^{-1} \end{cases} \tag{7–29}$$

$$\delta = \frac{1}{\left(5 + \dfrac{8 \cdot f'_{cu}}{f'_{cr}}\right)}, \;\; \log\beta^* = 6\delta - 2, \;\; f'_{cr} = 10 \text{ MPa}, \;\; \dot{\varepsilon}_s = 10^{-6}s^{-1} \tag{7–30}$$

Due to a lack of reliable models in the literature, the DIF_t of HSFRC in tension was either conservatively assumed to be equal to 1.0 or predicted using the Malvar and Ross (1998) model. At a strain-rate of $\dot{\varepsilon}_s$= 1 s^{-1}, this model predicts a DIF_t = 1.22 for concrete in tension.

7.3.3. DYNAMIC INCREASE FACTORS FOR STEEL REINFORCEMENT

The material properties of steel reinforcement are sensitive to the rate of loading. This research has shown that both the yield and ultimate stress of conventional steel show an increase in strength under dynamic loading (although the effect is smaller at ultimate stress). No reliable model is available in the literature to predict the dynamic increase factor of high-strength ASTM A1035 Grade 100 reinforcement; however, research indicates that the DIF of high-grade steel at yield and ultimate are reduced when compared to lower grade steel reinforcement (Malvar, 1998). In this research, the equations proposed by Saatcioglu et al. (2011) were selected to modify the static stress-strain curve of the high-strength steel reinforcement. In addition, the design dynamic increase factor proposed by the UFC-3-340-02 (2008) was also considered for analysis (DIF_u = 1.05).

Saatcioglu et al. (2011)

The relationships shown in Equation (7–31) were proposed by Saatcioglu et al. (2011) to define the dynamic increase factors of steel reinforcement at yield (DIF_y) and at ultimate (DIF_u). The bi-linear relationships are independent of steel grade, but predict higher DIF for steel at yield stress when compared to ultimate.

$$\begin{aligned} DIF_y &= 0.034ln(\dot{\varepsilon}) + 1.30 \geq 1.0 \\ DIF_u &= 0.010ln(\dot{\varepsilon}) + 1.10 \geq 1.0 \end{aligned} \tag{7–31}$$

Assuming a strain rate of 1 s^{-1} for the shock-tube experiments, equation (7-31) predicts the dynamic increase factors at yield and ultimate as $DIF_y = 1.30$ and $DIF_u = 1.10$, respectively. Since the high-strength steel reinforcement does not show a well-defined yield plateau, the entire stress-strain curve was modified with a single factor of 1.10, corresponding to the dynamic increase factor at ultimate stress.

7.3.4. SAMPLE DYNAMIC STRESS-STRAIN CURVES

Figure 7-4 shows typical stress-strain curves for high-strength concrete, HSFRC and high-strength steel reinforcement with and without DIF. The curves shown in the figure correspond to the default material stress-strain and DIF model combinations considered in the analysis: Concrete - Popovics (1973) & Saatcioglu et al. (2011); HSFRC - Mansur et al. (1999) & Zhang and Mindess (2011); steel reinforcement - ACI ITG-6 (2010) & Saatcioglu et al. (2011). It is noted that for analysis, the static concrete compressive strength in the beams was taken as 85% of the values recorded in the cylinder testing.

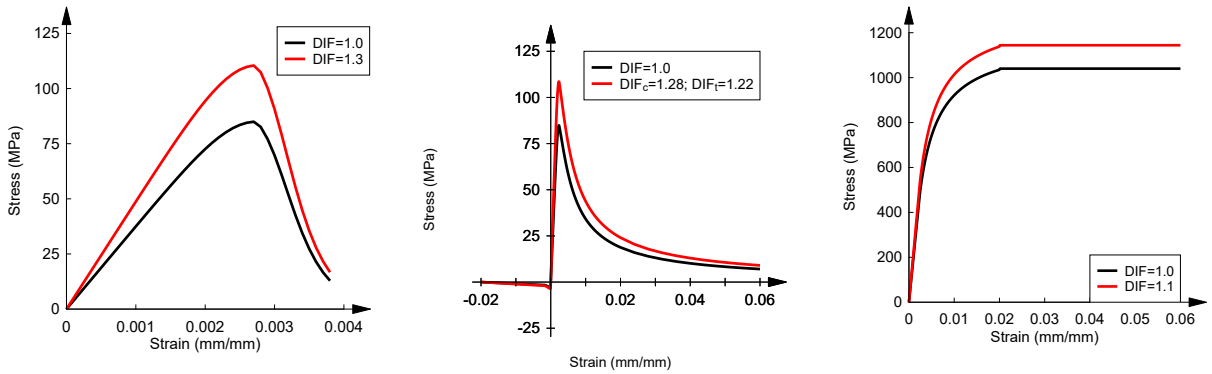

a) Plain concrete b) HSFRC specimens c) Steel

Figure 7-4 Typical stress-strain relationship with DIF

7.4. DYNAMIC ANALYSIS USING LUMPED INELASTICITY APPROACH

The dynamic response of structural members such as beams and columns can be simplified and estimated using a single-degree-of-freedom (SDOF) system approach. Figure 7-5 shows an example of a beam subjected to a dynamic load and an equivalent SDOF mass-spring system.

Figure 7-5 SDOF system

Ignoring damping, equation (7–32) can be used to analytically predict the SDOF response of a beam subjected to blast loading:

$$K_{LM} m\ddot{u}(t) + R\big(u(t)\big) = AP_r(t) \tag{7–32}$$

$$K_{LM} = \frac{K_M}{K_L} \tag{7–33}$$

$$K_M = \frac{M_e}{M} = \frac{\int_0^L m(x)[\varphi(x)]^2 dx}{mL} \tag{7–34}$$

$$K_L = \frac{P_e}{P(x)} = \frac{\int_0^L p(x)\varphi(x) dx}{pL} \tag{7–35}$$

where $u(t)$ is the deflection of the beam at mid-span; $\ddot{u}(t)$ is the acceleration at mid-span; K_{LM} is the load- mass transformation factor; $R\big(u(t)\big)$ is the resistance of the member as a function of the deflection; m is the total mass of the system; A is the area impacted by the blast pressure, and $P_r(t)$ is the reflected pressure as a function of time. For the beams in this study, the total mass of the system, which includes the weight of the load transfer device and the specimen, is estimated to be 450 kg. The area A corresponds to the area at the frame opening of the shock-tube, measured to be 3.4 m^3. The load-mass factor, K_{LM}, can be calculated using equation (7–33), where K_M is the mass factor defined as the ratio of the equivalent mass to the actual total mass (equation (7–34)); K_L is the load factor defined as the ratio of the force on the equivalent SDOF system to the actual force (equation (7–35)), where $p(x)$ is the loading function and $\varphi(x)$ is the shape function. More conveniently, the K_{LM} factor can be obtained using the transformation factor table developed by Biggs (1964) and also found in UFC 3-340-01 (2002) (see Table 7-2).

Table 7-2 Transformation factors for beams and one-way slabs with concentrated loads (UFC 3-340-01 2002)

Edge Conditions and Loading Diagrams	Range of Behavior	Load Factor K_L	Mass Factor K_M	Load-Mass Factor K_{LM}
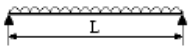	Elastic	0.64	0.50	0.78
	Plastic	0.50	0.33	0.66
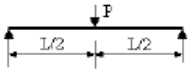	Elastic	1.0	0.49	0.49
	Plastic	1.0	0.33	0.33
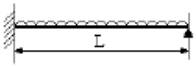	Elastic	0.58	0.45	0.78
	Elasto-Plastic	0.64	0.50	0.78
	Plastic	0.50	0.33	0.66
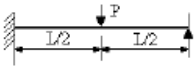	Elastic	1.0	0.43	0.43
	Elasto-Plastic	1.0	0.49	0.49
	Plastic	1.0	0.33	0.33
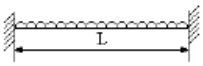	Elastic	0.53	0.41	0.77
	Elasto-Plastic	0.64	0.50	0.78
	Plastic	0.50	0.33	0.66
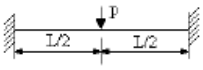	Elastic	1.0	0.37	0.37
	Plastic	1.0	0.33	0.33
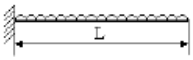	Elastic	0.40	0.26	0.65
	Plastic	0.50	0.33	0.66
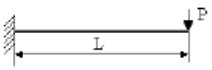	Elastic	1.0	0.24	0.24
	Plastic	1.0	0.33	0.33
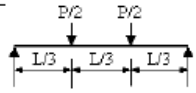	Elastic	0.87	0.52	0.60
	Plastic	1.0	0.56	0.56

The resistance functions used in the dynamic analysis were obtained using a lumped-inelasticity approach as discussed by Jacques et al. (2012), with dynamic analysis conducted using software *RCBlast*, developed by Jacques (2014) at the University of Ottawa.

Analysis in *RCBlast* begins by defining the dynamic material properties of concrete and steel, the beam cross-sectional dimensions, and the arrangement of the steel reinforcing bars. After defining these parameters, the software generates a moment-curvature relationship for the beam section. The resistance function is then obtained by idealizing the beam as a half-span symmetrical linear-elastic flexural member with a non-linear rotational hinge as shown in Figure 7-7. The current version of *RCBlast* does not include an option to generate resistance functions for beams subjected to four-point loading, therefore an excel based spreadsheet was developed in this study for this purpose. The relationships used to generate the load-deflection curves are outlined in equations (7–36) to (7–39) and Figure 7-7. Prior to yielding, displacements were obtained by integrating beam curvature using the moment-area method as shown in Figure 7-7 (a) and using equations (7–36) to (7–37). After yielding, the method illustrated in Figure 7-7 (b) and equation (7–37) was used to determine the displacements, where φ_u and φ_y are the curvature values at ultimate and yield, and where l_p' is the plastic hinge length (taken as equal to the effective depth of the beam cross-section, d = 200 mm).

The resistance function was obtained by solving the above-mentioned force-displacement relationships at incrementally increasing load stages. Based on the load configuration, the resistance P can be related to moment using equation (7–38). The transformation factors K_{LM} are taken using equations (7–39) before and after yield.

$$\frac{M}{EI} = \frac{d^2v}{dx^2} \Rightarrow v = \iint_0^{L/2} \frac{M(x)}{EI} dx \tag{7–36}$$

$$\Delta = \begin{cases} A_1 d_1 + A_2 d_2 = 531215\phi & \Delta \leq \Delta_y \\ \Delta_y + (\phi_u - \phi_y) l_p' \times \left(l - \frac{l_p'}{2}\right) = 513215\phi_y + 106600(\phi_u - \phi_y) & \Delta > \Delta_y \end{cases} \tag{7–37}$$

$$P = \frac{2M}{741} \tag{7–38}$$

$$K_{LM} = \begin{cases} 0.6 & \Delta \leq \Delta_y \\ 0.56 & \Delta > \Delta_y \end{cases} \tag{7–39}$$

The resulting resistance function and transformation factors, along with an idealized blast load pressure-time history were then used to conduct the dynamic analysis in *RCBlast*. Figure 7-8 shows the actual and equivalent triangular blast load used in the analysis (the loads have the same pressure and impulse; the positive phase duration is modified using equation (7–40) to obtain the same

impulse). The equation of motion was then solved by the software using the average acceleration numerical integration method (Jacques, 2014).

$$t_p' = \frac{2I}{P} \tag{7–40}$$

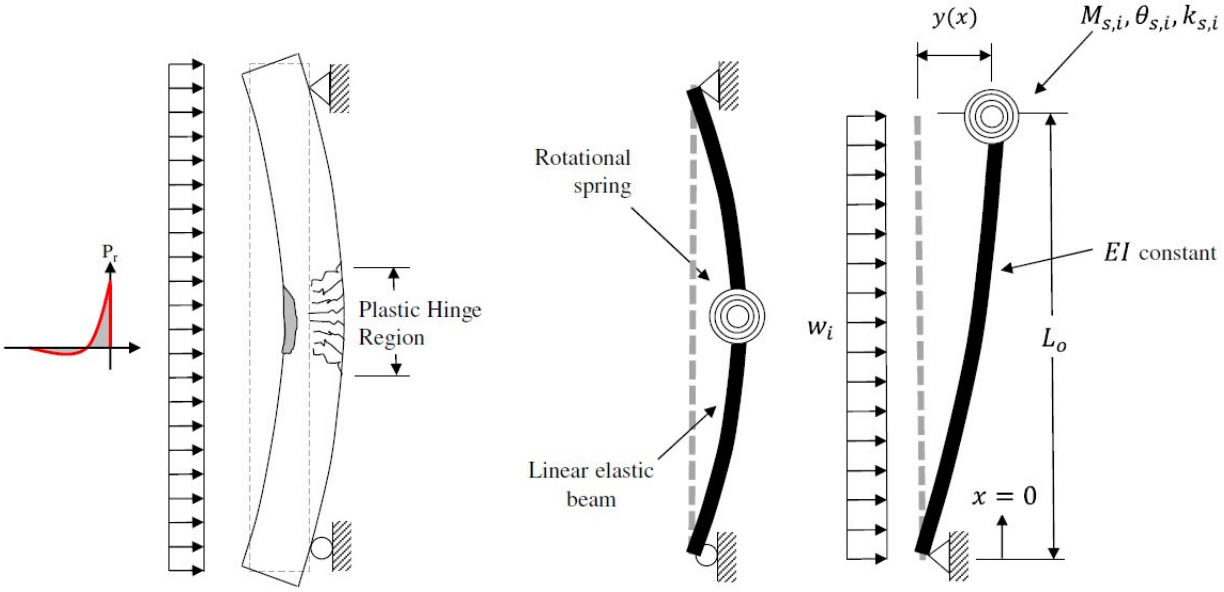

a) Real beam b) Idealized structure c) Half-span idealized beam

Figure 7-6 Reinforced concrete flexural member modelled using the lumped inelasticity approach (Adapted from Jacques et al. 2012)

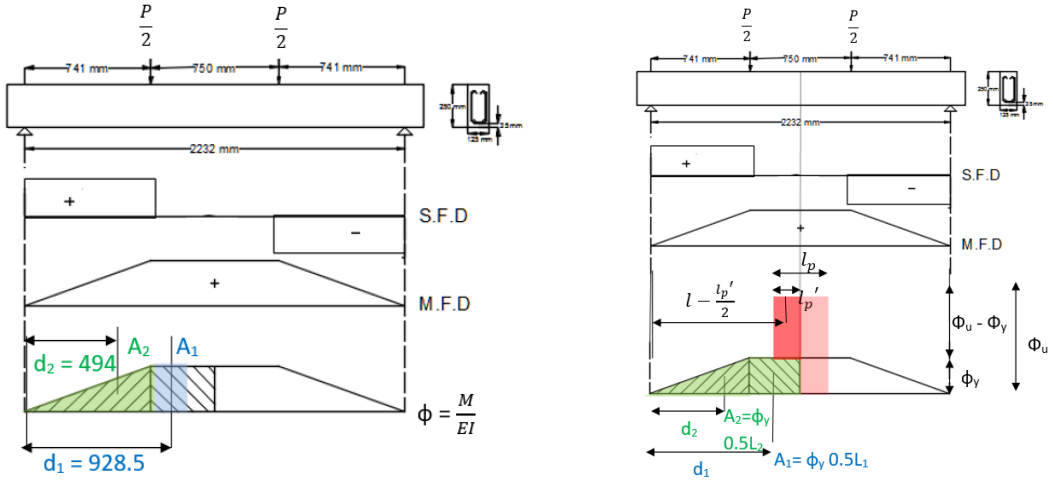

a) Before yielding b) After yielding

Figure 7-7 Moment – area method to get resistance curve

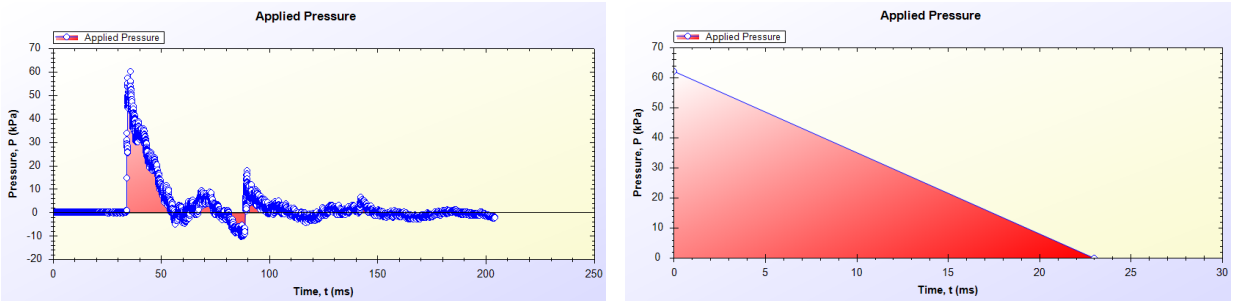

a) Actual Pressure-time history b) Idealized Pressure-time history

Figure 7-8 Actual and idealized pressure-time history

The table below summarizes the main steps for the analysis in software *RCBlast*. The results of the dynamic analysis are summarized and discussed in the next section.

Table 7-3 Steps for conducting an analysis using the *RCBlast* software

Step 1:	Define general member properties such as support conditions, load type, and member length.
	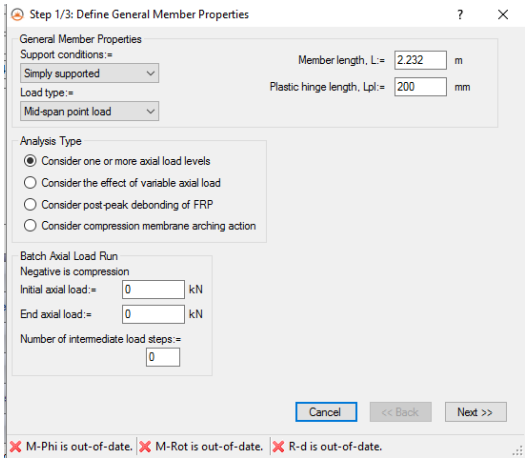

Step 2:	Input material properties such as concrete model, tension steel model and compression steel model
	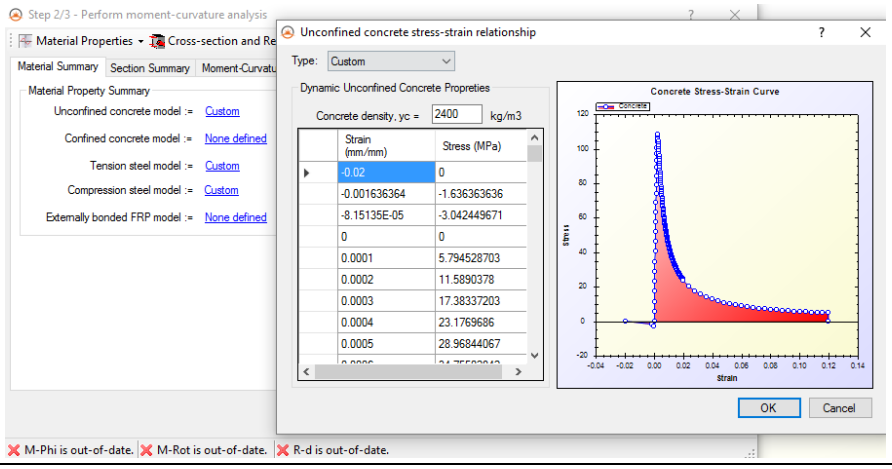
Step 3:	Input section geometry and reinforcement details.
	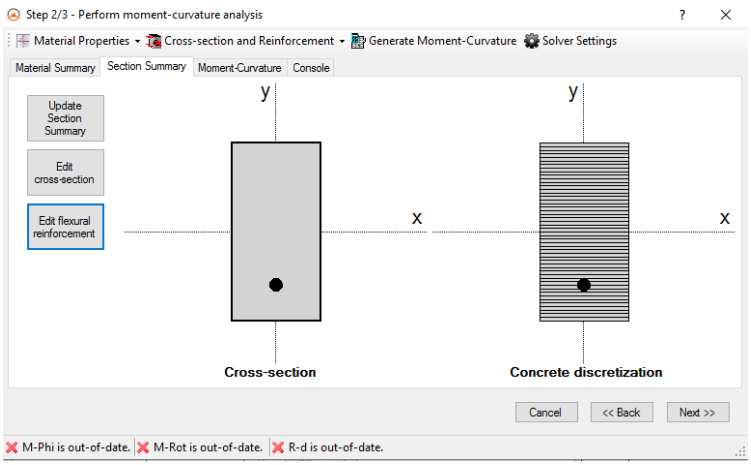
Step 4:	Generate moment-curvature curve using *RCBlast* software
	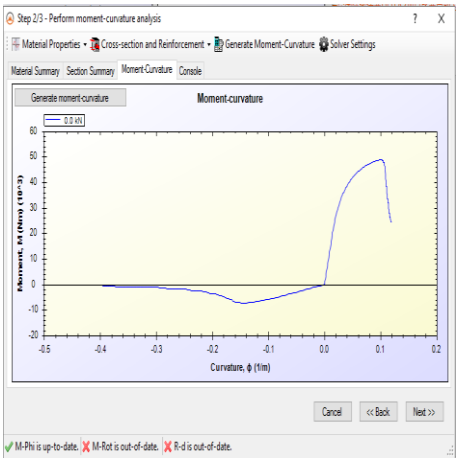

Step 5:	Paste the data to custom excel spreadsheet to generate load-displacement curve, then input the resistance curve back into *RCBlast*

ϕ (1/m)	M (Nm)	εtop	εbtm	Delta	Load	Klm
-0.56906457	-129.8429	-0.02786	0.1144061	-116.3859	-0.34951	0.56
-0.566640258	-135.1769	-0.02773	0.1139301	-116.12747	-0.363868	0.56
-0.564215942	-140.5113	-0.0276	0.113454	-115.86904	-0.378227	0.56
-0.561791727	-149.4785	-0.02747	0.1129779	-115.61062	-0.402365	0.56
-0.559459098	-157.1534	-0.02734	0.1125248	-115.36196	-0.423024	0.56
-0.557126467	-164.8286	-0.02721	0.1120716	-115.1133	-0.443684	0.56
-0.554793826	-172.5053	-0.02708	0.1116185	-114.86464	-0.464348	0.56
-0.55256467	-186.0933	-0.02695	0.1111912	-114.62702	-0.500924	0.56
-0.55036289	-197.088	-0.02682	0.1107707	-114.39231	-0.53052	0.56
-0.548175414	-210.6364	-0.02669	0.1103539	-114.15912	-0.566989	0.56
-0.546143995	-225.9358	-0.02656	0.109976	-113.94257	-0.608172	0.56
-0.544113466	-241.1414	-0.02643	0.1095984	-113.72612	-0.649102	0.56
-0.542272876	-262.4122	-0.0263	0.1092682	-113.52991	-0.706359	0.56
-0.540415411	-281.9587	-0.02617	0.1089339	-113.3319	-0.758974	0.56
-0.538604889	-302.9829	-0.02604	0.1086112	-113.1389	-0.815566	0.56
-0.536788248	-323.7594	-0.02591	0.1082871	-112.94525	-0.871492	0.56
-0.534848205	-341.2111	-0.02578	0.1079321	-112.73844	-0.918469	0.56
-0.532903719	-359.1845	-0.02565	0.1075759	-112.53116	-0.966849	0.56
-0.530760489	-369.521	-0.02552	0.1071701	-112.30269	-0.994673	0.56
-0.528595763	-381.4559	-0.02539	0.1067589	-112.07193	-1.026799	0.56
-0.526385963	-387.8906	-0.02526	0.1063365	-111.83637	-1.04412	0.56
-0.524024585	-394.8582	-0.02513	0.1058761	-111.58464	-1.062875	0.56
-0.521664158	-401.7982	-0.025	0.105416	-111.33302	-1.081556	0.56
-0.519303659	-408.1153	-0.02487	0.1049559	-111.08139	-1.098561	0.56
-0.516789127	-401.7585	-0.02474	0.1044573	-110.81334	-1.081449	0.56
-0.514237538	-403.8108	-0.02461	0.1039494	-110.54134	-1.086974	0.56
-0.511686028	-405.9241	-0.02448	0.1034415	-110.26935	-1.092662	0.56

Step 6:	Define the physical properties (mass) of the system and the blast parameters (pressure-time history), then run the SDOF analysis to obtain the maximum displacement.

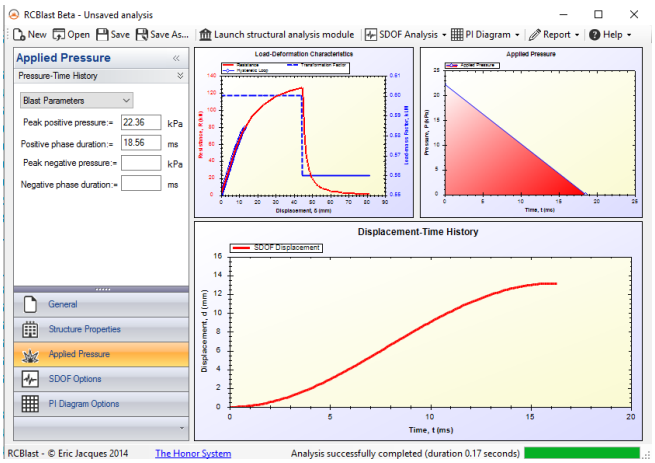

7.5.STATIC ANALYSIS RESULTS

This section presents the analysis of the three high-strength concrete beams which were tested under static loading. The analytical resistance curves (load vs. deflection) of beams HSC-F0-#4-S, HSC-F0-#5-S and HSC-F0-#6-S are predicted using the procedure outlined in the previous section and the analytical results are compared to the experimental results from the static tests.

7.5.1.MODELLING CASES

In addition to validating the analysis procedure, various cases were considered in the analysis to examine the effect of material model for the high-strength steel bars (see Table 7-4). For all cases,

the behaviour of concrete in compression was taken into account using the Popovics (1973) model, while tensile response was taken as linear, with a maximum stress of $0.33\sqrt{f_c'}$. The stress-strain behaviour of the high-strength steel reinforcement was modelled using either: (1) experimental coupon stress-strain data, (2) the ACI ITG-6R model, (3) the Ramberg-Osgood function, (4) a bilinear curve based on the ACI 318 code limitation of f_y = 550 MPa (80 ksi), or (5) a bilinear curve with f_y = 690 MPa (100 ksi) as suggested by Mast. et al. (2008). Figure 7-9 shows the stress-strain curves considered in the different cases (details on the models can be found in Chapter 2 and 7 of this thesis). Cases 1-5 were predicted using the lumped inelasticity approach as presented in Section 7.4 (with DIF = 1.0).

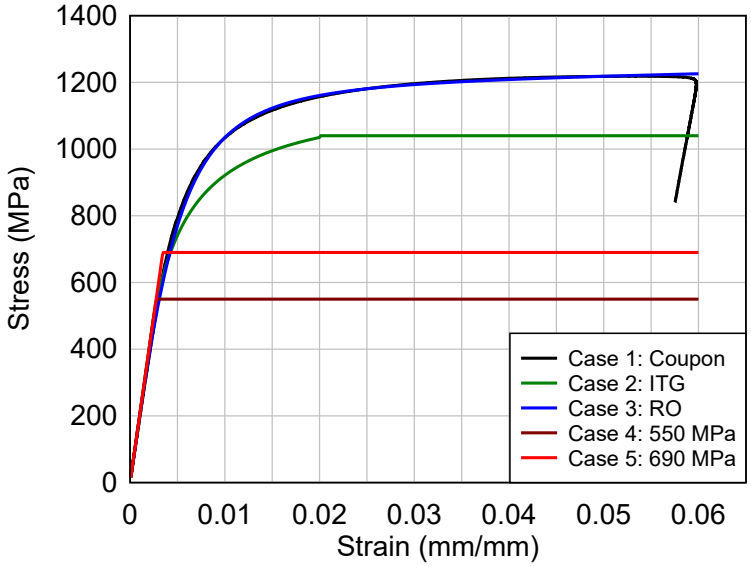

Figure 7-9 Stress-strain relationship for case 1-5

Table 7-4 Model combinations for each case

Models	Concrete in compression	Concrete in tension	Steel
Case 1	Popovics (1973)	Linear	Coupon
Case 2			ACI ITG-6R
Case 3			Ramberg-Osgood equation
Case 4			Bilinear curve with f_y = 550 MPa
Case 5			Bilinear curve with f_y = 690 MPa

7.5.2.ANALYSIS RESULTS

The analytical resistance curves for cases 1-5 are compared to the experimental load-deflection curves of beams HSC-F0-#4-S, HSC-F0-#5-S and HSC-F0-#6-S in Figure 7-10, Figure 7-11 and Figure 7-12, respectively. The analytical-to-experimental ratios for maximum loads (P_{max}) and peak displacements (Δ_{max}) for the various cases are summarized in Table 7-6.

In general, cases 1, 2 and 3, which used the coupon stress-strain data, ACI ITG-6R model and Ramberg-Osgood equation, were able to capture the general trend of the load-deflection curves, with reasonable prediction of maximum loads and peak displacements. However, all three cases over-predicted the stiffness of the beams. Since the ACI 318 and Mast et al. (2008) bi-linear approximations use conservative stress-strain curves for high-strength steel, cases 4 and 5 resulted in conservative predictions of maximum capacities.

Focussing in on Beam HSC-F0-#4, the predicted P_{max} for cases 1 and 2 (coupon data and ACI ITG-6R) were 126.19 kN and 127.52 kN respectively, compared to the experimentally obtained value of 126.7 kN. The peak displacements were not as accurate with predictions of 45.25 mm and 45.58 mm for Cases 1 and 2, versus 35.2 mm in the experiments. For Case 3 (Ramberg-Osgood), the predicted values of P_{max} and Δ_{max} were 127.88 kN and 45.14 mm, which are close to the results predicted using the coupon data. It is noted beam stiffness was over-predicted in all cases. The P_{max} and Δ_{max} ratios were 0.58/2.1 and 0.65/1.21 for Cases 4 and 5 (ACI 318, Mast et al.), respectively.

For the No. 5 specimen (HSC-F0-#5S), the predictions for P_{max} were 169.8 kN and 180.9 kN for cases 2 and 3 (ACI ITG-6R and Ramberg-Osgood) which compared well with the experimental result of P_{max} = 194.7 kN (analysis-experimental ratios of 0.87 and 0.93). Case 1 (Coupon data) gave an ultimate capacity of 181.85 kN, with a difference of 6.6% between the experimental and analytical results. The Δ_{max} ratios for these same 3 cases were 0.88, 1.06 and 0.95. The models captured the limited post-peak ductility of the beam, although beam stiffness was once again over-predicted. The P_{max} and Δ_{max} ratios were 0.57/1.34 and 0.63/0.87 for Cases 4 and 5 (ACI 318, Mast et al.), respectively, indicating that these models provided conservative predictions of ultimate capacity, with poor prediction of peak displacement.

For the over-reinforced beam with No. 6 bars (HSC-F0-#6S), the predictions for cases 1-2-3 (coupon data, ACT ITG-6R, Ramberg-Osgood) were 204.64 kN, 210.29 kN and 206.32 kN for P_{max}, which are close to the actual result of P_{max} = 199 kN (analysis-to experimental ratios of 1.03 1.06 and 1.04). The displacement ratios were 0.94, 0.93 and 0.96 for cases 1 through 3. While the three modelling cases captured the brittle failure of this over-reinforced beam, stiffness was once again over-predicted. The bi-linear design curves of cases 4 and 5 resulted in P_{max} ratios of 0.75 and 1.3 and Δ_{max} ratios of 0.66 and 0.88.

In conclusion, Case 1, 2 and 3 resulted in reasonable predictions of the static response of the high-strength concrete beams reinforced with high-strength steel bars. Case 2, which used the Ramberg-Osgood equation to model the stress-strain behaviour of high-strength steel, resulted in the best

overall predictions when considering all other cases, with average P_{max} and Δ_{max} ratios of 0.99 and 1.06, respectively.

Table 7-5 Ratio of resistance and displacement versus experiment results

	Case 1		Case 2		Case 3		Case 4		Case 5	
	Load Ratio	Disp. Ratio	Load Ratio	Disp. Ratio	Load Ratio	Disp. Ratio	Load Ratio	Disp. Ratio	Load Ratio	Disp. Ratio
HSC-F0-#4-S	99.6%	131.4%	100.6%	129.5%	100.9%	128.2%	58.4%	212.6%	64.8%	121.1%
HSC-F0-#5-S	93.4%	88.2%	87.2%	105.7%	92.9%	94.5%	56.7%	134.2%	62.8%	87.4%
HSC-F0-#6-S	102.8%	94.4%	105.7%	93.4%	103.7%	95.8%	75.1%	129.9%	66.0%	87.9%
Average	98.6%	104.7%	97.8%	109.5%	99.2%	106.2%	63.4%	158.9%	64.5%	98.8%
Standard Deviation	0.048	0.234	0.095	0.184	0.056	0.191	0.102	0.466	0.048	0.234

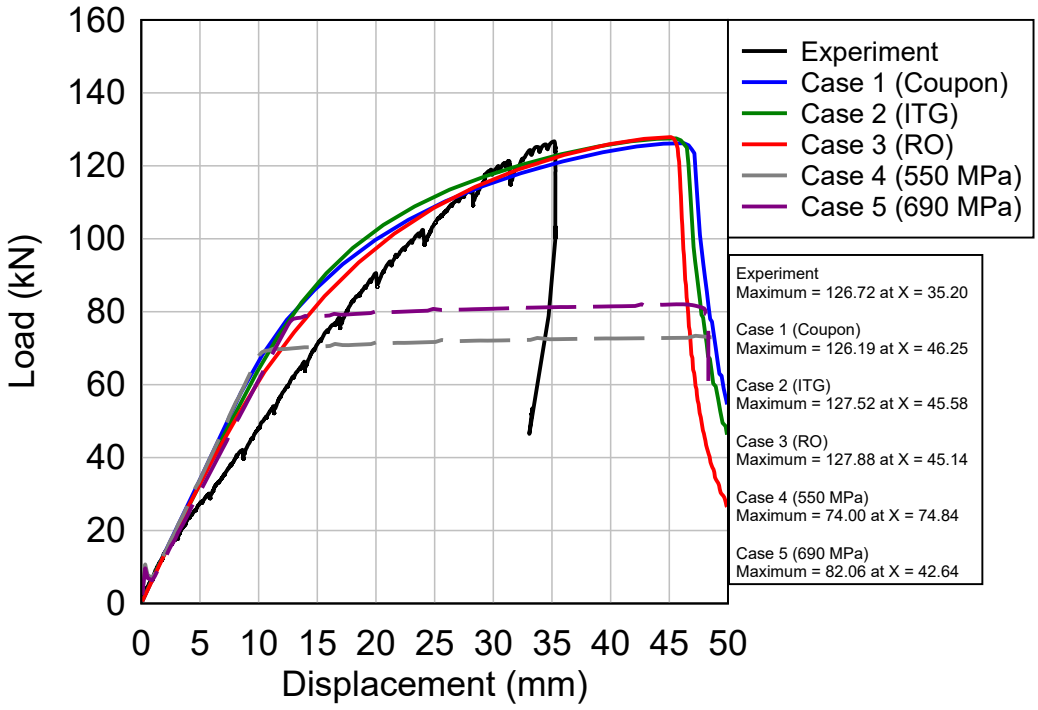

Figure 7-10 Analytical and experimental static resistance curves for HSC-F0-#4-S

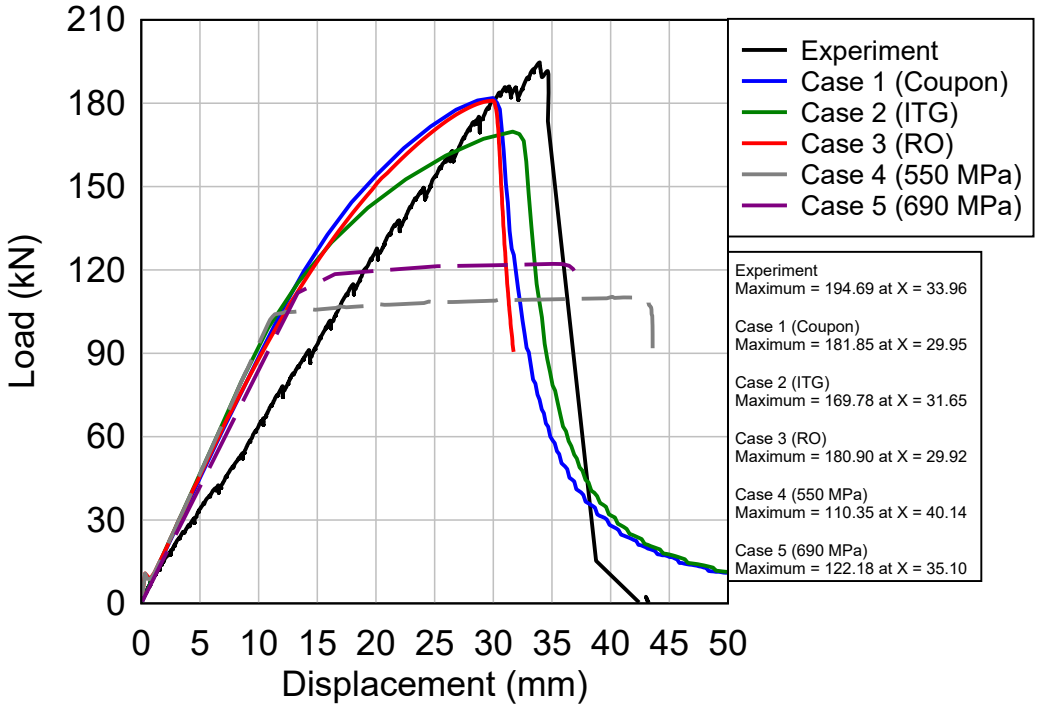

Figure 7-11 Analytical and experimental static resistance curves for HSC-F0-#5-S

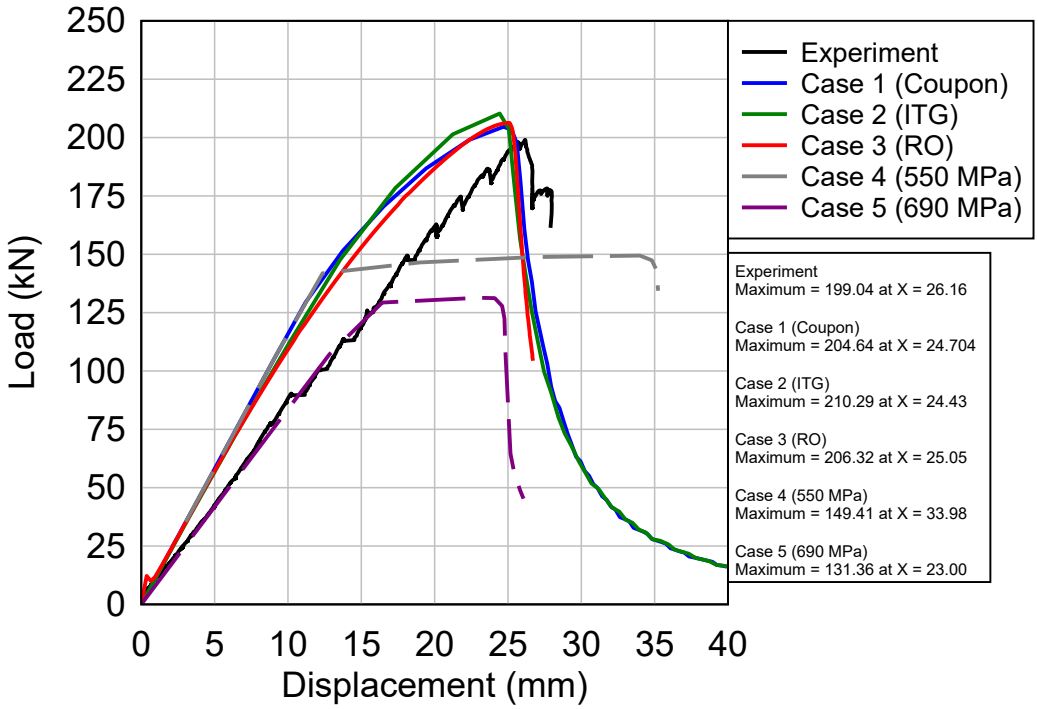

Figure 7-12 Analytical and experimental static resistance curves for HSC-F0-#6-S

7.6.DYNAMIC ANALYSIS RESULTS

This section summarizes the results from the dynamic analysis using the procedure outlined in the previous sections. The results are presented in the sub-sections that follow based on concrete type (plain vs. HSFRC specimen), with the analytically predicted maximum displacements compared to the maximum displacements obtained from the experiments.

Table 7-6 summarizes the default material constitutive models and DIF model combinations used in the analysis of each specimen. These models were selected based on the sensitivity analysis which will be presented in Section 7.7.

To summarize the analysis results, a series of tables and graphics are presented for each beam series. The summary tables include the idealized blast parameters used in the analysis (P_r: reflected pressure, I_r: reflected impulse, and T_d: positive phase duration), the experimental displacement results (δ_{exp}) and the analytical displacement results (δ_{anls}) as well as the analytical to experimental displacement ratios ($\delta_{anls}/\delta_{exp}$). Furthermore, statistical data for the displacement ratios for each series, including: error percentage, mean, standard deviation and coefficient of variation. The comparison of analytical and displacement, for each specimen (displacement time-history comparison) and for each series as a whole (δ_{anls} vs. δ_{exp}) are also presented graphically. Finally, the analytical resistance curves are compared to the experimental resistance curves obtained from the reaction load-cells during the shock-tube experiments (when available).

Table 7-6 Selected model combinations; results from the sensitivity analysis

Specimen	Concrete models		Steel models
	Compression [DIF]	Tension [DIF]	Tension [DIF]
SCC-F0-#4-S	Popovics (1973) Saatcioglu et al. [1.3]	Linear slope [1.0]	ACI ITG-6R (2010) Saatcioglu et al. [1.1]
HSC-F0-#4-S	Popovics (1973) Saatcioglu et al. [1.3]	Linear slope [1.0]	ACI ITG-6R (2010) Saatcioglu et al. [1.1]
HSC-F0-#5-S	Popovics (1973) Saatcioglu et al. [1.3]	Linear slope [1.0]	ACI ITG-6R (2010) Saatcioglu et al. [1.1]
HSC-F0-#6-S	Popovics (1973) Saatcioglu et al. [1.3]	Linear slope [1.0]	ACI ITG-6R (2010) Saatcioglu et al. [1.1]
HSC-F1-#4-S	Mansur et al. (1999) Zhang & Mindess [1.28]	Lok & Pei (1998) Malvar & Ross [1.22]	ACI ITG-6R (2010) Saatcioglu et al. [1.1]
HSC-F1-#5-S	Mansur et al. (1999) Zhang & Mindess [1.28]	Lok & Pei (1998) Malvar & Ross [1.22]	ACI ITG-6R (2010) Saatcioglu et al. [1.1]
HSC-F1-#6-S	Mansur et al. (1999) Zhang & Mindess [1.28]	Lok & Pei (1998) Malvar & Ross [1.22]	ACI ITG-6R (2010) Saatcioglu et al. [1.1]

7.6.1. DYNAMIC ANALYSIS RESULTS – PLAIN CONCRETE SPECIMENS

Table 7-7 summarizes the analysis and experimental displacement results as well as displacement ratios for the plain concrete specimens (δ_{anls}, δ_{exp} and $\delta_{anls}/\delta_{exp}$). Statistical analysis of the predictions is included in Table 7-8 (for all blasts, as well as shot by shot). The accuracy of the SDOF analysis for the series is also graphically displayed by plotting δ_{anls} vs. δ_{exp} in Figure 7-13. The resistance curves, along with a comparison of experimental and analytical displacement-time histories for each specimen are graphically displayed in Figure 7-14.

Considering all blasts, the average displacement ratios ($\delta_{anls}/\delta_{exp}$) were 93.0%, 107.5% and 100.3% for the SCC-F0-#4-S, HSC-F0-#4-S, and HSC-F0-#5-S specimens, with corresponding standard deviations of 0.056, 0.224 and 0.04. It can be concluded that the combination of the Popovics (1973) concrete and the ACI Group ITG-6 (2010) steel models with corresponding DIF factors of 1.3 and 1.1, as proposed by Saatcioglu et al. (2011) resulted in reasonably accurate analysis predictions for these specimens. The results are less accurate for specimen HSC-F0-#6-S, which

had the No. 6 high-strength steel reinforcement, with an average displacement-ratio of 80.7% with a standard deviation of 0.041. As noted previously, the experimental results confirmed that the No. 6 specimen was over-reinforced, and this is one possible reason for the reduced accuracy of the analytical predictions for this specimen.

Nonetheless, when considering all plain concrete specimens and all blast scenarios, the overall mean displacement ratio was 95.9% with a standard deviation of 0.156, further confirming that the analytical procedure provided reasonably accurate predictions of the beam displacements. When considering Blasts 1, 2 and 3 respectively, the mean displacement ratios were 102.7%, 99.1%, and 94.5%, respectively, which indicates the ratios were nearly 1.0 for these shots. The mean displacement ratio at the last shot (Blast 4) was 84.7%, which indicates reduced accuracy when compared to the previous shots. The result can be explained by the accumulated damage suffered by the specimens under repeated blast loading. The cumulative damage from previous blasts (cracking, crushing spalling of concrete) leads to reduced beam stiffness which was not accounted for in the analysis.

Figure 7-14 shows the analytical resistance curves for the HSC specimens with No.4 and No.5 high-strength steel reinforcement (HSC-F0-#4-S and HSC-F0-#5-S) as well as the SCC specimen with No. 4 high-strength steel (HSC-F0-#4-S). Also shown are the experimental resistance curves obtained from the support reactions at the failure blasts (the curves were obtained by summing the reaction load-histories recorded by the upper and lower load-cells). Finally, the experimental static resistance curves are also included for the HSC-F0-#4-S, HSC-F0-#5-S and HSC-F0-#6-S specimens.

Comparing the experimental resistance curves obtained from the static tests and dynamic reactions, it is found that the ultimate strengths of the HSC-F0-#4-S and HSC-F0-#5-S specimens are increased by approximately 19% and 25% under dynamic loading (although beam stiffness is similar). Similarly, the failure displacements are also increased under dynamic loading.

The analytical resistance curves generally follow the same trend observed in the experimental curves obtained from the dynamic reactions. Both resistance curves show a sharp increase in load until reaching peak, followed by sudden failure. However, the analytical curves show a more rounded ascending branch, with an over-prediction of stiffness, when compared to the experimental curves, which may result in errors in displacement predictions. For the SCC-F0-#4-S and HSC-F0-#5-S specimens, the predicted ultimate strengths are approximately 10% lower when compared to the experimentally recorded strengths obtained from the support reactions (similarly failure displacements are under-predicted). For the HSC-F0-#4-S specimen, the predicted and experimental ultimate strengths are similar, but the displacement at peak load is higher than in the experiments due to the over-prediction in beam stiffness.

Table 7-7 Summary of analysis for plain concrete specimens

Specimen	Idealized Shockwave				Maximum Mid-Span Displacement			
	Blast #	P_r kPa	T_d ms	I_r kPa-ms	δ_{exp} mm	δ_{anls} mm	$\delta_{anls}/\delta_{exp}$	% Error
SCC-F0-#4-S	-1	22.94	20.20	231.66	13.44	13.25	98.6%	-1.4%
	-2	38.51	18.57	357.54	24.32	23.57	96.9%	-3.1%
	-3a	50.12	17.69	443.22	37.3	32.82	88.0%	-12.0%
	-3b	60.26	17.10	515.28	64.52	57	88.3%	-11.7%
HSC-F0-#4-S	-1	25.29	18.17	229.76	10.17	13.46	132.4%	32.4%
	-2	40.37	20.00	403.62	22.39	25.87	115.5%	15.5%
	-3a	51.95	18.46	479.62	33.78	34.85	103.2%	3.2%
	-3b	58.21	18.56	540.28	52.74	41.7	79.1%	-20.9%
HSC-F0-#5-S	-1	22.33	19.38	216.41	9.08	9.35	103.0%	3.0%
	-2	43.8	17.24	377.63	17.72	18.46	104.2%	4.2%
	-3b	59.11	18.52	547.47	26.77	28.77	107.5%	7.5%
	-4	77.63	19.31	749.71	64.71	56	86.5%	-13.5%
HSC-F0-#6-S	-1	24.7	18.04	222.82	10.91	8.39	76.9%	-23.1%
	-2	39.7	16.85	334.57	16.59	13.21	79.6%	-20.4%
	-3b	55.47	19.44	539.23	26.15	20.8	79.5%	-20.5%

Table 7-8 Analysis statistics for plain concrete specimens per blast

Shot #	Mean	Standard deviation	Coefficient of variance	% Error
1-4	95.9%	0.156	0.163	4.1%
1	102.7%	0.228	0.222	-2.7%
2	99.1%	0.151	0.152	0.9%
3	94.5%	0.130	0.138	5.5%
4	84.7%	0.049	0.058	15.3%

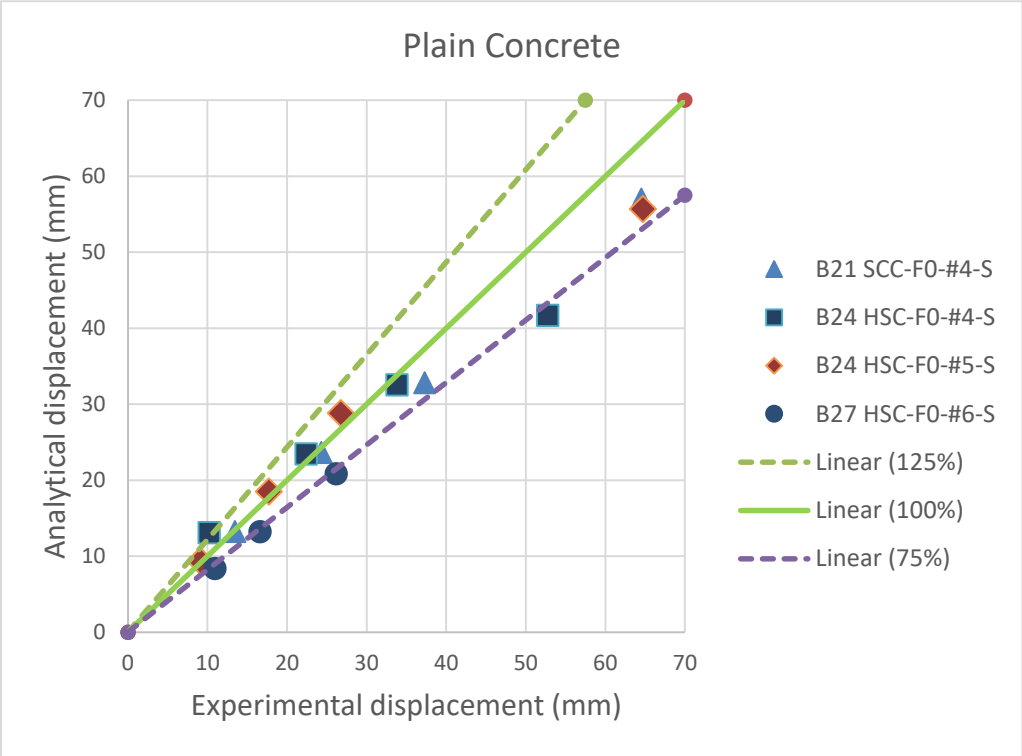

Figure 7-13 Experiment vs. Analysis Displacements - plain concrete specimens

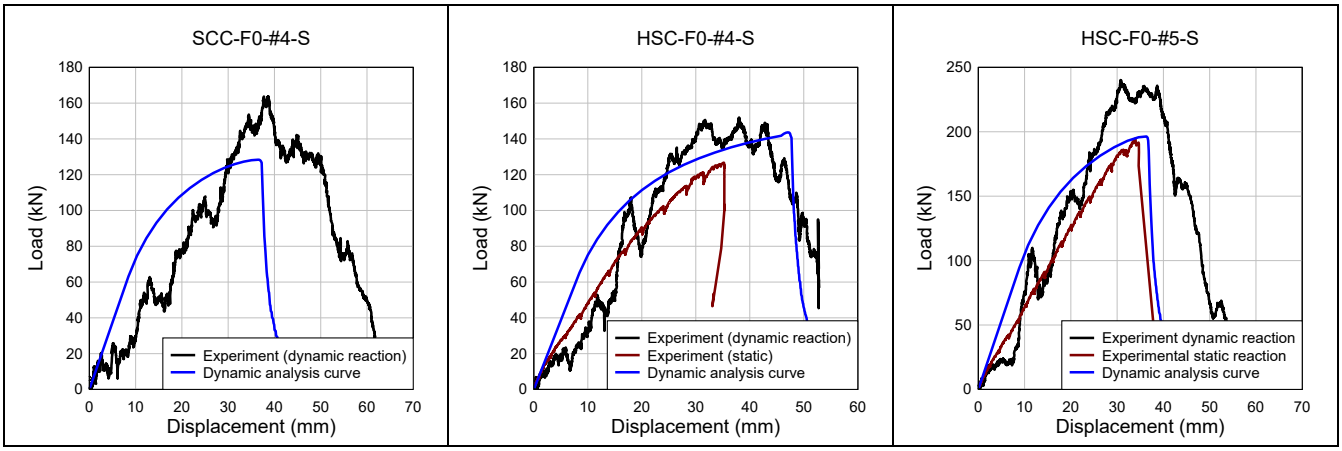

Figure 7-14 Experimental vs. Analytical resistance curves - plain concrete specimens

SCC-F0-#4-S			
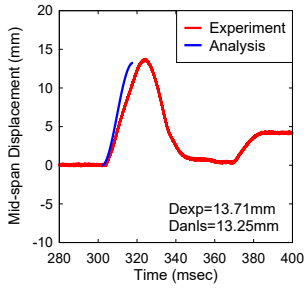	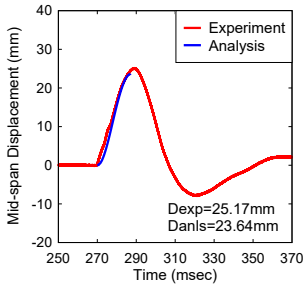	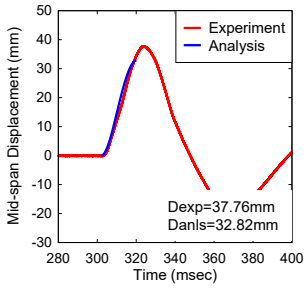	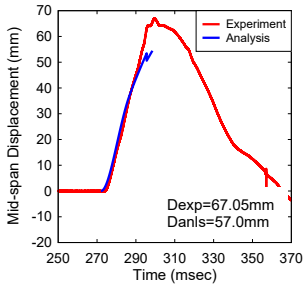
Blast 1 (17 psi)	Blast 2 (30 psi)	Blast 3a (40 psi)	Blast 3b (50 psi)
HSC-F0-#4-S			
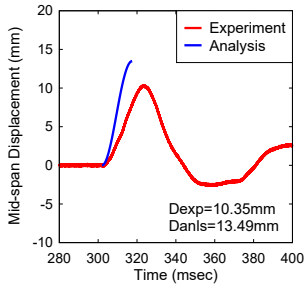	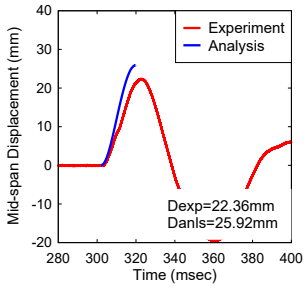	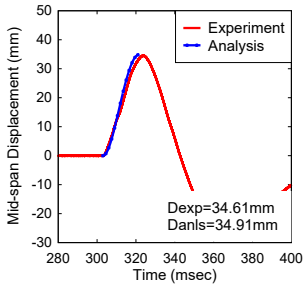	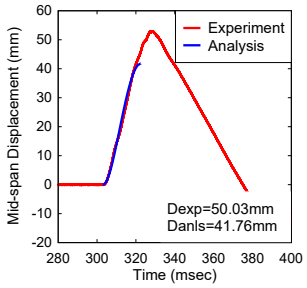
Blast 1 (17 psi)	Blast 2 (30 psi)	Blast 3a (40 psi)	Blast 3b (50 psi)
HSC-F0-#5-S			
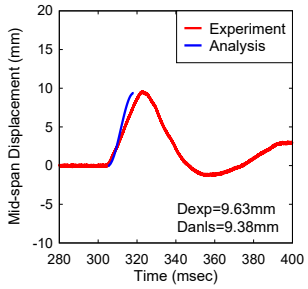	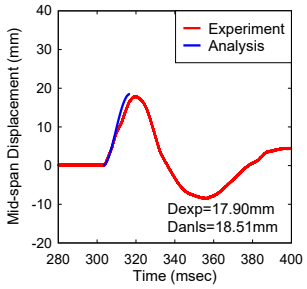	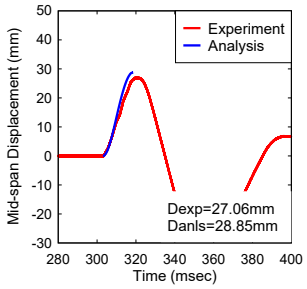	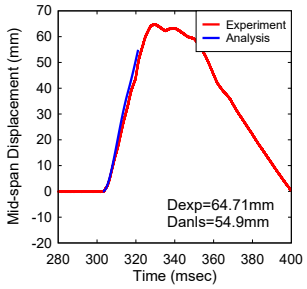
Blast 1 (17 psi)	Blast 2 (30 psi)	Blast 3b (50 psi)	Blast 4 (70 psi)
HSC-F0-#6-S			
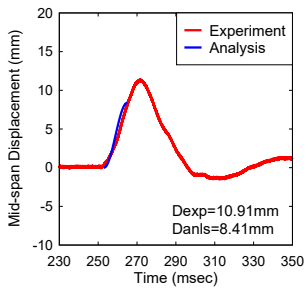	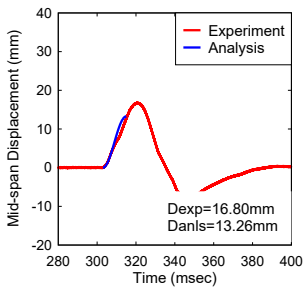	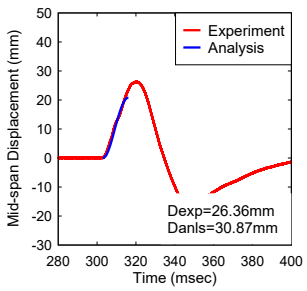	
Blast 1 (17 psi)	Blast 2 (30 psi)	Blast 3b (50 psi)	

Figure 7-15 Displacement predictions time-history for plain concrete specimens

7.6.2. DYNAMIC ANALYSIS RESULTS – HSFRC SPECIMENS

Table 7-9 summarizes the analysis and experimental displacement results as well as displacement ratios for the HSFRC specimens (δ_{anls}, δ_{exp} and $\delta_{anls}/\delta_{exp}$). Statistical analysis of the predictions is included in Table 7-10. The accuracy of the SDOF model is visually depicted in Table 7-10. Figure 7-16 shows the predicted displacement versus experiment results for all the HSFRC specimens.

Considering all blasts, the mean displacement ratios were 90.4% and 96.7% for the No. 4 and No. 5 specimens, with corresponding standard deviation values of 0.055 and 0.154 respectively. It can be concluded that the combination of the Mansur (1999), Lok and Pei (1998) fibre-reinforced concrete and the ACI Group ITG-6 (2010) steel models with corresponding DIF factors of 1.28, 1.22 and 1.1, as proposed by Zhang & Mindess (2011), Malvar & Ross (1998) and Saatcioglu et al. (2011) resulted in reasonably accurate analysis predictions for these specimens. The No. 6 specimen had an average analytical-to-experimental displacement ratio of 84.3% with a standard deviation of 0.158, which is less accurate than No.4 and No.5 specimens. As explained in the previous section, the No. 6 specimen is over-reinforced.

When considering all HSFRC concrete specimens and all blast scenarios, the overall mean displacement ratio was 90.5% with a standard deviation of 0.132. When considering Blast 1 to Blast 3 respectively, the average displacement ratios were 99.5%, 95.3%, and 95.7%, which indicates the ratios were nearly 1.0 for these shots. Whereas, at Blast 4 and Blast 5, the average displacement ratios were 88% and 73.9%, which indicates reduced accuracy when compared to previous shots. The cumulative damage from previous blasts (cracking, crushing spalling of concrete) leads to reduced beam stiffness which was not accounted for in the analysis.

Figure 7-17 shows the analytical resistance curves for the HSFRC specimens with No.5 and No.6 high-strength steel reinforcement (HSC-F1-#5-S and HSC-F1-#6-S). Also shown are the experimental resistance curves obtained from the support reactions at Blast 5 (the curves were obtained by summing the reaction load-histories recorded by the upper and lower load-cells).

The analytical resistance curves generally follow the same trend observed in the experimental curves obtained from the dynamic reactions. Both resistance curves show a sharp increase in load until reaching peak. However, the analytical curves show a more rounded ascending branch, with an over-prediction of stiffness, when compared to the experimental curves, which may result in errors in displacement predictions.

Table 7-9 Summary of analysis for HSFRC specimens

Specimen	Idealized Shockwave				Maximum Mid-Span Displacement			
	Blast #	P_r kPa	T_d ms	I_r kPa-ms	δ_{exp} Mm	δ_{anls} mm	$\delta_{anls}/\delta_{exp}$	% Error
HSC-F1-#4-S	-1	22.21	20.65	229.3	9.06	8.24	90.9%	-9.1%
	-2	39.38	19.36	381.21	19.18	18.49	96.4%	-3.6%
	-3a	46.64	19.84	462.68	26.02	24.72	95.0%	-5.0%
	-3b	54.96	19.15	526.24	37.65	31.6	83.9%	-16.1%
	-4	70.21	20.44	717.58	61.79	53.07	85.9%	-14.1%
HSC-F1-#5-S	-1	28.6	18.69	267.2	9.2	9.09	98.8%	-1.2%
	-2	43.09	18.96	408.46	14.6	15.61	106.9%	6.9%
	-3b	58.75	19.48	572.35	22.51	24.91	110.7%	10.7%
	-4	74.33	20.12	747.75	39.47	37.82	95.8%	-4.2%
	-5	79.42	21.28	845.02	63.11	44.95	71.2%	-28.8%
HSC-F1-#6-S	-1	25.29	16.87	213.36	6.11	6.64	108.7%	8.7%
	-2	41.23	18.45	380.31	14.76	12.19	82.6%	-17.4%
	-3b	53.87	21.28	573.1	22.33	18.16	81.3%	-18.7%
	-4	79.46	19.22	763.46	35.99	30.33	84.3%	-15.7%
	-5	97.06	19.32	937.81	66.84	43.12	64.5%	-35.5%

Table 7-10 Analysis statistics for HSFRC specimens per shot

Shot #	Mean	Standard deviation	Coefficient of variance	% Error
1-5	90.5%	0.132	0.146	9.5%
1	99.5%	0.089	0.089	0.5%
2	95.3%	0.122	0.128	4.7%
3	95.7%	0.147	0.153	4.3%
4	88.0%	0.068	0.077	12.0%
5	73.9%	0.109	0.148	26.1%

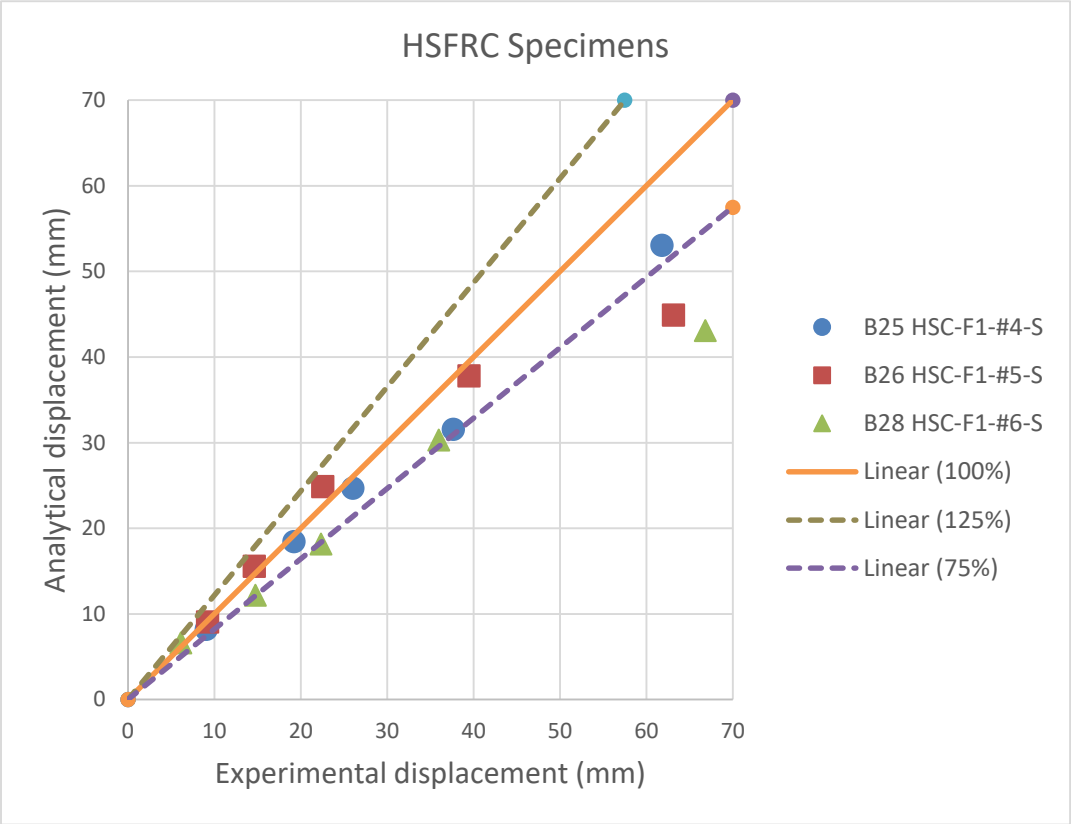

Figure 7-16 Experiment vs. Analytic Displacements - HSFRC concrete specimen

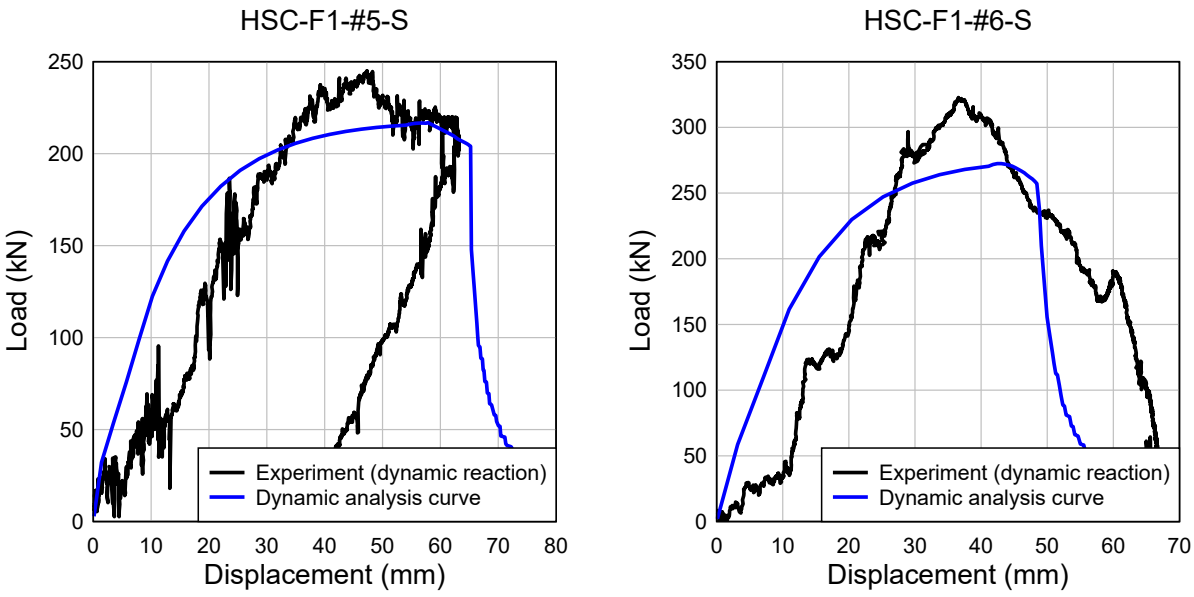

Figure 7-17 Experiment vs. Analysis resistance curves - HSFRC specimens

HSC-F1-#4-S		
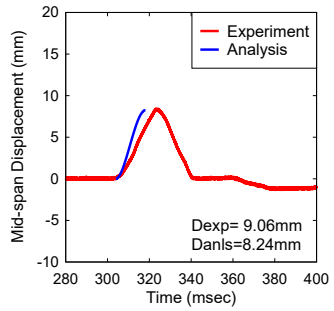	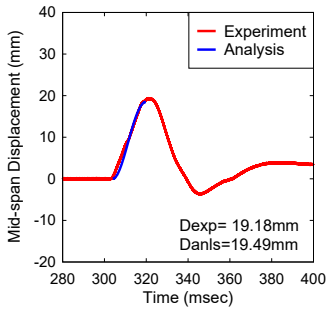	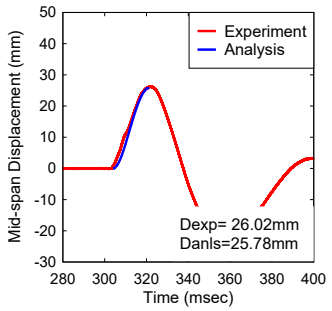
Blast 1 (17 psi)	Blast 2 (30 psi)	Blast 3a (40 psi)
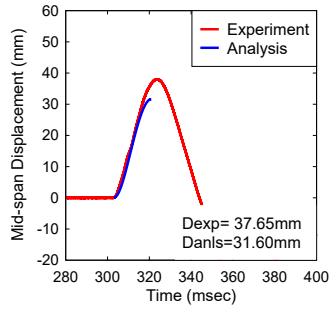	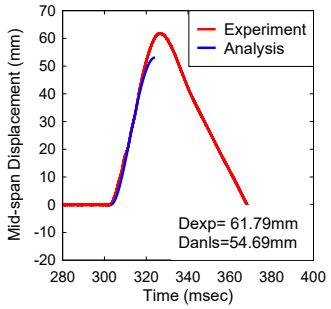	
Blast 3b (50 psi)	Blast 4 (70 psi)	

HSC-F1-#5-S		
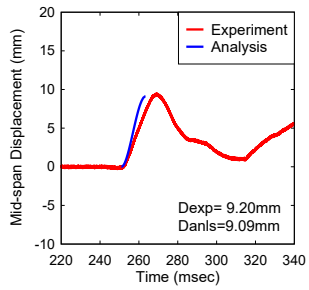	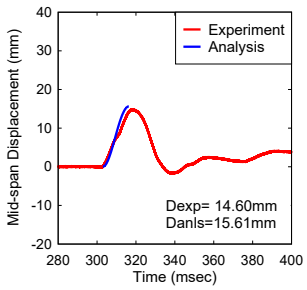	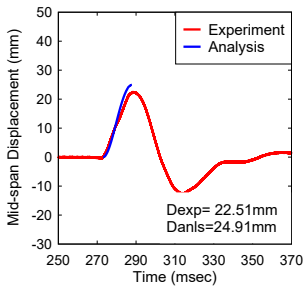
Blast 1 (17 psi)	Blast 2 (30 psi)	Blast 3b (50 psi)
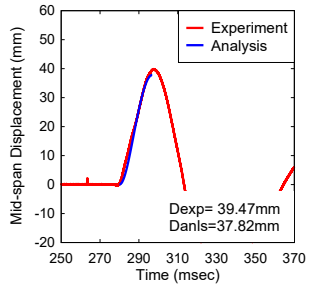	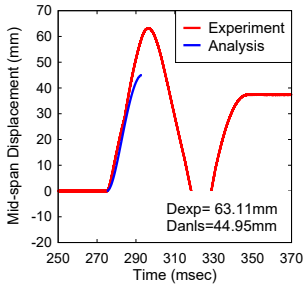	
Blast 4 (70 psi)	Blast 5 (90 psi)	

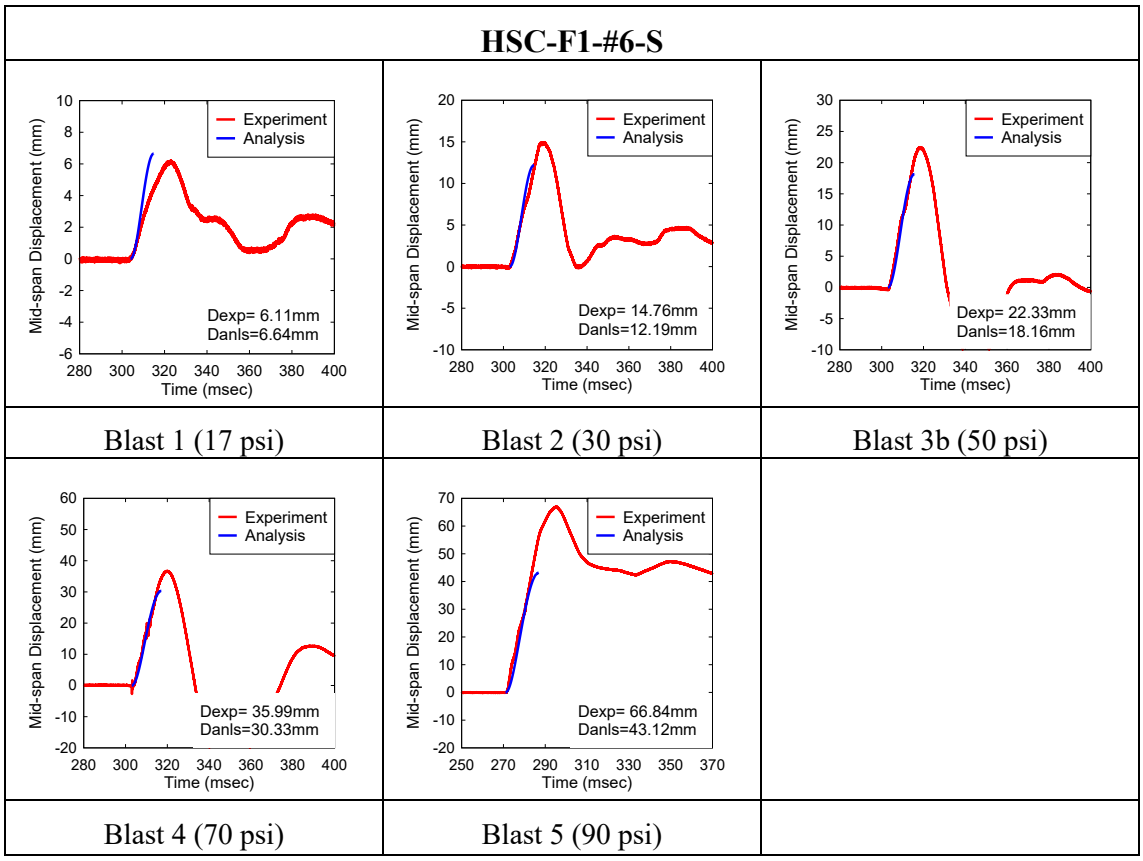

Figure 7-18 Displacement predictions time-history for HSFRC specimens

7.7.SENSITIVITY ANALYSIS

This section presents a sensitivity analysis that examines the effect of various modelling parameters on the SDOF dynamic analysis predictions. Parameters investigated include the effect of material models for concrete, HSFRC and steel reinforcement as well as the effect of the choice of dynamic increase factor model for each material.

For each parameter under investigation the analytical vs. experimental results are presented for each concrete type separately (plain concrete specimens, HSFRC specimens). Sections 7.7.1 and 7.7.2 examine the effect of material model selection (concrete and steel) on the analytical predictions for the plain concrete and HSFRC specimens, respectively. Sections 7.7.3 and 7.7.4 examine the effect of DIF model on the analytical predictions for the plain concrete and HSFRC specimens, respectively.

In all cases, only one modelling parameter is varied at a time, with the analysis results compared to those obtained using the default material/DIF models presented in Table 7-6.

7.7.1. EFFECT OF MATERIAL MODEL SELECTION (PLAIN CONCRETE SPECIMENS)

This section examines the effect of material model (concrete and steel) on the analytical predictions for the plain SCC and HSC specimens (SCC-F0-#4-S, HSC-F0-#4-S, HSC-F0-#5-S, HSC-F0-#6-S). Case-0 corresponds to the default material models presented in Table 7-11 (concrete: Popovics, steel: ITG-6). Case-1 examines the effect of concrete model, whiles Cases 2-3 examine the effect of steel model. The DIF values were kept constant for all cases and correspond to the default DIF models presented in Table 7-6.

7.7.1.1.Effect of concrete compression model

Two unconfined concrete compression models were considered for the plain concrete specimens. Table 7-11 shows the model and DIF combinations for Case-0 and Case-1. The only difference between the two cases was the concrete model; Case-0 (Default) was run using the Popovics (1973) model, while Case-1 used the Cusson & Paultre (1995) model. The average displacement ratios for all specimens (as well as the No. 4 and No. 5 specimens only) can be found in Table 7-12. Figure 7-19 shows bar chart comparisons of the Case-0 & Case 1 analytical-to-experimental displacement ratios for each specimen, for all blast scenarios.

Considering all of the blast scenarios for the No. 4 and No. 5 specimens, the Case-1 combination results in an average displacement ratio ($\delta_{anls}/\delta_{exp}$) of 106% for the plain concrete series, with a standard deviation of 0.140. In comparison, the average displacement ratio was 105.5% and the standard deviation was 0.126 under the default Case-0 combination. Similarly, when all plain concrete specimens are considered (No.4, 5 and 6), the average displacement ratio under Case-1 combination was 99.3% with a standard deviation of 0.171. This can be compared to an average displacement ratio of 98.8% and standard deviation of 0.162 under the default Case-0 combination. In general, the results show that the choice of unconfined concrete model in compression had little to no effect on the analytical predictions, although relatively better results are obtained using the Popovics (1973) model. This can be explained by the fact that the stress-strain curves of both models show almost identical ascending branches as shown in Figure 7-2 (a), and it is this portion of the stress-strain curve which has a greater influence on the predictions of maximum beam displacements. The descending branch of the Cusson & Paultre (1995) model is relatively stiffer, and this explains the slightly lower analytical displacement values obtained using this model.

Table 7-11 Sensitivity analysis combination cases - plain concrete

	Combination	Concrete models		Steel models
		Compression [DIF]	Tension [DIF]	Tension [DIF]
Default	Case-0	Popovics (1973) [1.3]	Linear slope	ACI Group ITG-6 (2010) [1.1]
Concrete in Compression	Case-1	CP (1995) [1.3]	Linear slope	ACI Group ITG-6 (2010) [1.1]

Table 7-12 Summary of analysis results for model selection – concrete in compression

Combinations	Avg. $\delta_{anls}/\delta_{exp}$	Standard Deviation	Avg. $\delta_{anls}/\delta_{exp}$ (Only No.4 and No.5 specimens)	Standard deviation (Only No.4 and No.5 specimens
Case-0	98.8%	0.162	105.5%	0.126
Case-1	99.3%	0.171	106.0%	0.140

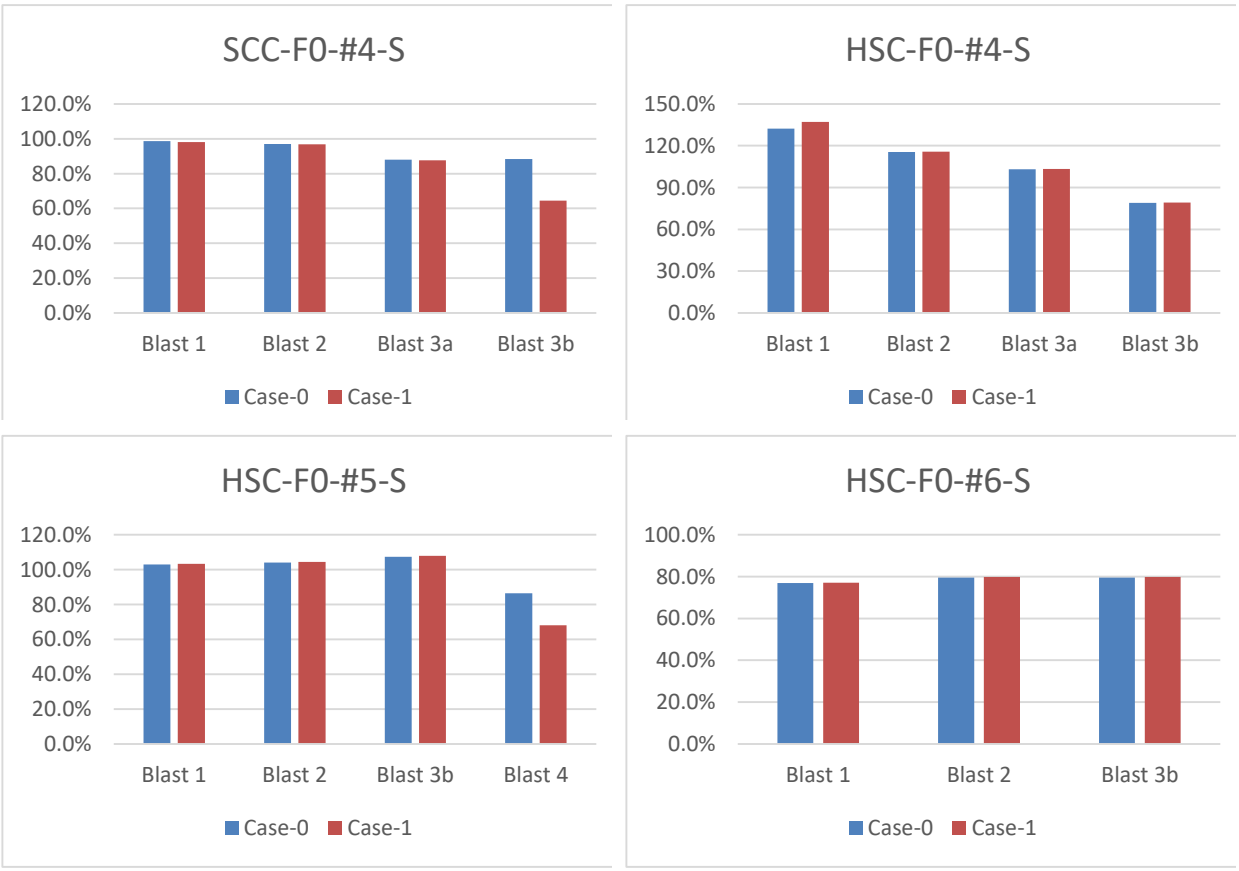

Figure 7-19 Sensitivity analysis for plain concrete specimens – effect of concrete compression model

7.7.1.2. Effect of steel reinforcement model

In order to examine the effect of steel reinforcement model three analysis cases are considered in this section. Table 7-13 shows the model combinations for Case-0, Case-2 and Case-3. The default combination (Case-0) was run with the ACI ITG-6 steel stress-strain model, Case-2 was run using the stress-strain curves obtained from the experimental coupon tests for the No. 4/5/6 rebar, and finally the Case-3 analysis utilized a bilinear design stress-strain curve with yield strength of 690 MPa. All other modelling parameters (concrete models and DIF models) were kept constant. The average displacement ratios for the different cases, considering all concrete specimens can be found in Table 7-14. Figure 7-20 compares the displacement ratios for each specimen for all blast scenarios.

Considering all blast tests, and the No. 4 and 5 plain concrete specimens, Case-2 and Case-3 combinations result in average displacement ratios ($\delta_{anls}/\delta_{exp}$) of 105.9% and 108.3% respectively, with corresponding standard deviations of 0.133 and 0.132. In comparison the default combination of Case-0 yielded an average displacement ratio of 105.5% and a standard deviation of 0.126.

The results considering all blast tests and all specimens (No. 4, 5 and 6 rebar) show similar trends with average displacement ratios of 99.4%, 100.8% under Case-2 and Case-3 respectively. In comparison, the average displacement ratio was 98.8% under the default Case-0 combination.

The analysis results show that the results obtained using the ACI ITG-6 model and the experimental coupon stress-strain curves are quite similar (the results are within 1% of each other) an indicator that the ACI ITG-6 model can be used to predict the blast behaviour of reinforced concrete beams with MMFX steel reinforcement. The results also indicate that the bi-linear model with f_y = 690 MPa yielded slightly more conservative results (larger $\delta_{anls}/\delta_{exp}$ ratios).

Table 7-13 Sensitivity analysis combination cases - plain concrete

	Combination	Concrete models		Steel models
		Compression [DIF]	Tension [DIF]	Tension [DIF]
Default	Case-0	Popovics (1973) [1.3]	Linear slope	ACI Group ITG-6 (2010) [1.1]
Steel in Tension	Case-2	Popovics (1973) [1.3]	Linear slope	Coupon [1.1]
	Case-3	Popovics (1973) [1.3]	Linear slope	Bilinear [1.1]

Table 7-14 Summary of analysis results for model selection – steel in tension

Combinations	Avg. $\delta_{anls}/\delta_{exp}$	Standard Deviation	Avg. $\delta_{anls}/\delta_{exp}$ (Only No.4 and No.5 specimens)	Standard deviation (Only No.4 and No.5 specimens
Case-0	98.8%	0.162	105.5%	0.126
Case-2	99.4%	0.163	105.9%	0.133
Case-3	100.8%	0.177	108.3%	0.132

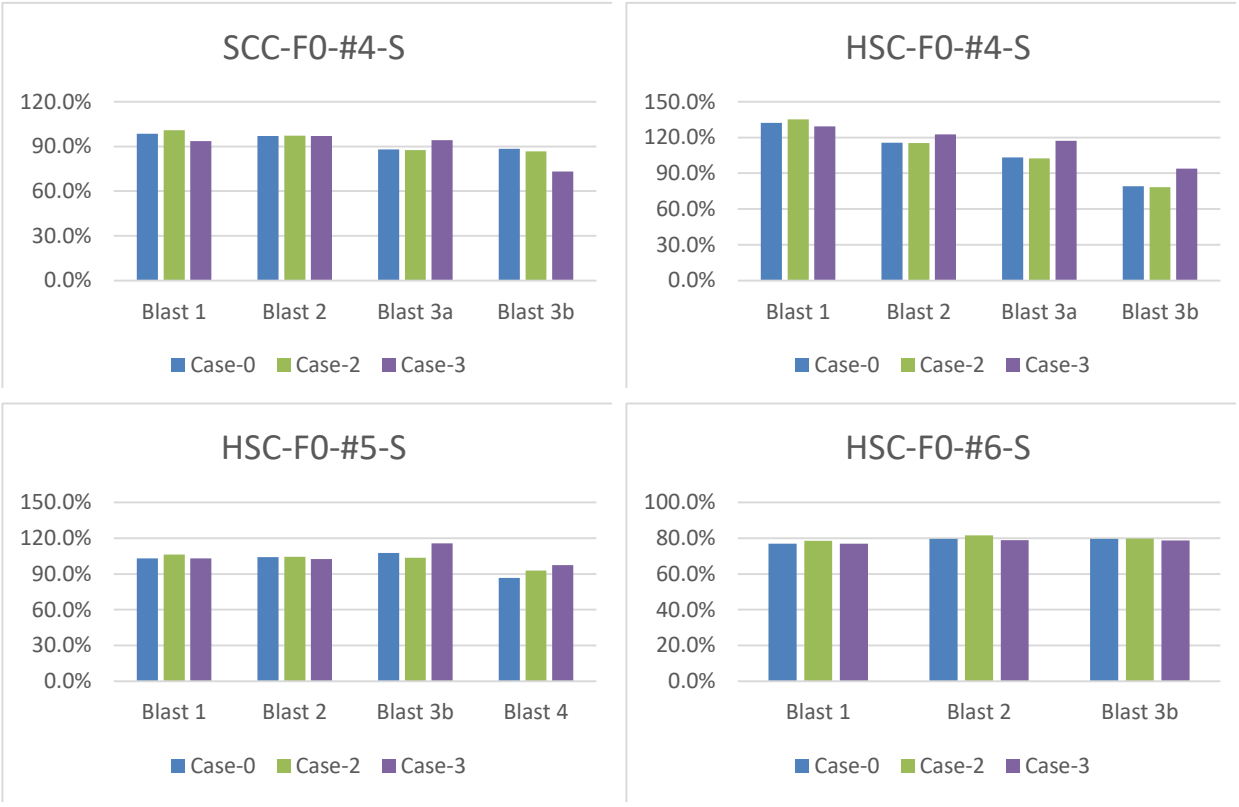

Figure 7-20 Sensitivity analysis for plain concrete – steel in tension

7.7.2. EFFECT OF MATERIAL MODEL SELECTION (HSFRC SPECIMENS)

This section examines the effect of material models on the analytical predictions for the HSFRC specimens (HSC-F1-#4-S, HSC-F1-#5-S, HSC-F1-#6-S). To examine the effect of FRC model, two compression models are considered: Ou et al. (2012) vs. Mansur et al. (1999), corresponding to Case-0 (Default) and Case-1 respectively. In all cases the tension curve is defined by the Lok and Pei (1998) model. The section also examines the effect of steel reinforcement model on the HSFRC displacement predictions with Cases 0, 2 and 3 run with different high-strength steel stress-strain curves (ACI ITG-6, coupon data, bi-linear 690 MPa).

7.7.2.1. Effect of HSFRC compression model

Table 7-15 shows the material and DIF combinations for Cases 0 and 1. Case-1 differs from Case-0 (Default) in that Case-1 analysis was run using the Ou et al. (2012) HSFRC compression model in place of the Mansur (1999) model. The average displacement ratios for the all HSFRC specimens, as well as the No. 4 and No. 5 specimens on their own, can be found in Table 7-16. Figure 7-21 includes the displacement ratios for each HSFRC specimen for all blast scenarios.

Considering the No. 4 and No. 5 HSFRC specimens and all blasts, the average analytical displacement ratio for Case-1 was 95.8% with a standard deviation of 0.085. This can be compared to the average displacement ratio of 97.3% and standard deviation of 0.085 under the default Case-0 combination. When all HSFRC specimens are considered, the average displacement ratios for Case-1 and Case-0 are 92.2% and 94.6% (standard deviations: 0.101 and 0.104).

It can be concluded that the choice of HSFRC compression model had a minor effect on the accuracy of the analytical predictions. In general, the use of the Mansur et al. (1999) model yielded more accurate displacement predictions, and this can be explained by the fact that the Mansur et al. model, which was specifically developed for high-strength FRC, was able to more closely predict the experimental HSFRC compressive stress-strain curves (the Ou et al. model generally over-estimated stiffness and post-peak response of HSFRC in compression).

Table 7-15 Sensitivity analysis combination cases - HSFRC concrete

	Combination	Concrete models		Steel models
		Compression [DIF]	Tension [DIF]	Tension [DIF]
Default	Case-0	Mansur (1999) [1.28]	Lok & Pei (1998) [1.22]	ACI Group ITG-6 (2010) [1.1]
Concrete in Compression	Case-1	Ou (2012) [1.28]	Lok & Pei (1998) [1.22]	ACI Group ITG-6 (2010) [1.1]

Table 7-16 Summary of analysis results for model selection – concrete in compression

Combinations	Avg. $\delta_{anls}/\delta_{exp}$	Standard Deviation	Avg. $\delta_{anls}/\delta_{exp}$ (Only No.4 and No.5 specimens)	Standard Deviation (Only No.4 and No.5 specimens)
Case-0	94.6%	0.104	97.3%	0.085
Case-1	92.2%	0.101	95.8%	0.085

Figure 7-21 Sensitivity analysis for HSFRC specimens– concrete in compression

7.7.2.2. Effect of steel reinforcement model

This section examines the effect of steel model on the analytical predictions for the HSFRC specimens. Table 7-17 shows the combinations for the three cases considered. Case-2 and Case-3 combinations substitute the ACI ITG-6 (2010) model in Case-0 with the experimentally obtained coupon test data and a bilinear model with yield strength of 690 MPa, respectively. The average displacement ratios for all HSFRC specimens (as well as for the No. 4 and No. 5 specimens on their own) can be found in Table 7-18. Figure 7-22 compares the displacement ratios for each specimen for all blast tests.

When considering the No. 4 and No. 5 HSFRC specimens, the average displacement ratios were 97.6% and 100.6% with standard deviations of 0.090 and 0.082 under Case-2 and Case-3 combinations respectively. In comparison, the average displacement ratio was 97.3%, with a standard deviation of 0.085 under the default Case-0 combination.

Considering all the HSFRC specimens, the average displacement ratios under Case-2 and Case-3 were 95.1% and 95.9%, with standard deviations of 0.107 and 0.110 respectively. These can be compared to the default combination of Case-0 which yielded an average ratio of 94.6% and a standard deviation of 0.104.

As was observed previously for the plain concrete specimens, the results indicate that the ACI ITG-6 and steel coupon stress-strain curves yield similar displacement predictions in the HSFRC specimens. Thus it can be concluded that the ACI ITG-6R model can be used to predict the blast response of HSFRC beams reinforced with high-strength MMFX reinforcement. It is however interesting to find that the use of the bilinear stress-strain curve resulted in a better overall prediction ratio (closer to 1.0). However, considering the limited tests which were conducted and that the ACI ITG-6 model performed better in the case of the plain concrete specimens, the use of the ACI ITG model is recommended.

Table 7-17 Sensitivity analysis combination cases - HSFRC concrete

	Combination	Concrete models		Steel models
		Compression [DIF]	Tension [DIF]	Tension [DIF]
Default	Case-0	Mansur (1999)	Lok & Pei (1998)	ACI Group ITG-6 (2010)
Steel in Tension	Case-2	Mansur (1999)	Lok & Pei (1998)	Coupon
	Case-3	Mansur (1973)	Lok & Pei (1998)	Bilinear

Table 7-18 Summary of analysis results for model selection – steel in tension

Combinations	Avg. $\delta_{anls}/\delta_{exp}$	Standard Deviation	Avg. $\delta_{anls}/\delta_{exp}$ (Only No. 4 and No. 5 specimens)	Standard Deviation (Only No. 4 and No. 5 specimens
Case-0	94.6%	0.104	97.3%	0.085
Case-2	95.1%	0.107	97.6%	0.090
Case-3	95.9%	0.110	100.6%	0.082

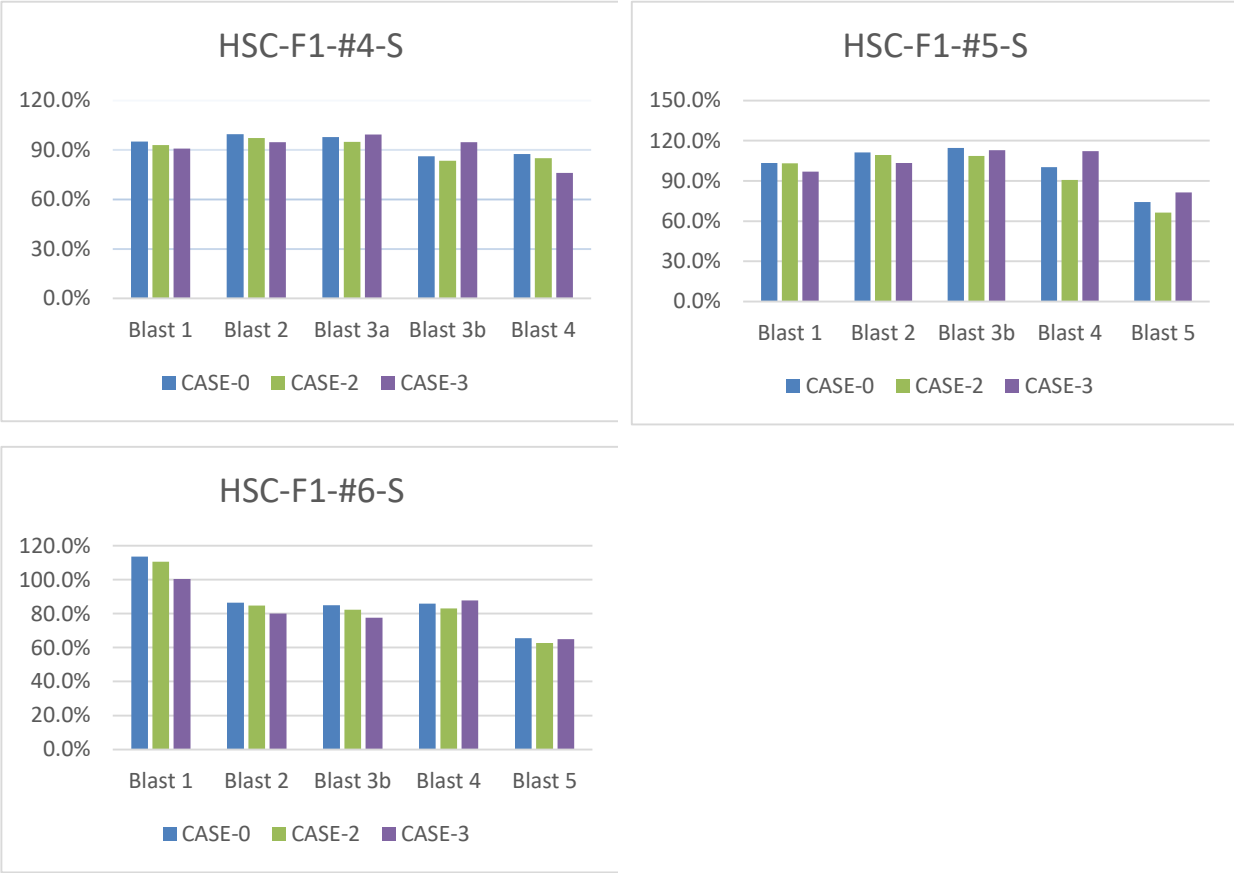

Figure 7-22 Sensitivity analysis for HSFRC specimens– steel in tension

7.7.3. EFFECT OF DYNAMIC INCREASE FACTORS (PLAIN CONCRETE SPECIMENS)

This section investigates the effect of material dynamic increase factor (DIF) combination on the dynamic analysis results for the plain concrete specimens. To isolate the effect of DIF, all material models were kept constant in the various cases which are considered (Popovics for concrete in compression, and the ACI ITG-6R for steel in tension). In the default combination (Case-0) the DIF values for concrete and steel correspond to those predicted using the Saatcioglu et al. (2011) equations; assuming a strain rate of 1.0 s^{-1} for the shock-tube experiments, the resulting DIFs are 1.3 for concrete and 1.1 for steel. Case-A and Case-B examine the effect of DIF for concrete in compression, while Case-C and Case-D investigate the effect of DIF for the steel reinforcement.

7.7.3.1. DIF equation for concrete in compression

Table 7-19 shows the model combinations for Case-0 (Default), Case-A, and Case-B. Cases A and B substitute the default Saatcioglu et al. (2011) DIF for concrete of 1.3, with DIF values of 1.19 and 1.14 as proposed by the UFC-3-340-02 (2008) and predicted by the CEB (1990) equations, respectively. The displacement ratios considering all plain concrete specimens can be found in Table 7-20. Figure 7-23 compares the displacement ratios for each specimen at all blast scenarios.

Considering the No. 4 and No. 5 plain concrete specimens, Case-A and Case-B combinations result in average displacement ratios ($\delta_{anls}/\delta_{exp}$) of 107.3% and 107.9% with standard deviations of 0.131 and 0.117, compared to the average displacement ratio of 105.5% and standard deviation of 0.126 under the default Case-0 combination.

Similarly, when considering all the plain concrete specimens, the average displacement ratios were 100.7%, 101.0% and 98.8% (with standard deviation of 0.163, 0.160 and 0.162) for combinations Case-A, B and 0.

The results indicate that the predictions were only slightly sensitive to the choice of DIF compression model. The results follow the expected trend, with the analytical-to-experimental displacement ratios increasing as the DIF values used in the analysis reduced. It was found that increasing of the DIF value from 1.14 or 1.19 to 1.3 slightly decreased the analytical displacement ratios by 2.4% and 1.8%, respectively. The Saatcioglu et al. (2011) DIF equations generally gave better predictions of displacements.

Table 7-19 Sensitivity analysis – dynamic increase factors for plain concrete specimens

	Combination	Concrete models		Steel models
		Compression	Tension	Tension
		[DIF]	[DIF]	[DIF]
Default	Case-0	Popovics (1973) [1.3]	Linear slope	ACI Group ITG-6 (2010) [1.1]
Concrete in Compression	Case-A	Popovics (1973) [1.14]	Linear slope	ACI Group ITG-6 (2010) [1.1]
	Case-B	Popovics (1973) [1.19]	Linear slope	ACI Group ITG-6 (2010) [1.1]

Table 7-20 Summary of analysis results for DIF selection – concrete in compression

Combinations	Avg. $\delta_{anls}/\delta_{exp}$	Standard Deviation	Avg. $\delta_{anls}/\delta_{exp}$ (Only No. 4 and No. 5 specimens)	Standard Deviation (Only No. 4 and No. 5 specimens)
Case-0	98.8%	0.162	105.5%	0.126
Case-A	100.7%	0.163	107.3%	0.131
Case-B	101.0%	0.160	107.9%	0.117

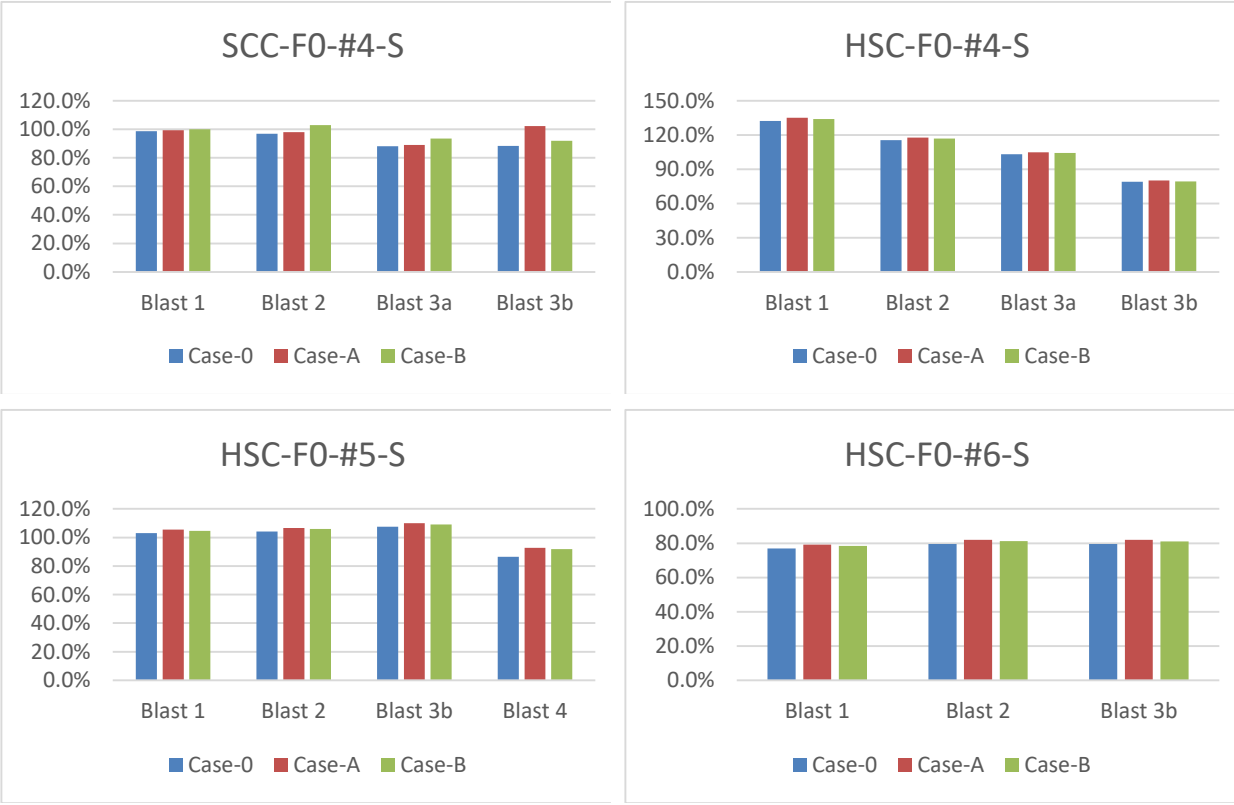

Figure 7-23 Sensitivity analysis for plain concrete – DIF for concrete in compression

7.7.3.2. DIF equation for steel in tension

Three DIF cases were considered for steel in tension. Table 7-21 shows the material and DIF combinations for the various cases. DIF values of 1.05 and 1.0 were implemented in Case-C and Case-D respectively, with the DIF kept at 1.1 for Case-0. The value of 1.05 corresponds to the DIF at ultimate stress proposed by the UFC-3-340-02 (2008). The average displacement ratios for all plain concrete specimens can be found in Table 7-22. Figure 7-24 compares the displacement ratios for each specimen under all blast scenarios.

Considering the No. 4 and No. 5 plain concrete specimens, Case-C and Case-D combinations resulted in average displacement ratios ($\delta_{anls}/\delta_{exp}$) of 110.9% and 113.7% with standard deviations of 0.131 and 0.134. In comparison, the average displacement ratio was 105.5% and the standard deviation was 0.126 under the default Case-0 combination.

Similarly, when considering all plain concrete specimens, the mean displacement ratios were 103.9% and 106.3% with standard deviations of 0.169 and 0.177 for Case-C and Case-D combinations, which compare to an average displacement ratio of 98.8% and standard deviation of 0.162 for the default Case-0 combination.

The results show that increasing the DIF for steel in tension from 1.05 to 1.10 decreased the $\delta_{anls}/\delta_{exp}$ ratio by 5.5%. This gap grew to 8.8% when comparing the results with DIF of 1.0 and 1.1. The results follow the expected trend with the ratios reducing as the DIF is increased. In general, the use of the Saatcioglu et al. (2011) equation resulted in an average displacement ratio which was closer to 1.0. It can be concluded that this default model resulted in the best overall predictions. Comparing to the results from the previous section, it can be noticed that the analysis is more sensitive to the DIF of steel when compared to the DIF of concrete.

Table 7-21 Sensitivity analysis – dynamic increase factors for plain concrete specimens

	Combination	Concrete models		Steel models
		Compression	Tension	Tension
		[DIF]	[DIF]	[DIF]
Default	Case-0	Popovics (1973) [1.3]	Linear slope	ACI Group ITG-6 (2010) [1.1]
Steel in Tension	Case-C	Popovics (1973) [1.3]	Linear slope	ACI Group ITG-6 (2010) [1.05]
	Case-D	Popovics (1973) [1.3]	Linear slope	ACI Group ITG-6 (2010) [1.0]

Table 7-22 Summary of analysis results for model selection – steel in tension

Combinations	Avg. $\delta_{anls}/\delta_{exp}$	Standard Deviation	Avg. $\delta_{anls}/\delta_{exp}$ (Only No. 4 and No. 5 specimens)	Standard Deviation (Only No. 4 and No. 5 specimens
Case-0	98.8%	0.162	105.5%	0.126
Case-C	103.9%	0.169	110.9%	0.131
Case-D	106.3%	0.177	113.7%	0.134

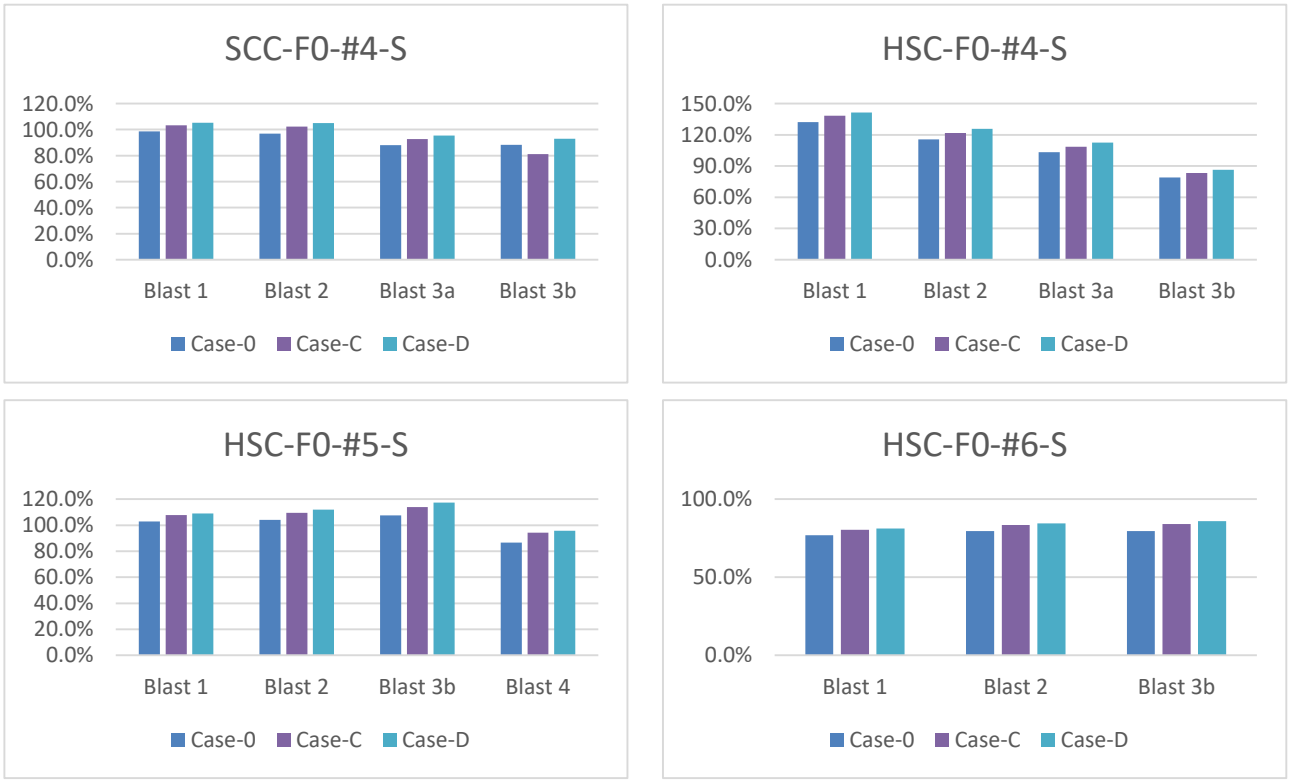

Figure 7-24 Sensitivity analysis for plain concrete – DIF for steel in tension

7.7.4. EFFECT OF DYNAMIC INCREASE FACTORS (HSFRC SPECIMENS)

In this section, the effect of DIF combination on the analytical displacement results for the HSFRC specimens is examined. In all cases the default material models were kept constant (for concrete in compression: Mansur (1999), concrete in tension: Lok and Pei (1998), steel in tension: ACI ITG-6 (2010)) and only the DIF parameters were varied. Case-A and Case-B were designed to investigate the effect of DIF for HSFRC in compression and tension, respectively. Case-C and Case-D examined the effect of steel DIF model on the analytical predictions.

7.7.4.1. DIF equation for HSFRC in compression

Two cases were considered to examine the effect of DIF of HSFRC in compression. Table 7-23 shows the material and DIF combinations for both Case-0 and Case-A. The only difference between the two cases is the use of conservative design DIF of 1.19 for HSFRC in compression for Case-A in place of the DIF of 1.28 which is used in the default Case-0 analysis. The average displacement ratios for all HSFRC specimens can be found in Table 7-24. Figure 7-25 compares the displacement ratios for each HSFRC specimen for all blast scenarios.

Considering the No. 4 and No. 5 HSFRC specimens, the average analytical displacement ratio under Case-A was 98.7% with a standard deviation of 0.087. This compares to an average displacement ratio of 97.3% and standard deviation of 0.085 under the default Case-0 combination. When including all specimens, the average displacement ratio is 96.1% with a standard deviation of 0.105 under Case-A, compared to a ratio of 94.6% and standard deviation of 0.104 for Case-0.

In general, it can be seen that the choice of DIF value for HSFRC in compression has a moderate effect on the accuracy of the analytical predictions. The results follow the expected trend with larger $\delta_{anls}/\delta_{exp}$ ratios for Case-A which utilized a more conservative DIF value. The results are generally more accurate for Case-A, which may indicate that the Zhang & Mindess model is over-predicting the DIF of high-strength SFRC in compression - further research is recommended.

Table 7-23 Sensitivity analysis – dynamic increase factors for HSFRC specimens

	Combination	Concrete models		Steel models
		Compression	Tension	Tension
		[DIF]	[DIF]	[DIF]
Default	Case-0	Mansur (1999) [1.28]	Lok & Pei (1998) [1.22]	ACI Group ITG-6 (2010) [1.1]
Concrete in Compression	Case-A	Mansur (1999) [1.19]	Lok & Pei (1998) [1.22]	ACI Group ITG-6 (2010) [1.1]

Table 7-24 Summary of analysis results for DIF selection – concrete in compression

Combinations	Avg. $\delta_{anls}/\delta_{exp}$	Standard deviation	Avg. $\delta_{anls}/\delta_{exp}$ (Only No. 4 and No. 5 specimens)	Standard deviation (Only No. 4 and No. 5 specimens
Case-0	94.6%	0.104	97.3%	0.085
Case-A	96.1%	0.105	98.7%	0.087

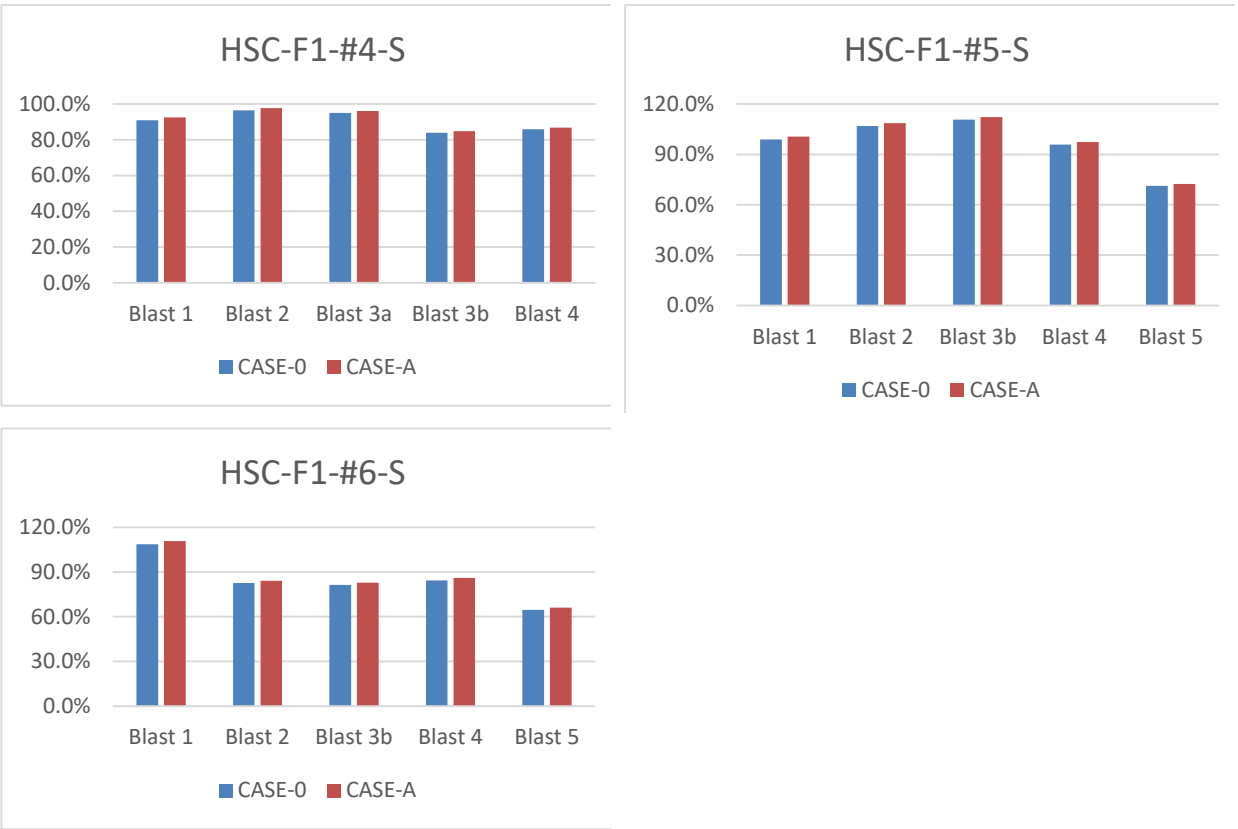

Figure 7-25 Sensitivity analysis for HSFRC specimens – DIF for concrete in compression

7.7.4.2. DIF equation for HSFRC in tension

One of the distinguishing features of HSFRC when compared to plain HSC is its ability to carry tensile stresses before and after cracking. However as noted previously, there is a lack of HSFRC tension model available in the literature. Two tension DIF cases were considered in the sensitivity analysis. Table 7-25 shows the combinations for Case-0 and Case-B. Case-B replaces the DIF value of 1.22 predicted by the Malvar and Ross (1998) model, with a more conservative DIF value of 1.0 for HSFRC in tension. The displacement ratios under both cases for all HSFRC specimens can be found in Table 7-26. Figure 7-26 compares the displacement ratios for each HSFRC beam under all blast scenarios.

For the No. 4 and No. 5 HSFRC specimens, the average displacement ratio was 101.4% (S.D. of 0.082) for the Case-B combination. This can be compared to an average displacement ratio of 97.3% (S.D. of 0.085) for the default Case-0 combination. Considering all HSFRC specimens, the average displacement ratio under Cases B and 0 are 98.2% (S.D. of 0.111) and 94.6% (S.D. of 0.104).

The results indicate that the predictions are influenced by the choice of DIF model for HSFRC in tension. In general, the predictions were more accurate (average ratio closer to 1.0) under the Case-B combination, an indicator that the more conservative DIF value of 1.0 may be more suitable when modelling the dynamic response of HSFRC in tension. Regardless, the results indicate the need for development of FRC-specific tension DIF models which can be used in the blast- design of fibre-reinforced concrete structures.

Table 7-25 Sensitivity analysis – dynamic increase factors for HSFRC specimens

	Combination	Concrete models		Steel models
		Compression	Tension	Tension
		[DIF]	[DIF]	[DIF]
Default	Case-0	Mansur (1999) [1.28]	Lok & Pei (1998) [1.22]	ACI Group ITG-6 (2010) [1.1]
Concrete in Tension	Case-B	Mansur (1999) [1.28]	Lok & Pei (1998) [1.0]	ACI Group ITG-6 (2010) [1.1]

Table 7-26 Summary of analysis results for DIF selection – concrete in tension

Combinations	Avg. $\delta_{anls}/\delta_{exp}$	Standard Deviation	Avg. $\delta_{anls}/\delta_{exp}$ (Only No. 4 and No. 5 specimens)	Standard Deviation (Only No. 4 and No. 5 specimens)
Case-0	94.6%	0.104	97.3%	0.085
Case-B	98.2%	0.111	101.4%	0.082

Figure 7-26 Sensitivity analysis for HSFRC specimens – DIF for concrete in tension

7.7.4.3. DIF equation for steel in tension

This final sensitivity analysis examines the effect of steel DIF on the HSFRC beam displacement predictions. Table 7-27 shows the combinations for Case-0, Case-C and Case-D. Case-C and Case-D combinations replace the DIF of 1.19 predicted by the Saatcioglu et al. (2011) model, with DIF values of 1.05 (based on UFC recommendation for steel DIF at ultimate stress) and a conservative value of 1.0, respectively. The average displacement ratios for the HSFRC specimens under the three scenarios can be found in Table 7-28. Figure 7-27 includes the displacement ratios for each specimen under all blast load cases.

Considering the No. 4 and No. 5 HSFRC specimens, the average l displacement ratios under Case-C and Case-D are 100.8% and 104.6% with standard deviations of 0.087 and 0.092, respectively. This can be compared to the average displacement ratio of 97.3% and standard deviation of 0.085 under the default Case-0 combination. A similar trend is observed when considering all specimens with average displacement ratios of 97.9%, 101.5% and 94.6% under Case-C, Case-D and Case-0 combinations.

The results show that analysis was sensitive to dynamic strength of the steel reinforcement, with the results following the expected trend; lower DIF = larger displacement ratios. For example, when the DIF value is increased from 1.0 to 1.1, the displacement ratios decreased by 7 percentage points. The DIF value of 1.1, calculated using the Saatcioglu et al. (2011) equation, results in acceptable prediction of the dynamic response of the HSFRC beams with high-strength reinforcement. The use of DIF of 1.0 results in more conservative predictions and may be more suitable for design purposes given the lack of experimental data related to the response of high-strength reinforcement under dynamic tension.

Table 7-27 Sensitivity analysis – dynamic increase factors for HSFRC specimens

	Combination	Concrete models		Steel models
		Compression [DIF]	Tension [DIF]	Tension [DIF]
Default	Case-0	Mansur (1999) [1.28]	Lok & Pei (1998) [1.22]	ACI Group ITG-6 (2010) [1.1]
Steel in Tension	Case-C	Mansur (1999) [1.28]	Lok & Pei (1998) [1.22]	ACI Group ITG-6 (2010) [1.05]
	Case-D	Mansur (1999) [1.28]	Lok & Pei (1998) [1.22]	ACI Group ITG-6 (2010) [1.0]

Table 7-28 Summary of analysis results for model selection – steel in tension

Combinations	Avg. $\delta_{anls}/\delta_{exp}$	Standard Deviation	Avg. $\delta_{anls}/\delta_{exp}$ (Only No. 4 and No. 5 specimens)	Standard Deviation (Only No. 4 and No. 5 specimens)
Case-0	94.6%	0.104	97.3%	0.085
Case-C	97.9%	0.106	100.8%	0.087
Case-D	101.5%	0.109	104.6%	0.092

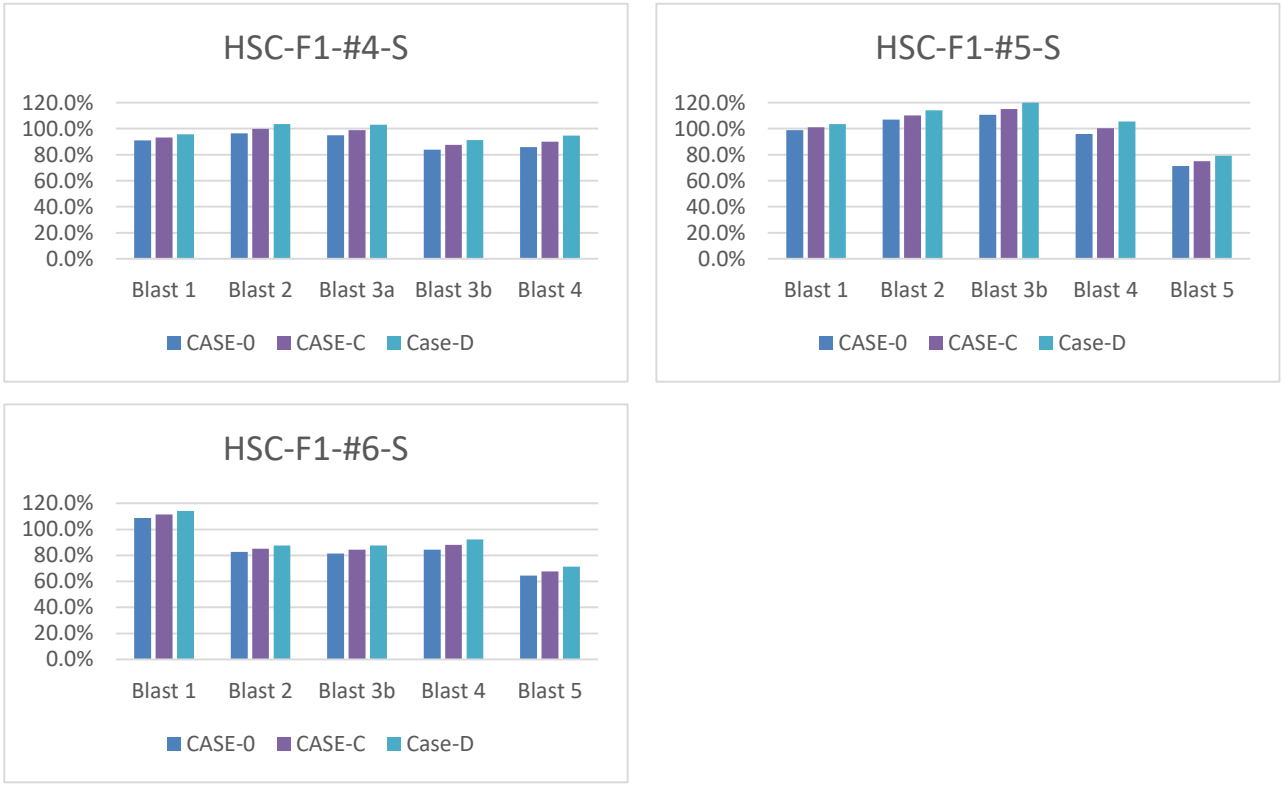

Figure 7-27 Sensitivity analysis for HSFRC specimens – DIF for steel in tension

7.8. DYNAMIC ANALYSIS POTENTIAL SOURCES OF ERROR

The maximum displacements of all the specimens were predicted using dynamic inelastic SDOF analysis. This section lists some potential sources of error which may have influenced the accuracy of the predictions:

- The specimens in this study were tested under repeated blast loads, resulting in accumulated damage from previous blast loading. The displacements at early shots were generally well predicted, however the errors became larger at later shots (e.g. Blasts 4 and 5). Shots 1 and 2 were meant to test the specimens under elastic and yield conditions and therefore the effect of repeated loading is minimal at these blasts. However, the effect of accumulated damage becomes more important at later blast loads owing to the cracking and crushing of concrete from previous test shots. This accumulated damage decreases the residual stiffness of the beams and was not accounted for in the analysis.
- The analytical predictions for No. 6 specimens were generally less accurate when compared to the companion beams with No. 4 and No. 5 reinforcement. The errors can possibly be related to the over-reinforcement of the No. 6 beams, which may have not been fully captured in the analysis.
- The analytical resistance curves generally over-predicted the pre-yield stiffness of the specimens. Furthermore, while the experimental curves show almost linear response up to peak load, the analytical curves showed a more rounded response with an initial linear branch followed by a non-linear parabolic branch. Although this non-linear response is found in the stress-strain response of the high-strength reinforcement it is less evident when examining the experimental beam resistance curves. The difference in the stiffness and shape of the resistance curves is another potential source of error in the analysis.
- Another potential source of error is the choice of plastic hinge length (assumed to be equal to the effective depth d). Some research has shown that the hinge length may be reduced for fibre-reinforced concrete structural members when compared to conventional reinforced concrete members, and this can influence the post-peak branch of the resistance curves and affect the analytical predictions.
- One final source error as shown in the sensitivity analysis is the choice of material and DIF models for concrete, HSFRC and high-strength steel reinforcement. The results are sensitive to the DIFs used in analysis and further research aimed at developing reliable DIF models for HSFRC and high-strength steel reinforcement is recommended.

CHAPTER 8. CONCLUSION

8.1. CONCLUSION

This thesis presented an experimental study which investigated the blast performance of high-strength concrete (HSC) and high-strength steel fibre-reinforced concrete (HSFRC) beams, reinforced with ASTM A1035 (MMFX) Grade 100 steel reinforcing bars. The main parameters of this research included concrete strength, steel fibres, steel reinforcement ratio, and strength of steel reinforcement.

In total, eleven beams were tested, including three beams tested under quasi-static four-point bending and eight beams tested under dynamic loads simulated using a shock-tube. The overall blast resistance, maximum and residual displacements, failure mode, crack control, damage behaviour and secondary fragmentation were considered as the main criteria to judge the behaviour of the specimens under dynamic loading. For the static tests, the main criteria included ultimate strength, mid-span displacement at failure, toughness, ductility and failure mode. The conclusions from the experimental research program can be summarized below:

- Increasing the longitudinal reinforcement ratio of the high-strength steel was found to improve the overall blast resistance of the HSC and HSFRC beams under dynamic loading. It was also effective in reducing maximum and residual displacements at equivalent blast loads. In terms of static response, reinforcing the HSC beams with higher reinforcement ratio led to an increase in ultimate strength, with a reduction in ductility;
- The results indicate the importance of carefully considering the reinforcement ratio in beams reinforced with high-strength bars. In the HSC series, the use of 2 - No. 6 bars led to over-reinforced conditions, which led to brittle failures under static and blast loads. The reinforcement ratio should be kept below balanced conditions to ensure an appropriate level of ductility and to fully utilize the strength of the ASTM A1035 bars;
- The dynamic results show the importance of ensuring beams with ASTM A1035 bars have sufficient transverse reinforcement to prevent brittle shear failures. In the SCC series, increasing the reinforcement from 2 - No. 4 to 2 - No. 5 bars was found to change the failure mode from flexure to shear owing to the increase in shear demand and insufficient amount of transverse reinforcement.
- Provision of 1% steel fibres significantly improved the blast behaviour of the high-strength concrete beams with high-strength bars. The addition of fibres led to increased blast load capacity, with a reduction of maximum and residual displacements at equivalent blasts. Reinforcing the beams with steel fibres also greatly reduced secondary fragmentation and increased damage tolerance.
- Concrete strength was found to have a moderate effect on the blast response of the beams in the No. 4 series, where HSC led to reduced displacements when compared to NSC. In the No. 5 series, the use of HSC increased shear capacity, preventing brittle shear failure,

and allowed the beam to resist a higher magnitude of blast load before failure. However, the HSC specimens tended to be more brittle, with more severe damage at failure.

- The responses of the specimens in this study were compared to those of a companion set of beams constructed with normal-strength reinforcement. Under static loads, plain HSC specimens with high-strength steel bars had higher ultimate load resistance, but reduced ductility. It is also noted that the specimens with conventional steel showed a clear yield plateau in their plastic response, while the MMFX specimens showed no distinct yield point and more limited plastic deformation capacity. Nonetheless, the benefits of using high-strength MMFX bars was clear in the dynamic test series, where the higher strength reinforcement led to increased blast resistance and reduced displacements at equivalent blasts. The provision of fibres further improved the blast performance of the beams reinforced with high-strength bars.

Dynamic inelastic analysis was used to predict the response of the test specimens. Resistance curves were first developed using dynamic material models for HSC, HSFRC and high-strength reinforcement. SDOF analysis was then conducted using the software *RCBlast*. The effect of various modelling parameters on the analytical predictions was also investigated using a sensitivity analysis. The analytical procedure was also used to predict the resistance curves of the statically tested beams. The conclusions from the analytical study are summarized below:

- The SDOF method, with appropriate development of dynamic resistance functions, was able to accurately predict the dynamic response of the beams. One potential source of error includes the over-estimation of beam stiffness in the analytical resistance curves.
- The sensitivity analysis showed that the Popovics (1973) model for plain concrete in compression; Mansur (1999) & Lok and Pei (1998) models for HSFRC in compression/tension and ACI ITG-6R (2011) model for high-strength steel in tension, resulted in the most accurate predictions when compared to all other model combinations.
- The DIF equations proposed by Saatcioglu et al. (2011) for concrete in compression, Zhang & Mindness (2011) for HSFRC in compression, with conservative values of 1.0 for the DIFs of high-strength steel and HSFRC in tension led to accurate analytical predictions. Using a DIF of 1.1 for high-strength steel, corresponding to the value at ultimate stress in the Saatcioglu et al. (2011) model, also resulted in acceptable analytical predictions of maximum displacements.
- The results also indicate the need to develop appropriate strain-rate sensitive material models for HSFRC in tension. Using the Malvar and Ross (1998) model may over-estimate the dynamic strength of HSFRC in tension.
- Analysis using the design DIF factors of the UFC-3-340-02 (2008) guidelines resulted in more conservative predictions of blast response when compared to the strain-rate sensitive models proposed by other researchers, with the analysis-to-experimental displacement ratio generally being less than 1.0.

- Prediction of the static response of HSC beams using either the Ramberg-Osgood (R-O) function, ACI ITG-6R expressions or coupon stress-strain data for high-strength steel, resulted in acceptable prediction of the experimental static resistance curves, although stiffness was over-estimated. The use of bi-linear stress-strain curves with more conservative design yield strengths of 550 MPa or 690 MPa resulted in conservative predictions of beam ultimate resistance.

8.2. RECOMMENDATIONS FOR FUTURE

The following recommendations for future research are suggested:

- Only a limited number of static tests were conducted in this study. Further tests examining the static flexural response of HSFRC beams reinforced with high-strength reinforcement is recommended;
- Further research examining the shear behaviour of HSC and HSFRC beams reinforced with high-strength reinforcement under static and blast loads;
- The effect of shear-span to depth ratio on the flexural response of HSC and HSFRC beams warrants further study;
- The effects of fibre properties (type, length, aspect-ratio, content) on the blast response of HSFRC beams tested under blast loads also requires further investigation;
- Further studies on the blast behaviour of other types of structural members built with HSC or HSFRC and high-strength reinforcement (columns, slabs and walls);
- Research leading to the development of reliable strain-rate dynamic increase factor models for HSFRC in tension and high-strength reinforcement;
- Finite element modelling of the blast response of reinforced concrete beams built with high-strength concrete, high-strength fibre-reinforced concrete and high-strength steel.

REFERENCES

Adhikary, S. D., Li, B., & Fujikake, K. (2014). Effects of high loading rate on reinforced concrete beams. ACI Structural journal, 111(3), 651.

Ashour, S. A., Hasanain, G. S., & Wafa, F. F. (1992). Shear behaviour of high-strength fibre reinforced concrete beams. Structural Journal, 89(2), 176-184.

ASTM A1035/A1035M-11. (2011). Standard Specification for Deformed and Plain, Low-Carbon, Chromium, Steel Bars for Concrete Reinforcement.

ASTM C 143. (2010). Standard Test Method for Slump of Hydraulic-Cement Concrete.

ASTM C1609. (2006). Standard Test Method for Flexural Performance of Fibre Reinforced Concrete (using Beam with Third-point Loading).

ASTM International. (2016). ASTM A1035/A1035M-16a Standard Specification for Deformed and Plain, Low-Carbon, Chromium, Steel Bars for Concrete Reinforcement. Retrieved from http://dx.doi.org/10.1520/A1035_A1035M-16A

ASTM, A. (2014). C1611 Standard test method for slump flow of self-consolidating concrete.

Bencardino, F., Rizzuti, L., Spadea, G., & Swamy, R. N. (2008). Stress-strain behaviour of steel fibre-reinforced concrete in compression. Journal of Materials in Civil Engineering, 20(3), 255-263.

Bentz, E. C. (2000). Sectional analysis of reinforced concrete members (Doctoral dissertation, University of Toronto).

Burrell, R. (2012). Performance of steel fibre reinforced concrete columns under shock tube induced shock wave loading. (M.A.Sc. thesis). University of Ottawa, Ottawa

Burrell, R. P., Aoude, H., & Saatcioglu, M. (2014). Response of SFRC columns under blast loads. Journal of Structural Engineering, 141(9), 04014209.

Casanova, P., & Rossi, P. (1999). High-strength concrete beams submitted to shear: steel fibers versus stirrups. Special Publication, 182, 53-68.

CEB-FIP (1993). Model Code 90 for concrete structures. Federation international de la preconstraint, CEB Bulletin No. 213/214, Paris.

Cheng, M. Y., & Giduquio, M. B. (2014). Cyclic Behaviour of Reinforced Concrete Flexural Members Using High-Strength Flexural Reinforcement. ACI Structural Journal, 111(4), 893.

Cohen, M. I. (2012). Structural behaviour of self-consolidating steel fibre reinforced concrete beams.

Collins, M., & Mitchell, Denis. (n.d.). Prestressed concrete structures (Prentice-Hall international series in civil engineering and engineering mechanics). Englewood Cliffs, N.J.: Prentice Hall.

Cusson, D., & Paultre, P. (1995). Stress-strain model for confined high-strength concrete. Journal of Structural Engineering, 121(3), 468-477. doi:10.1061/(ASCE)0733-9445(1995)121:3(468)

de Dios Garay-Moran, J., & Lubell, A. S. (2016). Behaviour of Deep Beams Containing High-Strength Longitudinal Reinforcement. ACI Structural Journal, 113(1), 17.

Desalegne, A. S., & Lubell, A. S. (2010). Shear Behaviour of Concrete Slabs Longitudinally Reinforced with High-Performance Steel. ACI Structural Journal, 107(2), 228.

Desalegne, A. S., & Lubell, A. S. (2015). Shear in Concrete Beams Reinforced with High-Performance Steel. ACI Structural Journal, 112(6), 783.

Dwairi, H., Dawood, M., Rizkalla, S., & Faza, S. Shear and Flexural Behaviour of Concrete Members Reinforced with MMFX Steel.

Feldman, A., Siess, C. P. (1958). Investigation of resistance and behaviour of reinforced concrete members subjected to dynamic loading, part I (No. 62 326). ILLINOIS UNIV URBANA ENGINEERING EXPERIMENT STATION.

Feldman, A., Siess, C. P. (1959). Investigation of resistance and behaviour of reinforced concrete members subjected to dynamic loading, part II (No. 62 326). ILLINOIS UNIV URBANA ENGINEERING EXPERIMENT STATION.

Feldman, A., Siess, C. P. (1962). Investigation of resistance and behaviour of reinforced concrete members subjected to dynamic loading, part III (No. 62 326). ILLINOIS UNIV URBANA ENGINEERING EXPERIMENT STATION.

Fujikake, K., Li, B., & Soeun, S. (2009). Impact response of reinforced concrete beam and its analytical evaluation. Journal of structural engineering, 135(8), 938-950.

Guan, Q., Zhang, P., and Xie, X. (2013). Flexural Behaviour of Steel Fibre Reinforced High Strength Concrete Beams, Research Journal of Applied Sciences, Engineering and Technology 6(1): 1-6, 2013

Gustafsson, J., & Noghabai, K. (1999). Steel fibers as shear reinforcement in high strength concrete beams. NORDIC CONCRETE RESEARCH-PUBLICATIONS-, 22, 35-52.

Hassan, T. K., Seliem, H. M., Dwairi, H., Rizkalla, S. H., & Zia, P. (2008). Shear behaviour of large concrete beams reinforced with high-strength steel. ACI Structural Journal, 105(2), 173.

Hognestad, E. (1951). Study of combined bending and axial load in reinforced concrete members. University of Illinois. Engineering Experiment Station. Bulletin; No. 399.

Ibarra, L., & Bishaw, B. (2016). High-Strength Fibre-Reinforced Concrete Beam-Columns with High-Strength Steel. ACI Structural Journal, 113(1), 147.

Jacques, E. (2014). RCBLAST (Version 0.5.1). Retrieved from www.rcblast.ca

Jacques, E. (2016). Performance Characteristic of reinforced concrete bond at high strin-rates. PH. D. Thesis, University of Ottawa, Ottawa

Jacques, E., Lloyd, A., & Saatcioglu, M. (2012). Predicting reinforced concrete response to blast loads. Canadian Journal of Civil Engineering, 40(5), 427-444. doi:10.1139/l2012-014

Kang, T. H., Kim, W., Massone, L. M., & Galleguillos, T. A. (2012). Shear-Flexure coupling behaviour of steel fibre-reinforced concrete beams. ACI Structural Journal, 109(4), 435.

Kwak, Y. K., Eberhard, M. O., Kim, W. S., & Kim, J. (2002). Shear strength of steel fibre-reinforced concrete beams without stirrups. ACI Structural Journal, 99(4), 530-538.

Lee, J. Y., Lee, D. H., Lee, J. E., & Choi, S. H. (2015). Shear Behaviour and Diagonal Crack Width for Reinforced Concrete Beams with High-Strength Shear Reinforcement. ACI Structural Journal, 112(3), 323.

Magnusson, J. (2006). Fibre reinforced concrete beams subjected to air blast loading. International Journal of Nordic Concrete Research, (35), 18-34.

Magnusson, J. (2007). Structural concrete elements subjected to air blast loading.

Magnusson, J., Ansell, A., & Hansson, H. (2010). Air-blast-loaded, high-strength concrete beams. Part II: Numerical non-linear analysis. Magazine of Concrete Research, 62(4), 235-242.

Magnusson, J., Hallgren, M., & Ansell, A. (2010). Air-blast-loaded, high-strength concrete beams. Part I: Experimental investigation. Magazine of Concrete Research, 62(2), 127-136.

Malvar, L. J. (1998). Review of static and dynamic properties of steel reinforcing bars. ACI Materials Journal-American Concrete Institute, 95(5), 609-616.

Malvar, L. J., & Ross, C. A. (1998). Review of strain rate effects for concrete in tension. Materials Journal, 95(6), 735-739.

Mansur, M. A., Chin, M. S., & Wee, T. H. (1999). Stress-strain relationship of high-strength fibre concrete in compression. Journal of materials in civil engineering, 11(1), 21-29.

Mast, R. F., Dawood, M., Rizkalla, S. H., & Zia, P. (2008). Flexural strength design of concrete beams reinforced with high-strength steel bars. ACI Structural Journal, 105(5), 570.

Munikrishna, A., Hosny, A., Rizkalla, S., & Zia, P. (2011). Behaviour of concrete beams reinforced with ASTM A1035 grade 100 stirrups under shear. ACI Structural Journal, 108(1), 34.

Narayanan, R., & Darwish, I. Y. S. (1987). Use of steel fibres as shear reinforcement. Structural Journal, 84(3), 216-227.

NCHRP Report 679(2011). Design of concrete structures using high-strength steel reinforcement, WASHINGTON, D.C.

Ngo, T., Mendis, P., & Krauthammer, T. (2007). Behaviour of ultrahigh-strength prestressed concrete panels subjected to blast loading. Journal of Structural Engineering, 133(11), 1582-1590. doi:10.1061/(ASCE)0733-9445(2007)133:11(1582)

Noghabai, K. (2000). Beams of fibrous concrete in shear and bending: experiment and model. Journal of structural engineering, 126(2), 243-251.

Oh, B.H. and Shin, S.B. (1987). "Dynamic behaviour of concrete in compression," Structural Mechanics in Reactor Technology, Vol H (Concrete and Concrete Structures), edited by F.H. Wittman (Balkema, Rotterdam, 1987), pp. 293-298.

Ou, Y.-H., Tsai, M.-S., Liu, K.-Y., & Chang, K.-C. (2012). Compressive behaviour of steel-fibre-reinforced concrete with a high reinforcing index. Journal of Materials in Civil Engineering, 24(2), 207-215. doi:10.1061/(ASCE)MT.1943-5533.0000372

Popovics, S. (1973). A numerical approach to the complete stress-strain curve of concrete. Cement and concrete research, 3(5), 583-599.

Russell, H. G., Ghosh, S. K., & Saiidi, M. (2011). Design Guide for Use of ASTM A1035 High-Strength Reinforcement in Concrete Bridge Elements with Consideration of Seismic Performance. Henry G. Russell, Inc, Glenview, IL, SK Ghosh Associates Inc., Palatine, IL, and University of Nevada, Reno, Nevada.

Saatcioglu, M., Lloyd, A., Jacques, E., Braimah, A., & Doudak, G. (2011). Focused research for development of a CSA standard on design and assessment of buildings subjected to blast loads. Interim report submitted to Public Works and Government Services Canada, Hazard

Mitigation and Disaster Management Research Centre, University of Ottawa, Ottawa, Canada.

Shahrooz, B. M. (2011). Design of concrete structures using high-strength steel reinforcement (Vol. 679). Transportation Research Board.

Shahrooz, B. M., Reis, J. M., Wells, E. L., Miller, R. A., Harries, K. A., & Russell, H. G. (2009). Flexural Behaviour and Design with High-Strength Bars and Those without Well-Defined Yield Point. University of Cincinnati, Department of Civil and Environmental Engineering, Cincinnati, OH.

Stolz, A., Fischer, K., Roller, C., & Hauser, S. (2014). Dynamic bearing capacity of ductile concrete plates under blast loading. International Journal of Impact Engineering, 69, 25-38.

Sumpter, M. S. (2007). Behaviour of high performance steel as shear reinforcement for concrete beams.

Tahenni, T., Chemrouk, M., & Lecompte, T. (2016). Effect of steel fibres on the shear behaviour of high strength concrete beams. Construction and Building Materials, 105, 14-28.

Talboys, L. N., & Lubell, A. S. (2014). Shear in Steel Fibre-Reinforced Concrete Slabs Reinforced with High-Strength Steel. ACI Structural Journal, 111(6), 1431.

Tavallali, H., Lepage, A., Rautenberg, J. M., & Pujol, S. (2014). Concrete Beams Reinforced with High-Strength Steel Subjected to Displacement Reversals. ACI Structural Journal, 111(5), 1037.

Thiagarajan, G., Kadambi, A. V., Robert, S., & Johnson, C. F. (2015). Experimental and finite element analysis of doubly reinforced concrete slabs subjected to blast loads. International Journal of Impact Engineering, 75, 162-173.

Wight, J., & MacGregor, James G. (n.d.). Reinforced concrete: Mechanics and design (6th ed.). Upper Saddle River, NJ: Pearson.

Wight, J., & MacGregor, James G. (n.d.). Reinforced concrete: Mechanics and design. (5th ed. / James K. Wight, James G. MacGregor. ed.). Upper Saddle River, N.J.: Pearson Prentice Hall.

Wiss, Janney, Elstner Associates, Inc. (2013). Determination of Yield Strength for Non-prestressed Steel Reinforcement, Pasadena, California.

Zhang, L., & Mindess, S. (2011). Dynamic compressive toughness of high strength fibre reinforced concrete. Special Publication, 281, 1-21.